Development of polymer films embedded with anisotropic metal nanoparticles and a photosensitizer dye for antimicrobial purposes

Francesco Rossi

A thesis submitted to the University College of London for the degree of Doctor of Philosophy in the Faculty of Mathematical and Physical Science, Department of Physics and Astronomy, Biophysics.

UCL Healthcare Biomagnetic and Nanomaterials Laboratory (UK), Institute of Materials Research and Engineering, A*STAR Agency for Science, Technology and Research, Singapore.

July 2020

Declaration of Originality

I, Francesco Rossi, confirm that the work presented in this thesis is my own. Where information has been derived from other sources, I confirm that this has been indicated in the thesis.

Abstract

The infections caused by drug resistant bacteria are an increasing concern for the health systems around the world, both for their cost and causality rate. An effective strategy to combat these infections is to prevent them, improving the disinfection of facilities where high concentrations of drugs are used.

This research presents a novel polymeric antimicrobial film containing gold nanorods (Au NRs) or nanostars (NSs) and a photosensitizer dye, able to kill bacteria by generating reactive oxygen species (ROS), when exposed to light.

Two types of anisotropic nanoparticles were synthetized and characterized with multiples techniques. While the introduction of the nanoparticles in the polymer film and the dye diffusion was followed through UV-vis spectroscopy.

Interactions between dye and gold NRs/NSs were studied inside the film and in solution. The surface plasmon resonance (SPR) of the particles, simulated with the finite-difference time-domain (FDTD) method was used to predict their coupling with the dye. While, the overlapping between SPR and dye absorption were confronted with the amount of ROS produced by the film.

The results against bacteria were calculated counting the surviving colony forming unit (cfu) after exposure to the activated film. Using the simulations, the parts of the SPR absorption participating to the plasmonic coupling were identified. While the efficiency against Gram(+) and Gram(-) bacteria was explored.

The films were more effective against *E. coli* than *S. aureus*. The film modified with AuNSs could kill 5 orders of magnitudes (5-log) of *E. coli* in 4 h and 4-log when modified with AuNRs. For *S. aureus*, it was able to kill 2.5-log when containing AuNSs and 3-log with AuNRs. There was direct dependency between ROS production and Gram(-) population reduction, at the same time the effect against Gram(+) suggests some difference in the type of ROS produced by the film according to the nanoparticles used.

Impact Statement

The rise in cases of diseases caused by drug resistant bacteria is causing a grievous cost in human lives and an increasing drain of resources in worldwide healthcare systems.[1] For example, resistant bacteria caused the death of 72000 hospital patients in the US in the 2019[2] and as much as 33000 causalities in the EU and costed to their sanitary systems more than 9 billion of dollars (US, 2019) and 1.1 billion of euros (EU, 2017) respectively.[3,4]

The development of new antibiotics is a slow process and new drugs will be as vulnerable to bacteria resistance as the one used nowadays. One of the viable methods to contain the spread of drug resistant bacteria is to improve the sterilization techniques used in facilities where the contamination could generate risk for the public health (food facilities and medical practice). Focusing on the surfaces situated in locations where high concentrations of antibiotics are used and the selection of drug resistant bacteria is more likely to be triggered.

The most common routine disinfection methods, as wiping with detergents and disinfectants, are not completely effective and require a constant effort from the working staff to maintain an acceptable sterility level.[5,6] Introducing periodical terminal sterilization procedures, as high intensity contactless disinfection methods can improve the efficiency of the cleaning process. But, they also shorten the lifetime of the surfaces and limit the access to the area while in use.[7]

To overcome the limitations of the traditional methods, it is necessary to develop new approaches. The solution explored in this thesis relies on the creation of light activated films, which are able to kill the bacteria on their

surface, when exposed to a commercially available white lamp without requiring the direct intervention of specialized personnel.

The work presented in this thesis offer some important contributions: i) to the study of the interactions between light, noble metal nanoparticles and photoactive molecules, dyes, contained inside a polymeric film; ii) to comprehend the effect of these interaction on the dyes capability of generating ROS; iii) to the theoretical and experimental analysis of the relation between the structural parameters of the nanoparticles (e.g. size and anisotropy) and the effectivity of the film against bacteria and iv) to the understanding of the efficiency of the film against different types of bacteria (e.g. Gram(+) and Gram(-)).

Furthermore, the work proposed in this thesis has potentials to be scaled up to a level that entire rolls of modified PU films to offer an easily deployable for renewable medical surfaces that require high levels of sterility (< 3/5 cfu/cm^2). The commercially availability of these type of antimicrobial surfaces could be important to reduce the incidence of hospital acquired infections (HAI) saving the lives of tens of thousands of patients and billions of dollars for the sanitary systems around the world every year.[8,9] This was a complex and multidisciplinary work, including aspects of nanotechnology, physical-chemistry, microbiology and material science and it led to the publication of two papers on a bio-material focused high impact international scientific journal. The first one focused on the antimicrobial properties against *E. coli* of a film modified with gold nanorods,[10] and the second aimed to understand the effect of the surface plasmon resonance of anisotropic gold nanoparticles on the antimicrobial activity of the film against Gram(+) and Gram(-) bacteria.[11]

The experiments in this thesis were conducted either in the Institute of Materials Research and Engineering (IMRE) Singapore or in the Healthcare Biomagnetic and Nanomaterials Laboratories of UCL in the United Kingdom. The work was funded by the agency for science, technology and research (A*STAR) of Singapore thanks to the A*STAR Research Attachment Programme (ARAP) IMRE A*STAR-UCL collaboration program. Thanks to the training and support of scientists of different fields of specialization, who was creating a worldwide research network, fundamental for the development of the medical application of nanotechnology.

Table of Contents:

Declaration of Originality **2**

Abstract **3**

Impact Statement **5**

Table of Contents: **8**

List of Figures: **14**

List of Tables: **23**

List of Equations: **24**

List of Abbreviations: **25**

Acknowledgments: **29**

Chapter 1: Introduction **30**

1.1. Background information **32**

1.1.1. Gold nanostructures 32

1.1.1.1. Historical notes 32

1.1.1.2. Relation between surface and volume in nanoparticles 33

1.1.2. Anisotropic nanoparticles 36

1.1.2.1. Seed mediated synthesis 38

1.1.2.2. Synthesis of gold nanorods 39

1.1.2.3. Synthesis of gold nanostars 42

1.1.3. Nanoparticles interaction with light 43

1.1.3.1. Surface plasmon resonance 43

1.1.3.2. Photo-induced hyperthermia 50

1.1.4. Photosensitizer dyes 52

1.1.4.1. Light activated therapy and photosensitizers 52

1.1.4.2. Crystal Violet 53

1.1.4.3. Light activated ROS production 55

1.1.5. Plasmonic coupling 57

1.1.6. Disinfection of medical facilities 61
1.1.6.1. Routine disinfection methods 61
1.1.6.2. Nosocomial infections 62
1.1.7. Gram positive bacteria 62
1.1.7.1. Gram positive model: S. aureus 66
1.1.8. Gram negative bacteria 67
1.1.8.1. Gram negative model: E. coli 71
1.2. Recent developments in antimicrobial surfaces 72
1.2.1. Low adhesion surfaces 73
1.2.2. Surfaces able to release antimicrobial substances 74
1.2.3. Light activated antimicrobial surfaces 74
Chapter 2: Synthesis and characterization of anisotropic gold nanoparticles 77
2.1. Introduction 77
2.2. Materials 78
2.3. Methods 79
2.3.1. Synthesis of gold nanorods 79
2.3.1.1. Synthesis of the seeds 79
2.3.1.2. Synthesis for gold nanorods with shorter aspect ratio 79
2.3.1.3. Synthesis of gold nanorods with longer aspect ratio 79
2.3.2. Synthesis of gold nanostars 80
2.3.2.1. Synthesis of spherical gold nanoparticles as seeds 80
2.3.2.2. Growth solution for gold nanostars 80
2.3.3. Surfactant removal procedure 80
2.3.4. Elemental concentration analysis 82
2.3.5. Spectrophotometric analysis 83
2.3.6. Transmission electron microscopy 83
2.3.7. Finite-difference time-domain simulations 85

2.4. Results and discussion 87

2.4.1. Synthesis of gold nanorods 87

2.4.1.1. Mechanism of formation of the seeds and consequence on growth of gold nanorods 87

2.4.1.2. Growth of gold nanorods 89

2.4.1.3. Importance of the size and aspect ratio in the SPR absorption 91

2.4.2. Synthesis of gold nanostars 94

2.4.3. Surfactant removal procedure 95

2.4.3.1. Characteristics of the stabilizing agents used for gold nanoparticles 96

2.4.4. Elemental concentration analysis of the concentration of nanoparticles 97

2.4.4.1. Analysis of AuNRs with short aspect ratio 98

2.4.4.2. Internal calibration standard analysis of the other particles 99

2.4.5. Spectrophotometric analysis 102

2.4.5.1. Spectra of AuNRs of shorter aspect ratio 102

2.4.5.2. Spectra of AuNRs of long aspect ratio 103

2.4.5.3. Correlation between the growth conditions and the SPR peak position . 104

2.4.5.4. Spectra of AuNSs 108

2.4.5.5. Influence of the capping agent on the SPR absorption 109

2.4.5.6. Analysis of gold nanorods with shorter aspect ratio 112

2.4.5.7. Analysis of gold nanorods of longer aspect ratio 115

2.4.5.8. Analysis of gold nanostars 117

2.4.6. Simulations 119

2.4.6.1. Simulation of the SPR of AuNRs short aspect ratio 120

2.4.6.2. Simulation of the SPR of AuNRs long aspect ratio 122

2.4.6.3. Simulation of the SPR of AuNSs 124

2.5. Conclusion 127

Chapter 3: Film preparation and characterization 129

3.1. Introduction 129

3.2. Materials 130

3.3. Methods 131

3.3.1. Fluorescence and absorbance spectroscopy 131
3.3.2. Swell-encapsulation-shrink method 132
3.3.3. Characterization of the nanoparticles in the film 132
3.3.4. Dye diffusion 133
3.3.5. Different dyes experiments 134
3.3.6. Detection and quantification of ROS 134
3.3.6.1. L-ascorbic acid test of radical inhibition 134
3.3.6.2. Methylene blue oxidizing species detection 134
3.3.6.3. ROS detection by fluorescein quenching assay 135
3.4. Results and discussion 136
3.4.1. Fluorescence emission intensity spectroscopy 136
3.4.2. Embedding of nanoparticles in the film 137
3.4.2.1. Absorption spectra of the Au nanoparticles encapsulated in the film 138
3.4.2.2. Dependence between the concentration of particles in solution and in the polymer 143
3.4.3. Dye selection 146
3.4.3.1. Dyes molecular structures and electronical consideration 148
3.4.3.2. Gold nanoparticles embedded in the polymer 150
3.4.3.3. UV-visible absorption in the polymer of the dyes with or without AuNRs 151
3.4.3.4. Fluorescence emission intensity in the polymer of the dyes with or without AuNRs 158
3.4.3.5. Antimicrobial efficiency against E. coli 167
3.4.3.6. Considerations on the dye selection 168
3.4.4. Diffusion of crystal violet in the film 170
3.4.4.1. Selection of the solution used for the diffusion 170
3.4.4.2. Estimation of the diffusion rate of crystal violet in water 176
3.4.4.3. Estimation of the amount of dye in the film 177
3.4.5. Interactions between particles and CV 178
3.4.5.1. UV-visible study of the interactions in solution 178
3.4.5.2. UV-visible study of the interactions in the film 183
3.4.6. ROS production and quantification 185

3.4.6.1. L-ascorbic acid test of radical inhibition 186
3.4.6.2. Methylene blue oxidizing species detection..... 188
3.4.6.3. Reactive oxygen species detection by fluorescein quenching assay 190
3.5. Conclusion 195
Chapter 4: Antimicrobial characterization and film efficiency 197
4.1. Introduction..... 197
4.2. Materials 198
4.3. Methods 198
4.3.1. Bacteria culture 198
4.3.2. Quantification of bacteria in solution 199
4.3.3. Bacteria propagation 199
4.3.4. Plate counting method 201
4.3.5. Antimicrobial experiments set up 203
4.3.5.1. Antimicrobial experiments set up in a closed container 206
4.3.5.2. Test of the hyperthermia effect connected to the film action 207
4.3.6. Data collection and mathematical analysis..... 207
4.4. Results and discussion..... 209
4.4.1. Factors influencing the antimicrobial activity of the film 209
4.4.1.1. Experimental conditions set for variability control..... 209
4.4.1.2. Antibacterial experiments in a closed container 210
4.4.1.3. Test on the hyperthermia effect in the film..... 212
4.4.1.4. Importance of spectra overlapping for the development of antimicrobial effect 213
4.4.1.5. Antibacterial effects of different intensity of illumination 216
4.4.2. Characteristics of bacteria influencing the activity of the film 220
4.4.2.1. S. aureus..... 220
4.4.2.2. E. coli 226
4.4.3. Antimicrobial activity test against different bacterium types 230
4.4.3.1. Effect on E. coli..... 232
4.4.3.2. Effect on S. aureus 236

4.4.3.3. Comparison of different activity against the bacterium types 238
4.5. Conclusions 240
Chapter 5: Summary, conclusions and further directions 242
5.1. Summary 242
5.2. Conclusions 243
5.3. Further directions 246
Appendix 248
A.1. Short spin off projects and collaborations 248
A.1.1. Nanoparticles for microwave frequencies hyperthermia. 248
A.1.2. Effect of curcumin silver nanoparticles on human-pterygium derived keratinocytes. 248
A.2. Minor contributions 248
A.2.1. Projects with master students 249
Publications, Presentations and Grants 250
1. Publications 250
2. Presentations 251
2.1. Oral presentations 251
2.2. Poster presentations 251
3. Grants 251
References 253

List of Figures:

Figure 1.1.1 Relation between volume of an object and surface depending on the subdivision 34

Figure 1.1.2. Effect of the subdivision on the separation of the conduction and valence band in nanoparticles 35

Figure 1.1.3. TEM picture of a batch of spherical nanoparticles prepared using the Turkevich method, showing the presence of prism like particles. 36

Figure 1.1.4. Relation between main dimension and surface for nanoparticles of different shapes 38

Figure 1.1.5. Propagation of surface plasmon polariton on the surface of bulk metal .. 44

Figure 1.1.6. Effect of an incident EM wave on the electron distribution of a small particle. 45

Figure 1.1.7. Model of the simple dipole oscillator for a nanoparticle exposed to light 46

Figure 1.1.8. Nanorod scheme, with the geometrical parameters labelled. 47

Figure 1.1.10. Examples of the electrical field polarization caused by the SPR simulated with the FDTD method. 49

Figure 1.1.11. Hyperthermia cycle of a gold nanoparticle. a) Normal standard temperature distribution of electrons; b) Light from a pulsed 10 fs laser displace the electron cloud creating hot electrons and holes; c) Charge carriers recombines according to the electrostatic attraction; d) The energy excess is released in the surrounding medium throughout the coupling with thermal phonons (thermalization). 50

Figure 1.1.12. Mechanism of ROS generation of a PS, crystal violet, exposed to light. . 56

Figure 1.1.13. Summary of the effect of the plasmonic coupling on the light interaction of the CV/Au nanoparticle system. 58

Figure 1.1.14. Mechanisms of ROS production for a coupled PS-gold nanoparticles system (CV/AuNRs). 59

Figure 1.1.15. Schematic classification of Gram positive bacteria according to their appearances and characteristics. 64

Figure 1.1.16. SEM picture of methicillin-resistant staphylococcus aureus (MRSA), picture acquired by Janice Carr and Jeff Hageman of the US centre for disease control and prevention (CDC) public domain. 66
Figure 1.1.19. Classification of Gram negative bacteria 68
Figure 1.1.20. SEM picture of E. coli of the strain O157:H7, picture acquired by Janice Carr of the US centre for disease control and prevention (CDC) public domain. 71
Figure 2.3.1. Simulation box used for the simulations of A) AuNRs and B) AuNSs. 87
Figure 2.4.1. UV-visible absorption spectra of different sizes (legend in Table 2.4.1) ... 91
Figure 2.4.2. Relation between aspect ratio and position of the LSPR peak for AuNRs of different sizes. 93
Figure 2.4.3. Results of the analysis of different solution prepared from an AuNRs stock solution of 1.255 O.D. 98
Figure 2.4.4. UV-visible spectra of a) 1X of $AuNRs_{(650\ nm)}$, b) 1X of $AuNRs_{(650\ nm)}$ + 1X of $AuNRs_{(835\ nm)}$, c) 1X of $AuNRs_{(650\ nm)}$ + 2X of $AuNRs_{(835\ nm)}$, d) 1X of $AuNRs_{(650\ nm)}$ + 3X of $AuNRs_{(835\ nm)}$ and e) 1X of $AuNRs_{(650\ nm)}$ + 4X of $AuNRs_{(835\ nm)}$; were nX = n x 100 $\mu L_{stock}/mL_{sample}$. 100
Figure 2.4.5. Representation of the ratio between the LSPR absorption of AuNRs (835 nm) and AuNRs (640 nm) against the ratio between the quantities added to the sample's solution. 101
Figure 2.4.6. UV-visible spectra of AuNRs a) in presence of CTAB; b) after CTAB removal and substitution with thiol-PEG-COOH; c) or substitution with CitNa. 103
Figure 2.4.7. UV-visible absorption spectra of AuNRs of longer aspect ratio, a) stabilized with CitNa and b) stabilized by CTAB. 104
Figure 2.4.8. Changes in the UV-visible absorption caused by the presence of a) 30 mM, b) 20 mM, c) 15 mM and d) 10 mM of NaBr. 105
Figure 2.4.9. UV-visible absorption of AuNRs prepared with a) 25 µL, b) 50 µL, c) 75 µL and d) 100 µL of $AgNO_3$ 0.01M. 106
Figure 2.4.10. Relation between position of the LSPR peak and the concentration of $AgNO_3$ in the growth solution 107
Figure 2.4.11. UV-visible absorption of AuNRs synthetized with a) 10 mM NaBr and 50 µL $AgNO_3$, b) 30 mM NaBr and 75 µL $AgNO_3$, c) 10 mM NaBr and 75 µL $AgNO_3$ and d) 30 mM NaBr and 125 µL $AgNO_3$. 107

Figure 2.4.12. UV-Visible spectra of AuNSs stabilized a) with thiol-PEG-OMe, b) with citNa and c) with CTAB. 108
Figure 2.4.13. UV-visible spectra of a) CitNa-AuNRs, b) thiol-PEG-OMe-AuNRs, c) citNa-AuNSs, d) thiol-PEG-OMe-AuNSs. 110
Figure 2.4.14. Collection of TEM images of AuNRs with shorter aspect ratio, the scale of all pictures (dark line) is 50 nm, magnification x25000 - x30000. 112
Figure 2.4.15. Size distribution of the shorter aspect ratio nanorods (batch of 726 images). 113
Figure 2.4.16 Aspect ratio distribution of AuNRs analysed in Figure 2.4.17. 114
Figure 2.4.17. Collection of TEM images of AuNRs with longer AR, the scale of the pictures (black line) is 50 nm and the magnification x30000 with the exception of the picture on the top left that has scale 100 nm and magnification x15000. . 115
Figure 2.4.18. Aspect ratio distribution of longer AuNRs 116
Figure 2.4.19. Size distribution of AuNRs of longer aspect ratio (batch of 735 images). 116
Figure 2.4.21. Collection of TEM images of AuNSs, top and bottom left (scale 200 nm and x9400 magnification), top right (scale 200 nm and x17000 magnification) and bottom right (scale 100 nm and x23500 magnification). 117
Figure 2.4.22. Size distribution of AuNSs (batch of 941 images). 118
Figure 2.4.23. A) Distribution of AuNSs core diameters and B) distribution of AuNSs spikes distribution. 119
Figure 2.4.24. Electrical field simulation for AuNRs (31.8 nm x 16.1 nm) stabilized with thiol-PEG-OMe. 120
Figure 2.4.25. Comparison between the UV-visible absorption of a) simulated AuNRs and b) thiol-PEG-OMe- AuNRs. 121
Figure 2.4.26. Electrical field simulation for AuNRs of longer aspect ratio 3.8 – 4.2 (65 x 17.5 nm). 122
Figure 2.4.27. Comparison between the UV-visible absorption of a) thiol-PEG-OMe - AuNRs and longer aspect ratio and b) their simulation. 123
Figure 2.4.28. Simulation of the SPR of the electrical field around AuNSs with 35.6 nm core with 16.1 nm spikes, stabilized with PEG. A) Model of the AuNSs used in the simulation; B) Graphical representation of the potential fluctuation of the

electrical field on the surface of the particles; C) Simulated spectrum of the AuNSs dispersion.....124
Figure 2.4.29. Electrical field resonance simulation for AuNSs (50 nm core with 10 nm spikes) stabilized with PEG A) simulated spectra of the spike system and B) simulated spectra of the core C) model of the AuNSs used for the simulation. 125
Figure 2.4.30. Comparison between the absorption peaks of a) simulation of AuNSs with the average dimensions calculated by TEM images, b) UV-visible absorption of AuNSs, c) simulation of AuNSs with ratio between the size of core and spikes (5:1).....126
Figure 3.1.1. Schematic representation of the film function.....130
Figure 3.4.1. UV-visible spectra of a) PU/citNa-AuNSs, b) PU/citNa-AuNRs, c) PU. 139
Figure 3.4.2. UV-visible spectra of a) subtraction curve between PU/citNa-AuNSs and PU, b) AuNSs in water, c) subtraction curve between PU/citNa-AuNRs and PU and d) AuNRs in water. The spectra in water were obtained by diluted solutions (20 % v/v) normalized to the scale of the subtraction curves and shifted up (b) and down (d) of 0.015 O.D.....140
Figure 3.4.3. Subtraction curve of film modified with a) thiol-PEG-AuNSs, b) spherical AuNPs, c) AuNRs maximum absorption 800 nm and d) thiol-PEG-AuNRs (PU-AuNPs – PU). 142
Figure 3.4.4. Intensity of the LSPR peak (648 nm) of the AuNRs embedded PU film as a function of the concentration of the AuNRs in the swell solution. 144
Figure 3.4.5. UV-visible absorption of Crystal Violet in water (25 µM). 147
Figure 3.4.6. Structure formula of a) Neutral Red (NeuR), b) Crystal Violet (CV), c) Alcian Blue (AB), d) Nile Red (NR), e) Janus Green B (JG), f) melamine (Me) and g) Alcian Blue Pyridine (ABP). 148
Figure 3.4.7. Subtraction curves of a) PU/citNa-AuNPs – PU (spherical) and b) PU/citNa-AuNRs - PU. 151
Figure 3.4.8. UV-visible spectra of the films: a) without modifications, b) with AuNRs, c) with Me, d) with AuNRs and Me, e) AB, f) with AuNRs and AB, g) ABP and h) with AuNRs and ABP. 152

Figure 3.4.9. UV-visible absorption of the films modified from dyes solutions in acetone. a) Film without any modifications, b) with AuNRs, c) with ABP, d) with AuNRs and ABP, e) with AB and f) with AuNRs and AB. 155
Figure 3.4.10. UV-visible spectra of a) the film modified with AuNPs, b) the film modified with AuNRs, c) NeuR with AuNRs, d) NeuR, JG with AuNRs, f) JG alone, g) JG with AuNPs, h) NR, i) NR with AuNRs. 157
Figure 3.4.11. Fluorescence intensity emission spectra, after excitation at 230 nm of a) PU/citNa-AuNRs, b) PU alone and c) subtraction curve PU/citNa-AuNRs – PU. 158
Figure 3.4.12. Emission fluorescence intensity spectra, after excitation at 230 nm of a) PU/citNa-AuNRs, b) PU alone, c) PU/citNa-AuNRs/CV, d) PU/CV, e) subtraction curve PU/citNa-AuNRs/CV – PU/CV 160
Figure 3.4.13. Emission fluorescence intensity spectra, after excitation at 230 nm of a) PU/citNa-AuNRs/Me, b) PU/Me, c) PU/citNa-AuNRs, d) PU alone, e) subtraction curve PU/citNa-AuNRs/Me - PU/Me. 162
Figure 3.4.14. Emission fluorescence intensity spectra, after excitation at 230 nm of a) PU/citNa-AuNRs/JG, b) PU/JG, c) PU/citNa-AuNPs/JG, d) subtraction curve PU/citNa-AuNRs/JG - PU/JG and e) subtraction curve PU/citNa-AuNPs/JG - PU/JG. 162
Figure 3.4.15. Emission fluorescence intensity spectra, after excitation at 230 nm of a) PU/citNa-AuNRs/AB (acetone) b) PU/citNa-AuNRs/AB, c) PU/AB, d) PU/AB (acetone), e) subtraction curve PU/citNa-AuNRs/AB – PU/AB (acetone) and f) subtraction curve PU/citNa-AuNRs/AB – PU/AB. 164
Figure 3.4.16. Emission fluorescence intensity spectra, after excitation at 230 nm of a) PU/ABP (acetone), b) PU/citNa-AuNRs/ABP (acetone), c) PU/ABP, d) PU/citNa-AuNRs/ABP, e) subtraction curve PU/citNa-AuNRs/ABP – PU/ABP and f)) subtraction curve PU/citNa-AuNRs/ABP – PU/ABP (acetone). 165
Figure 3.4.17. Emission fluorescence intensity spectra, after excitation at 230 nm of a) PU/citNa-AuNRs/NeuR, b) PU/NeuR, c) subtraction curve PU/citNa-AuNRs/NeuR - PU/NeuR 166

Figure 3.4.18. Emission fluorescence intensity spectra, after excitation at 230 nm of a) PU/NR, b) PU/citNa-AuNRs/NR and c) subtraction curve PU/citNa-AuNRs/NR - PU/NR. 166
Figure 3.4.19. Results of the antimicrobial test against E. coli for 2 h of light exposure at 11.7 klux, a) antimicrobial activity of the unmodified polymer (PU), b) antimicrobial activity of the film modified with crystal violet (PU/CV) and c) antimicrobial activity of the film containing crystal violet and AuNRs (PU/citNa-AuNRs/CV). 167
Figure 3.4.20. UV-visible absorption of CV solution of a) 100 µM, b) 50 µM, c) 25 µM, d) 10 µM, e) 5 µM, f) 1 µM and h) blank solution. 171
Figure 3.4.21. UV-visible absorption of the polymeric film prepared with the Ace method using acetone solutions of different concentrations: a) PU/citNa-AuNRs/CV 1 mM, b) PU/citNa-AuNRs/CV 0.5 mM, c) PU/citNa-AuNRs/CV 0.25 mM, d) PU/citNa-AuNRs/CV 0.125 mM, e) PU/citNa-AuNRs/CV 0.0625 mM, f) PU/citNa-AuNRs/CV 1 mM original method. 173
Figure 3.4.22. Activity of the film against E.coli for 2 h of light exposure at 11.7 klux after Ace process (a, b) compared to the standard method CV (c) and the PU/AuNRs/CV standard method (d). 174
Figure 3.4.23. UV-visible absorption at 600 nm of polymeric tiles after different times of incubation in a solution of CV 1 mM (15 min to 90 h). 176
Figure 3.4.24. UV-Visible absorption spectra of CV 10 µM in presence of 20% of nanoparticles solution (≈ 34 µM) A) citNa-AuNRs and B) thiol-PEG-AuNRs. a) Spectra of CV 10 µM, b) citNa coated AuNRs in presence of 10 µM of CV, c) spectra of ≈ 34 µM of citNa-AuNRs, d) subtraction curve [b-(a+c)] difference of absorption between the mixed solution and the sum of the components; e) thiol-PEG coated AuNRs in presence of 10 µM, f) spectra of ≈ 34 µM of thiol-PEG-AuNRs solution, g) subtraction curve [e-(a+f)] difference of absorption between the mixed solution and the sum of the components. 179
Figure 3.4.25. UV-Visible absorption spectra of CV 10 µM in presence of 20% of nanoparticles solution (≈ 34 µM) A) citNa-AuNSs and B) thiol-PEG-AuNSs. a) Spectra of CV 10 µM, b) spectra of ≈ 34 µM of citNa-AuNSs, c) citNa coated AuNSs in presence of 10 µM of CV, d) subtraction curve [c-(a+b)] difference of

absorption between the mixed solution and the sum of the components; e) spectra of ≈ 34 µM of thiol-PEG-AuNRs solution, f) thiol-PEG coated AuNRs in presence of 10 µM, g) subtraction curve [f-(a+e)] difference of absorption between the mixed solution and the sum of the components. 181
Figure 3.4.26. UV-visible spectra of a) 34 µM CV solution in water, b) 1 mM CV diffused in PU for 48 h (PU/CV film), c) PU/citNa-AuNSs/CV film, d) PU/citNa-AuNRs/CV film and e) PU alone..... 183
Figure 3.4.27. Scheme of the methylene blue / ascorbic acid reaction and of the effect of ROS produced by the film or by H_2O_2 on the reduced form of methylene blue. 188
Figure 3.4.28. Absorption at 664 nm of a solution of methylene blue reduced with L-ascorbic acid, after adding increasing aliquots of H_2O_2..... 189
Figure 3.4.29. Process of oxidation of fluorescein when exposed to ROS. 190
Figure 3.4.30. Fluorescence intensity against the estimated concentration of ROS by measuring the intensity of sodium fluorescein solution in the presence of different concentration of a) H_2O_2, b) PU/CV, c) PU/citNa-AuNRs/CV, d) PU/citNa-AuNSs/CV. 192
Figure 3.4.31. Comparison between the absorption peaks of a) simulation of AuNSs with the average dimensions calculated by TEM images, b) UV-visible absorption of AuNSs, c) simulation of AuNSs with ratio between the size of core and spikes (5:1) and d) absorption spectra of crystal violet diffused in the polymer. 194
Figure 3.4.32. Comparison between the absorption peaks of a) crystal violet embedded in the polymer, b) absorption of AuNRs solution and c) simulated absorption of AuNRs (with the dimensions obtained from TEM images). 195
Figure 4.3.1. Schematic picture of the inoculation method for plates, from higher concentration thick red lines to lower concentrations thin dotted lines..... 200
Figure 4.3.2. Scheme of the antibacterial film testing procedure: (A) PU/AuNRs/CV film samples are supported on a slide over some bi-distilled water to prevent dehydration, (B) after the inoculation with bacteria cells, the samples are protected with glass coverslips, (C) film samples and coverslips are washed with NaCl 0.9% to recover the remaining bacteria if any, (D) the bacteria solution is

serially diluted and plated on nutrient agar and (E) the colony formed are counted; (F) schematic representation of the lamp set up. 203
Figure 4.4.1. Comparison between the activity of the film with the standard set up and the experiment in a closed petri dish. From left to right: PU alone, PU/CV polymer modified with the dye, PU/citNa-AuNRs/CV complete antimicrobial film in standard conditions, film in a closed petri dish. 211
Figure 4.4.2. Temperature profile of a) the unmodified film and b) CV/citNa-AuNRs/PU while exposed to light (2 h, 11.7 klux). 213
Figure 4.4.3. UV-visible spectra of a) citNa-AuNPs 13 nm of diameter and b) citNa-AuNRs (800 nm) with aspect ratio 3 – 4. 214
Figure 4.4.4. Antimicrobial effect against E. coli for 2 h of light exposure (11.7 klux) on films with different pairs CV – AuNPs. From left to right: PU alone, PU and CV dye, CV and AuNRs with longer AR, CV and spherical AuNPs and CV and AuNRs with shorter AR.. 215
Figure 4.4.5. Effect of light power on the antimicrobial activity of the film against E.coli. A) Bacteria count after 2 h and 3 h of light exposition in relation of the light intensity used; dotted lines represent the exponential relation between light intensity and the reduction of the bacteria population. B) Bacteria count for different light intensity after 2 and 3 h: a) for samples kept in the dark; b) for a light exposure of 8.7 klux; c) for a light exposure of 9.4 klux and d) for a light exposure of 11.7 klux; ** $p < 0.01$. 217
Figure 4.4.6. Peptidoglycan barrier structure and components, a) N-acetylmuramic acid, b) N-acetylglucosamine and c) oligopeptide. 221
Figure 4.4.7. Structure of an S. aureus cell wall with schematic representation of the wall teichoic acids (WTA), covalently attached proteins (CAP), peptidoglycan barrier, lipoteichoic acids (LTA), internal membrane and internal membrane proteins (IMP). 222
Figure 4.4.8. Structure of an E. coli cell wall, with schematic representation of the O-antigen constituted by liposaccharides (LPS), outer membrane proteins (OMP), lipoproteins (LP) and integral membrane proteins (IMP). 226
Figure 4.4.9. Antimicrobial experiments result of the antimicrobial film against E. Coli for 1 to 4 h of light exposure at 11.7 klux. Labelled from a to f the film tested: a) PU,

b) PU/citNa-AuNRs, c) PU/citNa-AuNSs, d) PU/CV, e) PU/citNa-AuNRs/CV and f) PU/citNa-AuNSs/CV. All the results of PU/citNa-AuNRs/CV and PU/citNa-AuNSs/CV were statistically different compared to PU for the same time of exposure ($p \leq 0.001$). 232

Figure 4.4.10. Antimicrobial experiments result of the antimicrobial film against E. Coli. a) PU, b) PU/citNa-AuNRs, c) PU/citNa-AuNSs, d) PU/CV, e) PU/citNa-AuNRs/CV and f) PU/citNa-AuNSs/CV. All the results of PU/CV, PU/citNa-AuNRs/CV and PU/citNa-AuNSs/CV were statistically different compared to PU for the same time of exposure ($p \leq 0.05$)..... 236

List of Tables:

Table 1.1.2 Percentage of atoms exposed compared to the atoms bulk for a cube of 4096000 atoms. 34

Table 2.3.1 Operative conditions for the centrifuges used with the different types of gold nanoparticles 81

Table 2.3.2 List of passages for the removal of CTAB from the surface of Au nanoparticles 82

Table 1.1.1 List of physical dimensions used to simulate the nanoparticles used in the thesis. 86

Table 2.4.1. Size and structural parameter of AuNRs and their transversal SPR 93

Table 3.4.1 Relation between stock concentrations, swelling solution concentrations and the absorption changes according to the calculations and in the experimental samples and the percent of efficiency of embedding for the experimental samples. 146

List of Equations:

Equation 1.1.1 46
Equation 1.1.2 46
Equation 1.1.3 47
Equation 1.1.4 48
Equation 1.1.5 48
Equation 1.1.6 48
Equation 1.1.7 48
Equation 1.1.8 48
Equation 1.1.9 48
Equation 1.1.10 60
Equation 1.1.11 60
Equation 2.4.1 99
Equation 2.4.2 99
Equation 2.4.3 99
Equation 2.4.4 99
Equation 2.4.5 101
Equation 2.4.6 101
Equation 2.4.7 101
Equation 2.4.8 102
Equation 3.4.1 145
Equation 3.4.2 145
Equation 3.4.3 145
Equation 3.4.4 177
Equation 3.4.5 178
Equation 3.4.6 191
Equation 4.3.1 204
Equation 4.3.2 207
Equation 4.3.3 208

List of Abbreviations:

%wt	Percent in weight
AA	L-Ascorbic acid
AB	Alcian blue
ABP	Alcian blue pyridine variant
Abs	Unit of absorption (O.D.)
ANOVA	Analysis of variance
AR	Aspect ratio
[Au]	Concentration of gold
AuNPs	Gold nanoparticles
AuNRs	Gold nanorods
AuNSs	Gold nanostars
ATCC	American type culture collection
BCE	Before common era
CAP	Covalently attached protein
citNa	Sodium citrate
cfu	Colony forming unit
COST	European collaboration in science and technology
CTAB	Hexadecyltrimethylammonium bromide
Cu(II)	Cu^{2+}
CV	Crystal violet
Da	Dalton
d.f.	Degrees of freedom
DLS	Dynamic light scattering

DMEM	Dulbecco's Modified Eagle Medium
DMSO	Dimethyl sulfoxide
EDTA	2,2',2'',2'''-(Ethane-1,2-diyldinitrilo)tetraacetic acid
EM	Electromagnetic
ELVT	Endovenous laser treatment
EPA	USA environmental protection agency
EtOH	Ethanol
FBS	Foetal bovine serum
FDTD	Finite-difference time-domain
Fluo	Sodium fluorescein
Fur	Ferric uptake regulator
Gram(+)/(-)	Gram positive or negative
HAI	Hospital acquired infections
HPV	Hydrogen peroxide vapour
ICP-MS	Inductively coupled plasma mass spectrometry
IMP	Integral membrane proteins
ISO	International standards organization
JG	Janus green B
Kat(A,G, etc.)	Catalase (A,G, etc.)
L	Side of a cube or length of a rod
log	Log10
Loc-SPR	Localized SPR
LP	Lipoproteins
LPS	Lipopolysaccharides

LSPR	Longitudinal SPR
LTA	Lipoteichoic acid
MCF-7	Michigan cancer foundation-7
ME	melamine
MTT	3-(4,5-dimethylthyazol-2-yl)-2,5 diphenyltetrazolium bromide
N°	Number
NA	Nutrient agar
NAG	N-acetylglucosamine
NAM	N-acetylmuramic acid
NaPSS	Poly(sodium 4-styrenesulfonate)
NeuR	Neutral red
NMs	Nanomaterials
NAPDH	Nicotinamide adenine dinucleotide phosphate
NR	Nile red
NTDM	No-touch disinfection methods
OD	Optical density
OMP	Outer membrane proteins
PDT	Photodynamic therapy
PML	Perfectly matched layer
PS	Photosensitizer
PSPP	Propagating surface plasmon polariton
PU	polyurethane
RET	Resonance energy transfer
ROS	Reactive oxygen species

rpm	Round per minute
SEM	Scanning electron microscopy
SOD	Superoxide dismutase
SPR	Surface plasmon resonance
STSM	Short term scientific mission
TD	Terminal disinfection
TEM	Transmission electron microscopy
Thiol-PEG-COOH	Mercaptopoly(ethylene glycol) carboxylic acid
Thiol-PEG-OMe (thiol-PEG)	Mercaptopoly(ethylene glycol) methyl ether
TOF	Time of flight
t-SPR	Transversal SPR
UV (A, B & C)	Ultraviolet light (310 - 400 nm)
WHO	World Health Organization
WTA	Wall teichoic acid

Acknowledgments:

I would like to thank UCL and IMRE A*STAR for the M3S CDT ARAP program which funded my scholarship and for the facilities provided in UK and in Singapore. I would like also to thank the EPSRC (EP/M018016/1 and EP/M015157/1) and AOARD (FA2386-17-1-4042 award) for contributing to the funding for this research.

Thanks to my supervisors, Professor Nguyen T. K. Thanh and Dr Xiao Di Su for guiding me while I was working in London and in Singapore and for being very patient while I was finding my foot in the project. A special thanks to Professor MacRobert, Sandy Mosse and Kelvin Vine for helping with my first year report and with all the safety procedures related to the laser use.

Thanks to Nadia Waller for helping me to find some extra funding to help me with the last months of my writing.

Thanks to Niccolò and Amandaz for helping with the proofreads and together with my parents for supporting me during the writing.

Chapter 1: Introduction

The increasing occurrence of diseases caused by infection of drug resistant bacteria is causing a drain of resources for healthcare systems around the world. In the 2019, in the US HAI involved 1 every 31 patients admitted to hospital for more than 48 h causing 72000 causalities and costing more than 9 billion USD in direct costs.[3] While in the European Union, during the 2017, drug resistant bacteria caused 33000 causalities and a total burden on the health system of 1.1 billion EUR.[4] A current and effective strategy to fight this kind of infections is to improve the capability to disinfect the environments, especially for facilities were a great number of diseased and recovering people pass every day and high concentrations of drugs are used (i.e. medical wards and surgical theatres).[1]

With the aim of improving the disinfection of surfaces, the research work in this thesis was focused in developing a novel antimicrobial film able to kill the bacteria escaped to routine cleaning. Activated by light without the need of direct contact or the help of trained personnel.

The overall aim of the research presented in this thesis was to optimize the production and investigate the light activated antimicrobial efficiency of a polyurethane (PU) film containing anisotropic gold nanoparticles and a photosensitizer dye. On the theoretical side, this research was focused on the study of the interaction between the surface plasmon resonance (SPR) of the two types of anisotropic gold nanostructures and the dye. While, at the same time investigating how the plasmonic coupling of the film components interacted with light and increased the production of reactive oxygen species (ROS) of the film.

The specific objectives of this thesis were subdivided in smaller tasks, which formed the guideline for the experiments in this work:

1) Development and characterization of a synthetic procedure for the production of AuNRs and AuNSs. Focused on the production of particles with SPR peaks positions comparable with the absorption of crystal violet and the modification of their surface (section 2.3).
2) Characterization of the chemical-physical properties of the synthetized gold nanoparticles and the simulation of their SPR absorption (section **Error! Reference source not found.**).
3) Development and optimization of the procedures used for the preparation of the film (section 3.3)
4) Characterization of the embedding procedure of gold nanoparticles in the film and characterization of the diffusion of the dye in the film (sections 3.4.1 to 3.4.4).
5) Study of the interactions between gold nanoparticles and dye either in solution than in the film (section 3.4.5).
6) Study of the ROS production of the film in presence of dye or of dye and particles (section 3.4.6).
7) Bacteria culture and development of a reliable method of antimicrobial testing (sections 4.3 and **Error! Reference source not found.**).
8) Study of the relation between the light intensity and the activity of the film against bacteria (section 4.4.1).
9) Study of the film antimicrobial efficiency against Gram(+) or Gram(-) bacteria and its correlation with the bacteria structure (section 4.4.3).

The film was composed of three interacting components (i.e. film, anisotropic nanoparticles and photosensitizer dye) activated by light and it was used to kill bacteria. For this reason, the research in this work required a broad multidisciplinary approach spacing from physical-chemistry and nanotechnology to material science and microbiology. To help the reader to have the necessary information to follow the experiments in this work, in section (1.1) is contained a review of background information on the components, concepts and techniques used in this thesis; while section 1.2 presents the state of the art on antimicrobial surfaces.

1.1. Background information

1.1.1. *Gold nanostructures*

1.1.1.1. Historical notes

The properties of gold have always fascinated humanity, this element has a bright colour, is very ductile and resistant to corrosion. Gold is also relatively easy to melt (≈1063 °C)[12] and for its limited reactivity it was easy to find in pure form. Allowing our ancestor to begin collecting and using gold very early in their history (e.g. Egypt ≈ 4000 BCE).[13]

Gold nanomaterials were some of the oldest ever produced, as it has been demonstrated by classical era artefacts as the Lycurgus cup,[14] which was made of a vitreous paste containing gold nanoparticles. Another relatively common occurrence of nanoparticles in antiquity was the production of stained glass for gothic cathedrals, in which gold nanoparticles coloured the stained glass of shades from red to purple.[15]

These examples showed that the procedures to make gold nanoparticles were already known in ancient times as well as with a limited knowledge of their unique optical properties. But it was only a practical knowledge on

how to prepare gold to turn the glass purple, because the reason behind the change of colour was only discovered in recent times (XXI century). When crystallographic studies have demonstrated that the formation of gold nanoparticles was an effect of annealing glass using sand containing traces of gold.[15]

The first reported synthesis of nanoparticles in history has in the 1683 and it is credited to Andreas Cassius of Leyden in his book "*De Auro"* which described the alchemic procedure to create red-purple glass (historically labelled "Cassius Purple") from gold dissolved with *aqua regia* after reacting with tin chloride ($SnCl_2$). In the same period, other alchemists developed similar procedures, but neither them or Cassius of Leyden understood the reason why gold turned red as consequence of his reaction.[16]

The reason eluded the researcher until the 1857, when M. Faraday, was able to identify the faint red solution forming on his gold microscope slides after cleaning them with *aqua regia* as a gold colloid. Thanks to this experimental observation he was able to develop a systematic reaction for the production of gold colloids.[17,18]

From the beginning of the 20th century, thanks to the development of techniques for the characterization of nanomaterials and the systematic study of synthetic procedures, a large number of gold nanoparticles have been synthetized.[19] Demonstrating the full versatility of this element as building block of nanomaterials.[20]

1.1.1.2. Relation between surface and volume in nanoparticles

Nanomaterials have caught the interest of the scientific community, because they possess different properties compared to the bulk. These

properties are the direct consequence of the surface area of nanomaterials which is order of magnitudes larger than the surface of bulk objects with

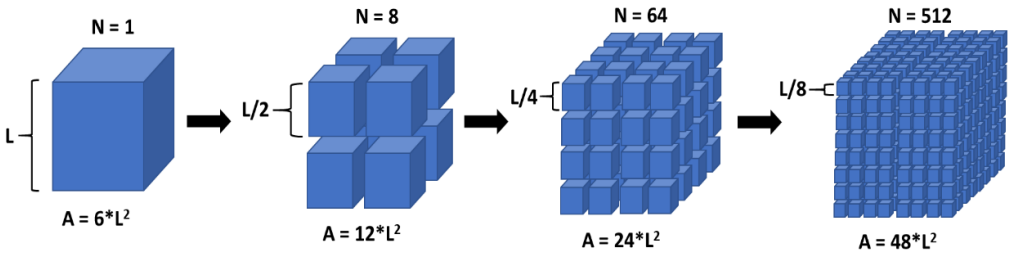

Figure 1.1.1 Relation between volume of an object and surface depending on the subdivision

the same mass. The excess of surface of a nanomaterial, compared to bulk is due to the total of the surfaces of the nanoscopic fragments which constitute it (example in Figure 1.1.1).

A direct consequence of the increase of the surface area was the change in the percentage of atoms exposed on the surface of the particles, as reported in **Error! Reference source not found.** for the subdivision shown in Figure 1.1.1.

Table 1.1.1 Percentage of atoms exposed compared to the atoms bulk for a cube of 4096000 atoms.

Total N° of Atoms	N° of cubes	N° Atoms per side	N° Atoms Exposed	N° Atoms Bulk	% Exposed	% Bulk
4096000	1	160	1.52E+05	3.94E+06	3.7	96.3
4096000	8	80	3.02E+05	3.79E+06	7.4	92.6
4096000	64	40	5.94E+05	3.50E+06	14.5	85.5
4096000	512	20	1.15E+06	2.95E+06	28.0	72.0
4096000	4096	10	2.13E+06	1.97E+06	52.0	48.0
4096000	32768	5	3.60E+06	4.92E+05	88.0	12.0

Atoms on the surface of nanoparticles do not have a complete coordination number, making them more mobile and reactive.[21] Which consequently, cause the nanomaterials to perform better as catalysts than their bulk form and explain their tendency to aggregate. To expand the surface area requires energy, because it increases the surface potential.

This potential could be reduced by the aggregation of particles, but on the other hand, increasing the number of free objects in a system causes a gain of entropy. The result of this balance is that nanoparticles are stable when their entropic contribution is larger than enthalpic gain of forming aggregates.

Because gold is a metallic element, reducing the size of its particles has also an effect on their electrical properties. Metals in bulk form have two distinct electronic bands: one of conduction (**Error! Reference source not found.**.a) and the other of valence (**Error! Reference source not found.**.b), when the size of the metal particles is reduced to the nanoscale, their bands split and begin to behave as atomic energy levels. At the same time, the energy gap between the two bands decreases proportionally with the reduction in size until the metal nanoparticles begin to behave more as a semiconductor

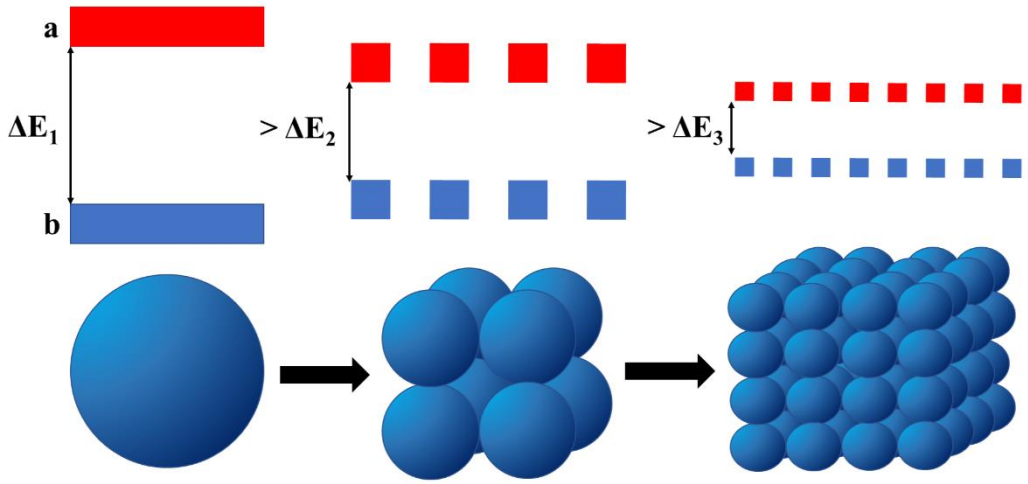

Figure 1.1.2. Effect of the subdivision on the separation of the conduction and valence band in nanoparticles

than a metal (**Error! Reference source not found.**).[21]

Magnetic properties and light interactions are also influenced by the subdivision of the metal nanoparticles causing the development of superparamagnetism and SPR (in section 1.1.3).[20]

1.1.2. *Anisotropic nanoparticles*

Few nanoparticles with shapes different from spheres were present from their first synthesis reported by Faraday in the 1857, as the crystalline *habit* of gold occasionally led to triangular or hexagonal prisms depending on the kinetics of the reaction between the $HAuCl_4$ and the reducing agent.[22]

For examples, one of the most common synthesis for nanoparticles is the "Turkevich method", which uses the reaction between $HAuCl_4$ and boiling sodium citrate to form spherical nanoparticles.[23–25] During this reaction, along with the spherical particles a small amount of non-spherical nanoparticles (≈ 5%) are generally formed.

The non-spherical particles formed by this synthesis could have shapes of short rods, rhomboids or triangular and hexagonal prisms (Figure 1.1.3).[26]

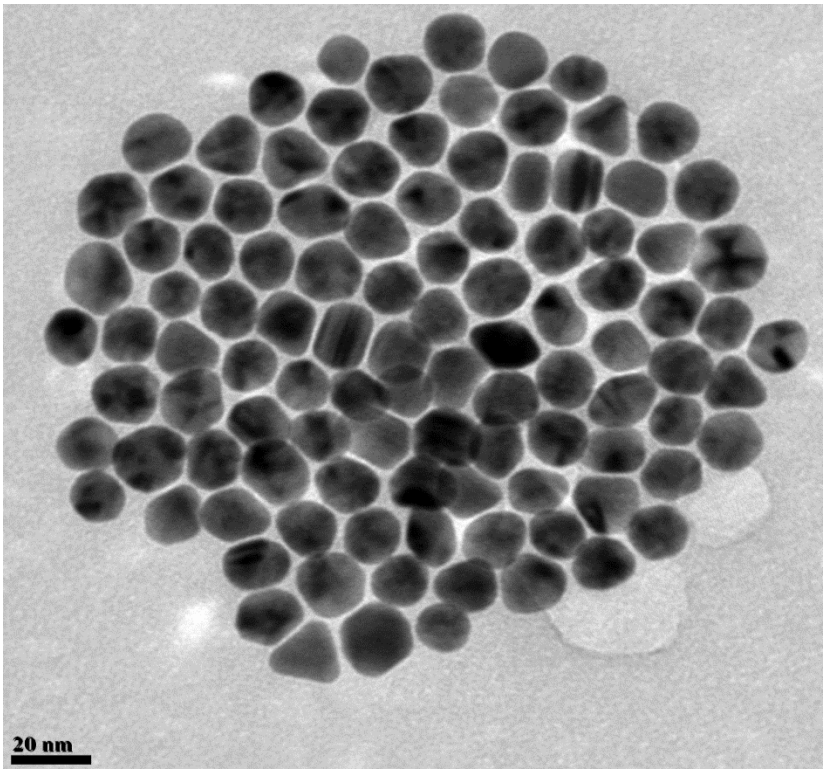

Figure 1.1.3. TEM picture of a batch of spherical nanoparticles prepared using the Turkevich method, showing the presence of prism like particles.

Historically, the development of nanoscience and the synthesis of anisotropic nanoparticles was hindered by the lack of reliable characterization techniques. This limitation lasted until the decade between the 50' and the 60' which led to the diffusion of the transmission electron microscopy (TEM) and scanning electron microscopy (SEM), which could provide pictures of sub-micro objects.[27,28] In the following years the production of nanoparticles increased but it was mostly achieved with electrochemical methods.[29]

The first step towards the wet synthesis of anisotropic nanoparticles began when Jana *et al.* (2001) obtained AuNRs through the growth of particles in presence of silver nitrate ($AgNO_3$) and hexadecyltrimethylammonium

bromide (CTAB).[30] This synthesis, was developed and studied in its modern form by B. Nikoobakht and M. El-Sayed.[31,32] That with their work opened the way to the synthesis of particles with different shapes.

The development of reliable synthetic procedure to form anisotropic nanoparticles and the continuous improvement of the characterization techniques led, in the first years of the new millennium, to the exponential increase of publications regarding new nanostructures, with a vast selection of shapes and structures.[20] Among the latest of this wave, Nehl *et al.* in the 2006 introduced AuNSs.[33]

Anisotropic nanoparticles had some advantages compared to spherical particles:

i) For a common main dimension (either diameter or length) anisotropic nanoparticles had a larger surface area compared to spherical nanoparticles (Figure 1.1.4).

ii) The presence of thinner parts in their structures helped the concentration of the electrical field.[11]

iii) The combination of electrical field and surface area massively increased their cross section and at the same time increased their catalytic properties and light absorption[34]

iv) their properties could be tuned by changing the ratio between their features (e. i. length/diameter or core size/spike length).[35,36]

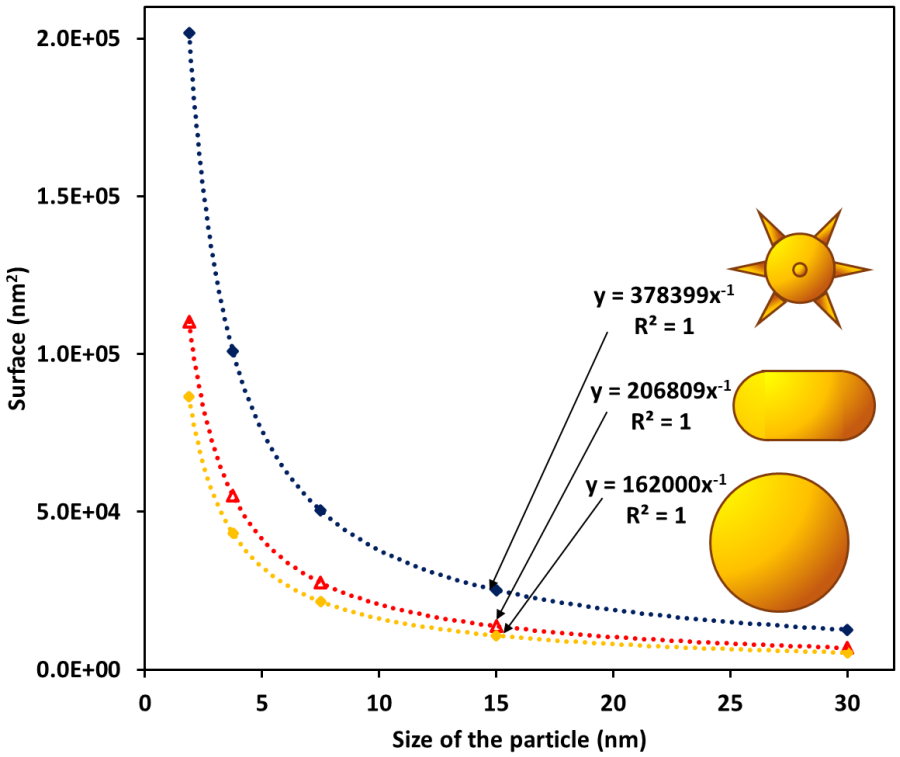

Figure 1.1.4. Relation between main dimension and surface for nanoparticles of different shapes

The trade-off for these advantages was the complexity of the synthetic procedure necessary to produce the particles and to obtain a reliable stabilization of their complex structure.[37]

1.1.2.1. Seed mediated synthesis

All the anisotropic nanoparticles used in this thesis were synthesized using a modified version of the seed mediated synthesis.[32,38–40] This type of synthetic procedures had two reaction steps which were performed in two

separated solutions: one for the formation of seeds and another for the actual growth of the nanoparticles.

This procedure could be applied to the synthesis of many different types of particles using different particles as seeds and applying small changes to the growth solution. For example the gold nanorods were synthetized using gold nanoclusters (< 2 nm) as seeds, while gold nanostars were seeded with small spherical gold nanoparticles (13 nm, diameter).[38,40,41]

One of the strongest point of using the seed mediated synthesis was the separation between the growth and seeds solution, which made possible to achieve a greater control on the reaction conditions and thus of the characteristics (i.e. size and aspect ratio) of the growing particles.[38,42] At the same time, this type of synthesis could be scaled up to the litre of sample by producing growing solution in parallel using the same seed solution (more than 60 nanoparticles batches of 12.5 mL could be prepared with the typical seeds solution prepared for the experiments in section 2.3.1.1). Another advantage of the seed mediated synthesis was the possibility to directly introduce the capping agent in the growth solution improving the stability of the particles, for example CTAB in the synthesis of gold nanorods, which was used both as a mould to form the rods and as capping agent to stabilize the particles after synthesis.[43]

1.1.2.2. Synthesis of gold nanorods

The gold nanorods used in this work were synthetized using the seed mediated method, using a modified version of the synthesis reported by R. Molto *et al.*[38] This synthetic procedure uses small spherical nanoparticles (< 2 nm) to seed the growth of the nanorods. While the presence of surfactant micelles in the growth solution acted as a template for the particles and

gave to this procedure a great degree of flexibility regarding the length and diameter of the rods formed.

The diameter and the length of the growing rods could be controlled by regulating the amount of ions in the growth solution, for example a small amount of $NaNO_3$ (10 mM concentration in the growth solution) would cause the formation of rods with higher aspect ratio (length/diameter) while a larger amount of NaBr (30 mM) would cause the rod to be shorter and thicker (AR: 2.1 – 2.4), the procedure is reported in details in section 2.3.1.

The reason behind the sensitivity of this synthesis to the presence of small amounts of selected ions, is not completely clear and different hypothesis are reported in literature. In order to understand the different theories, it is necessary to have a clear picture of the organization of the reagents in the growth solution during the formation of the rods.

The main component of the growth solution is a surfactant, CTAB, it is strongly positively charged, and it is only partially soluble in water. When dispersed in water, it forms bi-layered micelles segregating its organic component from the solution.[44] The layers of CTAB were maintained by a network of Br^- ions filling the space between the heads of the surfactant charged positively. When $AgNO_3$ and $HAuCl_4$ are added to the growth solution the three components form a complex with an intense orange colour. During the formation of this complex, the Cl^- ions, which are interacting with the Au^{3+} ions in $HAuCl_4$, are progressively displaced in favour of Br^- ions, which have a better affinity for gold ($AuBr_4^-$, has a dark orange colour).[45] Adding some concentrated HCl and L-ascorbic acid reduced all the Au^{+3} to Au^{+1}, which was the most stable species in acid

condition and at the same time prevented the disproportionation of Au^{+1} back to metal gold and Au^{+3} ($Au^{+3} + 2Au^{0} \leftrightarrow 3Au^{+1}$). After the reaction the solution turned transparent and the introduction of a small amount of seeds catalysed the growth of the nanorods. The use of a weak reducing agent, as L-ascorbic acid, prevented the reduction of the Ag^{+} to Ag^{0} which would have prevented the formation of the rods.[46]

The role of silver in the formation of gold nanorods and its interaction with the complex, the ions in solution and the surfaces of the forming rods is still open to debate in the scientific community. There are three main theories popular at the moment: i) the underpotential deposition of silver,[47] ii) the formation of the $Ag[BrCTA]_2$ complex acting as capping agent for specific facets of the growing gold nanoparticles (favouring the formation of Au [1,1,1])[48] and iii) the modification of the structure of CTAB micelles throughout silver bromide interactions.[38] The anion introduced in solution would either interact with the silver to change the deposition potential (i), contribute to the formation of the complex (ii) or change the micellar structure of the growth solution (iii).

In regards to this discussion, my opinion is that the role of silver is half way between the first and the second hypotheses, with the silver ions strongly bound in the $Ag[BrCTA]_2$ complex but instead of capping some faces of the gold crystal mostly act as a catalyst for the formation of rods with specific geometry. This would explain why adding aliquots of different salts does not correspond to a clear structural change of the rods (reported in section 2.4.5.3). Because some ions interact more strongly with the forming surface of gold and others instead with the silver complex causing different changes

to the growth of the rods (further considerations on this synthesis in section 2.4.1).

1.1.2.3. Synthesis of gold nanostars

The synthesis of gold nanostars have some similarities with the synthesis of gold nanorods: both are seeds mediated, they are performed at room temperature and used the same reagents, but they differ for the nature of the seeds used and the mechanism of the formation of the particles.

The seeds used in this synthesis were spherical nanoparticles of 13 nm diameter synthetized with the citrate method.[49] The nanoparticles synthetized with this method were uniform in shape and dimensions and cover with a layer of citrate, which offered stabilization while being easy to remove.

The synthesis procedure (reported in section 2.3.2), was very fast, requiring a series of time dependant injections of reagents. The growth solution contained $HAuCl_4$ and HCl to which an aliquot of seed solution was added, the resulting mix was extremely reactive because the surface of the nanoparticles used as seed acted as a catalyst for the reduction of gold.[40]

In this reactive environment, the injection of $AgNO_3$ and L-ascorbic acid caused spiky protrusion to form on the surface of the particles until the nanostars were produced. In this synthesis, the role of silver is clearer than for the synthesis of gold nanorods, because metallic silver have been proven to be present on the surface of the spikes, where it prevent their collapse on the core.[50]

Due to the nanostars' extensive surface potential, they were unstable and required to be stabilized either sterically or electrostatically.[51]

1.1.3. *Nanoparticles interaction with light*

1.1.3.1. Surface plasmon resonance

As discussed in the previous section (1.1.1.2) when metal was reduced in fragments of the size of nanoparticles, its conductive band was subdivided in discrete energy levels. While at the same time the relatively small band gap between the occupied and unoccupied energy levels of metal nanoparticles allowed them to acquire some of the properties of semi-conductors which determined their interaction with light.[52] The subdivision in discrete levels of the conductive band of the nanoparticles was a direct consequence of their size and involves the electrons of the atoms exposed to the surface of the nanoparticles. Consequently, the characteristic optical properties of a gold nanoparticle depends from the interactions between these accessible energy levels and the surface plasmon of gold.[53]

The plasmon of a metal is defined as the collective oscillation of the free electrons in it,[54] this oscillation have a defined and characteristic frequency. Thus, a "plasmon" is characterized as a bosonic quasiparticle excitation and corresponds to a quantum of the plasma oscillation. The term plasmon originated from the composition of the word plasma and the -on suffix generally used to indicate quasiparticles.[55]

In the bulk of the metal, this excitation is not allowed, but it could be induced in the superficial layers of the metal lattice by an electromagnetic radiation with an incident angle almost parallel to the surface.

In these conditions a part of the incident wave was reflected, but at the same time some of its energy was lost to form a wave propagating on the surface of the metal. This phenomenon is called propagating surface plasmon polariton (PSPP) (Figure 1.1.5).[56]

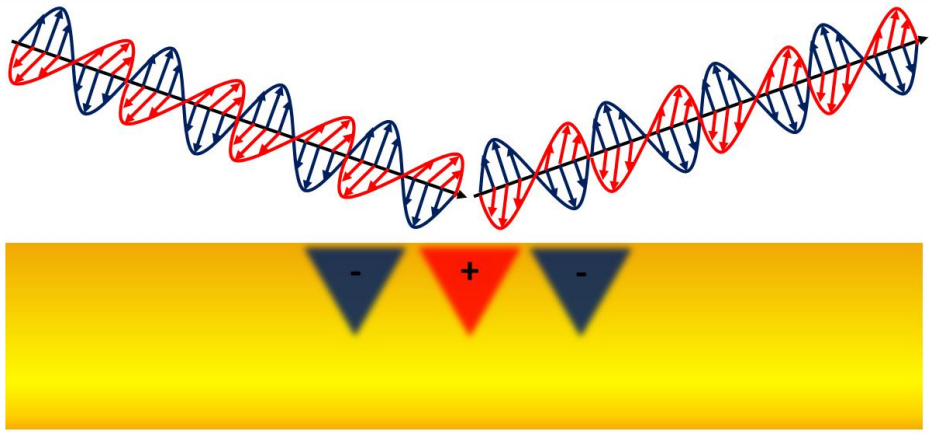

Figure 1.1.5. Propagation of surface plasmon polariton on the surface of bulk metal

When the dimensions of the metal particle are reduced to the nanoscopic scale, they become comparable both with the depth of propagation of the PSPP and with the wavelength of the incident wave ($R/\lambda < 0.1$; R = particles radius, λ = wavelength). When these conditions are met, the oscillation involves all the electrons of the particle.

But because of the size of the nanoparticle is very small (less than the mean free path of electrons), the plasmons formed are not able to move freely (as it happens in the bulk material) and they can only resonate from a side to another of the particle. Thus, this type of plasmon takes the name "localised surface plasmon resonance" (Loc-SPR).

An incident electro-magnetic (EM) radiation generates a displacement parallel to the direction of its electrical field and a particle is only able to interact with wavelengths coherent to the oscillation of its electrons (Figure 1.1.6).

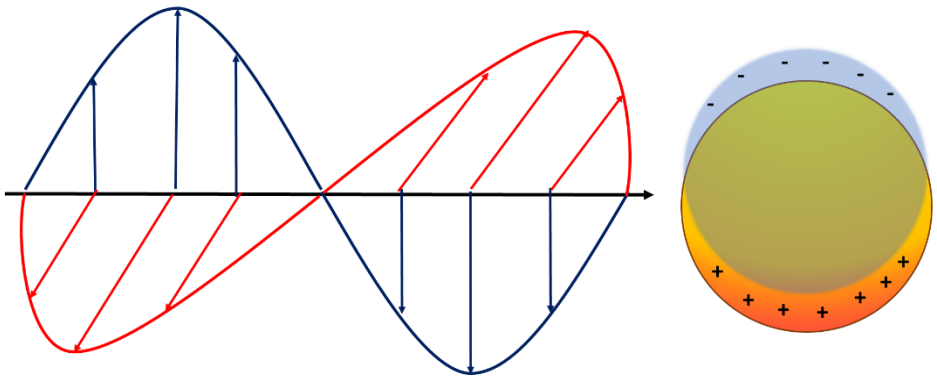

Figure 1.1.6. Effect of an incident EM wave on the electron distribution of a small particle.

Within a nanoparticle the distance between the displaced electrons and the nucleus lattice is very small, which allows the electrostatic attraction of the nuclei to generate a spring like response against the displacement created by the EM wave.

Considering this approximation, the electron cloud could be considered as a mass, negatively charged, attached to a spring connected to the positively charged surface of the nuclei lattice.

In this model the incident light produced the force that pulled the mass away from the lattice while the recall force of the spring was generated by the attraction between nuclei and electrons (Figure 1.1.7).[54]

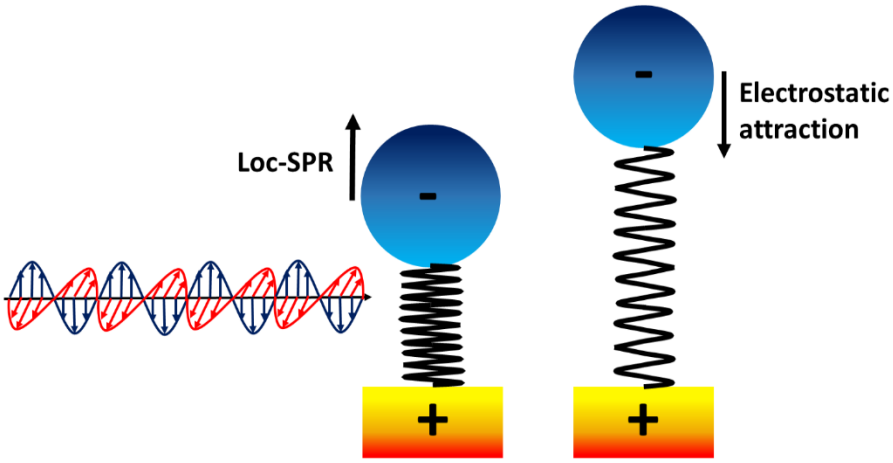

Figure 1.1.7. Model of the simple dipole oscillator for a nanoparticle exposed to light

In the situation described by the dipole oscillation method, assuming that the particle is surrounded by a non-absorbing medium during the excitation, the displacement of the electron cloud can be described as polarizability (Equation 1.1.1).

$$\alpha(\lambda) = 3\varepsilon_m(\lambda)V_{NPs}\frac{\varepsilon(\lambda)-\varepsilon_m(\lambda)}{\varepsilon(\lambda)+\chi\varepsilon_m(\lambda)} \quad (1.1.1)$$

Where λ is the wavelength of the incident light, ε_m is the dielectric constant of the medium around the particle while V_{NP} and χ are geometrical parameters indicating the volume of the nanoparticle and its geometry, respectively. For a spherical nanoparticle, χ = 2 and the polarizability is defined as (Equation 1.1.2):

$$\alpha(\lambda) = 4\pi\varepsilon_m(\lambda)R^3\frac{\varepsilon(\lambda)-\varepsilon_m(\lambda)}{\varepsilon(\lambda)+2\varepsilon_m(\lambda)} \quad (1.1.2)$$

From Equation 1.1.2 is clear that the polarizability can only be maximized when the denominator is close to 0, thus closest to $\varepsilon(\lambda) = -2\varepsilon_m(\lambda)$. Another important consideration is that the dielectric function of a metal depends from the frequency (ω) and it has a real and imaginary component ($\varepsilon(\lambda) = \varepsilon_r + i\varepsilon_i$).

Combining the polarization and the dielectric function is possible to calculate the extinction coefficient (σ) for spherical nanoparticles (Equation 1.1.3).

$$\sigma_{ext} = \frac{24\pi^2 R^3 \varepsilon_m^{3/2} N}{\lambda \ln(10)} \frac{\varepsilon_i}{(\varepsilon_r + 2\varepsilon_m)^2 + \varepsilon_i^2} \qquad (1.1.3)$$

This equation can be used to calculate the frequency which generated the peak of SPR absorption for which the polarizability was maximized ($\varepsilon_r = -2\varepsilon_m$). For nanoparticles made of gold the frequency obtained corresponded to an absorption in the visible (520 - 550 nm).

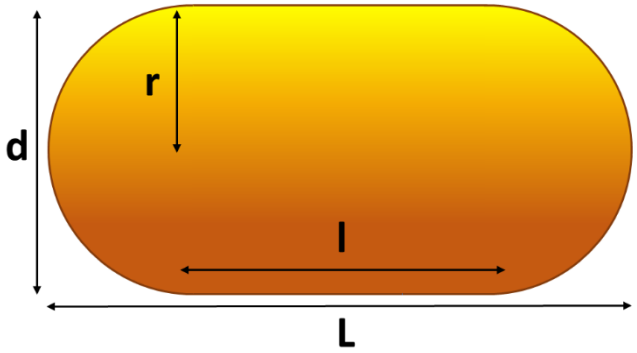

Figure 1.1.8. Nanorod scheme, with the geometrical parameters labelled.

For non-spherical nanoparticles the polarization is split along the main symmetry axis, for example the polarization of gold nanorods is split in two different independent modes. Consequently, the extinction coefficient for

the nanorods is calculated in function of their main dimensions (Equation 1.1.4 – 1.1.5; is based on AuNRs of aspect ratio L/d = 2 in Figure 1.1.8).[57]

$$\sigma_x = \frac{2\pi V_x}{3\lambda}\varepsilon_m^{3/2}\sum_j \frac{(1/P_j^2)\varepsilon_i}{(\varepsilon_r+\frac{1-P_j}{P_j}\varepsilon_m)^2+\varepsilon_i^2} \quad (1.1.4)$$

$$V_{AuNRs} = \pi l r^2 + \frac{4\pi r^3}{3};\quad l = 2r \quad (1.1.5)$$

$$\sigma_{AuNRs} = \frac{20}{9}\frac{\pi^2 r^3}{\lambda}\varepsilon_m^{3/2}\sum_j \frac{(1/P_j^2)\varepsilon_i}{(\varepsilon_r+\frac{1-P_j}{P_j}\varepsilon_m)^2+\varepsilon_i^2} \quad (1.1.6)$$

The extinction coefficient of AuNRs as described in Equation 1.1.6 depended from the depolarization factor P_j were the index j indicates the different independent modes of polarization. For a particle shaped as rods the modes of polarization were two: transversal and longitudinal. Consequently, the depolarization of the rods depended from their ellipticity (e^2) and was defined as the Equations 1.1.7 – 1.1.9.

$$e^2 = 1 - \left(\frac{d}{L}\right)^2 \quad (1.1.7)$$

$$P_L = \frac{1-e^2}{e^2}\left[\frac{1}{2e}ln\left(\frac{1+e}{1-e}\right) - 1\right] \quad (1.1.8)$$

$$P_d = \frac{1-P_L}{2} \quad (1.1.9)$$

As for spherical nanoparticles the polarization reached the maximum when the denominator was $\varepsilon_r = -\varepsilon_m\frac{1-P_j}{P_j}$. This term had two solutions for both the longitudinal (LSPR) and the transversal SPR (t-SPR). Consequently, the extinction coefficient of this type of particle is strongly influenced by small changes in the structural parameters.

The presence of a dielectric layer on the surface of the nanoparticles modifies the polarizability and the extinction coefficient in a similar way as

the shape changes. In presence of the dielectric layer the depolarization become $P = 1 - \left(\frac{r}{r+d}\right)^3$ where r is the radius of the nanoparticles and d is the thickness of the dielectric layer. Furthermore, the dielectric constant of the layer influenced both the particles and the media surrounding them.

For more complicated structure the direct calculation of the polarization and the extinction coefficients is too complicated to be approximated to a simple oscillator in a semi-static condition, thus requiring the use of more sophisticated simulation methods.

The SPR simulations used in this work have been realized using the finite-difference time-domain (FDTD), which used the Maxwell equations to resolve the variations of the electrical film surrounding the simulated nanoparticles.[58] These variations were then mapped and represented as the polarization of small units of volume filling the space surrounding the particles (examples of the simulation results in Figure 1.1.10).

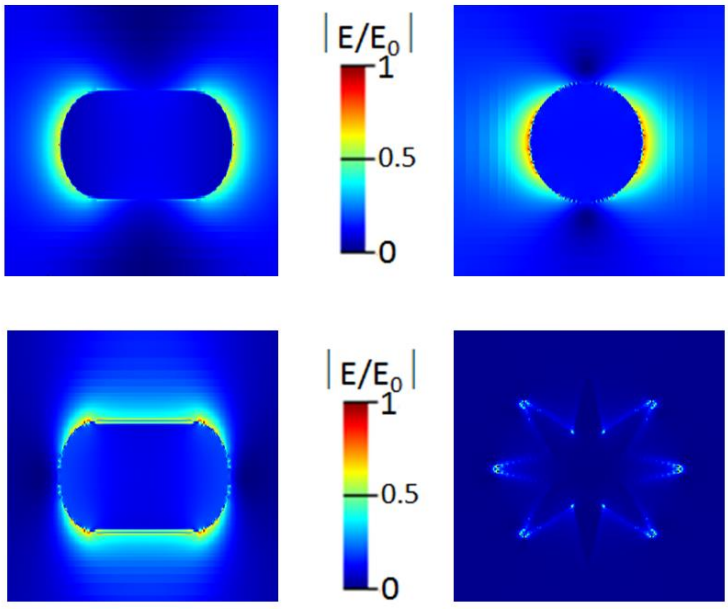

Figure 1.1.9. Examples of the electrical field polarization caused by the SPR simulated with the FDTD method.

1.1.3.2. *Photo-induced hyperthermia*

A direct consequence of the SPR of gold nanoparticle is their ability to absorb energy and release it in the surrounding medium as heat. As established in the previous chapter, the displacement of the electron cloud from its position around the nuclei could be represented as a mass attached to a spring. Where the spring was generated by the pull of the electromagnetic radiation and the attraction between electron cloud and atomic lattice to act as a recall force.

A macroscopic oscillator once pulled, would began going back and forth around an equilibrium position, until all its energy was shed as attrition to the surrounding environment, following a damped oscillator regime.[59]

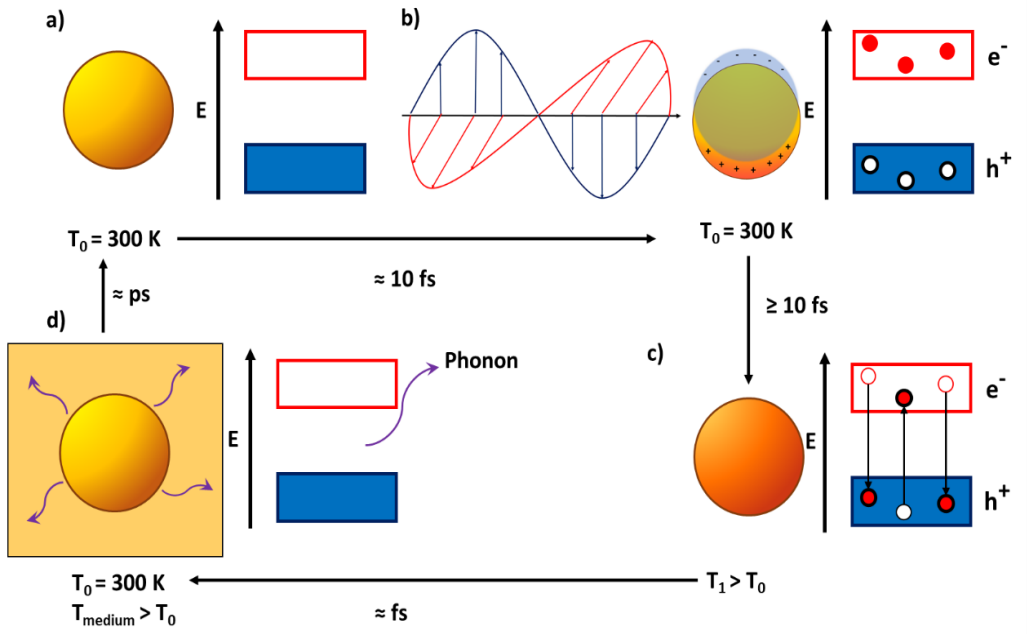

Figure 1.1.10. Hyperthermia cycle of a gold nanoparticle. a) Normal standard temperature distribution of electrons; b) Light from a pulsed 10 fs laser displace the electron cloud creating hot electrons and holes; c) Charge carriers recombines according to the electrostatic attraction; d) The energy excess is released in the surrounding medium throughout the coupling with thermal phonons (thermalization).

In a nanoparticle the energy cycle was much more complex. For example, for a system composed of a single nanoparticle excited by a 10 fs laser pulse (Figure 1.1.11.a). The energy given by the incident electromagnetic wave interacts with the SPR of the nanoparticle and in less than 10 fs decayed in hot electrons and holes (Figure 1.1.11.b). Because electrons are negatively charged and holes are positively charged, they evolve in time through coulombic interactions. The process leads to the neutralization of the charges and lasts only tens of femtoseconds (Figure 1.1.11.c).

Charge carriers recombine beginning with the particles with higher energy to the lower. The holes are not real particles, but being constituted by vacancies in the distribution of the electrons, which in this conditions behave as particles, they have a particle-like behaviour.[60]

After the recombination, in a time frame of few picoseconds, the energy acquired by the system is released through the coupling with phonons which transfer the excess of energy to the surrounding medium (Figure 1.1.11.d).[61,62] The process of converting the electron excitation in thermal phonon is called thermalization.

When studying the hyperthermia properties of anisotropic nanoparticles, all the characteristics previously established for the SPR properties have to be considered as relevant for the hyperthermia efficiency of the particles. The shape of the particles facilitated the charge separation, for example for AuNRs the t-SPR absorbed a similar amount of energy compared to spherical nanoparticles while the LSPR had a much more intense absorption of less energetic wavelength. Thus, it was able to generate a larger amount of hot electrons and consequently a larger hyperthermia effect.[63] Another advantage of anisotropic nanoparticles is the tuneability of their SPR which

could be attuned to the wavelength of the incident light. For example, the AuNSs used in this thesis, had a complex SPR spectra generated by the interactions of the core and spike system.[11] Thus, they were able to absorb a large band of wavelengths which could be used to trigger the hyperthermia effect.

1.1.4. *Photosensitizer dyes*

1.1.4.1. Light activated therapy and photosensitizers

The treatment of certain illnesses with the exposure to light (e. i. psoriasis, rickets and vitiligo) was a common practice used in ancient time in many different areas of the globe, like Egypt, China, India and Greece. As an example, in ancient Greece, vitiligo was treated by laying naked in holy grounds exposed to the sun. This ritual was abandoned with the advent of Christianity and the medical applications of light were forgotten in western countries until the late 18th century.[64] Only at the beginning of the 20th century with the work of Niels Finsen (Nobel price 1903) phototherapy was rationalized in a real science and popularized.[65,66] But the application of light on the treatment of diseases was limited by the amount of energy that could be safely concentrated in the affected part of the body.

While in the west, phototherapy was forgotten after the end of the classical period. In India, these practices were commonly used and reported in medical-religious books (e.g. Atharva-Veda, 14th century BCE). The main advantage of the eastern phototherapy over the western counterpart was the use of certain plant extracts (e.g. *Psoralea Corylifolia)* to improve the efficiency of the exposure to the sun.[67] Thus, marking the first historical report of the use of a photosensitizers.

Similar rediscovery of photoactive extracts containing psoralens happened many times in history. But only towards the end of the 21st century with the invention of artificial UVA light sources their application for phototherapy became more commonly practiced.

Another important step in the development of photodynamic therapy (PDT) was the synthesis of hematoporphyrin from blood (≈ 1820'), which was discovered to have an antimicrobial effect when exposed to light in presence of oxygen (1900).[64] After this discovery, for all the 21st century a great number of reactive molecules were synthetized and tested. Until now, all the molecules approved for the clinical use, need to weight efficiency against serious side effects (prolonged photo-sensibility, cumulation in the body, toxicity, etc.)[68] and there is not a clear agreement in the literature on the type of structures which can produce the safer and more reactive photosensitizer.[69]

To be suitable for PDT an ideal photosensitizer should: i) have a low level of toxicity in the dark or when administer to a patient, ii) absorb light in the infrared (IR) range where the optical window of human tissues is located, iii) be easy to synthetize and store and iv) be quickly excreted by the body or decomposed after the use, to reduce the side effects for the patient after the treatment.[69,70]

1.1.4.2. Crystal Violet

Crystal violet (IUPAC name tris(4-(dimethylamino)phenyl)methylium chloride, CV) is the main PS used in this thesis. This PS has been reported for the first time in the 1861 with the name "Violet de Paris"[71] and it was the first dye used as a staining agent for the Gram categorization of bacteria in the 1884.[72] From the 1912 with the name "Gentian Violet", it was used

as a drug against infections caused by bacteria and fungi and it became commonly used for the treatment of skin diseases or for the treatment of *Candida* infections and lesions. The discovery of antibiotics led to a progressive abandonment of CV as a drug, but it has recently been revaluated as an option against drug resistant bacteria.[71]

The structure of CV favours its interaction with the DNA (being CV aromatic and positively charged), but until now there are not been any conclusive proof of its toxicity for mammalian cells. Some of the tests conducted by the FDA showed an increased incidents of thyroid cancer for mice after two years from the treatment with CV.[73] But the quantities administered to the mice were much larger than the amount commonly used for the therapeutic use (expressed in mg per kg of body mass) and no conclusive evidence of toxicity in humans have been reported.[71]

The mechanism of action of CV against microorganisms has not been completely clarified with many competing theories about its interactions with bacterial cells: i) alteration of the redox potential in the cells, ii) inhibition of the NADPH oxidase, iii) free radical formation, iv) interactions with the cell wall or v) inhibition of the synthesis of certain proteins.[74] The interactions with the bacterial cells and the radical production are the two most accredited causes of the CV activity against bacteria and fungi.[75]

The capability of CV of interacting with light and releasing radicals made it a suitable candidate for the production of ROS for antimicrobial purpose[10,76,77] and it allowed this dye to establish a strong plasmonic coupling with the gold nanoparticles used in this thesis, in order to boost the ROS production.[10,11]

1.1.4.3. Light activated ROS production

The therapeutic effect CV, a PS, is connected to the release of ROS which are radical and reactive species able to quickly react with organic molecules damaging cancer cells and bacteria.

ROS are present as a product of the cellular respiration in healthy cells and microorganisms and they play a key role in many intracellular signalling pathways.[78] The balance between their use and the defence against them plays a major role in the cellular metabolism of all the organism living in an oxygen rich environment (aerobic organisms).

The complex nature of the relation between cells metabolism and the toxicity of ROS make them suitable to attack bacteria and cells which are prone to develop resistance to chemical substance, for their ability of overloading the natural defence mechanisms of the cells and triggering their destruction.

PS are able to produce ROS through the interaction between their excited states and the molecules dispersed in the medium in which they are immersed, as O_2, NO_2, NO, CO, CO_2 or organic species.

In Figure 1.1.12 the example of crystal violet (CV) and O_2.

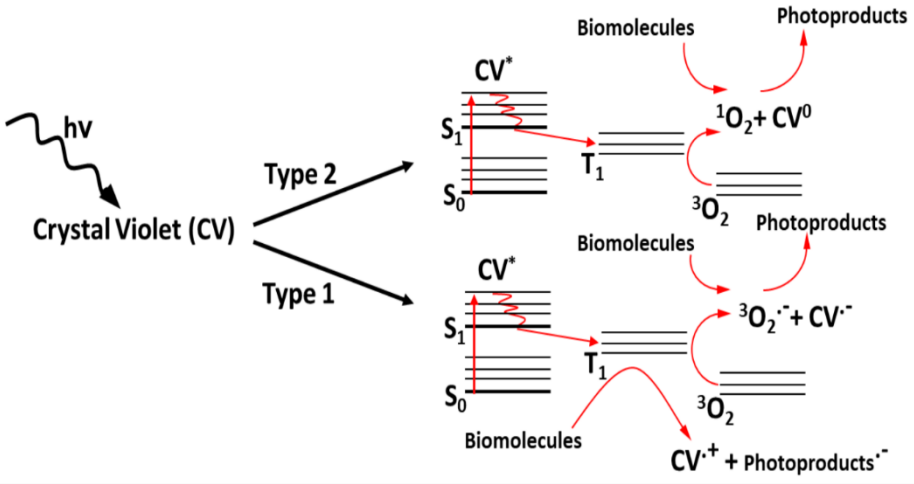

Figure 1.1.11. Mechanism of ROS generation of a PS, crystal violet, exposed to light.

The transfer of energy or electrons between the dye and the molecules in the medium is statistically rare, because it requires the excited state of the dye (S_1) to last for a relatively long time (for CV ≈ 130 ps in solid or viscous media) without releasing energy as fluorescence or heat.[79,80] When a PS is excited by light its electrons get promoted to an higher energy level, without causing a change of their spin, for example singlet to singlet ($S_0 \rightarrow S_1$).

From this state the system can evolve in three ways: i) radiative emission, fluorescence; ii) coupling with the vibrational states of the molecule, releasing heat or iii) by intersystem crossing, thus switching the excited electron configuration from a singlet state to a triplet state of lower energy ($S_1 \rightarrow T_1$).

From the triplet state the system could release energy as vibrations and heat going back to S_0, emit light (phosphorescence) or finally it could interact with other molecules in the triplet state to release energy (e.g. O_2),

either with a type 1 mechanism or donating an electron with type 2 mechanism (Figure 1.1.12).[81,82]

Compared to other dye and fluorescent substances, PS are able to produce ROS because they can maintain an excited state for a relatively long time. PS also possess a triplet state relatively easy to access with an energy level comparable with the base state of molecular oxygen in solution. Because these states are both triplets, they can easily exchange energy.

1.1.5. *Plasmonic coupling*

A consequence of the photo-electronic properties of PS and metal nanoparticles is the possibility for them to interact. Because this type of interactions involves quick transitions and orbital interactions, the distance between the PS and the particles influenced directly the strength of this effect.

For very short distances (< 10 nm) and in presence of a defined energy difference between the excited states of the nanoparticles and the PS the two components could cause a resonance energy transfer (RET) or the direct transfer of an electron from the conduction band of the metal particle to the excited state of the PS.[83–85]

On the other hand when the absorption peaks of the PS and the particles overlapped, the two systems did not only exchanged energy but they also can generate new energy levels shared between the components, this phenomenon is called plasmonic coupling (Figure 1.1.13).[86,87]

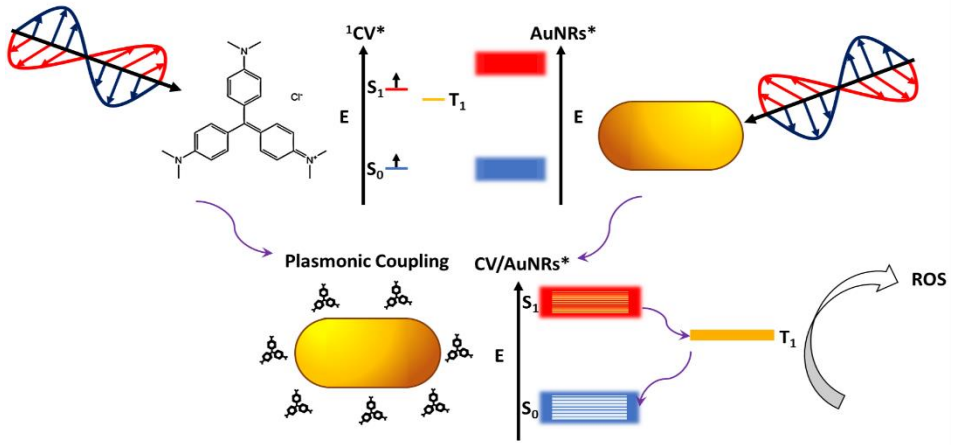

Figure 1.1.12. Summary of the effect of the plasmonic coupling on the light interaction of the CV/Au nanoparticle system.

The hybridization of the energy levels could results in the quenching of the peak of one of the components in exchange to the increases of the other (weak couplings) or the modification of both the absorptions and the appearance of new peaks corresponding to the new energy levels available (strong couplings).[88]

This property of plasmonic systems has numerous applications, from intensifying the fluorescent signal of a probe or the detection of single molecules adsorbed on the surface of metal nanoparticles.[85,89] When plasmonic coupling involved metal nanoparticles and PS dyes, it results in an increase of the ROS production (Figure 1.1.13).[10,11,90]

When a PS (as crystal violet used in this thesis) interacts with nanoparticles with overlapping SPR absorption peaks (i.e. AuNRs, AuNSs) their energy levels mixed. This interaction between particles and dye allows the dye to

benefit of the massively larger cross section and extinction coefficient of the nanoparticles. Nanoparticles are able to absorb light more efficiently than dyes while generating a strong polarization in the space surrounding the particles.

The combination of the polarization and the surplus of energy made available by the particle, dramatically increases the rate of the intersystem crossing, thus populating the triplet state of the PS molecules near to the surface of the particles and leading to an increase in the formation of ROS (Figure 1.1.14).

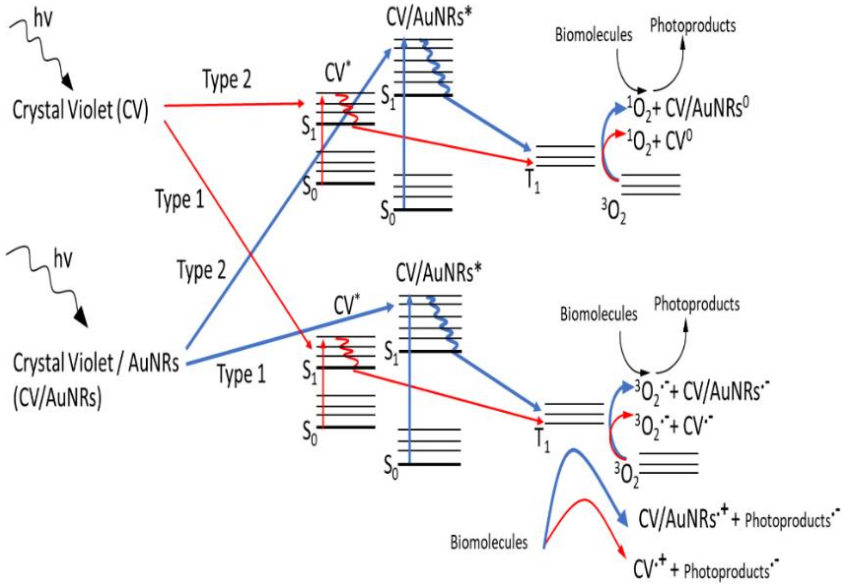

Figure 1.1.13. Mechanisms of ROS production for a coupled PS-gold nanoparticles system (CV/AuNRs).

There is not a complete accordance in literature on the theoretical basis of plasmonic coupling, mostly because there is the great variety of plasmonic systems and PS reported in literature, which hinders any attempt to generalize the theory behind it.[91,92] But on the other hand there is an

extensive literature covering the characterization of systems, where plasmonic coupling is present.[87,93,94]

A mathematical analysis that can be used to track the effect of the plasmonic coupling and the PS-particles interactions is to study the simulated fluorescent emission of the $^1O_2$ produced by the coupled system.[95]

The Equation 1.1.10 describes the intensity of phosphorescence emission of $^1O_2$ for a system containing in which a PS is generating ROS.

$$I = \gamma_{ex} \Phi_{ISC} P_T S_\Delta \Phi_P \quad (1.1.10)$$

Where I is the phosphorescence intensity emitted by $^1O_2$ while decaying to the triplet base state $^3O_2$; γ_{ex} is excitation rate of the PS; Φ_{ISC} is efficiency of intersystem crossing for the PS; P_T fraction of the triplet PS interacting with the $^3O_2$; S_Δ efficiency of the interaction between the triplets and Φ_p is the quantum yield of $^1O_2$ phosphorescence. The P_T term is a function which contained the term τ (lifetime of the PS excited state) and k_q constant rate for the reaction between the triplets (Equation 1.1.11).

$$P_T = \frac{k_q[O_2]}{\frac{1}{\tau} + k_q[O_2]} \quad (1.1.11)$$

The introduction of coupled particles changes some of the terms of these equations: i) γ_{ex} remains constant because we consider the SPR and the PS absorption perfectly overlapping, ii) $\Phi_{ISC} < \Phi'_{ISC}$ because the intersystem crossing is favourited by the polarization of the system, ii) P'_T is different from the PS because the coupling increases the time the PS spent in the excited state, iv) S_Δ is also increased by a combination of heavy atom effect

and the action of the polarization,[96] and finally v) Φ_p is a physical property of the excited state of oxygen and it is not influenced by the coupling.

As could be seen from these considerations plasmonic coupling is the name given to a complex series of interconnected interactions between the electrons and the level structure of system formed by the particles and the PS, which has an important role in the production of ROS of the film.

1.1.6. *Disinfection of medical facilities*

1.1.6.1. Routine disinfection methods

The disinfection of surfaces is necessary for all the environments open to the public and especially important for facilities involved in the medical sector or food production. In hospitals and medical facilities, the disinfection procedures are a complex and recurring endeavor causing a constant drain of resource and requiring a continuous effort from trained personnel.

Attempting to rationalize the balance between effort and efficacy of the disinfection process, the World Health Organization (WHO) regularly releases guidelines to optimize the methods and frequency of the routine procedures for cleaning medical facilities.[97,98]

The sheer scale of this task could lead to accidental errors, which consequently reduce the effectiveness of the cleaning procedures. Direct examinations of hospital surfaces (performed from the 1990 to the 2012) demonstrated that these procedures were so unreliable that 40% of the surfaces in close contact with patients could not achieve the required sterility standards, indicating a serious issue for public health.[5,99,100]

1.1.6.2. Nosocomial infections

The limited effectiveness of the routine methods of disinfection leads directly to one of the main issues faced by modern medicine, the progressive increases of the bacterial resistance to the most commonly used antibiotics and drugs.

Bacterial resistance is generally acquired by bacteria proliferating in environments where a large amount of drugs is used, and more concerning it happens in places, as hospitals and clinics, where the resistant bacteria can infect patients which are already weaken or suffering from other diseases.

Hospitals and clinics are the most vulnerable hotspots for these type of bacteria. But this issue is also related to food production facilities which process large quantities of products treated with antibiotics.

In the medical setting these types of diseases, called hospital acquired infections (HAI), involve 5% of the intensive care patients in developed countries (47.9 cases for 1000 hospital hours) and 15.5% of the patient of the developing countries.[101] While cross contamination during food production causes a great number of illnesses every year (e.g., 9.4 million of cases and 2612 casualties in the 2011 only in the US).[102]

Almost the 90% of the nosocomial infections are caused by bacteria while mycobacteria, parasites, protozoan, fungi and viruses have only a minor role in these type of infections.[103]

1.1.7. *Gram positive bacteria*

Bacteria are some of the most common, ancient and various lifeforms present on the planet. Because their variety is so vast, they are divided in

different groups and then in different species. A species of bacteria has similar characteristics but possess different mutations.

The first step in the categorization of bacteria began with the discovery by Hans Christian Gram in the 1884 that some bacteria became bright blue when stained with the crystal violet dye (CV), while others gained only a very faint violet colouration. He named the first Gram(+) and the others Gram(-).[104]

Gram staining classification is not as straightforward as marking bacteria with a dye. Most of the information used for the characterization are obtained by studying which solvent is able to remove the staining from the bacteria and which chemical can be used to fix the dye on them. Because all these passages are direct consequences of the chemical structure of the surface of the bacteria they were used to separate the bacteria in sub categories.[105]

As previously stated, Gram positive bacteria got their name from their response to the Gram staining method, which turn them of an intense blue colour.

The change of colour is caused by the CV dye intercalating with the peptidoglycan barrier, which is the main component of their bacterial membrane (see section 4.4.2.1.1 for details on the cell wall structure of Gram(+) bacteria). These bacteria are a serious concern for human health because for example they represented only 14% of the blood related HAI in the 2000; but they caused the 76% of the deaths caused by these infections.[106]

The increase in awareness about the morbidity and complications related to the HAI has brought an improvement on the disinfection procedure after the 2000' and a general decrease of this kind of infections was observed. But in the 2014 in US *C. difficile* and *S. aureus*, both Gram positive bacteria, were still the two most common causes of HAI generating the 22.8% of the total infections (*C. difficile* 12.1%, *S. aureus* 10.7%).[107]

Because Gram(+) bacteria have a large impact on public health, their categorization and the study of their properties is very relevant for the reduction of their infections.

The capability to absorb dye separate Gram(+) from the Gram(-), but this characteristic is common to a large number of species that have been further subdivided according to their physical characteristics (Figure

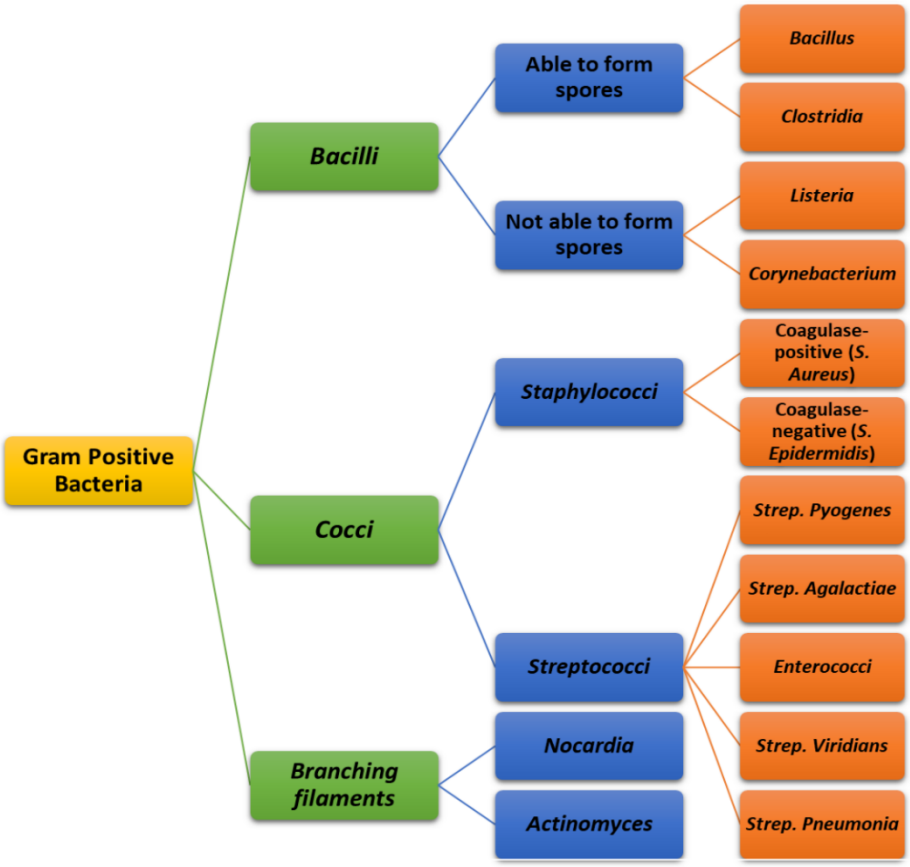

Figure 1.1.14. Schematic classification of Gram positive bacteria according to their appearances and characteristics.

1.1.15). The Gram(+) bacteria are divided into three main groups according to their shape: i) *bacilli*, rod shaped; ii) *cocci*, spherical and iii) branching filaments.

Bacilli further split into two groups according to their ability to form spores, for example the most common cause of HAI, *Clostridium difficile* is a Gram positive rod shaped bacteria able to produce spores. *Cocci* are divided into two groups which labelled with the prefix: *Staphylo* (*S.*) and *Strepto* (*Strep.*).

Staphylococci organized themselves in grape like aggregates while *Streptococci* form chains of bacteria organized head to tail. *Staphylococci* were further subdivided according to their ability to express the coagulase protein which was a test used in hospitals to narrow down the list of bacteria which may cause an infection. For example, *Staphylococcus aureus* is a Gram(+) spherical bacterium which organizes in clusters and produces coagulase. *Streptococci* are the most common type of Gram(+) bacteria and not all of them can cause illnesses. This group contains from 5 to 8 further subdivisions not all bacteria affecting in humans: *Strep. pyrogens* (Pharyngitis and "Scarlet fever"),[108] *Strep. agalactiae* (neonatal meningitis)[109] are the causes of many human diseases, while *enterococci* are common not pathogenic members of the gut biota.[110]

The branching filaments types of Gram(+) bacteria gets their name from the branch like structures. The similarity of their structure with fungi made them difficult to be identified. The two families of this type of bacteria, *nocardia* and *actinomyces,* are different because the first species can survive in normal laboratory conditions and is pathogenic while the second one is strictly anaerobic and it is the source of 80% of all known antibiotics.[111]

1.1.7.1. Gram positive model: S. aureus

S. aureus was chosen in this thesis as a model for the Gram(+) bacteria, because it can be commonly found in medical environments and can be safely handed in a laboratory setting. The first Gram(+) bacteria for number of cases, as previously reported, is *C. difficile.* But this bacterium is able to produce spores thus, is more difficult to control and requires a specialised laboratory set up to be safely used for research. For this reason, *S. aureus* was considered a better option.

S. aureus is a spherical bacterium with diameter varying between 0.5 µm and 1 µm. In presence of a rich culture substrate its dimensions tends to increase.[112] The cell wall of *S. aureus* looks smooth when observed with SEM (Figure 1.1.16)[113] and when it is cultured on a plate it forms small colonies of a faint yellow colour (which could get reddish for some strains). From this colour it gained its name *aureus* which means golden in Latin.

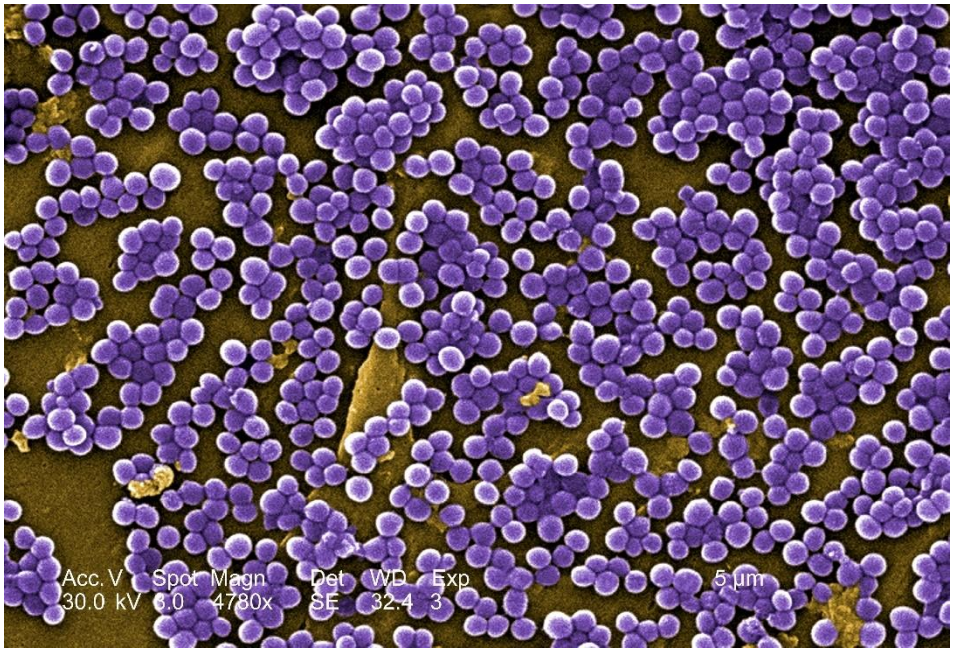

Figure 1.1.15. SEM picture of methicillin-resistant staphylococcus aureus (MRSA), picture acquired by Janice Carr and Jeff Hageman of the US centre for disease control and prevention (CDC) public domain.

S. aureus is mostly an aerobic bacterium, but it can also survive in anaerobic conditions. *S. aureus* can also survive in solutions containing up to 7.5% of NaCl.[112]

S. aureus is very diffused in the human population and it can be found with a nasal swab in the 30% of the people. But it generally does not cause infections in healthy subjects, while in subjects that are already debilitated, it can cause a large number of different conditions, varying from: i) skin lesion and infections, to ii) blood stream infections, to iii) *endocarditis* and iv) *osteomyelitis*.[114] Of these conditions the blood stream infections and consequential *endocarditis* are the most common causes of morbidity connected with this bacterium.

If we could be able to successfully contain the infections caused by this bacterium, especially in the post operational conditions it would eliminate the 18.7% of all the blood stream infections and greatly reduce the mortality rates between intensive care units patients.[115]

1.1.8. *Gram negative bacteria*

The bacteria which gained only a pink colour after the Gram staining were named Gram negative (Gram(-)). The cell wall of Gram(-) bacteria is constituted by an outer phospholipidic membrane, a thin peptidoglycan layer and finally another phospholipidic membrane, only the central layer could be stained with the Gram method which results in a faint pink colour instead of blue (in section 4.4.2.2.1, further details on the structure of this type of cell walls). The cause of this colour is the CV dye, which can have a range of different colours depending on its physical form or the chemical environment in which it is dispersed, varying from green in dry powder, to

dark purple in concentrated aqueous solution, to pink in a diluted one and to blue in organic solvent.

There is a large variety of different Gram(-) bacteria, for this reason, they are subdivided into groups and species to categorise them according their common characteristics(Figure 1.1.19).

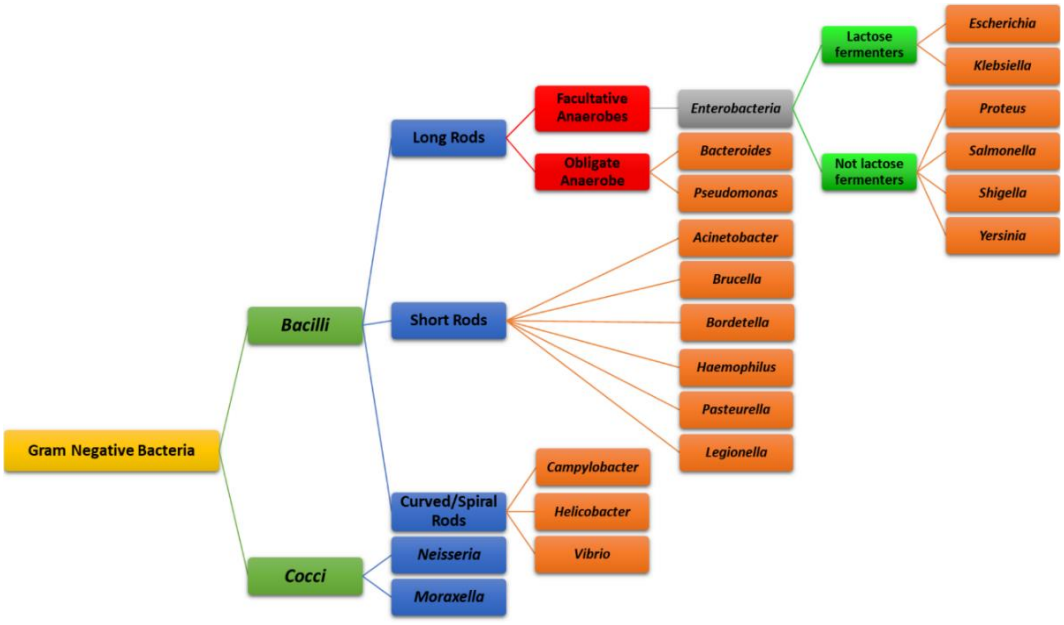

Figure 1.1.16. Classification of Gram negative bacteria

The first distinction used to group the bacteria is their general shape or rod like (*bacilli*) or spherical (*cocci*). *Cocci* were further subdivided into two main groups *Neisseria* and *Moraxella*. The bacteria of these groups are strictly aerobic, oxidase-positive, catalase-positive and DNAse-positive.

Neisseria can form a polysaccharide capsule and can oxidize carbohydrates and tributyrin fatty acids while *Moraxella* are non-capsulated and

asaccharolytic, which means that they are not able to use polysaccharides to produce energy.[116,117]

Bacilli are subdivided in three categories according to their shape: i) short rods, ii) long rods and iii) curved/spiral rods. Curved or spiral rods are subdivided in *Campylobacter*, *Helicobacter* and *Vibrio* the members of these groups are all motile thanks to flagella, situated on both poles for *Campylobacter* and *Helicobacter* or only on one pole for the *Vibrio*.

Helicobacter are urease positive while *Campylobacter* do not possess this enzyme, another difference between them is their opposite antimicrobial susceptibility. Both of these bacteria can cause food infections and are prone to develop antibiotic resistance.[118]

Of the same group, the vibrio bacteria are shaped as a comma with flagella departing from one of the poles, they are generally saprophyte but they can occasionally became pathological (e.g., *V. cholerae*) generally causing serious gastroenteritis.[119] They are usually identified by culturing faecal samples on thiosulfate-citrate-bile salts-sucrose agar culture gel (TCBS) a special substrate with basic pH, which is lethal for all the other types of bacteria.

A large subgroup of the Gram(-) bacilli are comprised of the short rods, all the bacteria of this group are pathogenic, able to form biofilm and increasingly causing concerns for their resistance to most common drugs. Particularly relevant to the field of hospital safety are the *Acinetobacter*

which represent one of the most common causes of nosocomial infection.[120]

The last group of Gram(-) bacteria to be listed are the long rods. These bacilli are categorized according to their tolerance to the exposure to air.

Bacteroides and *Pseudomonas* long rods are strict anaerobe bacteria. *Bacteroides* are a large group of bacteria generally living inside the human body, the vast majority of them are not pathological but one, *B. fragilis* are the most commonly isolated anaerobe human pathogen.[121]

The other bacteria of this group are the *Pseudomonas.* Bacteria of this group can be found on the surface of many parts of the human body and could become pathologic in presence of other infections, an example of this group of bacteria are *P. aeruginosa,* which commonly cause of secondary infection.[122]

The long rod Gram(-) bacteria that are not strictly anaerobe, are called *Enterobacteria,* this group is further divided according to the capability of these bacteria of fermenting lactose.

The lactose fermenting bacteria in this group are the *Escherichia* and the *Klebsiella* while the non-fermenting bacteria are the *Proteus*, *Salmonella*, *Shigella* and *Yersinia*.

Escherichia and *Klebsiella* are common bacteria found in the human population, they can cause grave illnesses and prone to develop resistance

to common drugs. *E. coli* which are used as Gram(-) model in this thesis, a member of this group and cause of many nosocomial infections.[123]

The remaining category contained many bacteria, which can be found in the human guts and can become pathological. An exception is the *Yersinia* group that contains mostly intestinal bacteria of pigs but when jumping species to human caused serious diseases as *Y. pestis* (black plague).

1.1.8.1. Gram negative model: E. coli

The Gram(-) bacteria chosen as model for this work of thesis was *E. coli.* This bacteria are a long rod (0.25 µm to 1.5 µm), able to ferment lactose commonly found in the human gut, fast growing and often used in literature as Gram(-) model (Figure 1.1.20).[124]

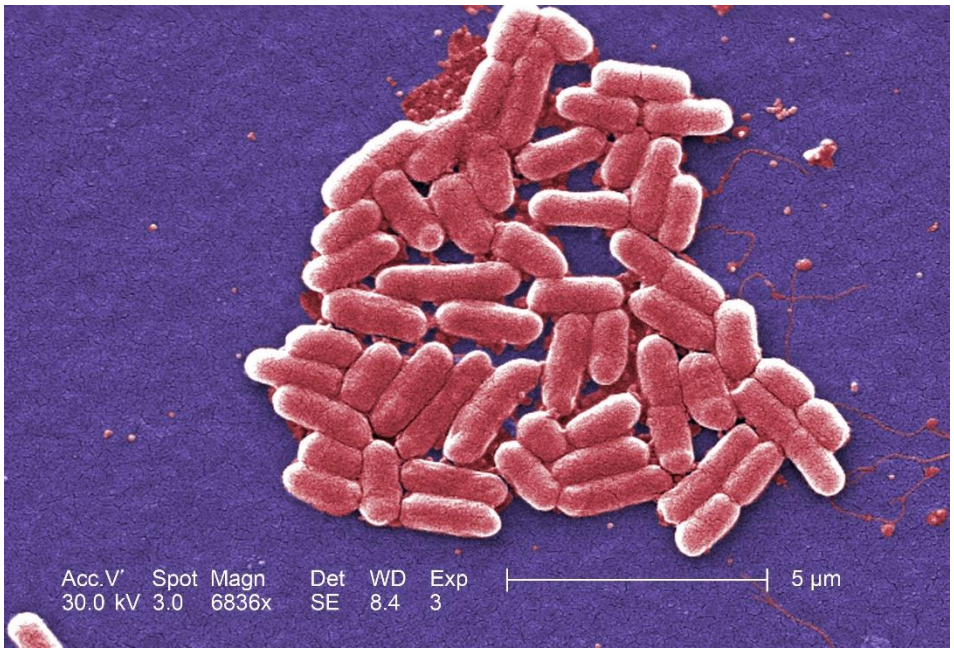

Figure 1.1.17. SEM picture of E. coli of the strain O157:H7, picture acquired by Janice Carr of the US centre for disease control and prevention (CDC) public domain.

The vast majority of the varieties of *E. coli* are not pathogenic but some can produce toxins as the Shiga toxins, which can cause serious illnesses as

"*diarrhoea"* and "*haemorrhagic colitis"* and in average they led to a 30% of hospitalizations.[125]

Because *E. coli* are so diffused in the human population and also one of the most common bacteria found in hospital settings and able to develop antimicrobial resistance. For this reason, *E. coli* are one of the most common cause of intestinal infections and involved in the majority of the catheter related infections.[126] Any improvement in the elimination of this type of bacterium from hospital surfaces and food production facilities would have a dramatic economic and health related benefit, for example in the 2012 in UK, the blood infections from this bacterium costed more than 14 million of pounds,[127] while between the 2013 and the 2016 E. coli alone caused the 24% of all the blood stream infections diagnosed.[115]

1.2. Recent developments in antimicrobial surfaces

As previously discussed in section 1.1.6, the disinfection of surfaces is a lengthy and costly endeavor, in case of errors or malpractices, which can cause an increase of dangerous infections. To improve on the performance of the routine cleaning procedures, no-touch disinfection treatments have been introduced in periodic cleaning routine of medical facilities.[128] These methods use reactive chemicals, high energy radiations or high temperature vapor to enhance the disinfection of surfaces, but they are difficult to use, toxic or dangerous to the personnel, they shorten the life of the surfaces disinfected and they are generally too expensive to use frequently.[7,128–130]

To overcome the limits of the routine disinfection and to avoid the limitations of the no-touch disinfection treatments, an attractive strategy is

to develop surfaces able to automatically reduce the bacterial charge on them.[131]

Because the sterilization of surfaces is a well reported problem, many groups have tried to develop self-disinfecting surfaces utilizing a great number of different components and mechanisms of action.[132,133]

Most of the antimicrobial surfaces reported in literature are based on three main general mechanisms of action: i) very low adhesion materials,[134,135] ii) surfaces able to release active antimicrobial substances,[134,136] and iii) surfaces able to release ROS when activated by a source of energy (UV, laser or white light).[10,11,137,138]

1.2.1. *Low adhesion surfaces*

The activity of low adhesion materials to reduce surface contamination is not driven by their active antimicrobic effect, but mostly from their surface properties, which make very difficult for bacteria to attach on and to produce a biofilm.[139,140] As a consequence of their adhesion properties, these surfaces are easier to clean compared to untreated surfaces, which improve the effectivity of the routine disinfection procedures. To complement this property, most of these surfaces include some types of antimicrobial component (e.g., silver nanoparticles, quaternary ammonium, MgO nanoparticles), which further reduce the risk of the formation of a biofilm.[139,141,142]

The main drawback of this type of surfaces is their durability, because the complexity of their structure (polymer modified by nanoparticles or active components) make them quite vulnerable to physical damage and aggressive disinfection methods.[143]

1.2.2. *Surfaces able to release antimicrobial substances*

Some surfaces generate an antimicrobial effect by slowly releasing active substances, many different types of active components used to produce them.[6,134,144] These surfaces can be made of, or ornated with i) nanoparticles containing noble metals, such as silver and copper,[145–148] ii) organic biocides (e.g., antibiotics, triclosan, polymers such as chitosan, sulfonium salts)[149–153] and iii) biological biocides (e.g., enzymes, antimicrobial peptides, bacteriophages.[154–156]

As seen for the low adhesion surfaces (1.2.1), the long term resistance of these types of surfaces is a concern especially for the last two categories. The first group is the one which is readily available, but the cost and the maintenance have limited its use on a larger scale.[144] One advantage of this type of surfaces is their effectiveness, which is able to greatly improve the sterilization level of a facility,[157] at least for a short period. But they often need to be renewed to maintain their antibacterial properties. Another concern, is their long term effect on the bacteria, because the constant exposure to antimicrobial substances can select resistant strains.[6]

1.2.3. *Light activated antimicrobial surfaces*

The last category contained the surfaces able to catalyze the formation of ROS when interacting with a source of energy (UV, laser or white light).[6] These antimicrobial surfaces were a relatively recent development. An early example, in the 2008, used spherical nanoparticles of TiO_2 to generate a photocatalytic effect that was able to kill bacteria when exposed to UV light.[137,158]

The use of nanoparticles increased the efficiency of the disinfection, compared to UV light or TiO_2 alone and required less energetic light sources

compared to the one previously seen for TD, but also for these surfaces the UV light used in their activation was still dangerous for surfaces and operators.[7]

A variation from the semiconductor nanoparticles contained in surfaces to generate ROS was to use a hybrid system composed by small spherical gold nanoclusters (< 5 nm, AuNPs) and a sensitizer dye.[138] The AuNPs based catalysis of ROS showed a great antimicrobial activity, under the exposure to a laser in the visible range.[159,160] In a normal white light conditions, they required as long as 6 h to reach a comparable level.[138]

The use of gold cluster as catalyst in conjunction with a PS dye compared to larger nanoparticles (which have been used in this thesis) has the advantage of being able to produce an antimicrobial effect in condition of weak light exposure, with the trade-off of a reduced activity and longer exposure time.[161] Another issue with these types of systems is that the exact mechanism in which the ROS are generated has not been completely clarified, as indicated by the many examples in literature where these types of systems exhibit some activity in the dark, which while contributing to the general efficiency cannot be explained with a photocatalytic effect.[82,138,160,161]

While the antimicrobial films, explored in this thesis, are instead based on the plasmonic coupling between anisotropic gold nanoparticles and PS.[11] The capability of metal nanoparticles, possessing a strong SPR, interacting with chromophores and photosensitizer has been proved in literature (section 1.1.5),[87,88] but for the first time in this thesis the plasmonic coupling between plasmonic gold nanoparticles (> 10 nm diameter) and dye has been used to produce an antimicrobial effect.[10,11] The system studied here

required the exposure to a stronger white light compared to the nanoclusters surfaces but it had a faster bacteria elimination rate and no toxicity in the dark. While still activated using only a harmless commercial white light thus, avoiding the problems caused by more intense types of radiation (UV and visible laser light).[10]

Chapter 2: Synthesis and characterization of anisotropic gold nanoparticles

2.1. Introduction

The core component of the antimicrobial film developed in this work was a coupled system between anisotropic gold nanoparticles and the photosensitizer dye. As described in section 1.1.5, to maximize the plasmonic coupling between the two components, their physical characteristics have to be tailored to obtain the highest degree of overlapping between the absorption of the dye and the SPR peaks of the nanoparticles used.[87] The PS dye is needed because it was fundamental to the formation of ROS (section 1.1.4.3).

Considering that the absorption of the dye cannot be changed, the only practical and flexible way to maximize the plasmonic coupling in the film was to tune the SPR of the nanoparticles to match the absorption of the dye. At the same time, because the intensity of the SPR of the nanoparticles depended from their morphology (section 1.1.3.1), their synthesis was tailored to form anisotropic or pointy structures. Thus, improving their ability to boost the activity of the coupled system.[162]

The synthetic procedures used in this thesis were based on the seed mediated synthesis (introduced in section 1.1.2, reported in sections 2.3.1 - 2.3.3). The seed mediated approach was selected because it enabled the synthesis to obtain the level of shape control and size tuning which was necessary to obtain an efficient plasmonic coupling. Nanorods and nanostars (AuNRs and AuNSs) were selected for the preparation of the antimicrobial film. AuNRs were characterized by a distinct two-dimensional anisotropy along both the length and diameter, while AuNSs possessed a

complex and three-dimensional symmetric structure caused by the irregular and variable size and distribution of the spikes.

Thanks to their shape and size, the particles used in this thesis had a high ratio between their surface and their mass (section 1.1.2) and an extinction coefficients of order of magnitudes more intense than the organic dye coupling with them.[163] These characteristics combined with their low toxicity and the tunability of their SPR absorption, made them suitable candidate for the preparation of the antimicrobial film.[164]

After the synthesis, the particles were analysed with a series of techniques aimed to determine: the concentration of their batches (using elemental analysis, section 2.3.4), the intensity and position of their SPR absorption (using UV-visible, section 2.3.5), their size and shape distribution (using statistical analysis of TEM pictures, section 2.3.6) and finally the fluctuation of the electrical field surrounding them caused by the SPR effect was simulated (using finite-difference time-domain simulation or FDTD, section 2.3.7).

2.2. Materials

Hexadecyltrimethylammonium bromide (CTAB, ≥ 98%) was purchased from Tokyo Chemical Industry. Hydrogen tetrachloroaurate solution ($HAuCl_4$, 30 %wt), sodium borohydride ($NaBH_4$, ≥ 98%), silver nitrate ($AgNO_3$, ≥ 99.0%), sodium bromide (NaBr, ≥ 99,99%), L-ascorbic acid ($C_6H_8O_6$, ≥ 99%), poly(sodium 4-styrenesulfonate) (NaPSS, Mw 70 kDa), sodium citrate (CitNa, > 99%), methoxy-PEG-thiol 3.5 kDa (thiol-PEG-OMe, > 99%), sodium chloride (NaCl, ≥ 99%). Hydrochloric acid (HCl, 36 – 38 %wt, Duskan Pure Chemical) was acquired from Duskan Reagents, Singapore.

2.3. Methods

2.3.1. *Synthesis of gold nanorods*

The synthesis of AuNRs followed a seed mediated process as introduced in section 1.1.2.2.

2.3.1.1. Synthesis of the seeds

The seeds solution was prepared by mixing an aqueous solution of $HAuCl_4$ (5 mL, 0.5 mM) with a concentrated solution of CTAB (5 mL, 0.2 M) and reducing them with ice cold $NaBH_4$ (0.6 mL, 10 mM). After the reaction, the solution was left to incubate for 1 h.

2.3.1.2. Synthesis for gold nanorods with shorter aspect ratio

The growth solution was prepared by adding to a solution of CTAB (5 mL, 0.2 M) a precise amount of $AgNO_3$ (75 µL, 10 mM), then adding an aqueous solution of $HAuCl_4$ (5 mL, 1.4 mM); followed by a concentrated solution of NaBr (0.25 mL, 1.25 M) and a small aliquot of HCl (12 µL, 37 %wt).

The growth of the particles was initiated with the addition of L-ascorbic acid (105 µL, 79 mM) and after 30 s of agitation, 60 µL of the seeds solution was added (section 2.3.1.1). The reaction required an overnight incubation at 30 °C to reach completion.

2.3.1.3. Synthesis of gold nanorods with longer aspect ratio

The growth solution could be tuned to produce longer rods with aspect ratio 3.5 to 4. The growth solution for long rods was prepared adding a precise amount of $AgNO_3$ (50 µL, 10 mM) to a solution of CTAB (5 mL of 0.1 M) and later adding $HAuCl_4$ (5 mL, 0.5 mM) to the solution. A small quantity of a concentrated solution of $NaNO_3$ (75 µL, of 2.78 M) and an aliquot of HCl (12 µL, 37% wt) were added subsequently. The synthesis was initiated by

adding L-ascorbic acid (75 μL, 79 mM) to the solution and seeding with 60 μL of seed solution. The reaction reached completion after an incubation overnight at 30 °C.

2.3.2. *Synthesis of gold nanostars*

The synthesis of AuNSs used the procedure introduced in section 1.1.2.3.

2.3.2.1. Synthesis of spherical gold nanoparticles as seeds

An aliquot of citrate solution (0.5 mL, 1 %wt) was added to a boiling solution of $HAuCl_4$, (9.5 mL, 0.5 mM) under fast stirring.[46] After 5-10 min from mixing the two reagents, the solution turned dark blue-purple and then, after approximatively 30 min the colour progressively turned wine red indicating the end of the reaction.

2.3.2.2. Growth solution for gold nanostars

The growth solution for the AuNSs was prepared by acidifying a solution of $HAuCl_4$ (10 mL, 0.25 mM) with HCl (10 μL, 1 M). To the resulting solution were then added in quick succession: 100 μL of seeds solution, an aliquot of $AgNO_3$ (100 μL, 3 mM), ascorbic acid (50 μL, 100 mM) and after 30 s, a solution containing a capping agent to stabilize the just formed AuNSs.

The AuNSs used in this work were stabilized at the end of the growth procedure by adding CTAB (1.74 mL, 48 mM) or a large steric stabilizer chosen between mercaptopoly(ethylene glycol)methylether (thiol-PEG-OMe) and mercaptopoly(ethylene glycol)carboxylate (thiol-PEG-COOH) (1.74 mL, 108 μM for both of them).

2.3.3. *Surfactant removal procedure*

An Optima Max Ultracentrifuge from Beckman Coulter was used to remove the capping agent during the experiments performed in the laboratory in

London, while in Singapore a high speed Mikro 220R Hettich microcentrifuge was used for the same procedures. In Table 2.3.1 a list of the settings used to process the different particles synthetized in this work.[165]

Table 2.3.1 Operative conditions for the centrifuges used with the different types of gold nanoparticles

Type of centrifuge	**Type of nanoparticles**	**Speed (g/rpm)**	**Temperature (°C)**	**Time range (min)**
Optima Max	AuNRs 640 nm	17000/ 20000	25	7 - 4
Optima Max	AuNRs 800 nm	17000/ 20000	25	5 - 3
Mikro 220R	AuNRs 640 nm	19064/ 14000	35	10 - 7
Mikro 220R	AuNRs 800 nm	9726/ 10000	35	6 - 4
Mikro 220R	AuNSs 700 nm	3501/ 6000	25	4
Mikro 220R	AuNPs 520 nm	875/ 3000	25	4

The centrifugation and removal of supernatant was used to eliminate the majority of the CTAB from the solution. Because this surfactant is a strong stabilizer, the first round of centrifugation required longer run (Table 2.3.1). After a first redispersion using water, a solution of NaPSS (2 – 3 mL per batch depending on the centrifugation vessel, 0.1 %wt) was used to redisperse the pellets. After two iterations of centrifugation with this solution the nanoparticles were redispersed with a solution containing the final capping agent, following the process is summarized in Table 2.3.2.[43]

Table 2.3.2 List of passages for the removal of CTAB from the surface of Au nanoparticles

Centrifugation passage	**Particles on which it applies**	**Redispersion solution**
1	AuNRs 640 nm and 800 nm	Ultrapure water
2	AuNRs 640 nm and 800 nm, AuNSs 700 nm	NaPSS 0.1% wt
3	AuNRs 640 nm and 800 nm, AuNSs 700 nm	NaPSS 0.1% wt
4	AuNRs 640 nm and 800 nm, AuNSs 700 nm	CitNa 20 mM or thiol-PEG-OMe 50 μg/mL or thiol-PEG-COOH 50 μg/mL.
5	AuNRs 640 nm and 800 nm, AuNSs 700 nm	CitNa 20 mM, or ultrapure water for all the other solutions

2.3.4. *Elemental concentration analysis*

The AuNRs dispersion in water was analysed with the inductively coupled plasma-mass spectrometry (ICP-MS) in order to establish its concentration for the spectroscopic studies. The tests were performed with a Bruker M90 ICP-MS from the department of Earth Science of the UCL.

A solution containing nanoparticles with known optical density (O.D. $_{\lambda=634\ nm}$ = 1.255) was used for the ICP-MS experiments. The experiments were performed by analysing a series of dilutions of the stock solution of nanoparticles. Aliquots of the stock solution (50, 45, 40, 35, 30, 25, 20, 15, 10, 5, 2.5 μL) were added to a fixed amount of nitric acid (2 mL, 2% wt) leading to final concentrations of 1.25, 2.50, 5.00, 7.50, 10.00, 12.50, 15.00, 17.50, 20.00, 22.50 and 25.00 μL_{stock}/mL in the final samples were used.

The concentrations of the other types of nanoparticles were obtained by comparing their absorption with the tested solution, using the internal standard calibration methodology.

2.3.5. *Spectrophotometric analysis*

The UV-visible spectra used in this work have been acquired using a Biotek Synergy 2 plate reader (for the measurements performed in Singapore) and with a Spectral Max plate and cuvettes reader (for the measurements performed in London). Cuvettes with an optical paths of 1 cm were employed for the experiments of UV-visible spectroscopy used to establish the concentration of a nanoparticle colloidal solutions. The concentrations obtained were expressed in O.D.. Quartz cuvettes were used for the measurements in the UV range. For the UV-visible analysis were used transparent plates from Corning of 96 or 384 well.

The dispersions of Au nanoparticles tested with the spectrophotometric analysis were diluted to have an absorption between 0 and 2 O.D. which was the range concentrations where the instruments had their greater accuracy (i.e. < 0.005 O.D. ± 0.1%, *SpectraMax*).[166]

The solution containing the nanoparticles have been tested in aliquots of 50 µL for the 384 wells, 200 µL for 96 wells and 3 mL for the analysis in cuvette. Spectrophotometric analyses were performed on wavelengths between 230 nm to 999 nm (2 nm/step) when using quartz cuvettes or 350 nm to 999 nm (2 nm/step) when using polymeric cuvettes and plates.

2.3.6. *Transmission electron microscopy*

The TEM pictures were used for the analysis of the size and shape of the particles were acquired using either a Philips CM300 FEG TEM operating at 300 kV (for the experiments in Singapore), or a JEOL 1200 EX 2 operating at 150 kV (for the experiments in London).

The TEM samples were prepared by dropping 10 – 20 µL of the dispersion

of nanoparticles (≈1.5 – 2 O.D. of concentration) on Cu/graphene grids with 100 squares mesh, then drying it for an overnight. They could be analysed after storing for 2-3 months inside a TEM grids holder preserved in dry cabinet.

Set up procedure for a TEM measurements changed slightly depending on the model used, but for all of them it needed: a comprehensive calibration to focus the electron beam, the reduction of the aberration and the astigmatism of the electron lenses and finally activate a system of refrigeration to reduce the thermal agitation of the samples. Because if a TEM sample is analysed at temperatures above liquid nitrogen, its picture would look blurred when zoomed to the nanometre scale (approximatively 30'000 magnifications onwards). This happens because the thermal agitation of the sample at room temperature was able to cause vibrations of fractions of nanometre thus making difficult to acquire a focused image.

Samples for TEM were introduced in the machine on copper grids which were then loaded on a sampler rod. This rod was used to carry the samples across three interlock chambers with progressively lower internal pressure, up to $1 – 4 \times 10^{-5}$ Pa.

Because the instrument required hard vacuum to operate efficiently all traces of solvent or volatile components must be eliminated from the samples, failing to do so would damage the tungsten filament used to produce the electrons or it could force the machine to an automatic shut-down.

Acquiring a single picture of the particles using a TEM was not sufficient to obtain real structural data on the nanoparticles analysed. A TEM picture to

be useful had to be taken to a level of magnification on which the particles were easily distinguishable, thus greatly limiting the number of particles that could be captured in a single picture. This led to a biased impression of the real composition of the sample, that was too large to be completely analysed. To reduce the bias was necessary to take many pictures of different areas of the sample and build a statistic of hundreds of particles (at least >200 but better >500).

The pictures were analysed with ImageJ, a software for image processing which could be used to: isolate the particles from the background, approximate their shape with a fitting, and count the number of particles in the pictures.[167] During the analysis, these data were divided in categories to identify the main sizes of the particles in the sample and their distribution.

The automatic acquisition method could not be used on AuNSs because their irregular spikes were too confusing for the sampling algorithm. Thus, limiting the size acquisition of the AuNSs to manual detection, with two separated acquisition per particle: one for the core and another on one of the spikes. The results were analysed with statistical methods and then plotted against their frequency using Matlab 3D plotting.

2.3.7. *Finite-difference time-domain simulations*

The simulations used in this work were performed with a Lumerical FDTD software.[58] Using cubic unit of volume of 1 nm size, while the space surrounding the particles was considered filled with a uniform polarizable media (water). At the same time, the particles were considered stabilized sterically with thiol-PEG-OMe to avoid all the electrostatic interactions on the surface that were not derived from the resonance of the electrons.

The nanostructures used in the simulation were modelled as made of pure gold. Simulations of the boundary conditions were carried out using perfectly matched layers (PML). The source inputs were plane waves of polarized light in the wavelength range between 350 nm and 900 nm.

The dimensional parameters used to describe the gold nanoparticles are reported in Table 2.3.3.

Table 2.3.3 List of physical dimensions used to simulate the nanoparticles used in the thesis.

Type of gold nanoparticles	**Aspect ratio**	**Dimensions**
AuNPs	1	13 nm diameter (D)
AuNRs	2.1 – 2.4	31.8 nm length (L) x 16.1 nm D
AuNRs	3.8 – 4.2	60 nm L x 15 nm D
AuNSs	5	50 nm core (C) x 16.1 nm spikes (S)
AuNSs	2	35.6 nm C x 15 nm S

To simulate the SPR absorption of the particles, the wavelengths of excitation, their spatial orientation and the conditions of the space surrounding the particles were defined.

A summary of the conditions applied is reported in Figure 2.3.1 (A & B), where the yellow line represents the PML conditions, while the white line (red dots) represents the sources of the polarized light. The results of the Maxwell equations are calculated for the electrical field in the area indicated by the orange boxes along the directions indicated by the arrows.

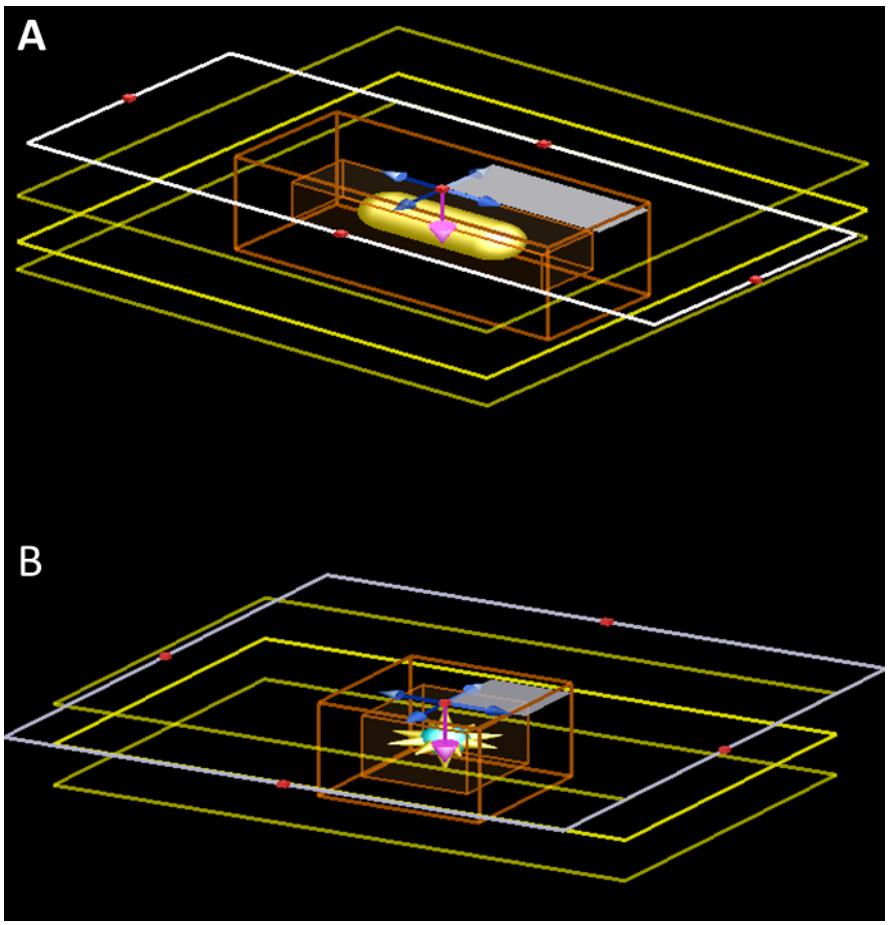

Figure 2.3.1. Simulation box used for the simulations of A) AuNRs and B) AuNSs.

2.4. Results and discussion

2.4.1. *Synthesis of gold nanorods*

2.4.1.1. Mechanism of formation of the seeds and consequence on growth of gold nanorods

As it is characteristic for the procedures based on the seed mediated synthesis (section 1.1.2.1), the preparation of AuNRs require two steps

using different solutions (details in section 2.3.1). Of these steps, the formation of the seed had simplest procedure and only two steps but required an accurate execution to prevent the growth phase from losing reproducibility.

One of the most important components used in the formation of the seeds was $NaBH_4$. Sodium borohydride is a strong reducing agent, which is able to quickly react with $HAuCl_4$ to form of a large number of very small nanocluster of Au^0 (1-2 nm of diameter).[168] While macroscopically, the solution changed colour from faint brown from pale yellow. The cluster created in this reaction were polydisperse both for shape and size but their distribution was quickly homogenized by the Ostwald ripening.[169] This process dissolved the particles with irregular shapes and smaller sizes in favour of the deposition of Au^0 on the surfaces of the larger clusters, which became more spherical and uniform.

There was no agreement in literature on the kinetics of this process with evidence supporting the thesis of a fast process reaching uniformity between 1 and 10 min and others suggesting a slower process requiring 1 to 2 h.[38,170]

According to my observation of the reaction, the batches reached maturity in 1 to 2 h at 30 °C. Synthesis performed using these incubation times generated particles with similar reproducibility and a limited polydispersity (further details on the TEM results section 0). From the practical point of view, using the seeds aged between 1 to 10 min would limit the number of growth solutions that could be seeded using the same batch of seeds, because every seeding procedure required 2 – 3 minutes.

After 2 h of incubation the colour of the solution gained a hint of red, indicating the beginning of a SPR inside the solution, this could be generated by the growing nanoparticles developing their SPR (> 2 nm in diameter) or more probably by the formation of aggregates of clusters which were close enough to generate a common SPR effect.[171,172]

2.4.1.2. Growth of gold nanorods

The second step of the synthesis of gold nanorods was the formation of the rods in the growth solution (details in sections 2.3.1.2 and 2.3.1.3) as discussed in the background section (1.1.2.2), this step presented numerous criticality and its mechanism is not fully understood.

In this section I want to collect some observations which can guide future students and help them to avoid some of the criticality of this reaction.

CTAB was the main components of the two solutions used to synthetize the nanorods, this surfactant is strongly positively charged and helped to stabilize the particles during the formation. Silver, CTAB, $HAuCl_4$ and other inorganic ions, in solution formed a very structured system of complexes and micelles, which controlled the final shape of the particles grown. Because the solution contained a multiphase colloidal system with a single surfactant minor changes in the ion concentration or temperature were able to cause macroscopic changes in its organization.[38,173,174]

A consequence of this variation was the extreme sensitivity of this synthesis in the presence of iodide impurity, where the introduction in the growth solution of as little as 570 nM of iodide could completely inhibit the formation of nanorods. This problem of the synthesis of AuNRs was fairly

common because some industrial process used to synthetize CTAB used iodide intermediates.[175]

There are two main tell-tale signs which indicate the presence of iodide, the first for large contaminations happens when adding the silver to the CTAB at the beginning of the preparation of the growth solution, if the batch turn foggy the solution is contaminated (the "fog" is formed by AgI precipitations). The second sign become apparent after reducing the solution with AA, in normal conditions the batch would turn from orange-brown to transparent in less than 20 s while in presence of iodide, the disappearing of the colour is slower. Furthermore, the solution after the addition of AA will gain a faint yellow colour that will slowly disappear. The second case may happen also if using AA that has been spoiled by humidity or exposure to light.

The speed of the growth reaction depends on the size and aspect ratio of the nanorods formed, with the short and thick rods requiring 2 – 4 h of incubation before developing a visible SPR while the long and thin rods generated SPR 1 h from the introduction of the seeds. Keeping the temperature constant during the overnight incubation reduced the polydispersity of the batch, because it regularized the growth process, 30 – 35 °C was the best range for these type of reaction. For lower temperature, CTAB had the tendency to crystalize while, above 35 °C it could decompose, which was indicated by a strong ammonia smell and led to an irregular growth of the particles.

In scaling up the reaction, it was more convenient to prepare a large number of 10 - 20 mL batches in parallel than a single larger batch in the

0.5 – 1 L range, this because larger batches were difficult to mix and to stir uniformly which resulted in an increase of polydispersity.

2.4.1.3. Importance of the size and aspect ratio in the SPR absorption

A clear example of the correlation between geometrical and optical properties could be seen when studying the LSPR of AuNRs as

To produce the particles, reported in Figure 2.4.1, a series of modification

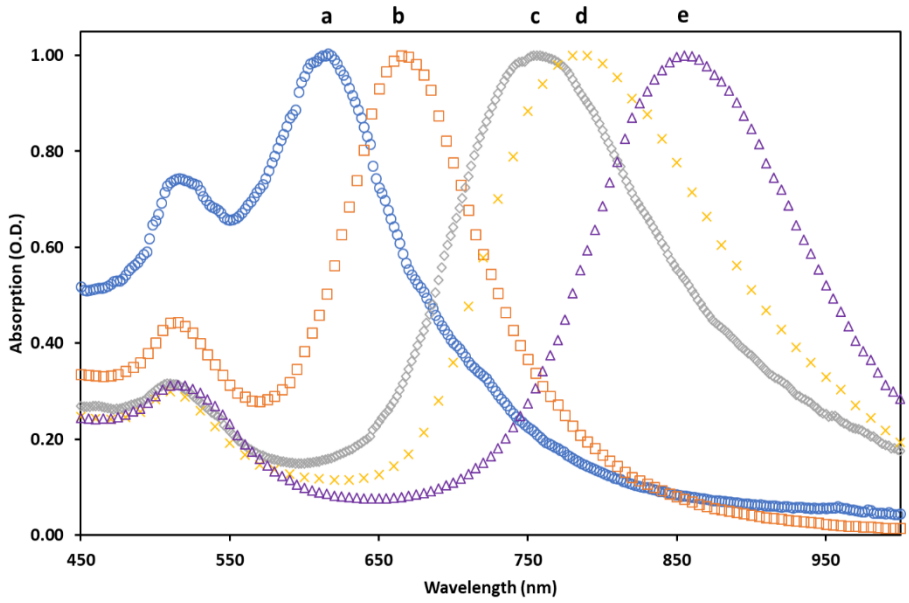

Figure 2.4.1. UV-visible absorption spectra of different sizes (legend in Table 2.4.1)

were introduced compared to the standard synthesis of AuNRs. A larger amount of $AgNO_3$ in the growth solution was used compared to the synthesis for standard shorter rods (section 2.3.1.2): "a" 14.4 mM and "b," 12.5 mM. The spectra “c”, “d” and "e" were obtained from particles synthesised using the procedure for longer rods (section 2.3.1.3). “c” and “d” were obtained by changing the amount of $NaNO_3$ in solution to 29.7 mM and 8.8 mM, respectively, while for “e” the amount of $AgNO_3$ was reduced to 5 mM.

Nanorods samples showing a LSPR with a symmetric bell shape had a uniform distribution of diameters, while tailing peaks indicates a certain degree of polydispersity.

The short rods synthesis produced particles with a larger and more variable diameter, while the diameter of the longer rods was more reproducible. In particular, changing the amount salts ($NaNO_3$) in the growth solution increased the length of the rods, without influencing the diameter.

Reducing the amount of $AgNO_3$ used in the nanorods synthesis reduced their diameter. While increasing the concentration of $AgNO_3$ limited the length of the forming nanorods. Below a certain concentration of $AgNO_3$ (≈ 5 mM) the rods formed where shorter than the average formed using the synthesis for long nanorods but also much thinner, which led to a higher aspect ratio and made them able to absorb at longer wavelengths. Table 2.4.1**Error! Reference source not found.** contains a summary of the dimensions of the particles, the number of particles column refers to the number of TEM images of rods used to collect the data in the previous columns.

Table 2.4.1. Size and structural parameter of AuNRs and their transversal SPR

Label	LSPR position (nm)	Length (nm)	Standard deviation (nm)	Diameter (nm)	Standard deviation (nm)	Aspect Ratio	Standard deviation	N° of Particles
a	615	31.8	6.4	16.1	3.7	2.1	0.6	726
b	665	50	10.7	19.9	5.2	2.6	0.6	332
c	756	51.1	12	16	4	3.3	0.9	244
d	786	53.8	14.7	15.2	3.7	3.6	0.9	735
e	850	47.4	6.0	10.8	1.7	4.5	1.0	202

Table 2.4.1**Error! Reference source not found.** shows that the LSPR peak position was not a function of the length of the AuNRs but it depended by their aspect ratio (AR).

This dependence is clearly shown by the Figure 2.4.2 when plotting AR against peak wavelength of absorption.

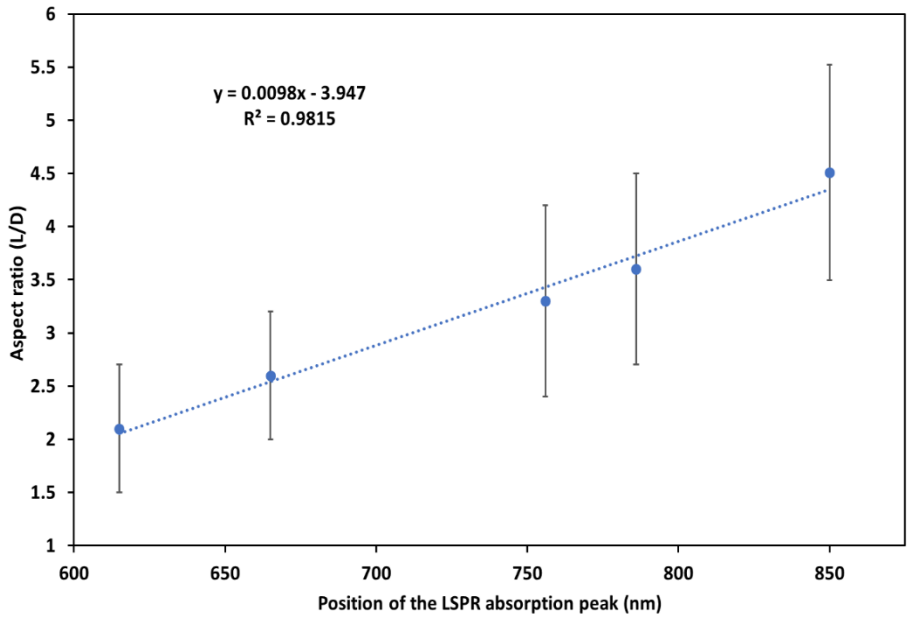

Figure 2.4.2. Relation between aspect ratio and position of the LSPR peak for AuNRs of different sizes.

Because the absorption was function of the AR not of the length, when increasing the length of rods of similar diameter, we could see that their LSPR shifted towards longer wavelengths (a, b, c, d). But at the same time, reducing the amount of $AgNO_3$ reduced the diameter of the rods thus allowing to obtain the same red shift for rods of substantially smaller size.

2.4.2. *Synthesis of gold nanostars*

The procedure used to synthetize AuNSs was introduced in section 1.1.2.3 and described in details in section 2.3.2. As previously reported, this synthesis was very fast and required a precise series of timely addiction of reagents to obtain reproducible results. With the beginning of the reaction macroscopically visible for the blue-green colour of the growing AuNSs.

The addition of the reagents had to be fast because their mixture in the growth solution was so reactive that environmental contaminations could give start to the reaction in absence of the reducing agent, causing the formation of very irregular AuNSs.

After the formation, AuNSs were not stable and needed to be stabilized with a capping and then centrifuged and redispersed (conditions indicated in section 2.3.3) to remove any trace of unreacted $HAuCl_4$. If the unreacted $HAuCl_4$ was left in the same solution with the AuNSs this would result in a progressive aggregation of the particles.

The correlation between the structure of AuNSs and their SPR absorption is not dependent from a single defined factor, AR, as for AuNRs. For AuNSs, the interaction with light was determined by a series of geometrical parameters: overall size of the particle, core/spikes ratio, length of the spikes and number of spikes for particle. The AuNSs used in this thesis had

a general spherical shape, with a reproducible average diameter (52 nm) while they had a variable number of spikes of different geometry and sizes (more details in the TEM results section 2.4.5.8). These spikes, with their interactions generated the broad absorption range characteristic of this type of nanoparticles (section 2.4.5.4).

2.4.3. *Surfactant removal procedure*

As reported in the previous sections (1.1.2, 2.3.1 and 2.3.2) CTAB played a fundamental role in the synthesis of AuNRs and acted as temporary stabilizer after the synthesis of AuNSs. CTAB was able to stabilize the nanoparticles forming a bi-layered barrier on their surface and using silver bromide to form a bound between the surface of the particles and its charged head.[176–178] This barrier contributed to the stability of the particles, thanks to its strong positive charge and the steric hindrance of the hydrophobic layer formed by the tails of the CTAB molecules forming the bi-layer.

CTAB was not suitable as final capping agent of the nanoparticles used in the film, because quaternary ammonium moiety of this molecule was toxic for humans (liver and heart)[179] and its strong positive charge could reduce the interactions between the nanoparticles and the positively charged CV.

In order to remove the CTAB from the surface of the particles a complex procedure requiring multiple centrifugations was required (section 2.3.3). The strength of the bound between the surface of the gold and the CTAB-Ag-Br complex explained why a dialysis or a simple exchange of dispersing media was not sufficient to remove completely the surfactant. For example the first passage of the cleaning process in section 2.3.3, was able to reduce the concentration of CTAB in solution below the foaming point (2.5×10^{-6}

M),[180] but it barely reduced the CTAB coverage of the nanoparticles.[177] The actual removal of the CTAB from the surface of the nanoparticles began with the introduction of PSSNa. This polymer (70 kDa of molecular weight) was able to softly bind the nanoparticles while sequestrating all the positive ions in solution, thus physically removing the CTAB and the silver ions which fixed it to the surfaces. At the same time PSSNa was able to stabilize the nanoparticles without strongly bind with them. Thus, opening the way to an exchange with another capping agent (citrate or thiol-PEG). Because of the large size of PSSNa and its thickening effect on the viscosity of the dispersion of particles only a small concentration of the polymer (0.1 %wt) was necessary to displace the CTAB.

The speed and the run time of the centrifugations used to remove the CTAB depended on the size of particles and on the surfactant concentration in the samples. For example, short rods were resistant to aggregation and formed in a concentrated solution of CTAB (0.1 M) thus, they needed to be centrifuged at high speed for a longer time. AuNSs instead were larger and prone to aggregation and they were stabilized with a small amount of CTAB (7 mM), thus they required short centrifugation time and low speed (Table 2.3.2).

2.4.3.1. Characteristics of the stabilizing agents used for gold nanoparticles

The particles used in this work were prepared with two types of stabilization: sodium citrate (citNa), a small molecule of 189.1 Da with a strong negative charge, and mercaptopoly(ethylene glycol)-carboxylic acid (thiol-PEG-COOH), a large molecular weight polymer (3500 Da) with a weak

negative charge. These two methods of stabilization had both advantages and pitfalls, which led them to be applied to different parts of the project. CitNa granted a good electrostatic stabilization but could be easily removed if exchanged with a different stabilizer, while its strong negative charge (≥ -30 mV, measured by dynamic light scattering, DLS) helped to generate an interaction with CV which was positively charged.[43] Thiol-PEG-COOH on the other hand was a very effective steric stabilizer due to its large molecular weight and it formed a thick polymeric coating, with a weak negative charge (≤ -15 mV, observed by DLS).[181] Particles stabilized with thiol-PEG-COOH were more stable at room temperature and less sensitive to the changes in the ionic strength of the surrounding solution, but their stability could complicate their use in the formation of the antimicrobial film and their interaction with the dye (sections 3.3.2 and 3.4.5).

2.4.4. *Elemental concentration analysis of the concentration of nanoparticles*

Obtaining a reliable and precise esteem of the concentration of a dispersion of anisotropic metal nanoparticles is one of the most complicated problems nanotechnology scientists are faced on a daily basis.

For spherical nanoparticles the light absorption could be correlated directly to their concentration.[182] Thus, UV-visible spectroscopy (section 2.4.5) was sufficient to have an esteem of the concentration of particles.[183] Unfortunately, this technique could not be used on anisotropic nanoparticles (rods and stars) without using an internal standard in the calibration curve, because their SPR depended on many factors, such as their aspect ratio, their interaction with the media and what was present on their surface.

To overcome these problems, it was necessary to compare spectral observations with elemental analysis (ICP-MS) so to build a calibration curve and to identify a dispersion of particles which could be used as reference standard to measure the concentration of the others in similar conditions.

ICP-MS used an inductively coupled plasma to decompose the components of a sample to elemental ions, which were then analysed by a time of flight quadrupole mass spectrometer.

ICP-MS was an extremely sensitive technique, which required to handle with care the preparation of the samples and to perform an extensive calibration. The dilution of the samples in nitric acid was used to remove part of the impurities, because the acid was able to oxidize all the elements in the sample and form nitrates which could be easily decomposed by the plasma flame.

2.4.4.1. Analysis of AuNRs with short aspect ratio

As reported in section 2.3.4, to identify the concentration of Au^0 in a dispersion of AuNRs of short aspect ratio, a stock solution of unknown concentration but known optical density (O.D. $_{\lambda=634\ nm}$ = 1.255) was used to

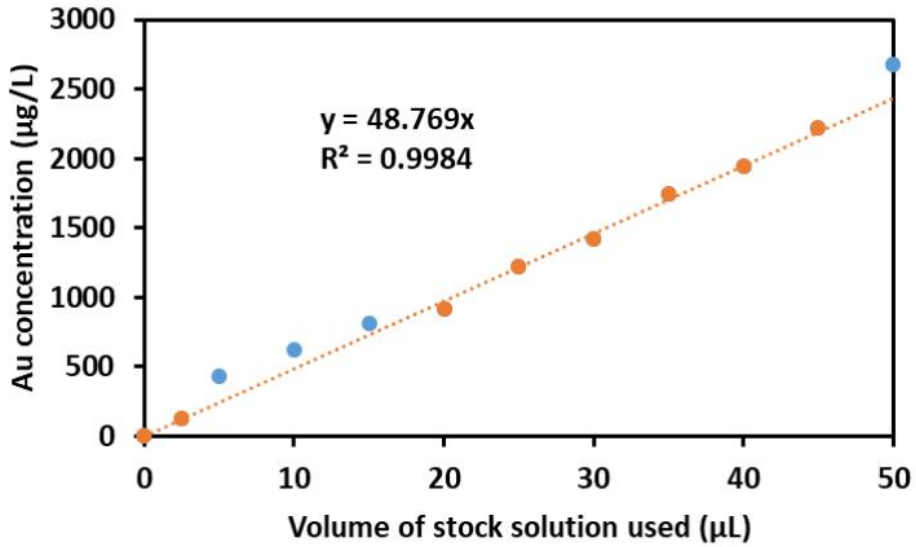

Figure 2.4.3. Results of the analysis of different solution prepared from an AuNRs stock solution of 1.255 O.D.

create a series of diluted solutions. The diluted solutions were analysed with an ICP-MS (TOF detector) obtaining the Au^0 concentrations of the solutions.

After repeating the measurement for all the dilutions, it was possible to produce a calibration curve and to exclude the measurements which deviated from the linear progression (blue dots, in Figure 2.4.3).

The slope of the curve identified by the experimental points was the result of the relation between the volume of stock used and the concentration of gold detected expressed as µg/L.

The concentration of gold in the samples was calculated using the Equation 2.4.1 – 2.4.4:

$$C_{Sample} = a * V_{stock} = 48.769 * 30 = 1463.1\,\mu g/L \qquad (2.4.1)$$

$$Molar\ concentration = {C_M}/{Atomic\ Mass\ of\ gold} = {0.00147\ {g}/{L}}/{196.97\ g/mol} = 0.007\ mM \quad (2.4.2)$$

$$C_{Stock} = \frac{C_{Sample} * 0.002\ L}{3 * 10^{-5} L} = 0.495\ mM \quad (2.4.3)$$

$$C_{mM/Abs} = \frac{C_{Stock}}{OD} = \frac{0.495\ mM}{1.255} = 0.40\ mM/OD \quad (2.4.4)$$

This value was used as reference to calculate the approximate concentration of all samples of AuNRs with similar dimensions and SPR absorption.

2.4.4.2. Internal calibration standard analysis of the other particles

The ICP-MS elemental analysis of a dispersion of gold nanoparticles was complicated and expensive process. It was not economical to use this method to calibrate every type of nanoparticles used in this thesis. Thus, an indirect method was used to calculate the mM/Abs ratio of longer AuNRs and AuNSs.

The relation between concentration of gold in solution and the absorbance of dispersions of rods with longer aspect ratio was calculated using the internal standard calibration method, Figure 2.4.4.[184]

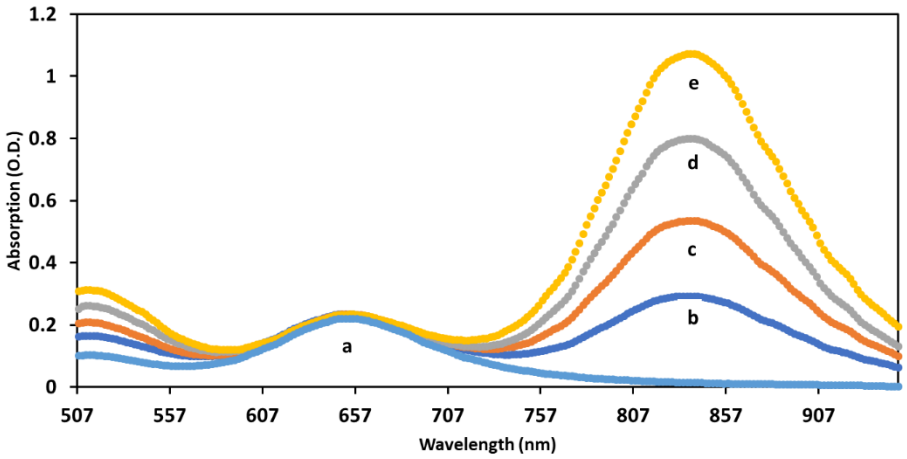

Figure 2.4.4. UV-visible spectra of a) 1X of AuNRs$_{(650\ nm)}$, b) 1X of AuNRs$_{(650\ nm)}$ + 1X of AuNRs$_{(835\ nm)}$, c) 1X of AuNRs$_{(650\ nm)}$ + 2X of AuNRs$_{(835\ nm)}$, d) 1X of AuNRs$_{(650\ nm)}$ + 3X of AuNRs$_{(835\ nm)}$ and e) 1X of AuNRs$_{(650\ nm)}$ + 4X of AuNRs$_{(835\ nm)}$; were nX = n x 100 µL$_{stock}$/mL$_{sample}$.

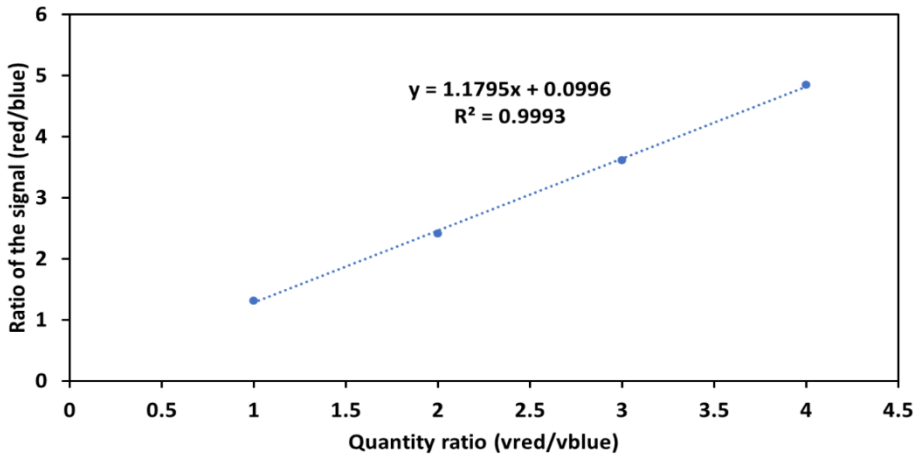

Figure 2.4.5. Representation of the ratio between the LSPR absorption of AuNRs (835 nm) and AuNRs (640 nm) against the ratio between the quantities added to the sample's solution.

The internal standard calibration method could be used in this experiment because the two nanoparticles dispersion had distinct and intense absorption peaks and they are both dispersed in the same solution (sodium citrate 20 mM).

As seen in Figure 2.4.5 there was an almost perfect dependency between the amount of stocks used in the samples and the ratio between the absorption peaks of the particles the solution containing both the types of nanorods. Using this relation and the value of concentration of the short aspect ratio AuNRs dispersion was possible to calculate the mM/Abs value of the longer AuNRs, if the value of extinction coefficient (ξ) was considered constant for both the dispersions. This assumption was not too farfetched because both the solutions contained the same components with the only difference of the geometrical shape of the particles.

$$CAuNRs_{(640\ nm)}/Abs = 0.395\ {}^{mM}/_{Abs}$$

$$OD_{Aliquot} = 0.219\ OD \quad CAuNRs = 0.0867\ mM \tag{2.4.5}$$

$$Abs_{Red} : Abs_{Blue} = C_{Red} : C_{Blue} \tag{2.4.6}$$

$${Abs\ Red}/{Abs\ Blue} = 1.18x + 0.0996 = 1.28 \tag{2.4.7}$$

$$C_{Red} = 1.28 * C_{Blue} = 0.111\ mM \tag{2.4.8}$$

Dividing the result of the Equation 2.4.8 for the absorption of the aliquot (O.D. = 0.289) gave 0.385 mM/Abs, indicating that AuNRs of different aspect ratio had similar concentration to absorption ratios. This consideration was used for calculating all the concentrations of nanoparticles using the original dispersion of AuNRs as reference. The mM/Abs of AuNSs was similar to the one of short AuNRs (0.395 mM/Abs), this similarity was understandable because AuNRs and AuNSs were both composed of the same material, had the main absorption peak in the same spectral area (640-660 nm for the AuNRs and 700 nm for the AuNSs) and comparable dimensions (32x16 nm AuNRs, 35 + 2x16 AuNSs).[163,185]

2.4.5. *Spectrophotometric analysis*

The procedure and settings of the spectrophotometric analysis were reported in section 2.3.5.

2.4.5.1. Spectra of AuNRs of shorter aspect ratio

Shorter AuNRs were tuned to be able interact with CV when introduced in a polyurethane film. Short AuNRs had an intense LSPR peak at 640 - 650 nm, Figure 2.4.6 a, and a weaker t-SPR near 520 nm.

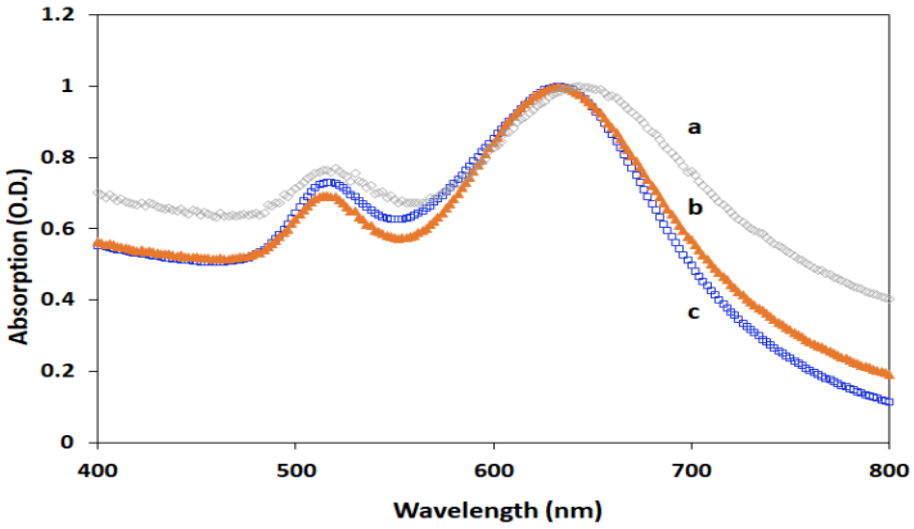

Figure 2.4.6. UV-visible spectra of AuNRs a) in presence of CTAB; b) after CTAB removal and substitution with thiol-PEG-COOH; c) or substitution with CitNa.

The particles after the synthesis were immersed in a concentrated solution of CTAB. This surfactant was necessary for the synthesis, but it was positively charged and toxic. The removal process explained in the method section (2.3.3), managed a complete exchange of the CTAB surfactant with in favour of a nontoxic stabilizer, i.e. sodium citrate (citNa, negatively charged) or thiol-PEG (weak negative charge).

The exchange of CTAB with citNa or thiol-PEG, blue shifted the lateral SPR peak of the particles by 10 nm, due to the change of the refractive index of

the solution and the density of charges in surrounding medium of the particles, Figure 2.4.6, “b” and “c”.[89]

2.4.5.2. Spectra of AuNRs of long aspect ratio

Longer AuNRs were designed to be able to interact with near IR light wavelengths (780 – 850 nm), as for the shorter nanorods these nanoparticles had two SPR absorption peaks, t-SPR near 520 nm and LSPR near 800 nm, Figure 2.4.7.b.

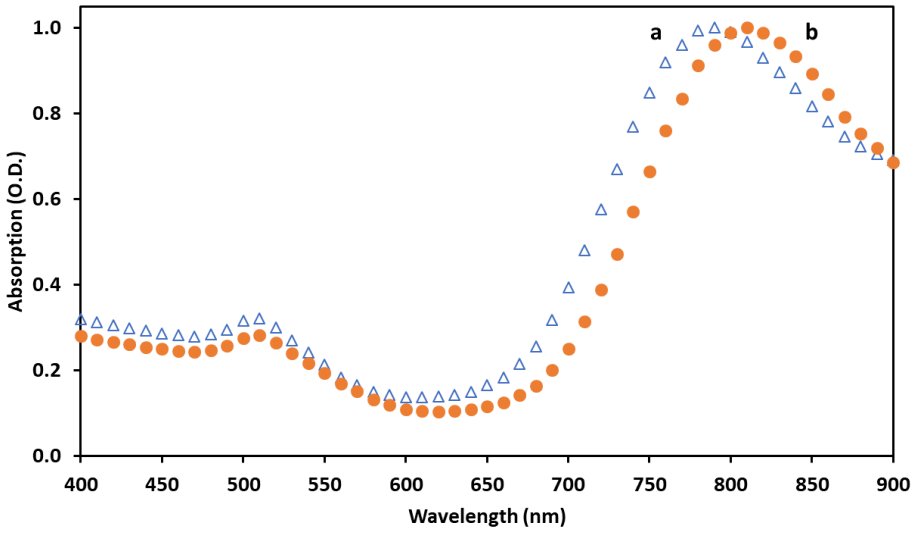

Figure 2.4.7. UV-visible absorption spectra of AuNRs of longer aspect ratio, a) stabilized with CitNa and b) stabilized by CTAB.

As seen for the AuNRs with short aspect ratio removing the CTAB blue shift the samples of approximatively 20 nm (Figure 2.4.7.a).

2.4.5.3. Correlation between the growth conditions and the SPR peak position

The main advantages of using AuNRs was their tunability, because introducing little changes to the growth solution could cause a great changes in the LSPR of the rods. In order to gain control of the size of the particles synthetized a series of experiments were devised focusing in small

changes in i) Br^- concentration, ii) silver nitrate or iii) a combination of the two.

The first modification of the synthesis tested was the concentration of NaBr introduced in the growth solution. This line of enquiry was based on the experiments reported by R. M. Pallares 2015 (a detailed discussion on the synthesis of nanorods and what influence its results is reported in sections 1.1.2 and 2.4.1), but, according to my experience and in contrast with what was reported in literature, the concentration of the salt in the growth solution did not have a clear cut changing effect on the LSPR peak position (Figure 2.4.8).[38]

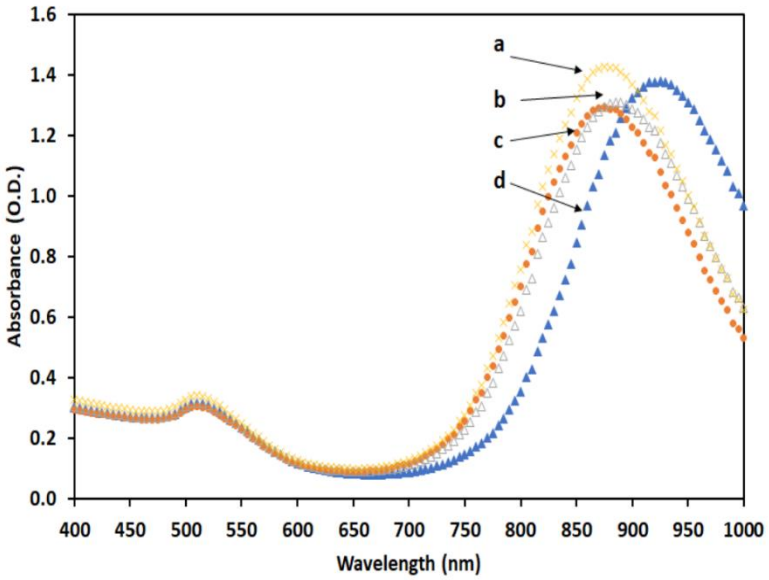

Figure 2.4.8. Changes in the UV-visible absorption caused by the presence of a) 30 mM, b) 20 mM, c) 15 mM and d) 10 mM of NaBr.

According to the experiments reproduced in this work only adding to the growth solution a concentration of 10 mM and 30 mM of NaBr (Figure 2.4.8.a & d) was possible to cause a significant shift in the LSPR peak of the forming rods as reported in the article from R. M. Pallares.[38]

While the intermediate concentrations of 20 mM and 15 mM had almost the same effect on the LSPR position as 30 mM (Figure 2.4.8.b & c), which indicates that above a certain concentration (15 mM), the concentration of salts did not cause any changes in the rods structure. It is possible that for low ion concentrations, the complex CTAB-Ag-Br could be very susceptible to small changes of ionic strength in the solution (especially Br^- which would increase the precipitation of AgBr) but above 15 mM, the excess of Br^- stopped interacting with the complex and while getting trapped by the large amount of CTA^+ ions available in solution.

The second synthesis variation tested was to change the concentration of $AgNO_3$, which was used to trigger the formation of rods. As previously reported (section 1.1.2.2), there is an extensive literature on the subject, but no research group has been able to have definitive words on this aspect of the nanorods synthesis.[46]

To contribute to this investigation a series of AuNRs were prepared with different silver concentration (Figure 2.4.9).

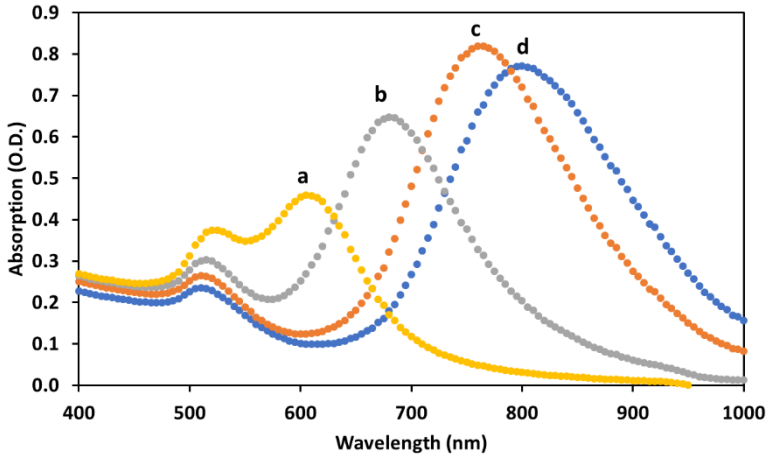

Figure 2.4.9. UV-visible absorption of AuNRs prepared with a) 25 µL, b) 50 µL, c) 75 µL and d) 100 µL of $AgNO_3$ 0.01M.

As seen from Figure 2.4.9, varying the amount of $AgNO_3$ used in the synthesis allowed to form batches with different LSPR absorption and with a substantial degree of control.

The direct correlation between the L-SPR peak position and the concentration of silver in the growth solution can be easily visualized if comparing the $AgNO_3$ concentration with the max LSPR absorption (Figure 2.4.10).

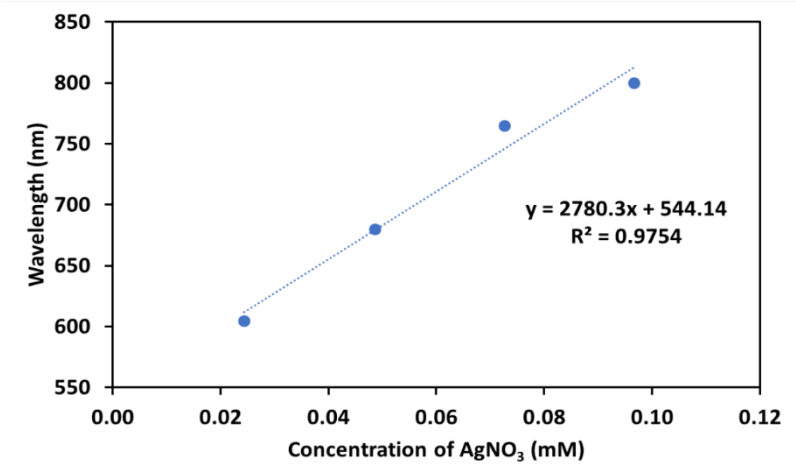

Figure 2.4.10. Relation between position of the LSPR peak and the concentration of $AgNO_3$ in the growth solution

To showcase the flexibility of the seed mediated synthesis of AuNRs, Figure 2.4.11 shows a collection of spectra of batches made by changing combination of $AgNO_3$ and salts concentrations.

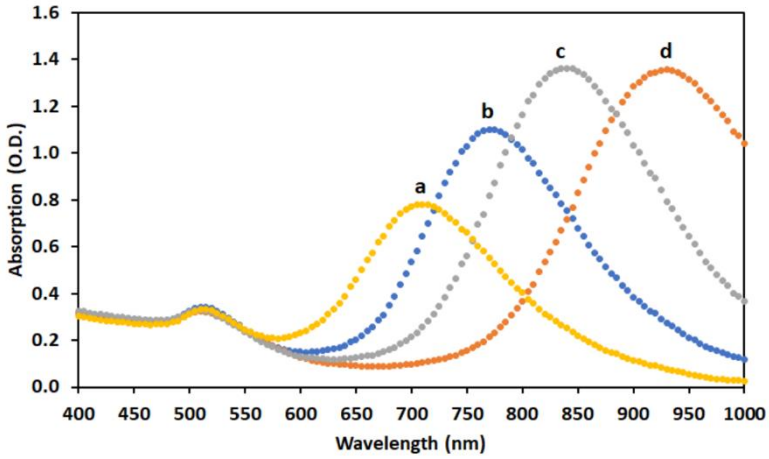

Figure 2.4.11. UV-visible absorption of AuNRs synthetized with a) 10 mM NaBr and 50 µL $AgNO_3$, b) 30 mM NaBr and 75 µL $AgNO_3$, c) 10 mM NaBr and 75 µL $AgNO_3$ and d) 30 mM NaBr and 125 µL $AgNO_3$.

This was one of the strongest advantages of the seed mediated method and the reason why it was possible to tune the LSPR absorption of the nanorods to maximize their plasmonic coupling with CV and to boost the production of ROS.

2.4.5.4. Spectra of AuNSs

Contrarily to AuNRs, AuNSs were directly synthetized with thiol-PEG-OMe or with CTAB on their surface, which were used to stop the process of growth of the AuNSs once initialized.

AuNSs could not be synthesised using citNa directly as a stabiliser. To obtain citNa stabilised AuNSs, CTAB (7 mM) was used as an intermediate to form CTAB-AuNSs. This conjugate was then exchanged with citrate using a cleaning procedure similar to the one used for AuNRs, as previously reported in section 2.3.3.

SPR absorption peak of AuNSs stabilized with CTAB, Figure 2.4.12.c, was located at 740 nm. Once substituted with citNa this peak blue-shifted by 30 nm to peak at 710 nm, Figure 2.4.12.b. Finally, AuNSs capped with thiol-PEG-OMe had max absorption of 690 nm, Figure 2.4.12.a.

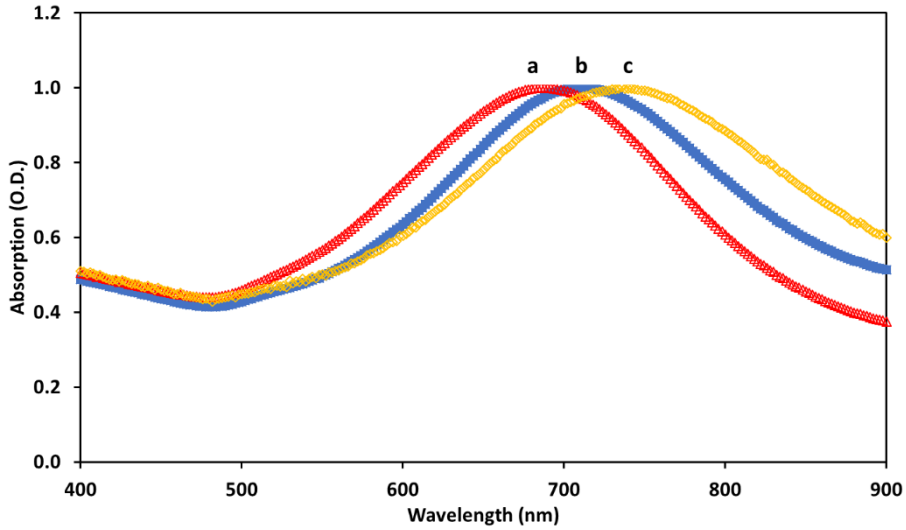

Figure 2.4.12. UV-Visible spectra of AuNSs stabilized a) with thiol-PEG-OMe, b) with citNa and c) with CTAB.

2.4.5.5. Influence of the capping agent on the SPR absorption

Another important factor to consider when preparing nanoparticles for optical applications was the type of molecules used for their stabilization. The type of stabilizing agent used shifted the position of SPR peaks of tens of nm (examples in sections 2.4.5.1, 2.4.5.2 and 2.4.5.4). This occurred by the modification of the dielectric constant of the media surrounding the particles: electrostatic stabilizers would polarize the molecules of water directly in contact with them and thus, generating a barrier which would prevent the particles to come near enough to be able to aggregate. Hydrophobic steric stabilizers instead, generated a space surrounding the particle, in which water was not able to penetrate, this caused the water outside of it to pack tightly in order to reduce segregation energy and consequentially repelling the other particles trying to aggregate.

The spectra of all the nanoparticles tested blue shifted 10 to 30 nm when the CTAB was removed from their surface (sections 2.4.5.1, 2.4.5.2 and 2.4.5.4), but the entity of this shift depended on the type of stabilizer, which was introduced in exchange of the CTAB.

For example, Figure 2.4.13 shows the spectra of AuNRs and AuNSs stabilized with thiol-PEG-OMe or citNa ("a" & "b" for AuNRs or "c" & "d" for AuNSs).

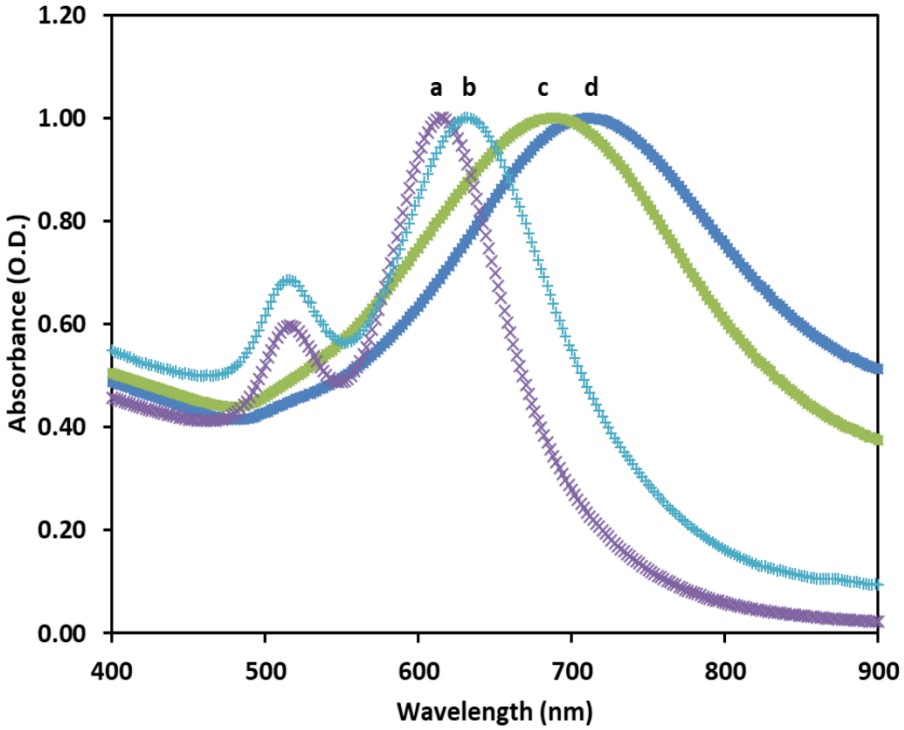

Figure 2.4.13. UV-visible spectra of a) CitNa-AuNRs, b) thiol-PEG-OMe-AuNRs, c) citNa-AuNSs, d) thiol-PEG-OMe-AuNSs.

As can be seen from Figure 2.4.13, the type of particles undergoing the surface modification influenced the magnitude of the shifts caused by the change of capping agent, with AuNRs blue shifting 10 nm from the original position and AuNSs blue shifting 20 nm when exchanging CTAB for the same types of stabilizer (citNa). This difference was probably due to the origin of their SPR peak, with AuNRs depending only from a single resonance for its LSPR while the peak of AuNSs was generated by the convolution of a series

of different SPR resonances (further details in section 2.4.6).Transmission electron microscopy

The characterization of anisotropic nanoparticles for the size presented some difficulties. Because DLS generally used to characterize the size and polydispersity of spherical nanoparticles, it could not be applied to anisotropic nanoparticles, while UV-visible analysis could only give information on the size and shape of the particles, TEM measurement is further needed.

As introduced in section 2.3.6, the only reliable method to obtain structural data on this type of particles was to acquire a collections of TEM images containing a large number of particles, i.e. at least 20 to 100 per image in order to acquire a total of images between 200 and 1000 sampling to be used to build a statistic.

2.4.5.6. Analysis of gold nanorods with shorter aspect ratio

As seen in sections 2.3.1.2 and 2.4.1, the synthesis of AuNRs could be tuned to form short and thick rods. In Figure 2.4.14 shows a collection of TEM images of these kind of particles.

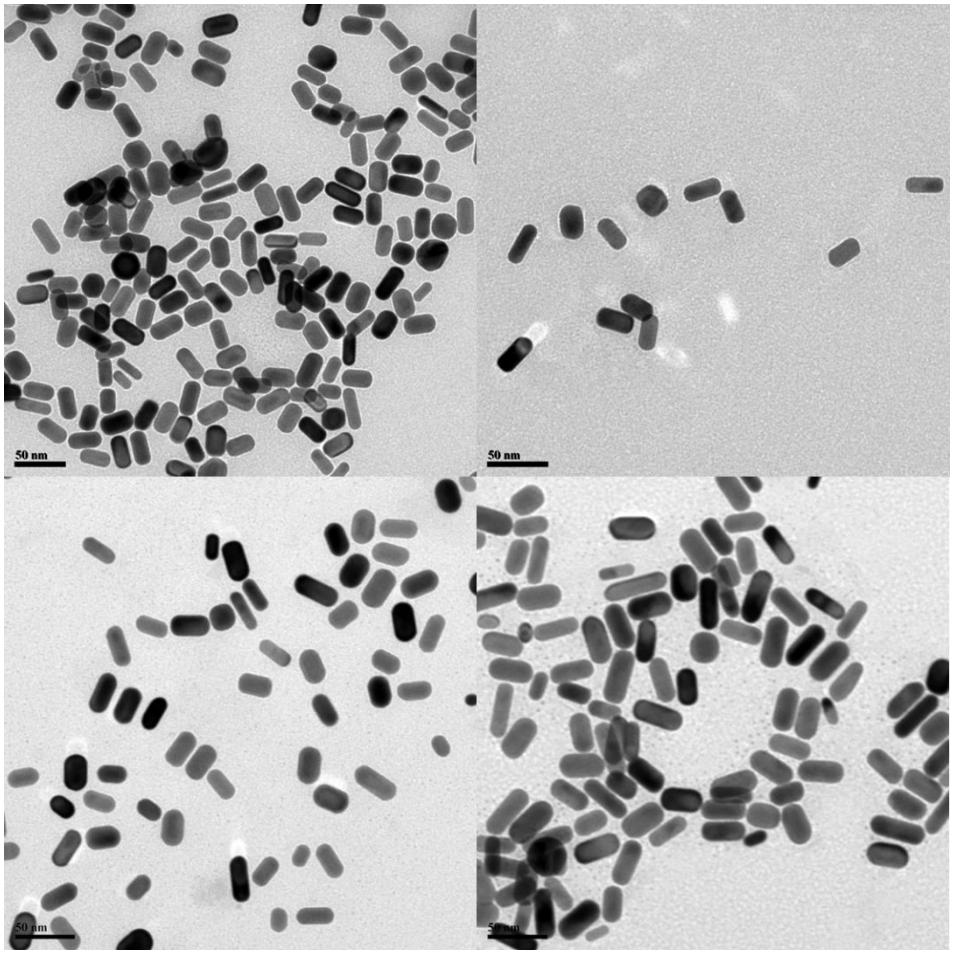

Figure 2.4.14. Collection of TEM images of AuNRs with shorter aspect ratio, the scale of all pictures (dark line) is 50 nm, magnification x25000 - x30000.

It is evident from the images that the particles formed were fairly regular in shape and sizes, but there was a small number of spherical particles or smaller rods.

Analysis of the size distribution of the particles captured in the TEM picture showed a relatively compact distribution of rods populations centred on 31.8 ± 6.4 nm of length and 16.1 ± 3.7 nm of diameter with an aspect ratio of 2.1 ± 0.2 (Figure 2.4.15).

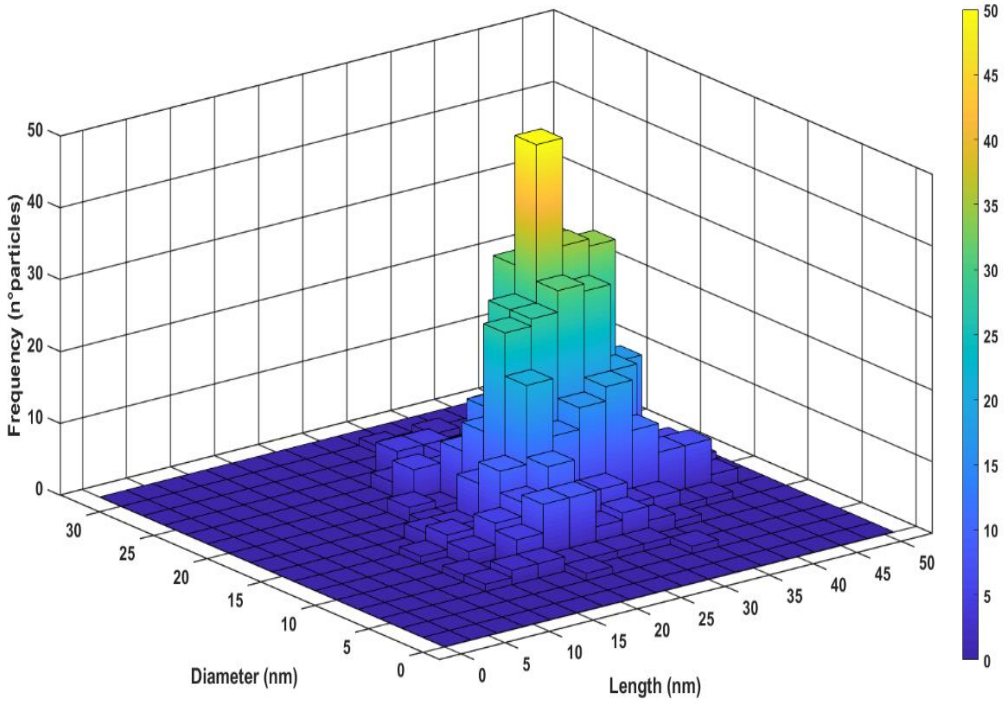

Figure 2.4.15. Size distribution of the shorter aspect ratio nanorods (batch of 726 images).

The majority of the particles included in this analysis had AR between 2.1 and 2.9 (294 particles, Figure 2.4.16) with two AR 1.8 (69 particles) and 2.0 (70 particles) being the most frequent in absolute but most of the distribution leaning towards slightly longer AR thus, resulting in an average AR centred in 2.1.

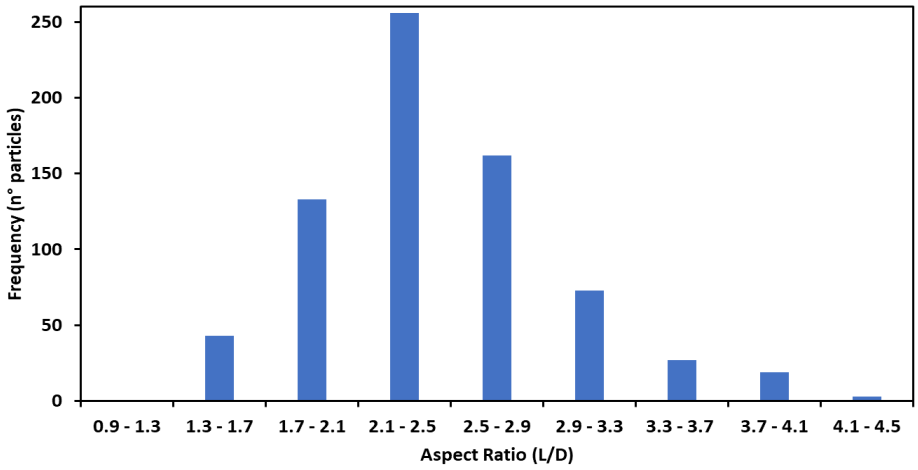

Figure 2.4.16 Aspect ratio distribution of AuNRs analysed in Figure 2.4.17.

The difference in AR was probably due to the small size of the rods in which a small variations in thickness would result in a great change in AR, which was confirmed by the relatively small variation of lengths and diameters obtained by the analysis of the TEM pictures.

2.4.5.7. Analysis of gold nanorods of longer aspect ratio

The synthesis of AuNRs described in section 2.3.1.3 led to the formation of long and thin nanorods with a very uniform shape and thickness, as can be seen in Figure 2.4.17.

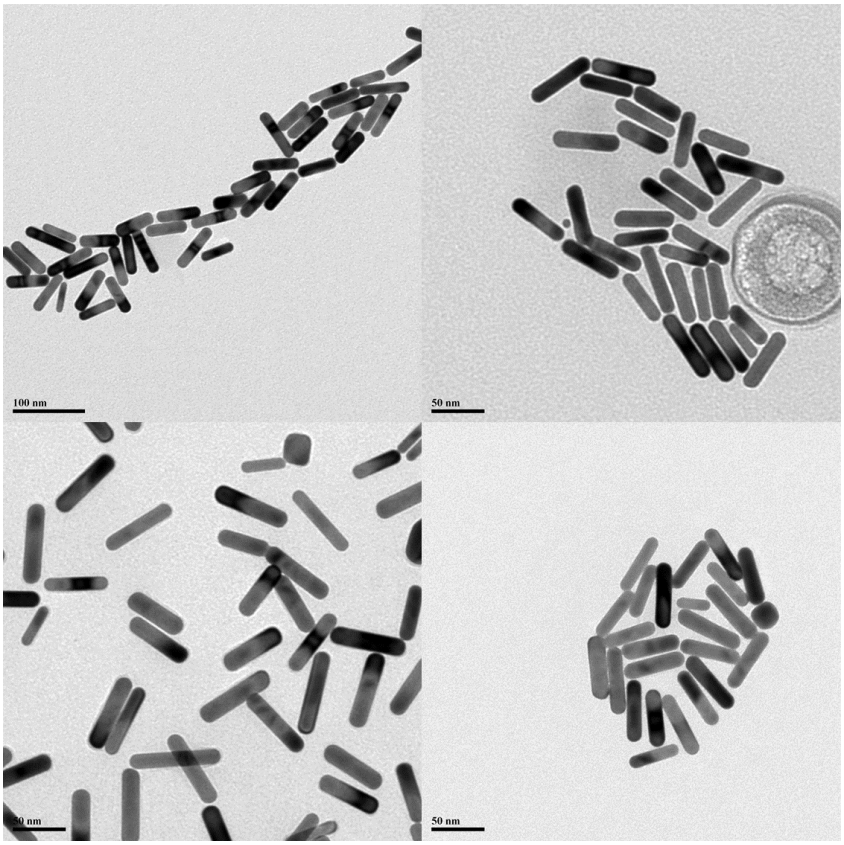

Figure 2.4.17. Collection of TEM images of AuNRs with longer AR, the scale of the pictures (black line) is 50 nm and the magnification x30000 with the exception of the picture on the top left that has scale 100 nm and magnification x15000.

The main source of polydispersity in these types of samples was caused by the occasional cubic particles and by a small fraction of the particles with longer or shorter AR compared to the average.

The analysis of the images collected with the TEM the AuNRs with longer AR showed an average length of 65 ± 5 nm and a diameter of 17.5 ± 2.5 nm (**Error! Reference source not found.**). This statistic also showed that most of the particles produced by this synthesis had a thin rod like structure (93.2%) while the 6.8% were spherical.

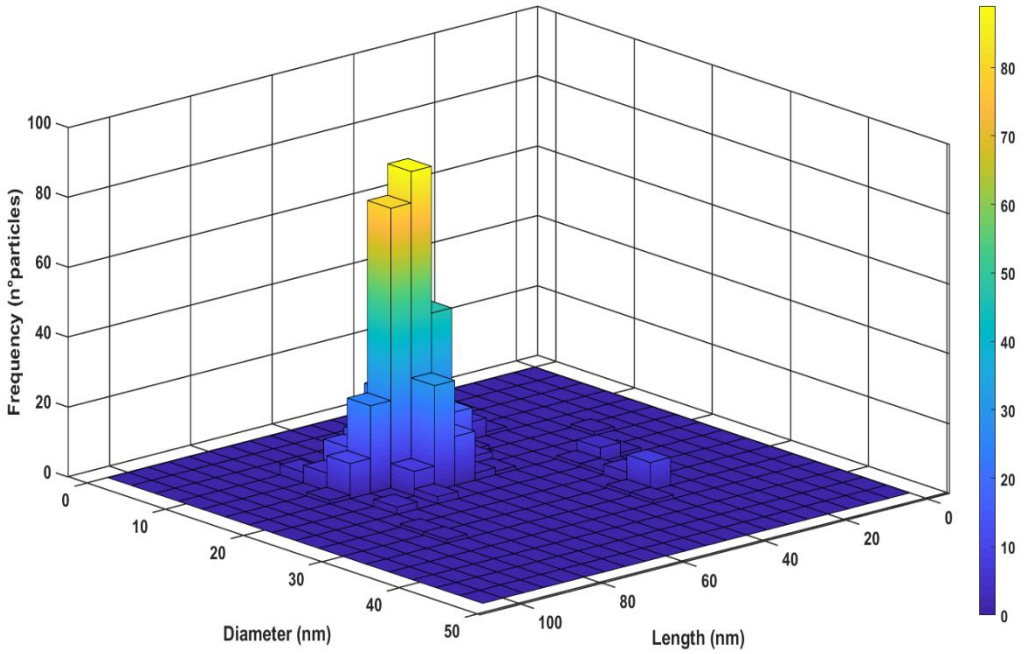

Figure 2.4.19. Size distribution of AuNRs of longer aspect ratio (batch of 735 images).

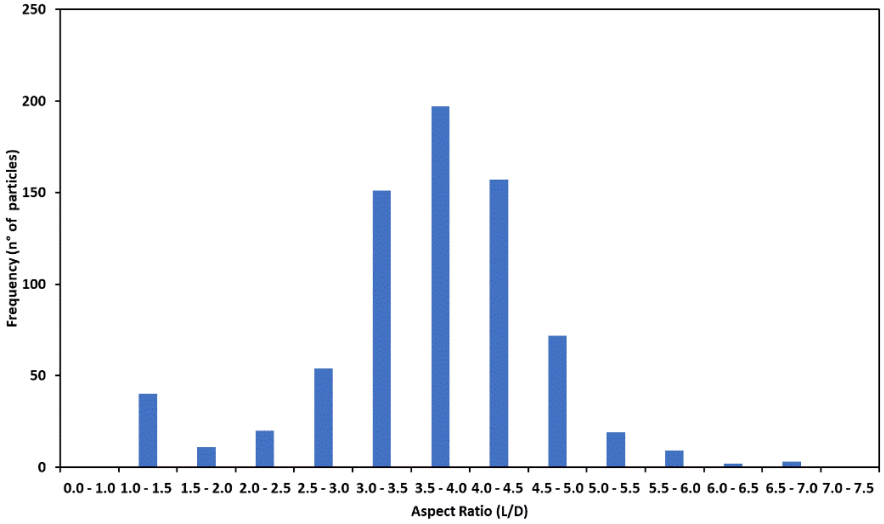

Figure 2.4.18. Aspect ratio distribution of longer AuNRs

The most common AR for these type of particles was 3.7 ± 0.9 (Figure 2.4.18) with the majority of the particles 68.2% were comprised between aspect ratio 3.0 and 4.5.

2.4.5.8. Analysis of gold nanostars

The synthesis for AuNSs reported in sections 1.1.2.3 and 2.3.2 formed sea urchin like nanostructures with a roughly spherical shape, the central core of these particles have a relatively monodisperse distribution of diameters from which numerous spike-like structures of different sizes and dimensions are projected in every direction (Figure 2.4.21).

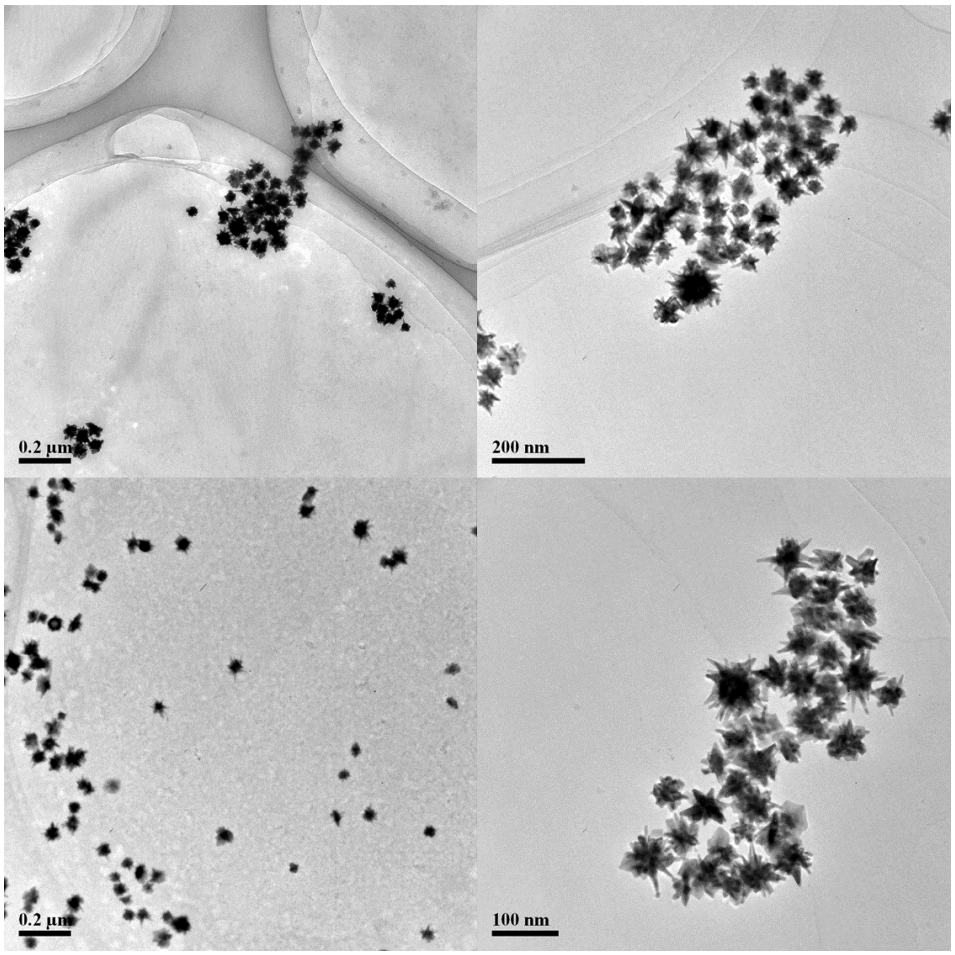

Figure 2.4.20. Collection of TEM images of AuNSs, top and bottom left (scale 200 nm and x9400 magnification), top right (scale 200 nm and x17000 magnification) and bottom right (scale 100 nm and x23500 magnification).

The analysis of the TEM images showed that AuNSs were characterized by a central core of 35.6 ± 7.9 nm from which spiky structures of average size of 16.1 ± 5.1 nm are projected. These observations also indicated but the typical AuNSs would possess spikes of different lengths and thickness.

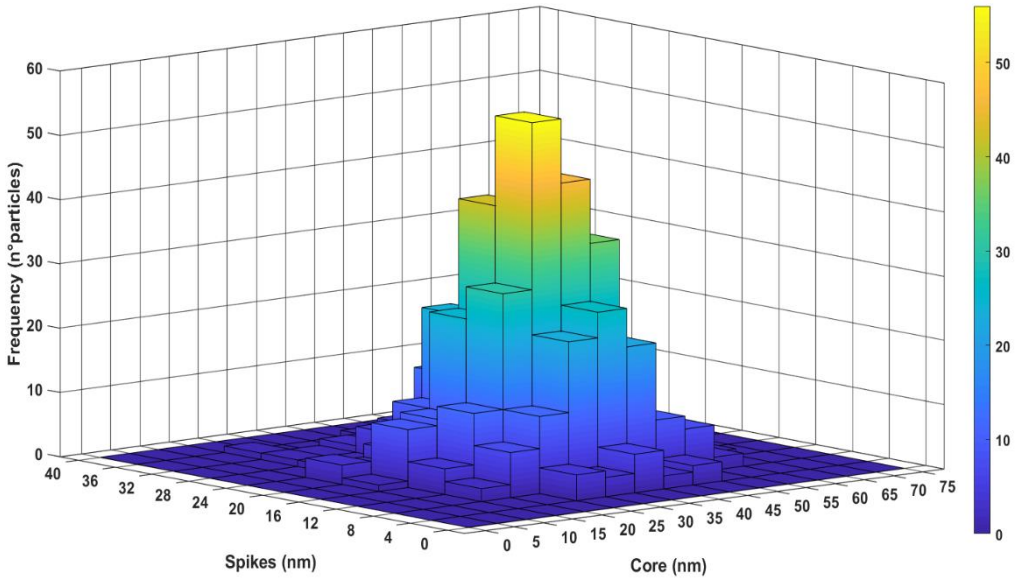

Figure 2.4.21. Size distribution of AuNSs (batch of 941 images).

Because every AuNSs has spikes of different lengths the distribution reported in Figure 2.4.22 was not completely representative of real AuNSs. Because it represented the AuNSs as possessing a single spike size (average length).

To better represent the size distribution of the AuNSs, the collection of data from the AuNSs core and of the spikes have been analysed separately. The

distribution of the core sizes has been presented in Figure 2.4.23 A, while the collection of the spike lengths have being reported in Figure 2.4.23 B.

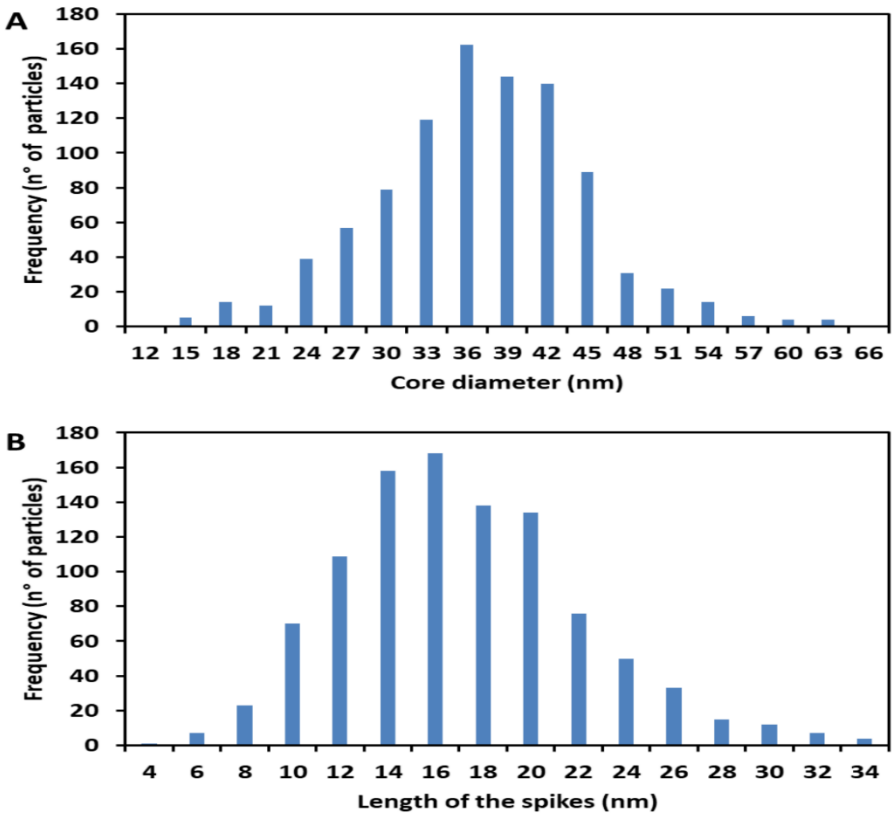

Figure 2.4.22. A) Distribution of AuNSs core diameters and B) distribution of AuNSs spikes distribution.

These analyses showed that the most common size for AuNSs cores were comprised of 36 and 42 nm diameter, with a certain amount of smaller particles (which lower the average to 35.6 ± 7.9), while the spikes showed a greater variety of sizes, with peak of frequency between 14 and 20 nm (with an average of 16.1 ± 5.1).

2.4.6. *Simulations*

Mathematical simulations of the nanoparticles used in this thesis were performed to study the SPR effect on the electrical field surrounding them, when exposed to light. The parameters of these simulation are reported in section (2.3.7).

2.4.6.1. Simulation of the SPR of AuNRs short aspect ratio

The spectra of AuNRs with short AR had two characteristic SPR peaks and it was relatively easy to simulate because their position was directly connected with the dimensions of the particles and their shape could be easily modelled with a three-dimensional geometrical object (capsule).[186]

Using the dimensions obtained by the analysis of the TEM images (section 2.4.5.6) as parameters for the simulation resulted in a spectrum only a few nanometres blue-shifted compared with the experimental samples (Figure 2.4.24).

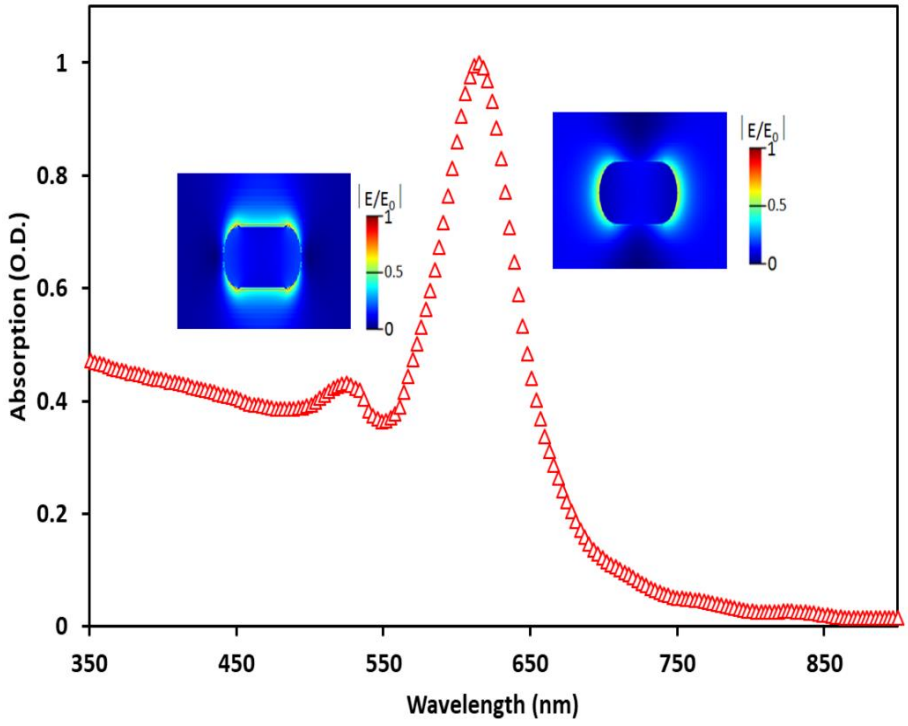

Figure 2.4.23. Electrical field simulation for AuNRs (31.8 nm x 16.1 nm) stabilized with thiol-PEG-OMe.

The insets, the starting conditions of the simulation, were the near field distribution of the nanorods, excited by x and y polarizations and the PML boundary conditions were applied to the simulations. The polarized light on the y axis interacted with the transversal SPR resulting in a peak at 525 nm while the x polarized light interacted with the longitudinal SPR resulting in

the peak at 615 nm. The mesh size was 1/20 of the excited wavelength. While the intensity of the electrical field was depicted in the graphical representation as a bright coloured area surrounding the nanorods (Figure 2.4.24).

As can be seen in Figure 2.4.25, the peak at 615 nm in the simulation was much more defined and sharper than in the experimental sample. While at the same time the experimental sample had a stronger slightly blue-shifted, peak at 525 nm (Figure 2.4.25, “b”).

The spreading of the LSPR in the experimental sample can be easily explained by the unavoidable polydispersity of synthetic samples, while the intensity and definition of the peak at 525 nm, it is more difficult to explain. The change in this peak could be generated by the small amount of spherical and cubical particles generated by the synthesis, but the intensity of the peak was not really consistent with the relatively low amount of spherical particles formed (5 – 6%, sections 2.4.5.6 and 2.4.5.7). Another possible hypothesis is that the polydispersity in the thickness of the nanorods could increase and spread the t-SPR peak of the nanorods dispersion.

2.4.6.2. Simulation of the SPR of AuNRs long aspect ratio

AuNRs with longer aspect ratio had also two defined SPR peaks that could be reproduced using a FTDT simulation. As for the previous simulation PML conditions were used as for the directions of the polarized light. The polarized wave form y interacted with the t-SPR at 530 nm while the wave from x interacted with the LSPR at 786 nm (Figure 2.4.26).

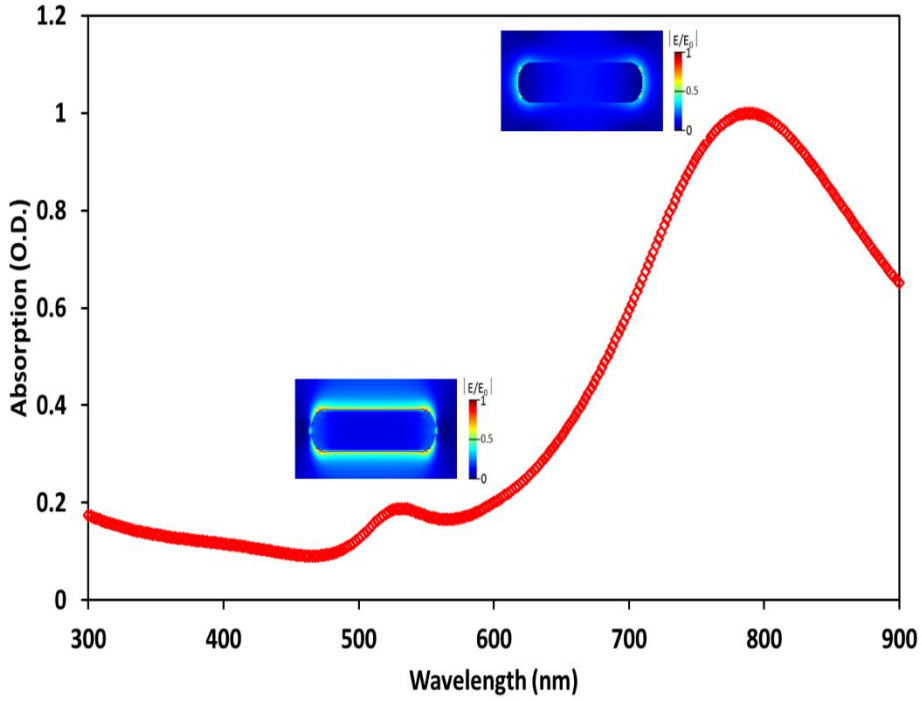

Figure 2.4.25. Electrical field simulation for AuNRs of longer aspect ratio 3.8 – 4.2 (65 x 17.5 nm).

When compared with their simulation AuNRs with longer aspect ratio had a sharper SPR peaks with a clear separation between longitudinal and transversal resonance peaks. The position of the main resonance peak remained unchanged between the experimental sample and the simulation, but the position of the t-SPR was 20 nm blue-shifted in the experimental sample.

Another difference between the simulation and the experimental results was the ratio of intensity between the two SPR peaks, in the simulated

spectra the LSPR was 6 times more intense than the t-SPR. Instead in the experimental sample this ratio was closer to 1:3 (Figure 2.4.27).

AuNRs with longer AR were more complicated to properly simulate, because the simulated spectra have a less intense and less defined t-SPR, while the LSPR of the simulation was broader and less defined than the experimental counterpart. The sharpness of the peak may be explained by the method of simulation, which simulated the rod as freely moving in a uniform media (section 2.3.7). While the real particles may be limited to few favourite configurations, which resulted in a sharper absorption of the incident light or possibly be able to stacks side to side contributing to the absorption in the area.

2.4.6.3. Simulation of the SPR of AuNSs

The spectra of the AuNSs acquired experimentally showed a broad peak between 620 to 780 nm (Figure 2.4.12), the simulations instead indicated the presence of multiple peaks. According to the simulations results these peaks were derived by the resonance of the electrical field surrounding the various features of the nanostar structure (e.g. core, spikes). To better characterize the various components of the SPR of AuNSs two sets of simulations were devised introducing two sets of geometrical parameters representing AuNSs with different AR between their core and their spikes.

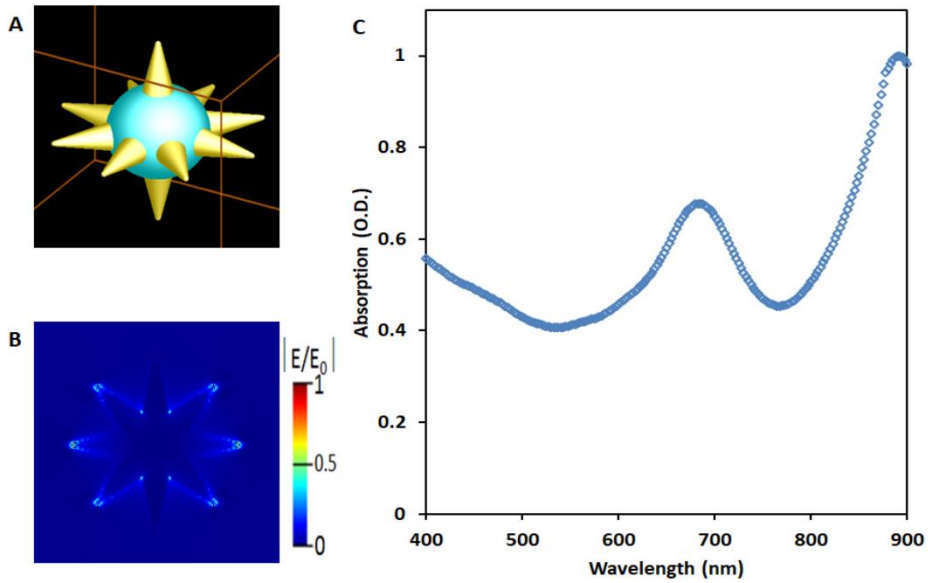

Figure 2.4.27. Simulation of the SPR of the electrical field around AuNSs with 35.6 nm core with 16.1 nm spikes, stabilized with PEG. A) Model of the AuNSs used in the simulation; B) Graphical representation of the potential fluctuation of the electrical field on the surface of the particles; C) Simulated spectrum of the AuNSs dispersion.

The simulation in Figure 2.4.28 C, represented nanostars with the core size and spike length obtained by the analysis of TEM pictures (aspect ratio core: spikes = 2.1, Figure 2.4.21). The application of x and y wavelengths to the AuNSs resulted in two resonance peaks. The first for the fluctuation of the electrical field on the entire spikes systems (690 nm, excited by x

polarization) and the second at 900 nm, excited by y polarization, representing the situation in which the electrical field was mostly concentrated on the tips of the spikes (Figure 2.4.28, B). This last peak, near 900 nm, was not connected with an absorption peak in the experimentally acquired spectra of AuNSs in solution. Because this simulation could only model the main peak, but it did not give any information on the components of the SPR of AuNSs a new simulation with different geometrical parameters have been carried out.

This simulation used a ratio core spikes 5:1 in order to improve the quality of the model and to describe the influence of the core on the spectra of the particles (Figure 2.4.29).

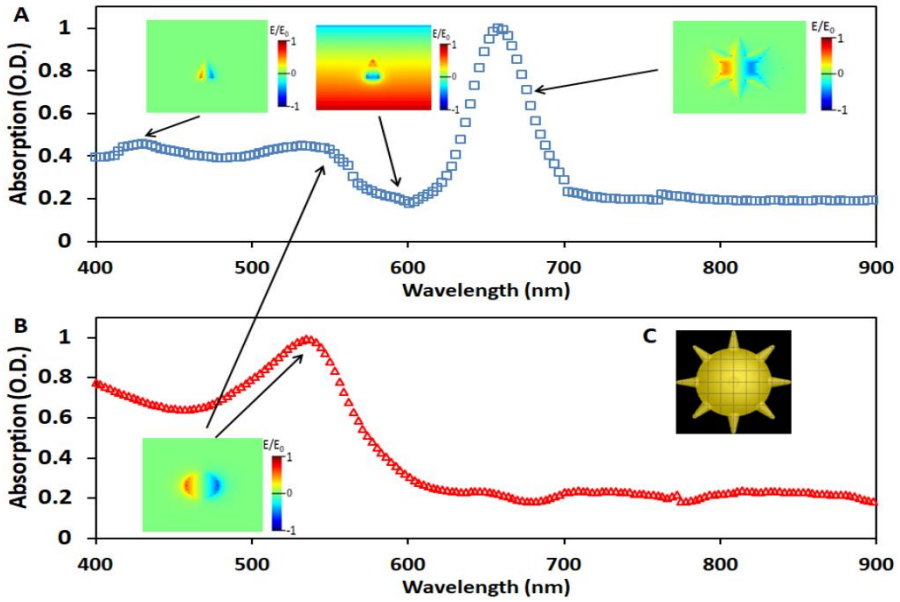

Figure 2.4.28. Electrical field resonance simulation for AuNSs (50 nm core with 10 nm spikes) stabilized with PEG A) simulated spectra of the spike system and B) simulated spectra of the core C) model of the AuNSs used for the simulation.

This simulation was divided into two spectra: the first for the spikes (Figure 2.4.29, A) and the second for the core (Figure 2.4.29, B). The insets conditions used for the simulation were the near field distribution of the spike and core was excited by x and y polarization.

The excitation resulted in the appearance of three peaks for the spikes system simulation as seen in Figure 2.4.29, A and a single peak for the AuNSs core in Figure 2.4.29, B.

This simulation identified four possible resonances, in order from left to right: i) the resonance of the spikes as single objects (428 nm), ii) the electrical field along the length of the spikes (585 nm), iii) the resonance of the core at 534 nm (comparable with the resonance of a spherical particle of the same size) and finally iv) the resonance of the entire spikes system (658 nm). The resonance of the core and the one due by a single spike were both excited by the x polarization while the resonance on the length of the spikes and of the entire spikes system were excited by the y polarization wave.

As stated previously, there was a defined difference between the simulated spectra and the one obtained experimentally (comparison shown in Figure

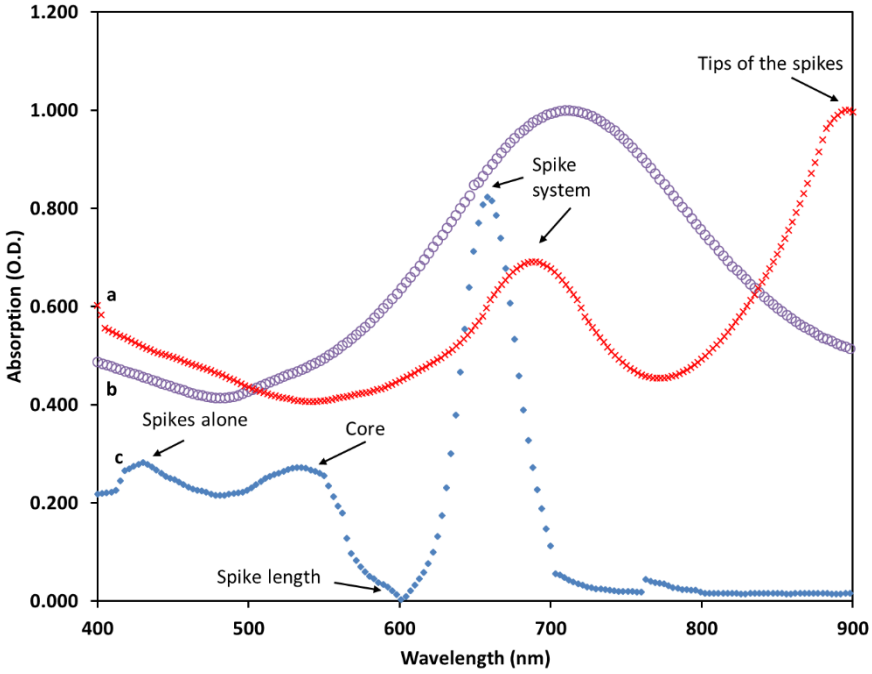

Figure 2.4.29. Comparison between the absorption peaks of a) simulation of AuNSs with the average dimensions calculated by TEM images, b) UV-visible absorption of AuNSs, c) simulation of AuNSs with ratio between the size of core and spikes (5:1).

2.4.30). The spectra of the AuNSs acquired experimentally (Figure 2.4.30.b) showed a single broad peak between 620 nm to 780 nm, with a maximum centred near 700 nm, while the simulation showed multiple peaks (Figure 2.4.30.a & c).

The comparison between the peaks obtained from the simulation and the experimental samples showed that the real sample spectra was formed by a convolution of all the individual components identified by the simulations. The only exception was the peak at 900 nm which did not correspond to the range of absorption of the real sample. Both the simulations identified the resonance on the entire spike system as the largest component of the spectra with peaks at 658 nm and 690 nm respectively.

The reason why the peak at 900 nm is not visible in the experimental spectra is not clear. It might be that concentration of the electrical field on the tips of the particles may cause a transfer of energy on the surrounding media hindering the absorption.

2.5. Conclusion

In this chapter the procedures used to synthetize the anisotropic nanoparticles were explored and optimized (sections 2.4.1 and 2.4.2). The methodology to modify the surface of the particles and to remove the surfactant used in the synthesis, exchanging it with sodium citrate and thiol-PEG was optimized according to the centrifuge used and the type of particles processed (section 2.4.3).

The factors contributing to the AR of AuNRs were explored and a wide range of AuNRs with different LSPR peaks were prepared (615 nm to 850 nm, section 2.4.1.3). Concentrations of the AuNRs was fully characterised using

ICP-MS and the nanorods solution was used as reference for calculating the concentration of the other dispersions of particles throughout the internal calibration method (section 2.4.4). The quality of the batches was established by UV-visible, the correlation between small changes in the growth solution and the final LSPR absorption of the resulting particles was explored in sections 2.4.5 and 2.4.5.3, respectively.

While the actual physical dimensions and shapes of the particles were confirmed by statistical analysis of hundreds of particles images captured by TEM (section 0). Finally, the nanoscopic fluctuations of the electrical field surrounding the particles were simulated to understand how their different features (sides, spikes and core) participated to the total SPR effect of the particles and the simulation results compared with the spectra experimentally acquired (section 2.4.6).

Chapter 3: Film preparation and characterization

3.1. Introduction

The core research in this thesis was focused on the production and characterization of an antimicrobial light activated films composed of three main components, i.e. metal nanoparticles, an organic dye and polymer matrix or sheet. The preparation of the films required two multi-phase processes: the diffusion of the dye from a solution to the polymer sheet and the embedding of the nanoparticles from solution to the film. These procedures required numerous tests in order to be optimized either in their components or according to the preparation procedure.

Because the antimicrobial films in this thesis, were complex and hybrid structure in which the active components were anisotropic metal nanoparticles and organic photosensitizer. A series of experimental procedures were developed to study their interactions and to characterize the intensity of their plasmonic coupling.

One of the fundamental components of this system was the polymeric matrix, which had a major role in ensuring the activity of the film supporting the active components and forcing them in a confined space exposed to the environment. The confinement of the active components happened in the crevices and rugosity of the polymeric surfaces which trapped the gold nanoparticles and could be impregnated with the PS dye.

Thanks to the polymer support structure dye and nanoparticles could come near enough to be able to generate a strong plasmonic coupling, a schematic summary of the process of ROS production happening in the film is reported in Figure 3.1.1.[87]

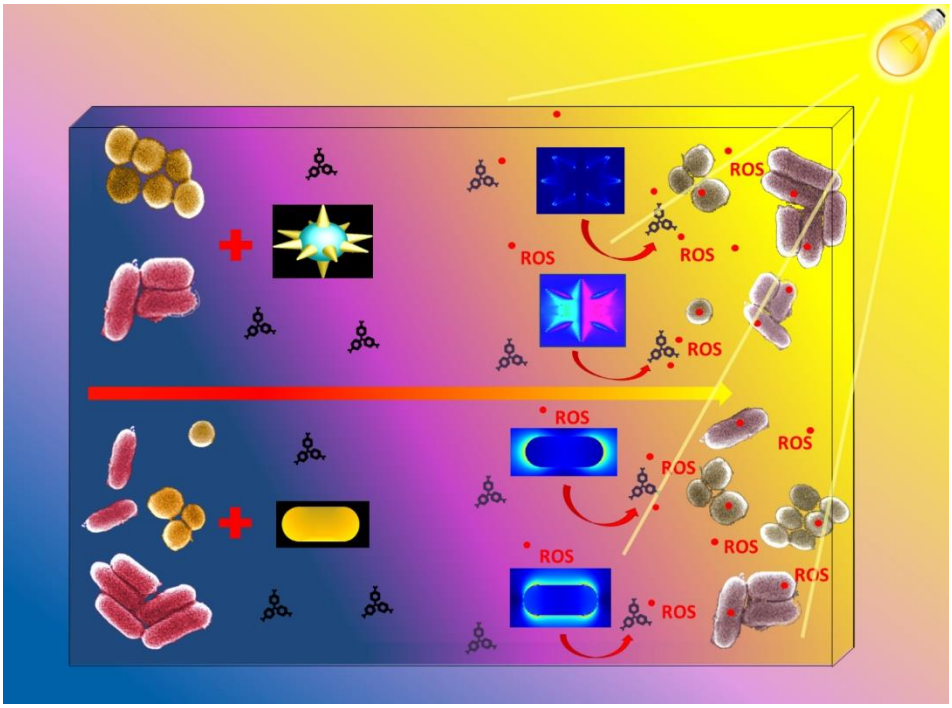

Figure 3.1.1. Schematic representation of the film function

As stated previously, the complexity of the film required a large set of experiments in order to understand its structure and mechanism of action: beginning with assessing the successful introduction of the nanoparticles in the film (3.4.2); the selection of the PS to be used in the film (3.4.3) and its method of introduction (3.4.4); the interactions between dye and particles in solution and within the polymer (3.4.5) and finally the demonstration and quantification of the ability of the film to produce ROS (3.4.6).

3.2. Materials

In addition to the reagent used in the synthesis of the gold nanoparticles (in section 2.2) a list of reagents were used for the experiments in this chapter:

Sodium fluorescein (fluorescent tracer grade), sodium hydroxide (NaOH, ≥ 97%), Janus Green B (JG, ≥ 65%), Nile Red (NR, > 98%), Neutral Red (NeuR, > 90%), Alcian Blue Pyridine variant (ABP, > 85%), Melamine (ME, 99%), 3-(4,5-dimethylthyazol-2-yl)-2,5 diphenyltetrazolium bromide (MTT, 98%) were obtained from Sigma Aldrich, Singapore. Alcian Blue (AB, 45 – 65%) was obtained from Fluka, United Kingdom. H_2O_2 solution (30 – 32% wt) was acquired from QüreC (quality reagents chemical, New Zealand). Nutrient Agar (NA) CM0003 was obtained from Oxoid Ltd. Polyurethane (1 mm thick, Swees engineering co. Pte Ltd), Crystal Violet (CV, ≥ 99%, Certistain) was obtained from MERK, Singapore.

3.3. Methods

3.3.1. *Fluorescence and absorbance spectroscopy*

Fluorescence emission intensity measurements were used in this chapter for the estimation of the ROS production and to study the energy transfer between AuNRs and different dyes. Fluorescence intensity emission analysis of the ROS production were performed using black bottom 96 or 384 wells plates, while using an excitation wavelength of 485 nm ± 20 nm, emission filter 580 nm ± 20 nm, gain 70 and mirror position 635 nm (Biotek plate reader). Fluorescence emission of the films were instead excited at 230 nm ± 5 nm, while acquired from 275 nm and with a gain 35.

In the experiments to test the interactions between CV and nanoparticles in solution (section 3.4.5), the following parameters were applied to keep the total absorbance of the solution between 0 and 1 O.D.:

1) The gold nanoparticles solution was diluted with CV (reported below) to obtain a solution 20% concentrated of the standard stock (≈ 34 µM of Au^0).

2) A very diluted solution of CV (12.5 µM) was used to dilute the stock nanoparticles to obtain a final concentration of 10 µM.

The resulting spectra was compared with the sum of the single components to identify the peaks caused by the interaction between dye and particles.

3.3.2. *Swell-encapsulation-shrink method*

The particles were introduced in the polymer using the swell-encapsulation-shrink method.[138] A 30 cm^2 film, 1 mm thick of medical grade polyurethane (PU) was immersed in 15 mL of a solution containing a 9:1 ratio between acetone and nanoparticles dispersion (1.5 O.D.; approximatively 0.65 mM) and incubated overnight under moderate stirring (250 rpm).

After the period of incubation, the swollen polymer samples were washed with ultrapure water. The remaining organic solvent was extracted from the polymer, drying the film with a benchtop extractor for 3 h at 35 °C.

3.3.3. *Characterization of the nanoparticles in the film*

The main technique used to analyse the film samples was the UV-visible spectroscopy (the parameters used are reported in section 2.3.5). The results of the experiments were normalized to compensate for the difference between the optical path of 1 cm generally used for the UV-visible spectroscopy and the thickness of the film (1 mm).

The successful embedding of the gold nanoparticles was confirmed throughout UV-visible spectroscopy of fragments of the film. For the analysis in a 96 wells plate film squares of approximatively 5 mm of lateral size were used, while in for 384 wells plates the samples where closer to 2

mm of lateral size. For the samples analysed in a cuvette the film samples were cut into fragments of 1x3 cm of dimension.

3.3.4. *Dye diffusion*

The last passage of the film preparation was the diffusion of the photosensitizer dye, crystal violet (CV), into the film.[138] For this passage samples of the film previously swollen with acetone (section 3.3.2) were immersed in a CV solution (15 mL, 1 mM 0.41 mg/mL) for 48 h under moderate stirring (250 rpm). After the diffusion, the film was washed with ultrapure water and dried using a cloth.

The rate of dye diffusion was tested incubating square tiles of 1 cm^2 in a 1 mM solution of CV and collecting them at numerous time points between 0 and 90 h. The samples collected were analysed for UV-visible absorption and the results at 600 nm (main absorption peak of CV), were plotted against time to determine the diffusion rate. The preparation of the film using the standard method used in this thesis required approximatively 72 h, 48 h for the dye diffusion and 24 h for the swell-encapsulation-shrink method.

A variation of dye diffusion method using acetone instead of water to introduce hydrophobic dye in the polymer was created, exploiting similar conditions as used for the swell-encapsulation-shrink procedure (in section 3.3.1). This method (labelled Ace) required to immerse 30 cm^2 of polymer in a solution 9:1 acetone/water, 13.5 mL acetone and 1.5 mL of aqueous dispersion of AuNPs (1.5 O.D.) for an overnight incubation under moderate stirring (250 rpm). After the incubation the samples were washed with ultrapure water and dried for 3 h at 35 °C under benchtop extractor.

3.3.5. *Different dyes experiments*

The dye diffusion in the polymer was tested using different dyes: Melamine (Me), Janus Green B (JG), Neutral Red (NeuR), Nile Red (NR), Alcian Blue (AB) and Alcian Blue Pyridine (ABP). The experiment had similar set up as the basic experiment with CV (section 3.3.4). For AB and ABP the experiment was repeated using a solution 9:1 acetone water as bath for the infusion (similar conditions to section 3.3.2). In these experiments films and film samples modified with the different dyes were compared with the one containing AuNRs. The only exception was the experiment with Janus Green B (JG), where the film was also compared with one containing spherical AuNPs.

3.3.6. *Detection and quantification of ROS*

The detection and quantification of the ROS produced by the film was a lengthy and complex endeavour, which required the development of three different experiments, which were able to offer complementary information on the mechanism of action of the film.

3.3.6.1. L-ascorbic acid test of radical inhibition

The pH of a solution of NaCl (0.85% w/w) and L-ascorbic acid (20 mM) was set to 7.4 using small aliquots of NaOH (10 mM). To preserve the sterility of the experiment, the solution was filtered with a 0.25 µm filter in a biosafety hood. The purified solution was used to disperse bacteria pellets and to inoculate the plates of controls and film samples.

3.3.6.2. Methylene blue oxidizing species detection

Equal amounts of methylene blue (MB; 1 mL, 0.4 mM) and L-ascorbic acid (1 mL, 40 mM) were diluted with ultrapure water (8 mL). The solution was then alkalinized with a small amount of concentrated NaOH (100 µL, 1 M)

resulting in a transparent solution. This solution was then exposed to light on film samples after which its absorbance was measured and compared to the absorbance of other aliquots exposed in the surface of unmodified polymer. These measurements were correlated with a calibration curve created by the absorbance of a MB solutions containing increasing aliquots of H_2O_2 from 0.001 mM to 100 mM.

3.3.6.3. ROS detection by fluorescein quenching assay

The fluorescent solution used for the quenching assay (Fluo solution) was obtained by diluting in ultrapure water (9 mL) and aliquot of fluorescein (1 mL, 5 µg/mL) and a small amount of NaOH (50 µL, 1 M). The solution was stored in ice and protected from light.

For the experiments of intensity of fluorescence emission, aliquots of 25 µL of Fluo solution were placed on polymer and film tiles and exposed to the light (11.7 klux) for 1h. After the exposure, 10 µL aliquots of the solutions were collected and mixed with 40 µL of ultrapure water on a 384 well plate (black for fluorescence analysis).

In order to calibrate the system, aliquots 25 µL of Fluo solution were applied on PU tiles and exposed for 1h to the lamp light, 10 µL for each of the samples were then transferred in 384 wells plate for fluorescence and mixed with different concentration of H_2O_2 to imitate the exposure to different concentration of ROS. The measurement was repeated after overnight incubation.

3.4. Results and discussion

3.4.1. *Fluorescence emission intensity spectroscopy*

Measurements of fluorescence emission intensity were used to explore the energy exchange between the particles and the dyes (section 3.4.3.4) and to calculate the quenching effect of ROS on the fluorescence of fluorescein (section 3.4.6.3). Some considerations are necessary to understand the parameters chosen for the analysis and their effect on the experimental results:

1) In section 3.4.3, the excitation wavelength was 230 nm, but the emission was analysed from 275 nm.

The excitation wavelength was chosen because it was the shortest and more energetic available to the plate reader (section 3.3.1), thus being able to excite the UV fluorescence of the PU matrix while possibly interacting with the dyes and the particles. The choice of wavelengths closer to the absorption of the dye would be more efficient in exciting its fluorescence, but at the same time block any fluorescence emission of shorter wavelengths. Furthermore, the excitation wavelength was selected using a filter out of a polychromatic light source, which resulted in a bell shaped excitation band order of magnitudes larger than the fluorescence of the films. For this reason, a safety range of approximatively 40 to 50 nm was left between excitation and the shortest wavelength detected, thus avoiding acquiring any tail of the excitation band, which would overload the detector.

2) There is a peak at 460 nm in the emission spectra excited at 230 nm.

This was a consequence of scattering of the polymer, which was able to send back to the detector a small amount of the second-harmonic scattering of the exciting light.[187] Because this phenomenon depended only on the scattering properties of the material it could be used to track changes to the scattering properties of the film caused by the introduction of the dyes or the particles (section 3.4.3.4).

3) In section 3.4.6.3, the excitation wavelength was 485 nm, but the emission was analysed from 585 nm.

The excitation wavelength at 485 nm was chosen because was the nearest filter available to the maximal emission of fluorescein at 515 nm. While the detection wavelength was selected at 585 nm because it was on the tail of the fluorescence emission of fluorescein and far from the excitation wavelength. In a spectral area where all emissions of the sample that could be detected was generated only by the fluorescein contained in the solution.

3.4.2. *Embedding of nanoparticles in the film*

As described in chapter 3.3.2, the gold nanoparticles used in the film were introduced using the swell-encapsulation-shrink method. On the macroscopic level, the introduction of the particles could be easily confirmed as it caused a change of the film colour. Changing the colour from faint yellow to green-blue for AuNRs and AuNSs or ochre for spherical AuNPs and longer AuNRs. The detection and quantification of the nanoparticles in the polymer was less straightforward to determine analytically because most of the techniques generally used to analyse gold nanoparticles were easier to apply to a sample in solution instead of a polymer tile.

For example, SEM could analyse solid samples, but it possessed lower resolution than the one required to analyse the particles (≤ 10 nm) while the difference in conductivity between the particles and the polymer would made the procedure complicated.

To overcome these issues the polymeric samples in this thesis have been analysed using a spectrophotometer (as reported in section 3.3.3) and their spectra compared with the one obtained from unmodified polymer to see their differences.

3.4.2.1. Absorption spectra of the Au nanoparticles encapsulated in the film

The analysis of the films was difficult and needed multiple repetition to obtain reliable results. The introduction of gold nanoparticles caused only a slight change of the film absorption, while at the same time the sample was thin and possessed two reflective surfaces thus creating a large amount of cumulative error of the analysis. To reduce the variability, six different pieces of the film were tested for each type of film analysed and the experiment was repeated at least twice.

Due to the thinness of the film and its transparency the absorption of the samples was very weak (Figure 3.4.1.c), but it still showed a detectable change between the samples after the introduction of AuNSs or AuNRs (Figure 3.4.1.a & b).

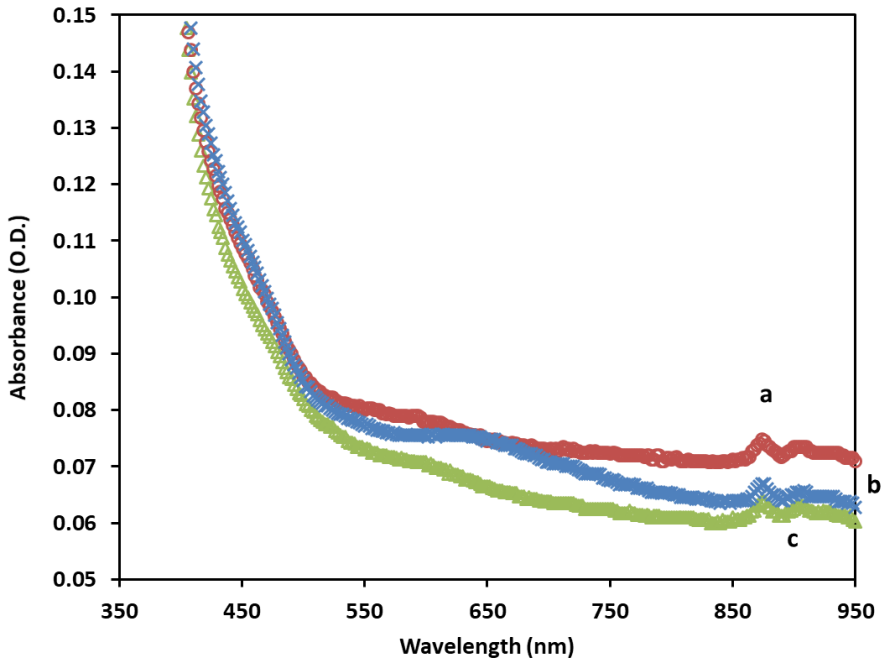

Figure 3.4.1. UV-visible spectra of a) PU/citNa-AuNSs, b) PU/citNa-AuNRs, c) PU.

Because the changes in the spectra of the polymers were very small, in the range of hundredths of O.D., the direct study of the spectra could only give limited information. To help with the visualization, the baseline of the three spectra in Figure 3.4.1 was normalised and the spectrum of the unmodified polymer was subtracted to the spectra of the samples containing the nanoparticles .

The curves obtained from these subtraction are reported in Figure 3.4.2, indicating with “a” the subtraction curve of PU/citNa-AuNSs – PU and “c” the subtraction curve of PU/citNa-AuNRs – PU.

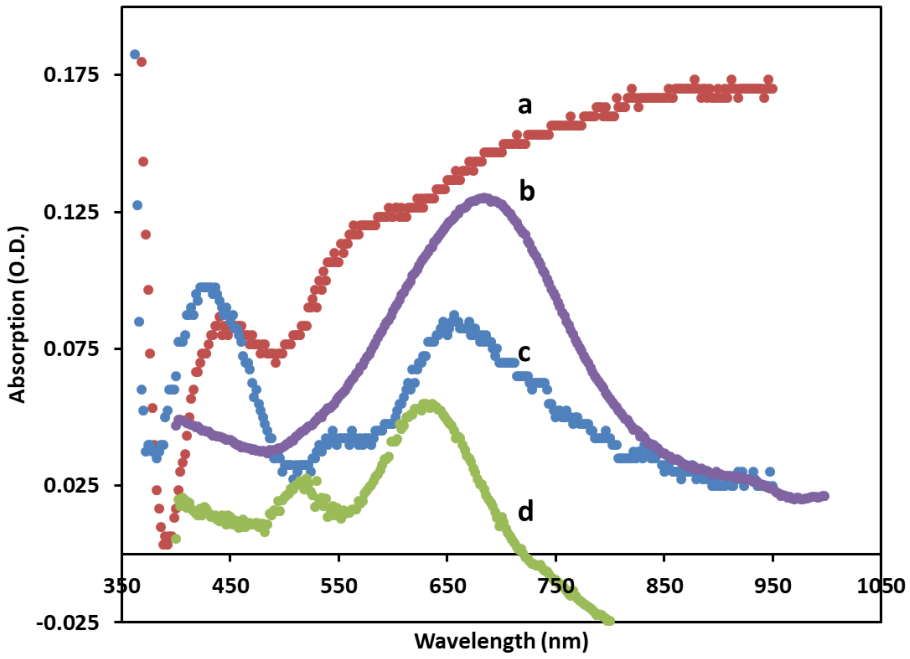

Figure 3.4.2. UV-visible spectra of a) subtraction curve between PU/citNa-AuNSs and PU, b) AuNSs in water, c) subtraction curve between PU/citNa-AuNRs and PU and d) AuNRs in water. The spectra in water were obtained by diluted solutions (20 % v/v) normalized to the scale of the subtraction curves and shifted up (b) and down (d) of 0.015 O.D.

Additionally, to better understand how the introduction of the particles in the polymer changes their absorption spectra, examples of AuNSs and AuNRs spectra in solution were added to Figure 3.4.2 as “b” and “d” respectively. To avoid crowding the graph, “d” was moved down by 0.015 O.D., while “b” was shifted up also by 0.015 O.D..

From the observation of the subtraction curves, it is possible to see how the light absorption of the film was increased in the range between 400 and 500 nm for both the particles, with peaks at 440 nm for AuNRs and 450 nm for AuNSs. This peak was characteristic of nanoparticles embedded in a

polymeric matrix and could not be detected in nanoparticles dispersed in water (Figure 3.4.2.a AuNSs & c AuNRs).

At longer wavelength the film modified with the different types of nanoparticles had different absorption peaks. Films containing AuNRs showed two peaks at 540 and 650 nm, characteristic of these type of particles (Figure 3.4.2.c). When AuNRs were embedded in the film their SPR peaks were red-shifted of approximatively 20 - 30 nm. The shift was probably caused by the change in the dielectric constant of the environment surrounding the particles between water and the polymer.

A similar shift could be observed when the capping agent of a nanoparticles was exchanged from citNa, polar and charged, to thiol-PEG-OMe, non-polar and neutral as reported in section 2.4.5.

On the other hand, embedded AuNSs, generated a broad increase of the absorption between 550 and 950 nm, with bumps indicating convoluted peaks at about 540 nm and 652 nm. The two wavelengths of these convoluted peaks have the same SPR peak positions identified from the simulations for the spherical core and the spike system (section 2.4.6.3).

While the increase of absorption at longer wavelengths could be attributed to the SPR resonance for the electrical field on the tips of the AuNSs spikes at 900 nm, that was identified by one of the simulations with PEG (Figure 2.4.28.C), but it could not be detected for AuNSs dispersed in water.

All the gold nanoparticles used in this work thesis were similarly analysed in Figure 3.4.3.

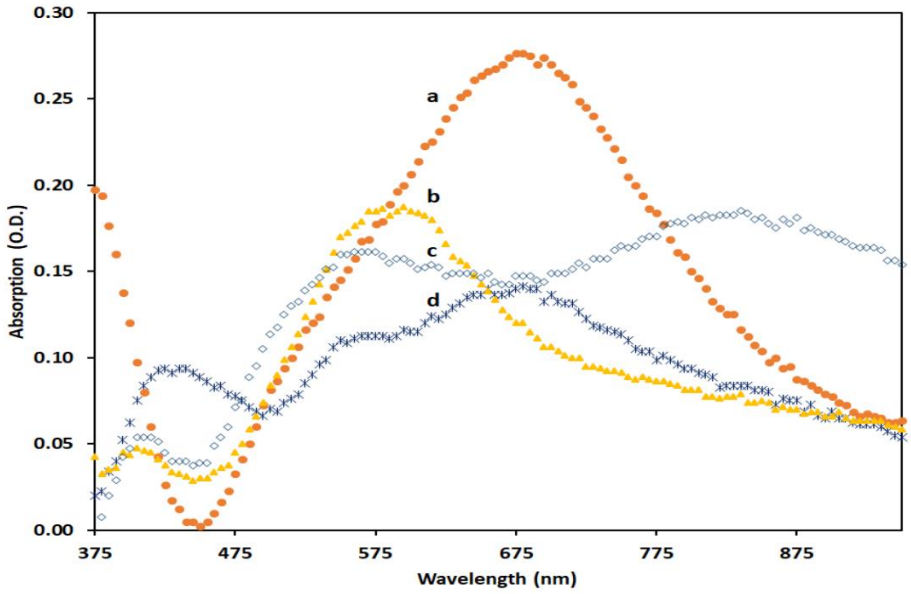

Figure 3.4.3. Subtraction curve of film modified with a) thiol-PEG-AuNSs, b) spherical AuNPs, c) AuNRs maximum absorption 800 nm and d) thiol-PEG-AuNRs (PU-AuNPs – PU).

Particles stabilized with thiol-PEG seemed to have a stronger absorption intensity compared to the citNa counterparts. Particularly relevant was the absorption peak of AuNSs which maintained a more defined peak structure compared with the citNa version. Spherical AuNPs (Figure 3.4.3.b) had a red-shift of 55 nm while broadening compared to the particles in solution, which it is probably a sign of aggregation or clustering.

AuNRs with absorption 800 nm maintained the two peaks spectrum of the sample in solution without a shift of the LSPR peak position (Figure 3.4.3.c), but in the polymer the ratio between the two SPR peaks seems nearer to 1 while both peaks seem to broaden. The reason for this flattening of the spectrum can probably be found in the experimental conditions, because for some of these film samples, the UV-visible analysis was performed on three layers of polymer stack, which helped to boost the particle signals but

also increased the background noise, thus the flattened spectrum, this variation of the set up was only used for few of the control particles (as AuNRs with long AR).

The position of the t-SPR peak of AuNRs remained unchanged regardless of the capping agent used or the introduction in the polymer. While the variations in the LSPR made clear that the type of stabilization directly influenced the interactions polymer-nanoparticles after the embedding. Analysing the subtraction curves in Figure 3.4.3, it is evident that the samples stabilized with citrated reacted more strongly to the introduction into the film, thus, leading to the broadening and shift of the peaks. Because this shift was towards red region, it indicated some type of destabilization, but not followed by a complete aggregation, which would have caused a complete change in the structure of the spectra.

3.4.2.2. Dependence between the concentration of particles in solution and in the polymer

The presence of the AuNRs in the film could be detected using UV-visible spectroscopy, but in order to establish which concentration of nanoparticles to use for its preparation, it was necessary to develop a method to quantify the particles embedded in the film.

To prove the relation between the concentration of particles in solution and the amount embedded in the film, a number of polymer tiles were prepared using dispersions of nanoparticles of increasing concentrations.

The samples were then tested to understand if changing the amount of particles in the swelling solution corresponded to an increase of the particles in the film (Figure 3.4.4).

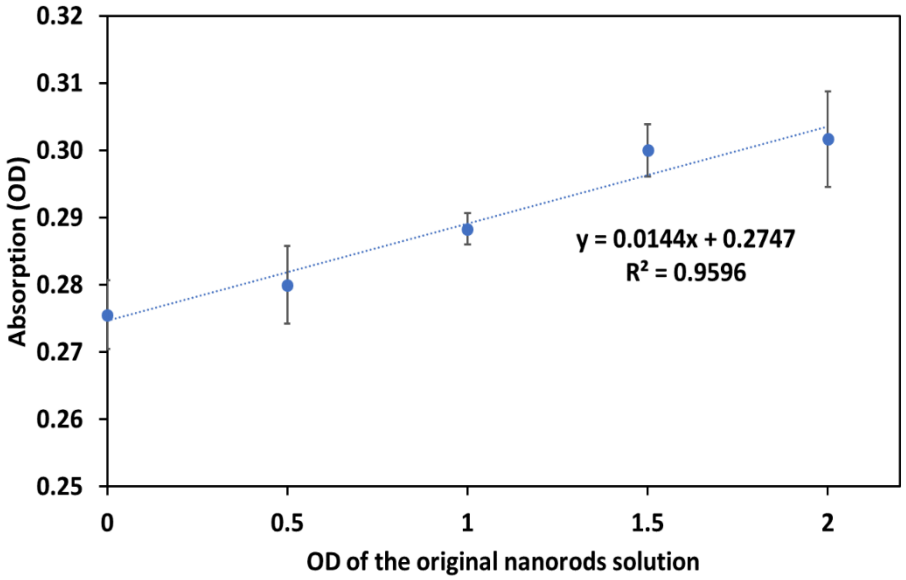

Figure 3.4.4. Intensity of the LSPR peak (648 nm) of the AuNRs embedded PU film as a function of the concentration of the AuNRs in the swell solution.

As reported in the previous section (3.4.1) the absorption of the films was very weak and the measurements on polymers were prone to casual errors but from the results in Figure 3.4.4 there was a clear relation between the that the amount of light absorbed by the film and the concentration of the AuNRs solution used in its preparation.

To reach an actual quantification of the AuNRs in the film, from these optical observations was necessary to accept some degree of approximation and required some assumptions. For example, if the totality of the particles introduced in the swelling solution was able to be trapped in the polymer the concentration in gold inside the polymer would be obtained through the Equation 3.4.1 – 3.4.3:

$$V_{AuNRs} = 1.5\ mL;\ C_{O.D.} = 1.5\ O.D.;\ mM\ concentration\ per\ O.D. = 0.43\ {}^{mM}/_{O.D.} \rightarrow\ C_{AuNRs}\ Stock = 0.645\ mM \quad (3.4.1)$$

$$V\ of\ polymer\ per\ batch = 30\ cm^2 * 1\ mm = 3\ cm^3 \quad (3.4.2)$$

$$C_{film} = \frac{V_{AuNRs} * C_{AuNRs}}{V_{polymer}} = \ 0.323\ mM \quad (3.4.3)$$

According to Equation 3.4.3 the amount of gold in the film was 0.323 mM equal to 0.032 µmol/cm^2 or 53.6 mg/Kg of film.[11] The estimation of the concentration Au^0 in the film was overestimated, because, according to the analysis done in section 2.4.1., the concentration calculated should increase the absorption of the film by 0.139 O.D., however the spectrum of the polymer showed a change of only 0.025 O.D. (0.300 O.D. for the film and 0.275 O.D. for the polymer), Figure 3.4.4.

To produce a better estimation of the efficiency of the embedding process, it was necessary to change the starting point of the process, considering the AuNRs uniformly distributed in the swelling solution (0.072 mM). From this point the efficiency of the encapsulation process was calculated comparing the particles in the polymer against the effective concentration in solution (

Table 3.4.1**Error! Reference source not found.**).

Table 3.4.1 Relation between stock concentrations, swelling solution concentrations and the absorption changes according to the calculations and in the experimental samples and the percent of efficiency of embedding for the experimental samples.

Conc. (O.D.)	Conc. (mM)	Swelling Conc. (mM)	Calculated ΔAbs	Experimental ΔAbs	%
0.5	0.215	0.0215	0.009	0.004	48.1
1.0	0.430	0.0478	0.021	0.013	62.2
1.5	0.645	0.0717	0.031	0.024	79.3
2.0	0.860	0.0956	0.041	0.026	63.5

When analysing the data using these considerations a better accordance between the variations of absorption of the film and the amount of particles used in the embedding process was revealed. The process showed an overall average efficiency of 64.4 % calculated according to Figure 3.4.4 corresponding to a gold concentration in the polymer of 0.048 mM (0.0048 µmol/cm^2 or 8.09 mg/Kg) when using the standard embedding conditions reported in section 3.3.2.

Experimental analysis of the antimicrobial efficiency of the film samples (methods and set up in section 4.3.5) prepared with different concentrations of particles indicated the optimal concentration of the gold nanoparticles solution for the preparation of the polymer was 1.5 O.D. (1.5 mL, 0.645 mM). Lower concentrations were less efficient while higher concentrations did not evidently improve the efficiency of the film.

3.4.3. *Dye selection*

One of the two core components of the antimicrobial film developed in this thesis was the PS, which had the capability of converting the light absorbed by the film in ROS which killed the bacteria (section 1.1.4). To be used in the film, the PS had to possess an overlapping absorption spectrum with the

particles SPR and an efficient ROS yield when exposed to light. If the overlapping condition was met, the presence of dye molecules in close proximity to the particles, was able to induce a strong plasmonic coupling between dye and AuNRs (section 1.1.5).

The coupling with the nanoparticles greatly increased the amount of energy absorbed by the dye.[93,188] Thus, it increased the amount of ROS produced and the antimicrobial effect generated by the film.

Crystal violet was the dye used for most of the experiments performed for this work. CV was characterized by two absorption peaks: one weaker at 540 nm and another stronger at 590 nm (Figure 3.4.5). The position of these peaks overlaps with the two peaks of AuNRs (520 nm, 615 nm) and the broad peak of AuNSs (700 nm) (further discussion in section 3.4.6.3).

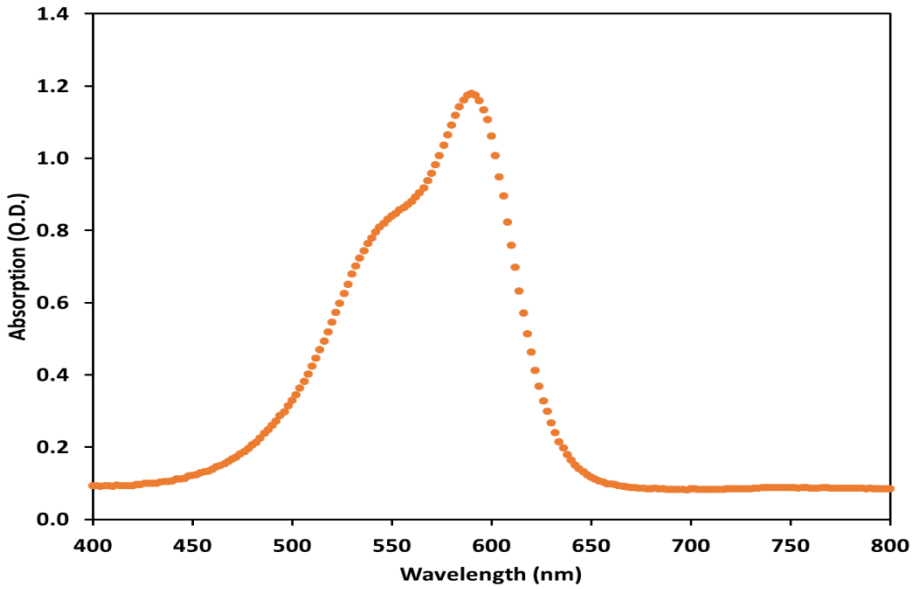

Figure 3.4.5. UV-visible absorption of Crystal Violet in water (25 µM).

CV was a well-studied dye (section 1.1.4.2) with a good capability in converting light in ROS, but it required an intense light to be activated and it could be vulnerable of photodecomposition.[189] In the following section a number of dyes have been tested as active component of an antimicrobial

film, to search for a possible substitute for CV and investigate how the structure of the dye influence the efficiency of the film.

3.4.3.1. Dyes molecular structures and electronical consideration

As reported previously (section 1.1.4.2), CV (Figure 3.4.6.b) was the dye used as PS for the development of the antimicrobial film.

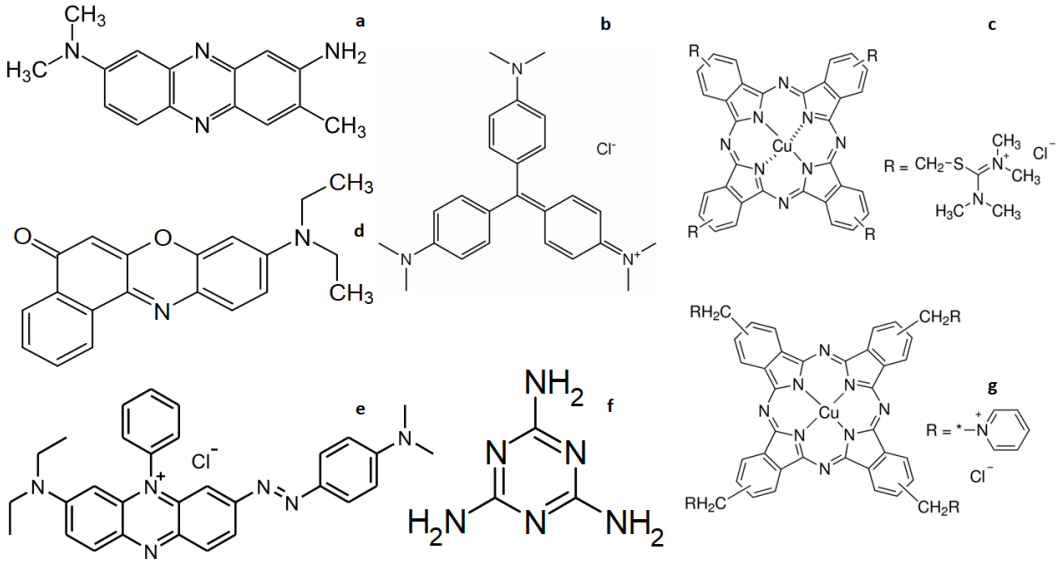

Figure 3.4.6. Structure formula of a) Neutral Red (NeuR), b) Crystal Violet (CV), c) Alcian Blue (AB), d) Nile Red (NR), e) Janus Green B (JG), f) melamine (Me) and g) Alcian Blue Pyridine (ABP).

Structurally it was characterized by a large delocalized aromatic system where a positive charge was diffused on the entire extent of the molecule. To identify which characteristic of the molecule contributed to the efficiency of the film as ROS producer, a series of dyes were selected according their structure and functional groups as candidate for the film creation.

In the experiments in different films, with or without AuNRs (615 nm) embedded in them have been modified with the different dyes. The only exception to this procedure was done for JG (maximum absorption 550 nm)

that was also tested in a film containing spherical gold nanoparticles (AuNPs, 13 nm diameter, 518 nm max absorption).

To better understand the properties of the dyes used in this section, they were divided in groups according to their molecular structure (Figure 3.4.6). The dyes of the first group were all positively charged and possessed absorption peaks close to the SPRs of AuNRs (either t-SPR, LSPR or both), thus having the possibility of triggering the plasmonic coupling. This group included “Alcian Blue” (AB), “Alcian Blue Pyridine” (ABP) and JGB.

AB (Figure 3.4.6.c) and ABP (Figure 3.4.6.g) were positively charged phthalocyanine rings containing copper (II) ions and attached on their external rings they could have four thiourea groups or pyridine groups, respectively. Both these dyes had a strong UV-visible absorption at 612 and 660 nm and possessed a delocalized system with positive charges localized on dimethylammonium or pyridinium moieties. Compared with CV the positive charges were not directly connected with the resonating aromatic system while the presence of the Cu(II) and multiple heteroatoms in their structure probably led to a complex charge distribution in the molecule.

The last of member of the first group was JG (Figure 3.4.6.e), as CV this molecule had a delocalized resonating aromatic system with a positive charge connected and two peaks of absorption at 395 nm and 660 nm.

The second group tested was comprised of “Neutral Red” (NeuR) and “Nile Red” (NR), which in opposition to the dye of the first group did not possessed a stable positive charge, but could generate temporary charges separations, which were free to resonate in their aromatic structure. Both

NeuR and NR had a central polyaromatic structure in which some heteroatoms were inserted.

NeuR is more electron poor than NR or CV, containing only nitrogen atoms connected with the resonant structure and a main absorption peak at 475 nm, while NR is more electron rich, because it contained some oxygen atoms in its rings structure. NR has two convoluted absorption peaks at 560 and 675 nm.

The last organic molecule tested, did not fit in any of the groups, because "Melamine" (Me) did not have any strong visible absorption. At the same time, Me had a strong capability to stabilize free radicals and absorb wavelength in the UV. Thus, it could be used to confirm the hypothesis that the ROS were generated mostly by the dye instead of by the particles.[190] Because in presence of melamine the hypothetical free electrons generated by the particles would be stabilized by the aromatic system, thus increasing the possibility for them to interact with the oxygen in the media surrounding the bacteria to form ROS.

3.4.3.2. Gold nanoparticles embedded in the polymer

In order to set a base line for the effect of the dyes on the films, the absorption of PU containing AuNRs 615 nm and 13 nm AuNPs have been analysed and compared with the unmodified polymer, following the same procedure reported in sections 3.3.3 and 3.4.2.

The subtraction curves obtained by these comparisons are reported in Figure 3.4.7.

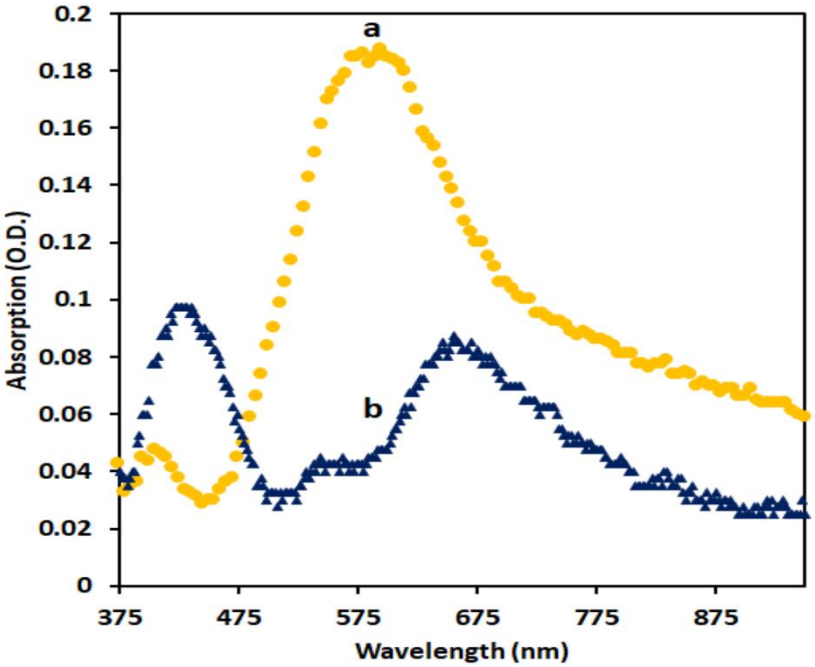

Figure 3.4.7. Subtraction curves of a) PU/citNa-AuNPs – PU (spherical) and b) PU/citNa-AuNRs - PU.

Consistently with the samples analysed in section 3.4.3.2, the SPR peak of the AuNPs (Figure 3.4.7.a) was red-shifted of approximatively 50 nm, while maintaining the same peak structure. The peaks of AuNRs instead red-shifted only of 20 nm (Figure 3.4.7.b). As observed previously, after the introduction of Au nanoparticles in the polymer a new peaks at 400 nm for AuNPs and 450 nm for AuNRs was revealed, with the peak of the AuNRs much more intense than the one for AuNPs.

3.4.3.3. UV-visible absorption in the polymer of the dyes with or without AuNRs

As introduced previously (section 3.4.3.1), the dyes were tested on samples of polymer with or without gold nanoparticles. The aim of this set of tests was to establish if the absorption of the dyes would change in presence of

the AuNRs (or AuNPs for JG), thus proving the existence of an interaction between particles and dye.

The spectra in Figure 3.4.8 toFigure 3.4.18 were grouped according to their maximal O.D. absorption instead of by their molecular structure, to help with the visualization. According to this principle, Figure 3.4.8 shows the UV-visible spectra of the molecules which produced the lower visible light absorption: Me, AB, ABP. To offer a term of comparison, the spectra of polyurethane alone and of the film containing AuNRs were added to the plot (Figure 3.4.8.a and b respectively).

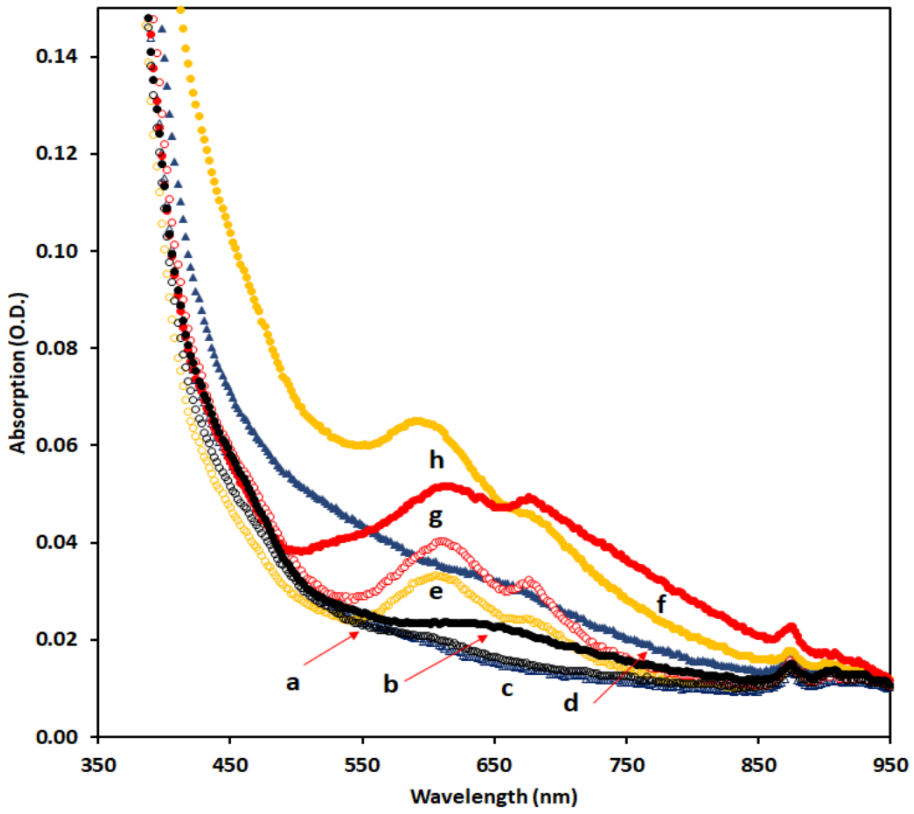

Figure 3.4.8. UV-visible spectra of the films: a) without modifications, b) with AuNRs, c) with Me, d) with AuNRs and Me, e) AB, f) with AuNRs and AB, g) ABP and h) with AuNRs and ABP.

Me was the only molecule tested which was not a dye and as expected, it produced no increases of absorption when introduced in the polymer alone (Figure 3.4.8.c). In contrast, in presence of AuNRs, it generated a broad

increase of absorption (macroscopically visible by a faint reddish colouration of the film, Figure 3.4.8.d).

Me in combination with the AuNRs (Figure 3.4.8.d) boosted the film absorption at 500 nm. Indicating clearly the presence of an interaction, but the effect generated was very weak, changing the max absorption of only by 0.02 O.D.

The reason why the change of colour happened only in presence of the AuNRs is not clear. Me, when used for radical polymerizations, is a reticulating agent, which is a process that can generate the development of colours in delocalized systems. It is possible that the presence of the AuNRs was able to catalyse the reaction between PU and ME thus causing the appearance of the colour.

When introduced in the polymer AB generated two weak peaks at 575 and 680 nm (Figure 3.4.8.e). In presence of AuNRs the entire spectra increased of intensity (Figure 3.4.8.f). The increase was particularly strong for wavelengths between 400 to 850 nm, while it generated a weak increase of absorption at longer wavelengths. The increase of absorption was probably caused by the surface charge of the nanoparticles (strongly negative because stabilized with citrate) which was able to drive a larger amount of dye to diffuse inside the polymer. The rise of absorption was spread along the spectra, but more intense at short wavelengths and weak at long wavelengths, which is an indication of an increase of the background scattering more than an electronic interaction between dye and particles. The increase of scattering indicates an increases of the light diffused by the film, similarly to a solution forming flocculates.[191]

Finally, ABP (Figure 3.4.8.g) had a similar absorption with AB, but it interacted in a different way with the particles. In presence of AuNRs (Figure 3.4.8.h) the dye generated a sharp increase of absorption at 500 nm and in the range between 670 and 850 nm. Also, for this dye the increase of background scattering has an important role.

These instances of scattering could be caused by aggregates of particles and dyes or by particles formed by aggregates of the dyes on the surface of the polymer.

A common issue with all the molecules used in this experiment was their poor penetration inside the polymer. This problem for AB and ABP was caused by their lack of solubility in water (less than 1 mM), which disrupted the diffusion process (section 3.3.4). To improve the diffusion process and increase the amount of dye introduced in the polymer, a new procedure in which the particles were loaded in the film through the immersion in a solution 9:1 acetone to water was prepared (section 3.3.4).

This method of dye diffusion was performed repeating the same conditions already used for the embedding of the AuNRs in the films (as reported in section 3.3.2) the results were reported in Figure 3.4.9.

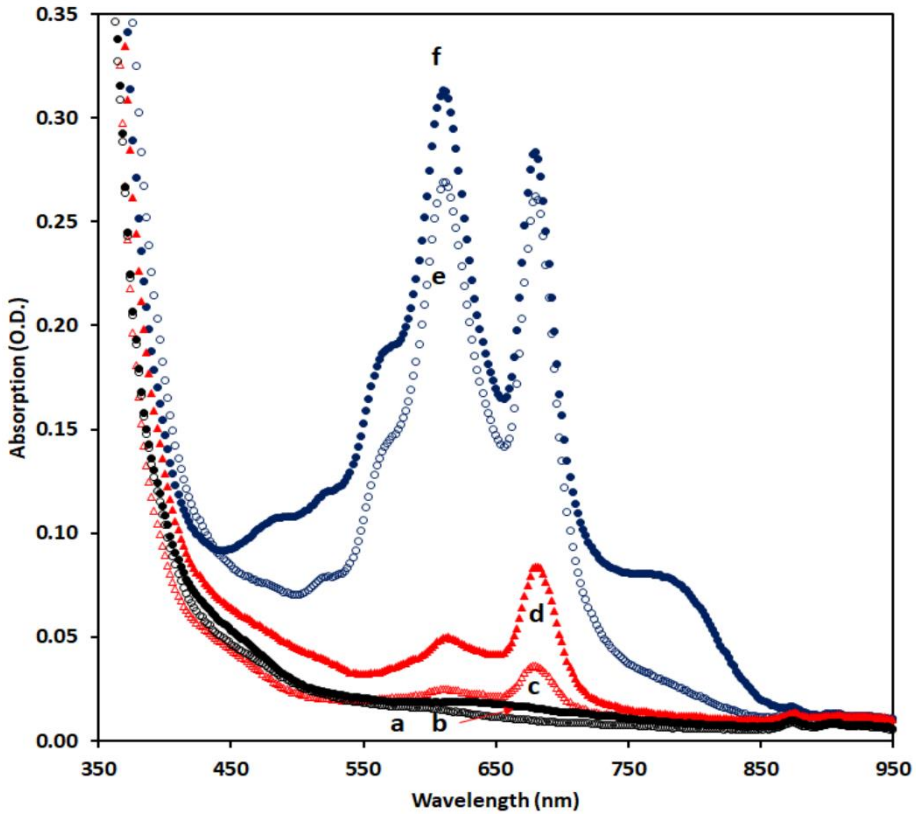

Figure 3.4.9. UV-visible absorption of the films modified from dyes solutions in acetone. a) Film without any modifications, b) with AuNRs, c) with ABP, d) with AuNRs and ABP, e) with AB and f) with AuNRs and AB.

Introducing AB and ABP using the acetone solution generated a greater absorption, compared to the previous method but it also changed the structure of the dye spectra in the polymer.

ABP (Figure 3.4.9.c), introduced with acetone, showed the same two peaks seen previously (Figure 3.4.8.g.) but with different relative intensity between the peaks. In these conditions, the absorption peak at 675 nm of ABP was almost twice as intense as the peak at 575 nm. This was almost the opposite situation for the samples from aqueous solution, in which the 575

nm peak was the most intense (Figure 3.4.8.g) with an approximate ratio 3:2.

Introducing the AuNRs (Figure 3.4.9.d), increased the absorption at shorter wavelengths and further increase the intensity of the dye peaks and their difference. AB benefited more from this introduction procedure, with the relative intensity of its peaks increased of approximatively of 5 times while the structure of its spectra was strongly modified by this procedure.

The two main peaks of AB in the polymer, were sharp and roughly of the same intensity (Figure 3.4.9e), in contrast with the dye spectra when diffused from water were the peak at 575 nm was the most intense (Figure 3.4.8.e).

With this introduction method the dye generated additional absorption peaks at 475 nm, 560 nm and a rise of the baseline at 800 nm.

The introduction of AuNRs and AB (Figure 3.4.9.f), modified the general absorption of the film generating an absorption peak at 475 nm, while the intensity of the peaks at 500 nm and 550 nm greatly increased when compared with the dye alone. Finally, a new peak at 800 nm with similar intensity as the peak at 475 nm was generated by the interaction between AuNRs and dye.

The appearance of new peaks and their change of intensity are both connected to the increase of concentration of the dye in the polymer. In the samples with the dye alone, these new peaks are probably connected to the formation of dimers and other dye to dye interactions, which probably were further intensified by the introduction of AuNRs. The two new peaks around 475 nm and 800nm for the system dye/AuNRs/PU could be a consequence of a strong plasmonic coupling between the components of the film (described in section 1.1.5).

The next spectral collection included: NeuR, JG, and NR.

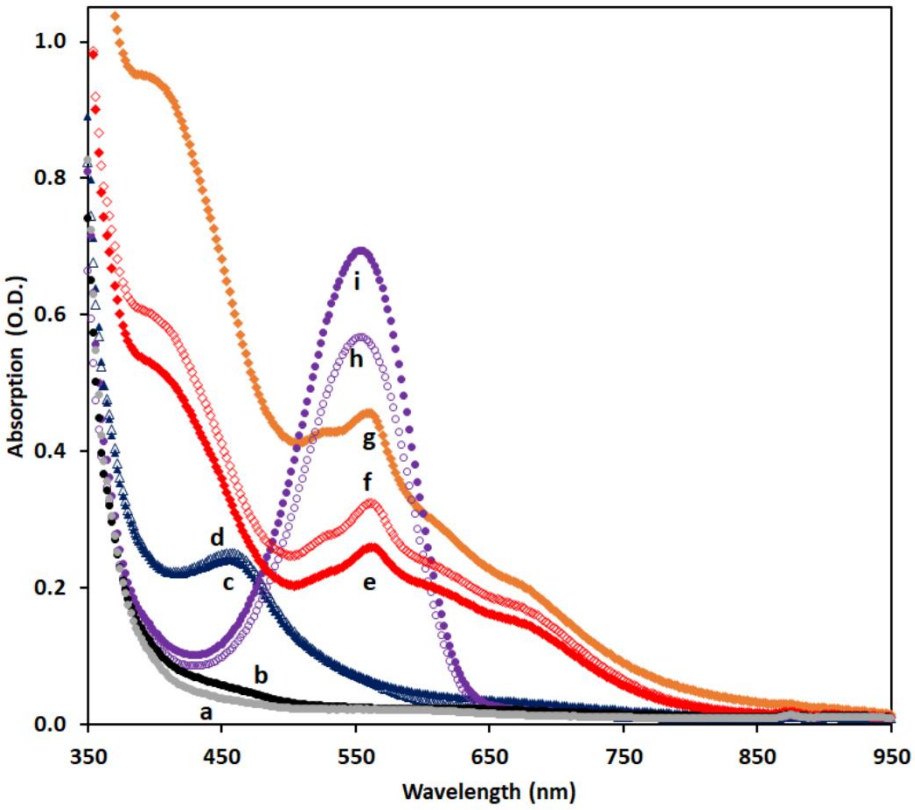

Figure 3.4.10. UV-visible spectra of a) the film modified with AuNPs, b) the film modified with AuNRs, c) NeuR with AuNRs, d) NeuR, JG with AuNRs, f) JG alone, g) JG with AuNPs, h) NR, i) NR with AuNRs.

NeuR (Figure 3.4.10.d), did not show any interactions with AuNRs (Figure 3.4.10.c), while NR (Figure 3.4.10.h), increased its absorption when interacting with the AuNRs (Figure 3.4.10.I).

In exception to the other dyes tested, JG (Figure 3.4.10.f), have been analysed in presence of AuNRs (Figure 3.4.10.e) and AuNPs (Figure 3.4.10g). Exhibiting a different behaviour in relation with the two types of particles: interacting with AuNRs the intensity of the JG spectra decreased in the range between 400 to 800 nm, while when interacting with AuNPs (Figure 3.4.10.a) the absorption between 400 to 600 nm greatly increased. This increase was larger at short wavelength 400 to 500 nm and it progressively decreased going towards 800 nm. JG had a similar behaviour to AB and ABP,

where the interaction between dye and nanoparticles seems to cause an increase of the background scattering.

AB, ABP and JG were all positively charged, which increased their interaction with the negatively charged nanoparticles, but this interaction could also explain the increase of the background scattering, as caused by aggregates on the surface of the film.

3.4.3.4. Fluorescence emission intensity in the polymer of the dyes with or without AuNRs

The fluorescent emission of the films was measured with the settings reported in section 3.3.1. To understand if the interaction between the dyes and AuNRs were influencing the fluorescence emission of the films, thus implying an energy transfer between the film components.

In order to produce a control for these experiments the emission spectra of the polyurethane film (PU; Figure 3.4.11.b) and PU/citNa-AuNRs (Figure 3.4.11.a) were acquired, a subtraction curve comparing the fluorescence

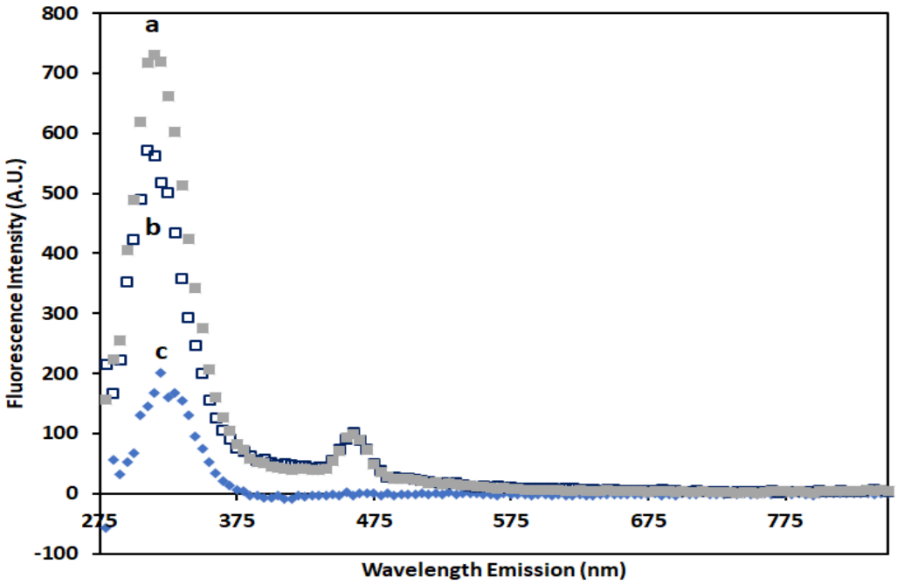

Figure 3.4.11. Fluorescence intensity emission spectra, after excitation at 230 nm of a) PU/citNa-AuNRs, b) PU alone and c) subtraction curve PU/citNa-AuNRs – PU.

of the film with and without AuNRs was prepared (Figure 3.4.11.c) to highlight the changes the introduction of particles caused to the fluorescence of the film.

The two spectra had a small peak at 460 nm, due to the second order scattering of the excitation wavelength (described in section 3.4.1) and a main peak centred in 315 nm generated by the fluorescence of the polymer.

Comparing the two spectra it is evident that in presence of the AuNRs the emission of the polymer increased (subtraction curve between PU/citNa-AuNRs – PU in Figure 3.4.11.c) while the second order scattering peak instead remained constant showing that the particles did not modify the diffractive index of the film, thus the change of the short wavelength peaks can demonstrate a certain type of interaction between the polymer and the particles. This is probably due to their intense electrical field and surface charge which was able to interfere with the electron density of the aromatic system of the polyurethane.

3.4.3.4.1. Crystal violet:

Once established the controls, the first dye tested was CV, because this PS was the most used throughout the project and the only one with a proven and tested antimicrobial activity (section 1.1.4.2). The fluorescence emission spectra of CV was characterized by a weak fluorescence peaking between 640 and 675 nm, which was visible for the samples with or without AuNRs (Figure 3.4.12.c & d).

The introduction of CV in the film (Figure 3.4.12.d) caused a small reduction of the peak at 315 nm compared with the polymer alone (Figure 3.4.12.b), while introducing the dye in presence of AuNRs (Figure 3.4.12.c) increased

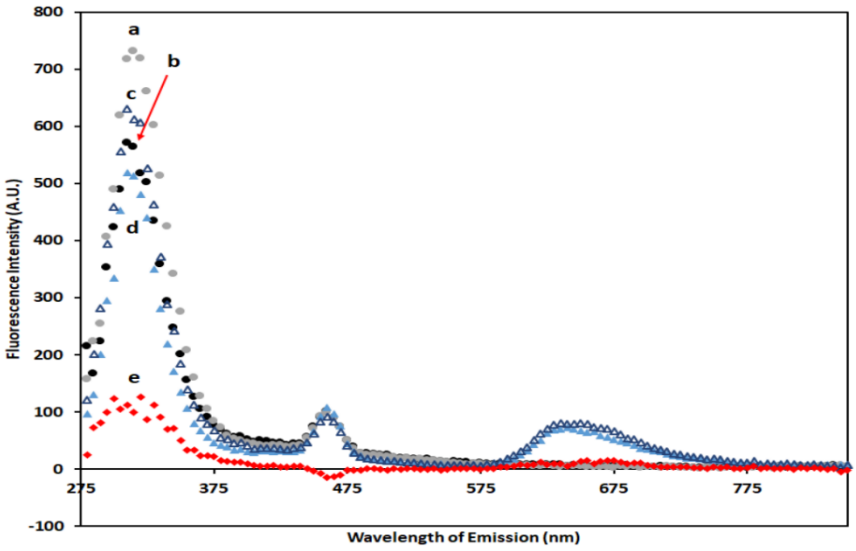

Figure 3.4.12. Emission fluorescence intensity spectra, after excitation at 230 nm of a) PU/citNa-AuNRs, b) PU alone, c) PU/citNa-AuNRs/CV, d) PU/CV, e) subtraction curve PU/citNa-AuNRs/CV – PU/CV.

the peak intensity, compared to the polymer alone, but this increase was less than the one caused by the AuNRs alone (Figure 3.4.12.a).

The comparison between the spectra of PU/citNa-AuNRs/CV and PU/CV (Figure 3.4.12.e), showed an increase of the peak at 315 nm, as seen for the samples containing only AuNRs, but in presence of CV this peak was broader

and less defined. The reduction in peak definition may be caused by a small change in the refractive index of the polymer as suggested by the small difference in intensity of the second order scattering peak between the films with or without AuNRs. It is also worth noticing that the broad peak at 580 – 700 nm did not change in presence of AuNRs, indicating that the plasmonic coupling between dye and particles had no influence on the dye fluorescence.

3.4.3.4.2. Melamine:

The next molecule tested was Me, which did not have any visible absorptions (Figure 3.4.8) but possessed a delocalized structure which could result in fluorescence or energy transfers with the AuNRs (Figure 3.4.6).

The introduction of Me in the polymeric film (Figure 3.4.13.b), did not add any new fluorescence emission peaks to the film. But compared with the controls (Figure 3.4.13.c & d) it increased the in intensity of the peak at 315 nm and of the second order diffraction peak at 460 nm.

These results gave a clear indication that this molecule only modifies the scattering properties of the film. The introduction of AuNRs (Figure 3.4.13.a) only produces a small increase of the apparent emission at shorter

wavelengths (275 nm to 490 nm), which was probably an artefact caused by the scattering of the light from the excitation source.

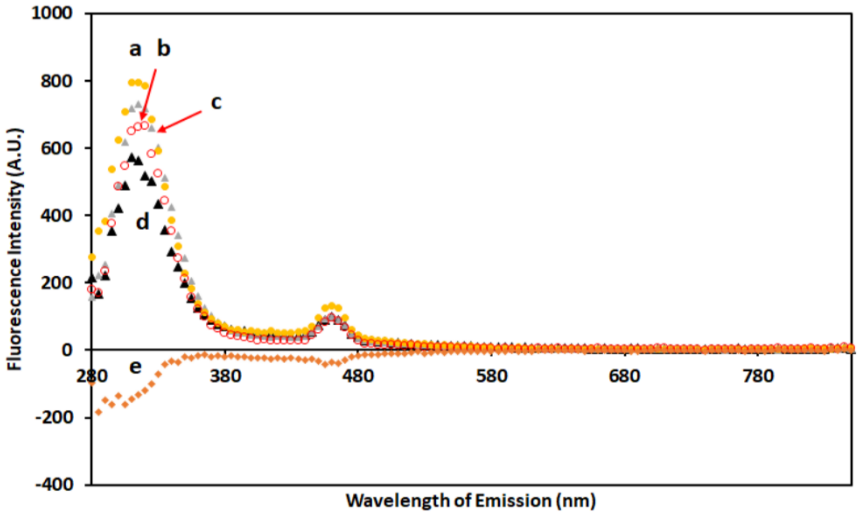

Figure 3.4.13. Emission fluorescence intensity spectra, after excitation at 230 nm of a) PU/citNa-AuNRs/Me, b) PU/Me, c) PU/citNa-AuNRs, d) PU alone, e) subtraction curve PU/citNa-AuNRs/Me - PU/Me.

3.4.3.4.3. Janus green B:

JG (Figure 3.4.14.b) was tested in combination with AuNRs (Figure 3.4.14.a) and AuNPs (Figure 3.4.14.c), similarly for what have been seen for Me

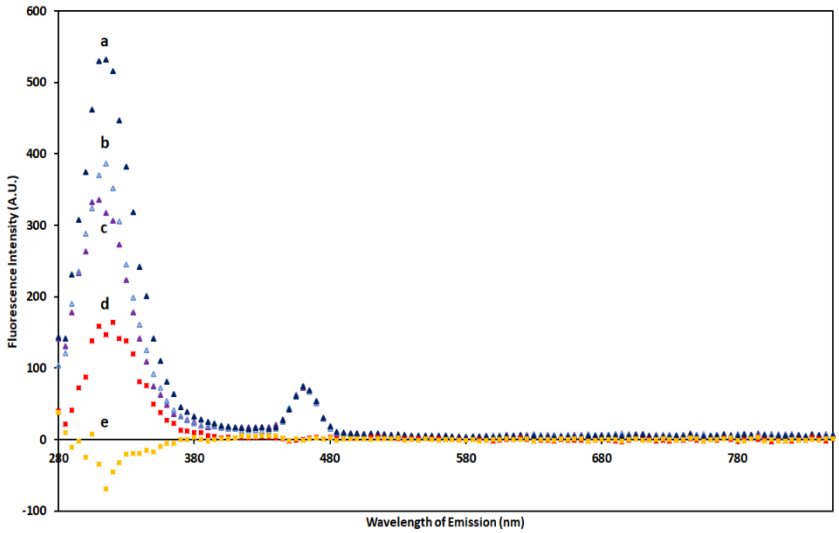

Figure 3.4.14. Emission fluorescence intensity spectra, after excitation at 230 nm of a) PU/citNa-AuNRs/JG, b) PU/JG, c) PU/citNa-AuNPs/JG, d) subtraction curve PU/citNa-AuNRs/JG - PU/JG and e) subtraction curve PU/citNa-AuNPs/JG - PU/JG.

(section 3.4.3.4.2), JG do not add new emissions to the fluorescence of the film.

At the same time, when interacting with AuNRs it caused an increase of the emission at 315 nm (Figure 3.4.14.d) while on the other hand when JG was in presence of AuNPs, its emission decreased (Figure 3.4.14.e).

This difference of reaction indicated a distinct type of interaction between JG and the particles, in presence of AuNRs there was no coupling thus the charge of the dye only caused a larger charge separation in the polymer and consequently more fluorescence, while with AuNPs the interaction dye-particles was strong, thus their pairing absorbed some of the energy of the film.

3.4.3.4.4. Alcian blue:

AB as many of the other dyes tested, have no distinctive fluorescence emission, thus, to understand its effect on the film, the effect of AB on the main peak of PU have been characterized.

The emission of fluorescence of the films containing AB have been tested, after the diffusion from water or acetone (Figure 3.4.15.c & d respectively) the two methods of diffusion had a strong effect on the intensity of the emission.

If the film containing only AB was prepared with acetone, it had a lower fluorescence intensity compared to the sample prepared from water, the introduction of AuNRs balance this difference restoring the emission peak at 315 nm to the same level of the dye alone (Figure 3.4.15.a & b for acetone and water, respectively).

Comparing the emissions of the samples with and without AuNRs prepared with the same method (Figure 3.4.15.e & f) was evident how the films prepared from water had approximatively the same emission, while for the

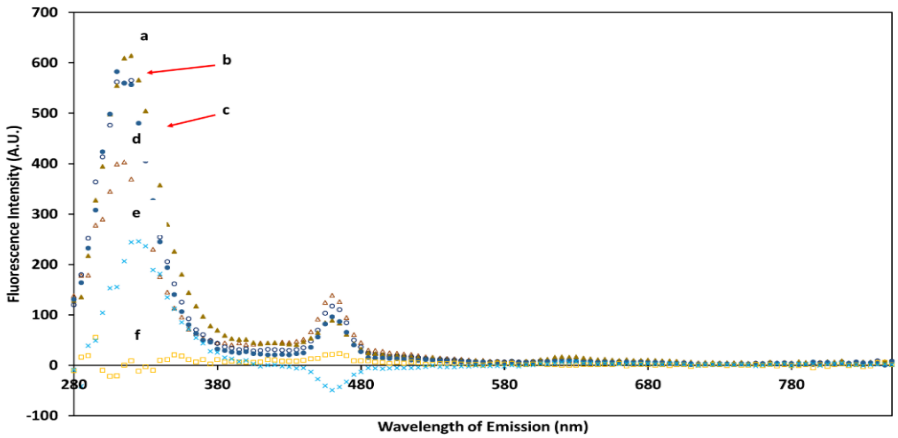

Figure 3.4.15. Emission fluorescence intensity spectra, after excitation at 230 nm of a) PU/citNa-AuNRs/AB (acetone) b) PU/citNa-AuNRs/AB, c) PU/AB, d) PU/AB (acetone), e) subtraction curve PU/citNa-AuNRs/AB – PU/AB (acetone) and f) subtraction curve PU/citNa-AuNRs/AB – PU/AB.

film without particles prepared from acetone had a weaker emission.

The cause of this effect may be connected with the increase of the concentration of the dye in the polymer which caused a self-quenching of the fluorescence with a reduction of the emission. The introduction of the AuNRs seemed able to revert this effect and to bring back the fluorescence emission to the same level of the sample prepared from water solution of the dye.

3.4.3.4.5. Alcian blue pyridine:

ABP did not have any influences on the fluorescence of the film, (Figure 3.4.16.a & c for acetone and water, respectively) neither it was influenced by the introduction of AuNRs (Figure 3.4.16.b & d) or by the method of diffusion.

Subtracting the emission spectra of the dye, with or without the AuNRs, only a small increased of emission below 300 nm (Figure 3.4.16.e & f), which could be connected to a very weak scattering effect.

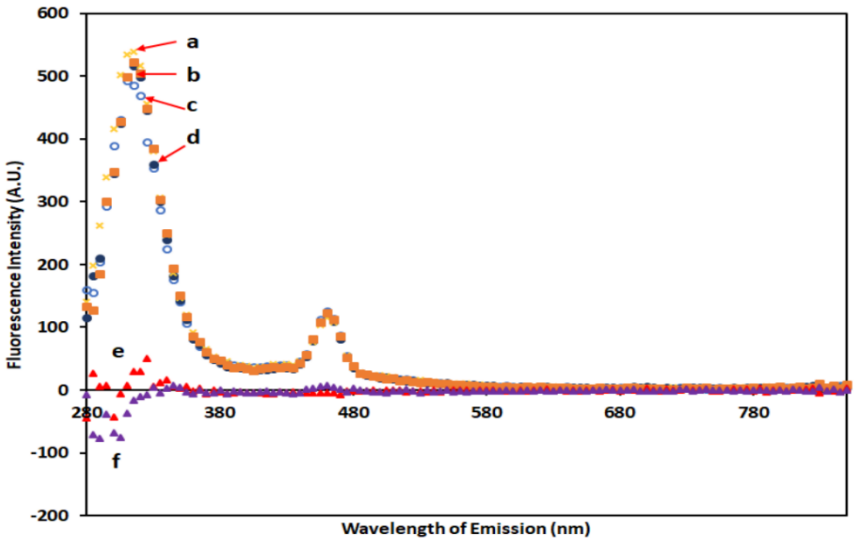

Figure 3.4.16. Emission fluorescence intensity spectra, after excitation at 230 nm of a) PU/ABP (acetone), b) PU/citNa-AuNRs/ABP (acetone), c) PU/ABP, d) PU/citNa-AuNRs/ABP, e) subtraction curve PU/citNa-AuNRs/ABP – PU/ABP and f)) subtraction curve PU/citNa-AuNRs/ABP – PU/ABP (acetone).

3.4.3.4.6. Neutral Red:

NR in contrast to the majority of the dyes tested had a weak and broad fluorescence peaking at 580 nm (Figure 3.4.17.b) and ranging between 520 nm to 700 nm. This peak in presence of AuNRs had a very small increase of intensity (Figure 3.4.17.a) suggesting a weak energy transfer between the particles and the dye. Or, as suggested from the subtraction curve of the two films containing NeuR (with or without AuNRs Figure 3.4.17.c), could be the result of how the introduction of AuNRs changed the diffractive

index of the film. Thus, changing the emission at 460 nm and in minor part the emission of the polymer.

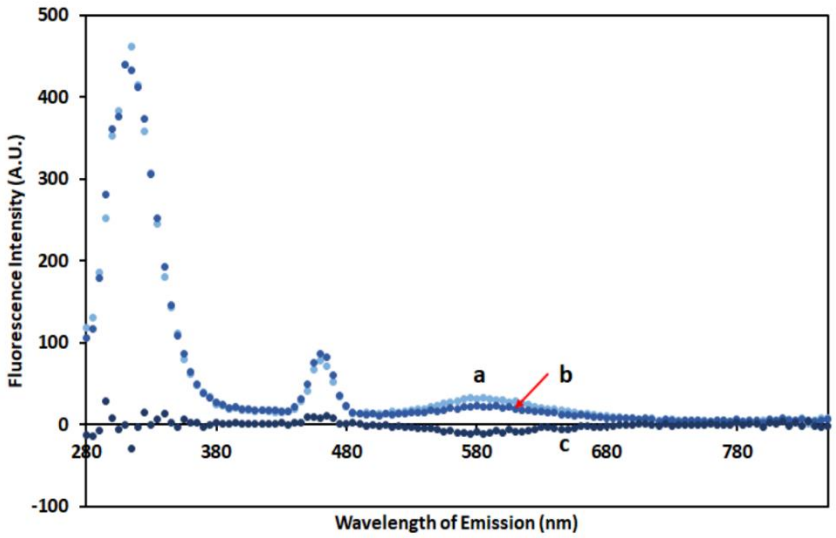

Figure 3.4.17. Emission fluorescence intensity spectra, after excitation at 230 nm of a) PU/citNa-AuNRs/NeuR, b) PU/NeuR, c) subtraction curve PU/citNa-AuNRs/NeuR - PU/NeuR

3.4.3.4.7. Nile red:

NR (Figure 3.4.18.a) had a similar fluorescent emission intensity of CV (Figure 3.4.12). This fluorescence, in presence of AuNRs (Figure 3.4.18.b), is strongly quenched as it can be seen from the subtraction curve in Figure 3.4.18.c.

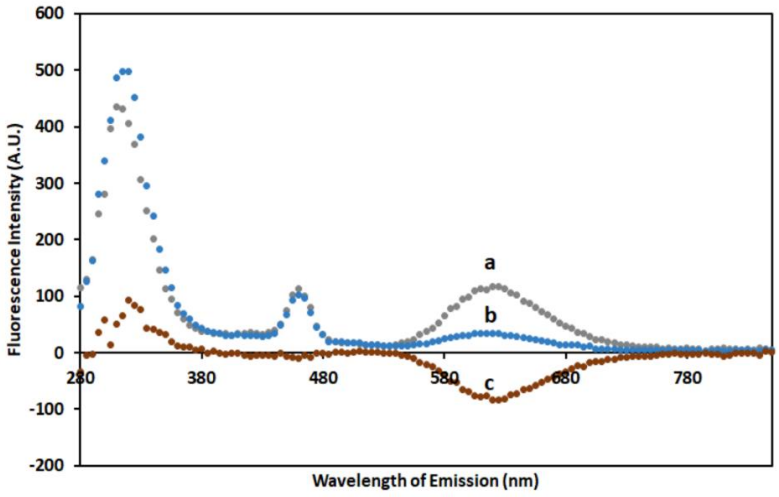

Figure 3.4.18. Emission fluorescence intensity spectra, after excitation at 230 nm of a) PU/NR, b) PU/citNa-AuNRs/NR and c) subtraction curve PU/citNa-AuNRs/NR - PU/NR.

The reduction of fluorescence could be the indication of an energy transfer between the dye and the particles, causing the excitation energy to dissipate in a different way compared to light emission.

3.4.3.5. Antimicrobial efficiency against E. coli

The films modified with the different molecules were tested against *E. coli* for exposure of 2 h at 11.7 klux to see how differences in their molecular structures influenced the activities of the film (details of this procedure are in section 4.3.5.).

The results of the films prepared with the different dyes were compared with the antimicrobial efficiency of PU alone, Figure 3.4.19.a; against the activity of PU and CV, Figure 3.4.19.b and finally against the activity of the film containing CV and AuNRs, Figure 3.4.19.c.

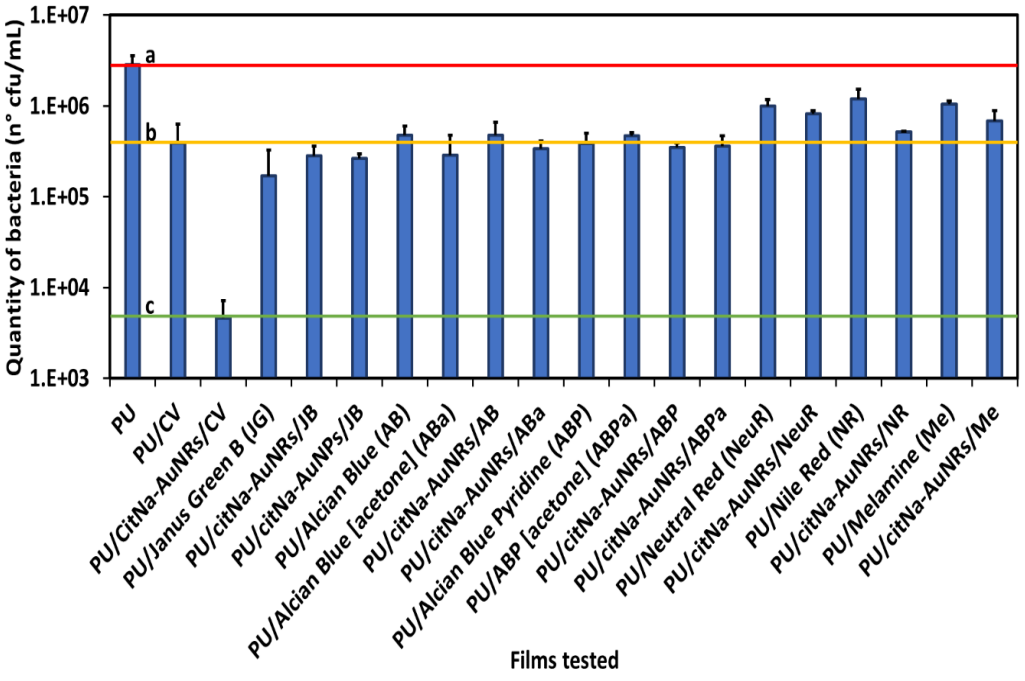

Figure 3.4.19. Results of the antimicrobial test against E. coli for 2 h of light exposure at 11.7 klux, a) antimicrobial activity of the unmodified polymer (PU), b) antimicrobial activity of the film modified with crystal violet (PU/CV) and c) antimicrobial activity of the film containing crystal violet and AuNRs (PU/citNa-AuNRs/CV).

The results of the activity of the films were organised according to their efficiency against *E. coli*. The least effective against *E. coli* were NeuR, NR and Me, these dyes had a lower activity than CV (0.5-log against 1-log) and only NR seemed able to produce a positive interaction with the AuNRs increasing the efficiency to 1-log, which was the same activity registered for CV alone.

The next group of films tested were as efficient as CV alone, but they did not manage to perform better than it. This category contained: AB and ABP. The efficiency of the films containing these dyes either when introduced by water or by acetone, was not affected by the presence of the AuNRs. Suggesting that the interaction between the two components did not produced an increase in the ROS production. AB introduced with acetone was partially more efficient than CV, but its efficiency decreased in presence of AuNRs, showing that the transfer of energy between the two components was detrimental to the ROS production process.

Finally, the samples containing JG showed better activity than CV alone but less activity than the couple CV-AuNRs. Also, when paired with AuNRs or AuNPs the activity film was slightly decreased. Suggesting that the interactions particles-dye were not leading to an increase of the generation of ROS.

3.4.3.6. Considerations on the dye selection

Between the molecules tested only Crystal Violet, Neutral Red and Nile Red had a defined fluorescence peaks and when interacting with all these substances the introduction of AuNRs caused a decrease in the fluorescence emission, demonstrating the existence of an energy transfer between dye and AuNRs (very weak for CV, section 3.4.3.4.1).

The other molecules tested were able to absorb light but not to emit fluorescence. Regardless of their fluorescence, all the molecules tested were capable to interact with the polymeric matrix and to change the way the film interacted with light.

Melamine increased the emission of the film at shorter wavelength especially in presence of AuNRs, while Alcian Blue and Alcian Blue Pyridine (acetone or water) did not influence the fluorescence of the polymer. Two exceptions to this trend were Alcian Blue and Janus Green B which in presence of AuNRs increased strongly the fluorescence of the dye at 300 nm.

Apart from the considerations connected to the interactions of the films with light, from these experiments was evident that the combination of CV and AuNRs was particularly efficient for the production of ROS. Being able to cause the greatest bacterial reduction than any other combination tried.

Molecules as Neutral Red and Nile Red, which absorbed at short wavelengths and emitted to longer wavelengths (close to the absorption of the second SPR peak of AuNRs) did not seemed capable to interact with the particles to generate ROS, in amounts comparable with CV, alone or with the particles.

Melamine or Melamine and AuNRs had very little activity on bacteria, mostly due to the toxicity of melamine. While Alcian Blue and Alcian Blue Pyridine had an overlapping absorption with AuNRs and a delocalized aromatic system, but their antimicrobial efficiency was limited with or without AuNRs.

A possible reason for their reduced activity may be the Cu(II) ion at the centre of these molecules, because heavy metal ions had an ambivalent action on ROS, either as promoters of their formation or quenchers depending on the situation. Another important factor in this case was that the interaction with the particles did not increase the activity of the film.

The limit of these interactions was particularly evident for films loaded from acetone. In this films was loaded a larger amount of dye than in the standard samples which in theory should have promoted a larger interaction with the particles, but instead it did not influence the activity of the film. An exception to the general trend was Janus Green B that had a partial efficiency by itself, but it lost its activity when interacting with AuNRs and AuNPs. Thus, showing that the energy transfer between the components was not the only factor influencing an increase in the ROS production.

3.4.4. *Diffusion of crystal violet in the film*

As discussed in the previous section (3.4.3) the dye chosen as standard for the antimicrobial film was CV, while the preferred method of dye introduction was the diffusion from a water solution (section 3.3.4). This method depended on the repartition coefficient of CV between water, in which it was poorly soluble, and the polymer in which the dye could diffuse more efficiently. This method had some limitations, it was time consuming and limited the amount of polymer prepared to 30 cm^2. For these reasons a series of experiments were devised to improve the efficiency of the procedure.

3.4.4.1. Selection of the solution used for the diffusion

In the attempt to improve the diffusion process, two different diffusion procedure were developed: one based on the exchange of CV from an aqueous solution and another realised using a mix of acetone and water (9:1), which were already tested on the nanoparticles or for the introduction of hydrophobic dyes (section 3.3.4).

3.4.4.1.1. Diffusion from water

The quality of the diffusion process depended strongly on a complete solubilization of CV in water, which for a solution 1 mM of CV, it was difficult to determine because the solution was too dark to spot partial solubilizations (Figure 3.4.20).

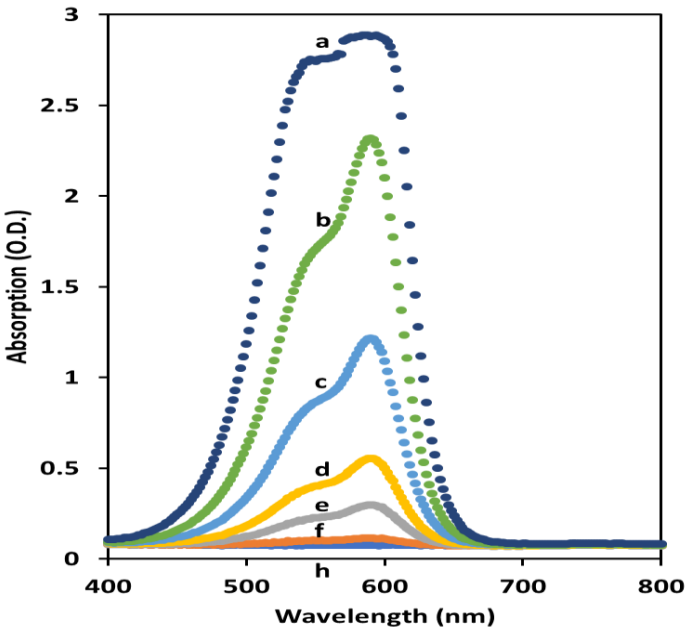

Figure 3.4.20. UV-visible absorption of CV solution of a) 100 µM, b) 50 µM, c) 25 µM, d) 10 µM, e) 5 µM, f) 1 µM and h) blank solution.

For very diluted solution (for concentrations above 25 µM CV has O.D. > 1, Figure 3.4.20.b & a) CV followed a linear progression between concentration and absorption ($y = 0.0424x + 0.0914$, calculated on the peak 590 nm, $R^2 = 0.9992$).

As evident from Figure 3.4.20, CV had a very intense light absorption which in aqueous solution was able to overcome the linearity range of a spectrophotometer for concentrations as low as 100 µM (2.99 O.D. of experimental results against 4.33 O.D. of theoretical absorption, Figure 3.4.20.a).

Moreover, in literature there is not agreement on the actual limit of solubility of CV, that has been reported to vary from 1 g/L (2.45 mM)[192] to 170 g/L (416 mM)[75] at 25°C. In my personal experience, using CV acquired from Sigma-Aldrich (reported in section 3.2) the solubility limit of CV was closer to 2.5 mM than 0.4 M.

As stated before, a poor CV solubilization reduced the reproducibility of the diffusion process, but in this regard, the main problem to the diffusion of the dye in the polymer was the inhomogeneity of the polymeric matrix. Some areas of the film had a greater density compared to the average, causing the dye to diffuse more slowly, causing the appearance of bubble-like areas in the polymer in which the dye had a fainter colour. On the point of view of the activity of the film, the inhomogeneity was not a great problem, because the surface of the film was saturated with the dye regardless of the local density inside the polymer.

3.4.4.1.2. Diffusion from acetone

The diffusion of CV in acetone was tested in order to speed up the preparation of the antimicrobial film and to improve the film reproducibility. This method was more efficient in diffusing the dye in the polymer causing the film prepared from 1 mM and 0.5 mM (Figure 3.4.21.a & b respectively) solutions to be too concentrated for UV-visible analysis (O.D. > 3.0).

At the same time, samples prepared using 0.25 mM and 125 µM and 62.5 µM solutions had intense but analysable absorptions (Figure 3.4.21.c, d & e). Comparing all the concentrations tested, only 62.5 µM was revealed to have a comparable absorption with the samples produced with the standard method, which was estimated to be approximatively 50 µM (Figure 3.4.21.e & f).

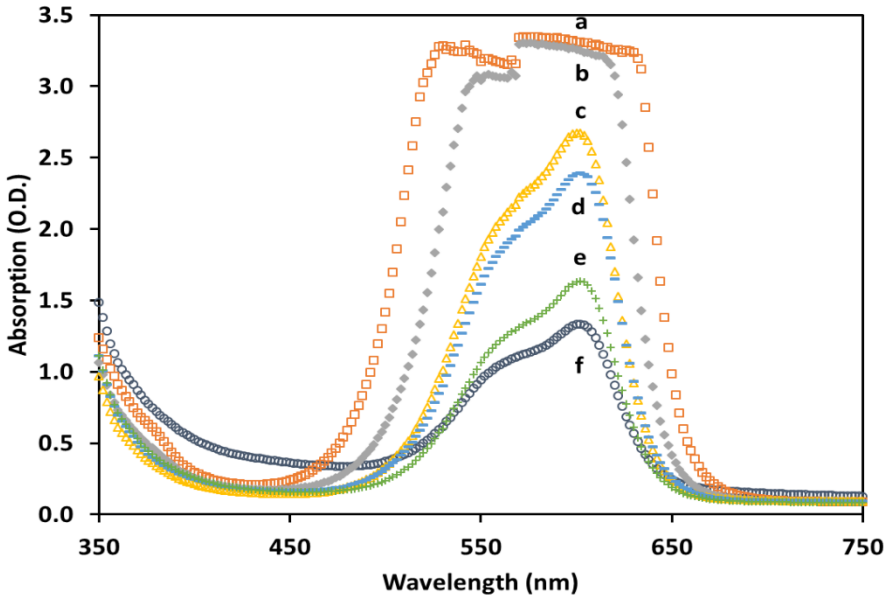

Figure 3.4.21. UV-visible absorption of the polymeric film prepared with the Ace method using acetone solutions of different concentrations: a) PU/citNa-AuNRs/CV 1 mM, b) PU/citNa-AuNRs/CV 0.5 mM, c) PU/citNa-AuNRs/CV 0.25 mM, d) PU/citNa-AuNRs/CV 0.125 mM, e) PU/citNa-AuNRs/CV 0.0625 mM, f) PU/citNa-AuNRs/CV 1 mM original method.

This method of diffusion was much faster than the diffusion from water being able to produce uniformly painted films after only an overnight incubation. But in order to determine if the time of incubation influenced the concentration of CV diffused in the polymer, the procedure was tested for 24 h and 48 h of incubation. No differences were detected between the samples.

3.4.4.1.3. Efficiency against E. coli of the films with different diffusion methods

As seen for the films prepared with different dyes (section 3.4.3) the definitive test of the quality of a modification procedure to prepare the film was the estimation of antimicrobial activity.

The antimicrobial activity of the films prepared with AuNRs, 1 mM and 50 µM of CV (Ace method) was tested against *E. coli* for 2 h exposure at 11.7 klux (method reported in section 4.3.5.). While films prepared with the standard method containing CV alone or containing CV and AuNRs were tested at the same time to have a term of comparison (Figure 3.4.22.c & d).

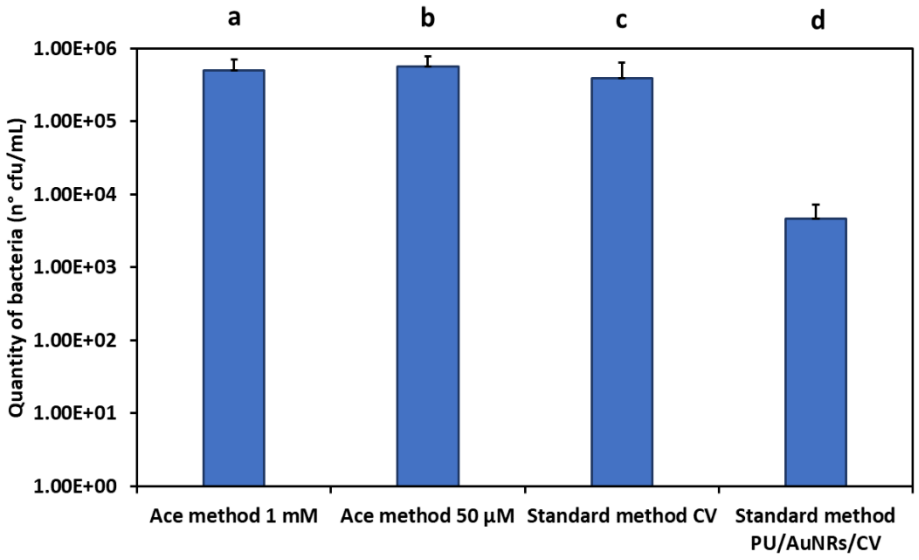

Figure 3.4.22. Activity of the film against E.coli for 2 h of light exposure at 11.7 klux after Ace process (a, b) compared to the standard method CV (c) and the PU/AuNRs/CV standard method (d).

From this experiments it is clear that the samples prepared with the either for 1 mM or 50 µM of CV (Ace method) showed an activity similar to the one of the film containing only CV introduced with the standard method (Figure 3.4.22.c; 1-log reduction after 2 h), while neither of them reached a

level of activity comparable with the film containing dye and particles (Figure 3.4.22.d).

A possible explanation for these results may be a consequence of the introduction of the particles and dye at the same time, being both charged and immersed in an organic solvent, their introduction could result in the formation of particles/dye aggregates. Thus, reducing on the amount of particles being trapped in the polymeric matrix. At the same time the increase of CV embedded in the films when prepared with the Ace method, did not correspond to an increase of activity (Figure 3.4.22.a & b) and furthermore, the presence of AuNRs did not influenced the activity of the film as much as it would have done in the film prepared with the standard method (Figure 3.4.22.d).

The reasons of this discrepancy are not completely clear but some considerations could be made to explain it: i) it could be possible that only the dye on the surface of the film was able to release ROS against the bacteria, if this condition was true introducing extra dye in the film with the Ace method would not increase to the antimicrobial activity, or ii) Increasing the amount of dye in the polymer could generate a phenomenon similar to auto-quenching where the ROS produced by one molecule of dye would be trapped by the other molecules nearby.

Regardless of the reasons causing this decrease of activity, the method of diffusion from water was proven to be more reliable in forming consistently active films thus, it was used for the rest of the work.

3.4.4.2. Estimation of the diffusion rate of crystal violet in water

As demonstrated previously (section 3.4.4.1.2), the CV diffusion method from water produced the most active films, but this method as it was described in literature required an incubation time of 72 h.[138] Thus, pushing the time consumed to fabricate a film sample to a total of 96 h plus drying times (≈ 100 – 104 h) which posed a serious limit on the number batches which could be prepared to support all the experiments.

In order to confirm the necessity for an incubation of 72 h and to find the timing most suitable for the film production, a series of polymer tiles were tested for UV-visible absorption after incubation in an aqueous solution of CV (15 mL, 1 mM) for time points from 15 mins to 90 h (Figure 3.4.23).

For the first 8 h, the dye diffusion in the polymer was very fast, causing the

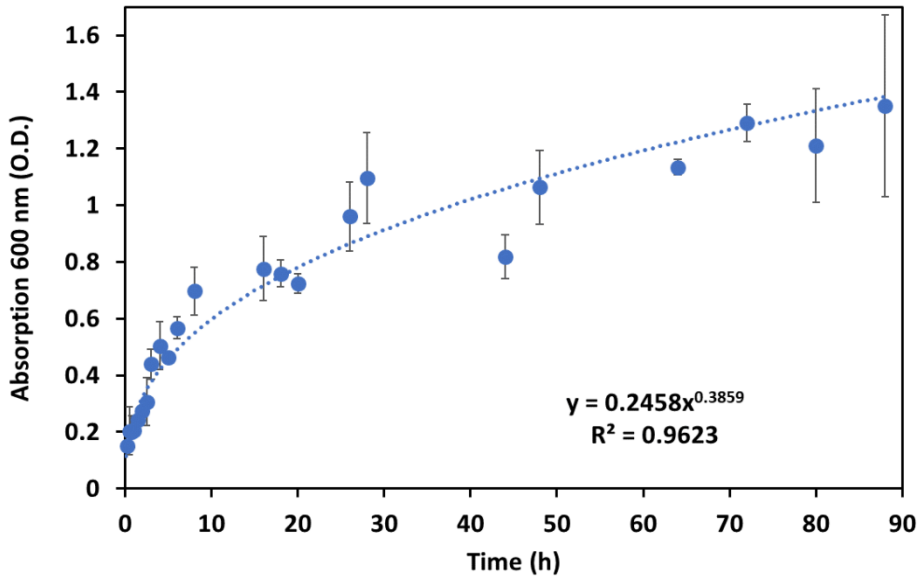

Figure 3.4.23. UV-visible absorption at 600 nm of polymeric tiles after different times of incubation in a solution of CV 1 mM (15 min to 90 h).

absorption of the dye in the polymer to increase linearly (y = 0.0701 x+ 0.1534, R^2 = 0.9564). After this linear phase, the dye diffusion slowed progressively to a pseudo-plateau. In this phase the absorption of the film

increased very slowly, the 48 h timepoint halfway in the pseudo-plateau range was chosen as endpoint of the incubation process and as the most suitable diffusion time for the film preparation.

3.4.4.3. Estimation of the amount of dye in the film

In the previous sections (3.4.4.1 and 3.4.4.2), the procedure for the dye diffusion in the polymer and the most suitable incubation time were established. The next step in the characterization of the film was to calculate the actual concentration of dye accumulated in the film.

But because this calculation was affected by numerous variables, some assumptions has been considered in order to obtain a definite result:

1) For diluted concentrations, the intensity of the peak of CV at 590 nm in solution and the peak at 600 nm in the film had the same dependence from the concentration.
2) The thickness of the polymer was exactly 1 mm (as indicated by the supplier).

With these points established and given the absorption of the PU/CV film at 600 nm of 1.552 O.D. the amount of dye in the polymer could be calculated using the equation for the absorption of a CV solution in water described in the section 3.4.4.1.1 ($Abs_{590\,nm} = 0.424x + 0.0914$).

Because the polymer was only 1 mm thick while the solutions used to calculate the equation had 10 mm of optical path, the absorption of the film was multiplied 10 times. Thus, simulating a film with the same thickness of the cuvette used to acquire the spectra of the solution (Equation 3.4.4 – 3.4.5).

$$Abs_{590\,nm} = 0.424x + 0.0914 = \quad (3.4.4)$$

$$Abs_{600} * 10\ of\ the\ dye\ in\ the\ film = 15.52 = 0.0424x + 0.0914 \rightarrow \frac{15.52-0.0914}{0.0424} = x = 344.5\ \mu M \quad (3.4.5)$$

Which corresponded to 0.12 g of CV per Kg of polymer or 141 g/m^3 (the density of PU is 1.175 kg/dm^3).

Comparing the dye concentration in the polymer with that in the diffusion solution, the efficiency of the process resulted to be of approximatively 34.5 %, thus lower than the calculated efficiency of the particles embedment in the polymer which reached the 60.4 % (section 3.4.2).

3.4.5. *Interactions between particles and CV*

In the previous sections (3.4.3 and 3.4.4) we discussed how the selection of the dye and the method used for its introduction in the film changed the antimicrobial activity of the system.

As introduced previously (sections 1.1.4.2 and 1.1.4.3), CV was able to produce ROS and when interacting with the particles to boost the antimicrobial activity of the film, but the nature of this interaction was not easy to determine.

A series of experiments either in solution or in the polymeric matrix were developed, to better understand the nature of the interaction between the dye and the nanoparticles (energy transfer, electron transfer or plasmonic coupling).[85,93,193]

3.4.5.1. UV-visible study of the interactions in solution

Mixed solutions of gold nanoparticles stabilized either with citNa or thiol-PEG-COOH and CV were tested for UV-visible absorption, similar testing was then produced for samples in the film (sections 2.3.5 and 3.3.1).

3.4.5.1.1. Interactions of gold nanorods with crystal violet in solution

CV interacted in a different way when mixed AuNRs stabilized with citNa (Figure 3.4.24.A.c) or thiol-PEG-COOH (Figure 3.4.24.B.f).

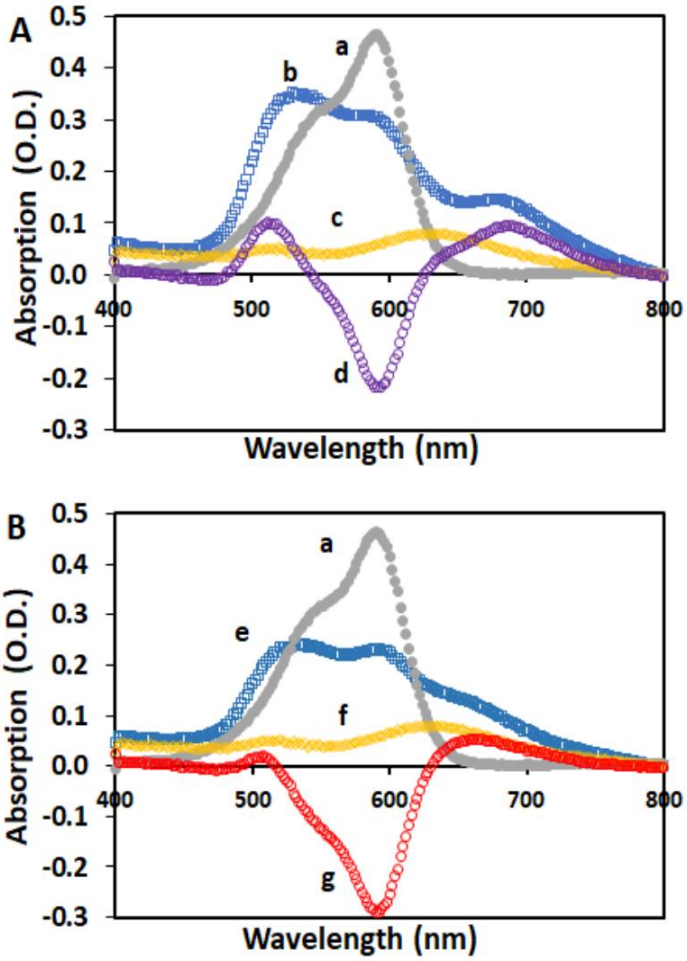

Figure 3.4.24. UV-Visible absorption spectra of CV 10 µM in presence of 20% of nanoparticles solution (≈ 34 µM) A) citNa-AuNRs and B) thiol-PEG-AuNRs. a) Spectra of CV 10 µM, b) citNa coated AuNRs in presence of 10 µM of CV, c) spectra of ≈ 34 µM of citNa-AuNRs, d) subtraction curve [b-(a+c)] difference of absorption between the mixed solution and the sum of the components; e) thiol-PEG coated AuNRs in presence of 10 µM, f) spectra of ≈ 34 µM of thiol-PEG-AuNRs solution, g) subtraction curve [e-(a+f)] difference of absorption between the mixed solution and the sum of the components.

In order to study the differences between the interactions, the mixed solutions were compared against their components Figure 3.4.24 (d & g). The differences between the thickness and the charge of the barrier formed by the two capping agents used to stabilize the gold nanoparticles changed

the interactions between AuNRs and dye and consequently caused changes in the absorption profile of the two mixed samples.

The CV molecules are positively charged and possessed a main signature peak at 590 nm accompanied by a shoulder peak at 540 nm (Figure 3.4.24.A & B, a). When mixed with AuNRs, a significant peak at 520 nm was observed for the citNa-coated AuNRs (Figure 3.4.24.A.b), and a similar, but less intense, for the thiol-PEG-COOH coated one (Figure 3.4.24.B.e). These peaks could be seen in the spectra of the mixed solution and from subtraction of the spectra of 10 µM CV and 34 µM nanorods solutions (Figure 3.4.24.A & B, d & g respectively).

Since the citNa coating was composed of a thin layer of small molecules, the strong electrostatic interaction between CV and citNa allowed the dye molecules to come close enough to the AuNRs surface. Thus, improving the coupling effect between the SPR of the particles and the dye resulting in the enhancement of the peak at 520 nm.[87,93,188]

Both spectra of the mixed solutions containing AuNRs either coated with citNa or thiol-PEG showed a strong reduction of the CV peak at 590 nm wavelength, suggesting the presence of a strong plasmonic and electronic interaction between the dye and the nanorods.

Another clue of the CV-AuNRs interactions, especially in the case of citNa-AuNRs, was the increase of absorption in the range between 660 and 700 nm showing that in solution AuNRs aggregate in presence of CV molecules. This aggregation was more evident for citNa coated AuNRs than thiol-PEG coated AuNRs. Probably caused by the positive charge of CV interacting

with the particles and neutralizing their surface charge. Thus, removing the electrostatic protection of the citNa coating.

3.4.5.1.2. Interactions of gold nanostars with crystal violet in solution

As seen for AuNRs, the interactions of AuNSs and CV were tested for particles stabilized with citNa and thiol-PEG. On AuNSs, the difference in stabilization caused a great change in the absorption profile of the mixed

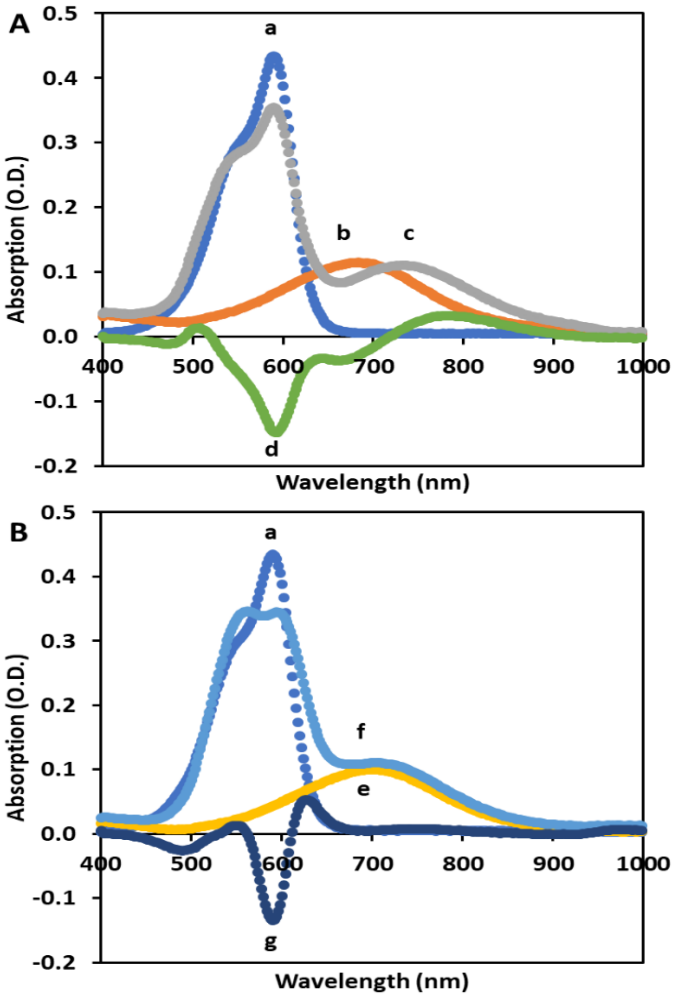

Figure 3.4.25. UV-Visible absorption spectra of CV 10 µM in presence of 20% of nanoparticles solution (≈ 34 µM) A) citNa-AuNSs and B) thiol-PEG-AuNSs. a) Spectra of CV 10 µM, b) spectra of ≈ 34 µM of citNa-AuNSs, c) citNa coated AuNSs in presence of 10 µM of CV, d) subtraction curve [c-(a+b)] difference of absorption between the mixed solution and the sum of the components; e) spectra of ≈ 34 µM of thiol-PEG-AuNRs solution, f) thiol-PEG coated AuNRs in presence of 10 µM, g) subtraction curve [f-(a+e)] difference of absorption between the mixed solution and the sum of the components.

solution. In Figure 3.4.25.A.c the spectrum of the nanostars stabilized with citNa and in Figure 3.4.25.B.f the spectrum of nanostars stabilized with thiol-PEG.

As for the previous chapter subtraction curves of the absorption spectra of the mix solution minus their components were reported in Figure 3.4.25.A.d for citNa and Figure 3.4.25.B.g for thiol-PEG-COOH. The effect of the different stabilization was more evident for this type of particles than for AuNRs not only for its effect on the spectra of the particles (Figure 3.4.25.b & e), but also for the presence and position of the particles peak after mixing with the dye solution.

Before mixing dye and particles, citNa-AuNSs had a broad absorption at 690 nm while thiol-PEG-AuNSs was centred at 700 nm, after mixing with CV the peak of citNa-AuNSs shifted to 742 nm while the peak of thiol-PEG-AuNSs shifted to 712 nm. For both the stabilizations the original peak of AuNSs was clearly evident in the mixed solutions.

The red shift of their peak, which usually indicated an aggregation, in this case could be a sign of the formation of dimers and interconnected structures. Because the peak of the particles did not lose intensity after the introduction of CV and it did not increase in width, both signs of aggregation.

The changes in the CV spectra were also interesting (Figure 3.4.25.A & B.a). The solution mixed with citNa-AuNSs had a small reduction of the main peak at 590 nm and a small increase of the absorption at 520 nm, particularly evident in the subtraction curve (Figure 3.4.25.A.d).

The interaction with thiol-PEG-AuNSs on the other hand changed completely the ratio between the two peaks of CV (540 and 590 nm) rising 540 nm and lowering 590 nm (shifted to 600 nm) levelling to almost the same intensity. This type of change in the dye spectra was reported in literature as typical of the dimeric form of CV, which could appear in solution for concentrations above 0.5 mM, 50 times the concentration used (10 µM).[194]

This effect on the local concentration of the dye was probably caused by the difference in polarity between thiol-PEG-COOH and the aqueous solution, which pushed the dye to diffuse in the organic layer formed by thiol-PEG-COOH on the surface of the particles.

3.4.5.2. UV-visible study of the interactions in the film

After the diffusion in the film, CV maintained a similar absorption profile as in solution with two intense peaks partially overlapping (Figure 3.4.26, curves a & b, respectively).

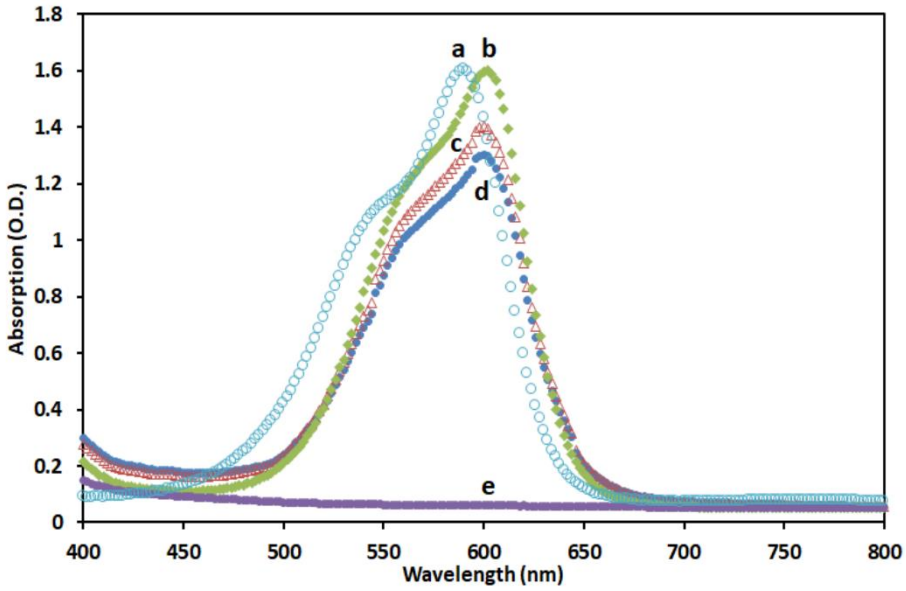

Figure 3.4.26. UV-visible spectra of a) 34 µM CV solution in water, b) 1 mM CV diffused in PU for 48 h (PU/CV film), c) PU/citNa-AuNSs/CV film, d) PU/citNa-AuNRs/CV film and e) PU alone.

But when the dye was introduced in the film the two peaks of the CV were red-shifted by 14 nm and the ratio between their intensities changed from 1.46 (590/540 nm, in solution) to 1.28 (604/554 nm in polymer).

The changes in the spectrum of CV depended on the change in environment surrounding the dye molecules. From being surrounded by a polar media (water) to non-polar in solid state (film) (Figure 3.4.26.a & b). Furthermore, the spectrum of CV diffused in a film containing metal nanoparticles was slightly different to the spectrum of the dye alone (Figure 3.4.26, curves c & d).

Specifically, the intensities of the absorption peaks were reduced to certain degree depending on the type of particles; while the position of the peaks was red-shifted for about 12 nm compared to the dye in water and blue-shifted for about 2 nm compared to the dye alone in PU film, regardless the type of particles embedded.

In the presence of AuNRs the absorption peaks of CV decreased in intensity by the 19% (Figure 3.4.26.d) while at the same time the plasmonic coupling between the AuNRs and the dye increased the absorption at shorter wavelength. On the other hand, the presence of AuNSs in the film reduced the peaks of CV by 7% and increased the absorption at shorter wavelength to a lesser amount compared to the AuNRs (Figure 3.4.26.c.). At the same time, the presence of AuNSs caused an increase of absorption between 640 and 660 nm.

The changes in the absorption spectra of the film containing particles and dye in comparison to the sum of the components seen in this experiments

showcased how the plasmonic coupling between the components of the film modify the energy absorption of the system.[87]

3.4.6. *ROS production and quantification*

The detection of ROS was a challenging endeavour, because these types of molecules were very reactive, short lived and after reacting, they were converted to water and oxygen. For example, H_2O_2 which has been used as control for some of the experiments in this chapter, after reacting with organic molecules was converted in H_2O and O_2.

At the same time, the standard methods used to detect ROS in literature were mostly developed to detect the generation of ROS in presence of live bacteria. For example, one of the most common fluorescent probe for ROS, fluorescein diacetate required to interact with the enzyme esterase in living cells in order to remove their terminal acetate groups and become fluorescent.[195]

The last and more important obstacle encountered in this thesis in selection of a commercially available ROS detection probe was the light used to activate the film, which was able to decompose many of the radical scavenger or fluorescence probes.[196]

The three methods tested in this chapter have been developed to try to overcome these problems. The first was used as proof of concept of the relation between film activity and the presence of oxidizers (as ROS) in the media exposed to it. This method was tested adding to the bacteria dispersion a certain amount of L-ascorbic acid (details in section 3.3.6.1). This molecule was a reducing agent able to quench the ROS in solution, causing the bacteria to survive the antimicrobial test (details in section

4.3.5). The second test was focused on using methylene blue to detect the presence of O_2^- in solution throughout the change of colour of the solution (details in section 3.3.6.2). The last method used the quenching of sodium fluorescein, as indicator for the presence of ROS and used comparable amounts of H_2O_2 to confirm the results (section 3.3.6.3).[197–199]

3.4.6.1. L-ascorbic acid test of radical inhibition

The first of the methods used to establish the correlation between production of ROS and antimicrobial activity was to measure the reduction of antimicrobial activity of the film in presence of L-ascorbic acid, which was a weak reducing agent and a radical scavenger.[200]

L-ascorbic acid is an organic molecule found in many biological systems and frequently found in many complex organisms and bacteria.[201] For this reason, it was safe to add to the saline solution used to transfer the bacteria (*E. coli*), from the growth plate to the film, without damaging them or reducing their vitality (the procedures used for the bacteria propagation and testing are reported in sections 4.3.3 and 4.3.5).

To preserve the vitality of the bacteria and to obtain the best radical scavenging activity from L-ascorbic acid, the pH of the solution was set to 7.4.

According to literature, this pH matched the best conditions for growing *E. coli* and to boost the scavenging potential of L-ascorbic acid.[202] Thus, creating the perfect conditions for the ROS produced by the film to be quenched and neutralized as soon they were created, while at the same time, preserving the vitality of the bacteria tested.

The experiment with L-ascorbic acid resulted in reduction of activity of the film against *E. coli* of 15 times, thus showcasing the connection between the presence of ROS and the activity of the film.

This test had as some limitations: i) the actual pH control of the L-ascorbic acid solution was very poor, because this acid is a polyprotic molecule and the live bacteria were able to change the pH with their metabolic processes. ii) L-ascorbic acid could be decomposed by the exposure to light, especially in a solution containing live bacteria. The bacteria could introduce in the media unexpected ions which would trigger the decomposition (e.g. Fe^{3+}, Cu^{+2}, etc.). iii) Furthermore, the set up required some contact between the solution and the biosafety hood environment which would expose the solution of chemical contaminants, triggering the decomposition.

All these factors considered, the reduction of the activity of the film in presence of a reducing agent with radical quenching ability it was a clear proof of concept that oxidizing molecules as ROS had a role in the antimicrobial activity of the film, but unfortunately this method was not sensitive enough to determine the amount of ROS formed by the film.

3.4.6.2. Methylene blue oxidizing species detection

The second method used to identify the presence of reactive species was the use of methylene blue (MB) as redox indicator (section 3.3.6.2). If MB is exposed to a reducing agent in alkaline environment, its colour changes from blue to transparent.[203] While in presence of a strong oxidizers, as the ROS, it reverts to dark blue (Figure 3.4.27).

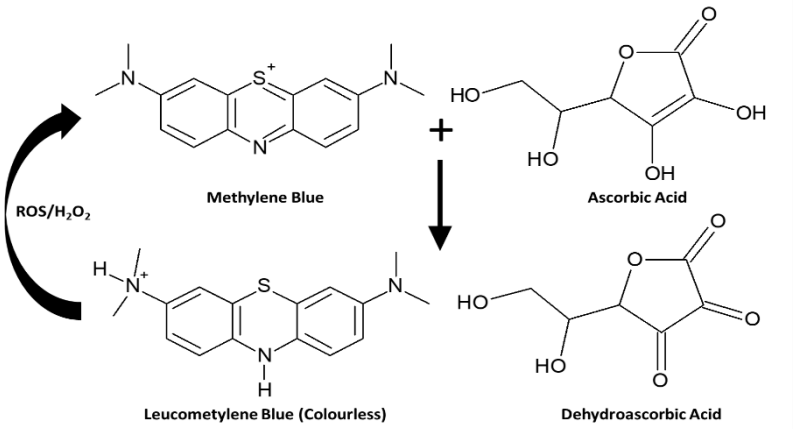

Figure 3.4.27. Scheme of the methylene blue / ascorbic acid reaction and of the effect of ROS produced by the film or by H_2O_2 on the reduced form of methylene blue.

In this experiment, a solution of methylene blue in water was reduced with L-ascorbic acid in basics conditions (quantities in section 3.3.6.2) and then exposed to light on the surface of the film for 1 h. At the end of the exposure its absorption was measured.

If the film was able to produce oxidizing species the effect of the ascorbic acid would be neutralised, and the MB in solution would turn from colourless to dark blue.

To test the sensitivity of the analytical procedure and to establish a calibration curve for this method the absorption spectra of the MB solution was tested after adding increasing aliquots of H_2O_2 from 0.001 mM to 100 mM (Figure 3.4.28).

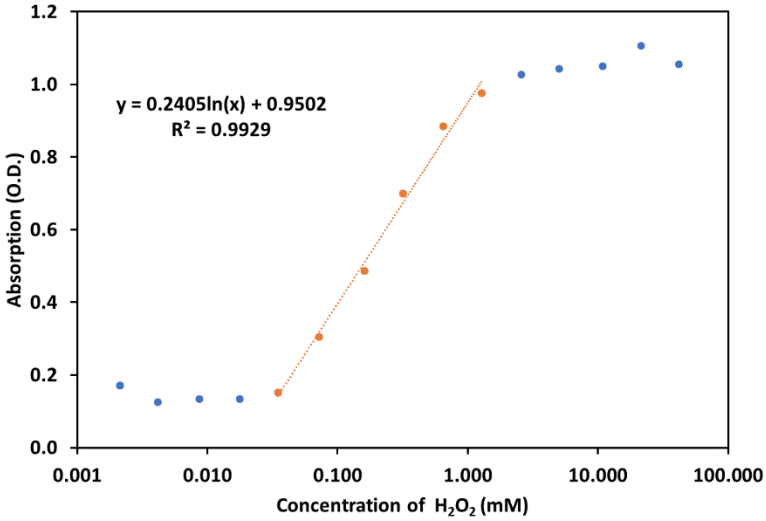

Figure 3.4.28. Absorption at 664 nm of a solution of methylene blue reduced with L-ascorbic acid, after adding increasing aliquots of H_2O_2.

The concentration of H_2O_2 in Figure 3.4.28 was reported in logarithmic scale and it showed that the reproducible range of the light absorption recovery was between 35 µM and 1.27 mM of H_2O_2.

When tested on the film, this method did not produce significative results. Because, when exposed to oxygen, the reduced form of methylene blue was able to recover its colour. In the controls, this reaction did not cause any problems, because the reaction between MB and H_2O_2 was quick and performed directly in the plate used for the analysis. On the other hand, for samples analysed after light exposure on the film (and subjected to a transfer between the film and the plate well) the colour recovery was large enough to hide the recovery caused by the ROS production of the film. For this reason, the method was abandoned.

This experiment demonstrated that the film, was not able to produce a large amount of the O_2^- radical, because it was one of the main decomposition products of H_2O_2 and would have caused a defined turn of the MB solution to dark blue. On the other hand, radicals as for example $HO^{\cdot}$ or $NO^{\cdot}$ reacted more slowly with MB and their effect could be overwhelmed by the action of molecular oxygen.

3.4.6.3. Reactive oxygen species detection by fluorescein quenching assay

The third and last method used to demonstrate the production of ROS and their amount was the most successful (details in section 3.3.6.3). It exploited two properties of sodium fluorescein: i) of having a reproducible fluorescence quenching when exposed to light and ii) to quickly reduce its fluorescence intensity when exposed to radicals, which were able to convert fluorescein to the oxidized form (Figure 3.4.29).[197–199]

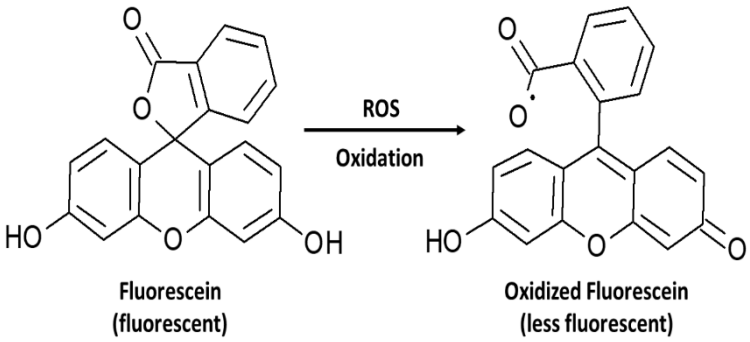

Figure 3.4.29. Process of oxidation of fluorescein when exposed to ROS.

The quenching of the florescence emission intensity of fluorescein when exposed to light, had a constant rate in time and was reproducible. Thus, it was assumed that the differences in fluorescence detected between two aliquots of the same solution exposed to light on a polyurethane (PU) tile

and on a sample of the antimicrobial film, could only be attributed to the activity of the film.[204]

To obtain quantitative information from the decrease of fluorescence of the Fluo solution, we had to assume that the reaction between fluorescein and ROS required a ratio 1:1 and that the process could not be reversed.

In this condition the relation between fluorescence bleaching and concentration of quencher (ROS) was defined from the Stern-Volmer equation (Equation 3.4.6).[205] Additionally, fluorescence readings on the solutions were acquired after 1 h of light exposure, in order to detect the ROS production per h.

$$\frac{I_0}{I} = 1 + \tau_0 k_q [Q] \qquad (3.4.6)$$

The Stern-Volmer equation was comprised of two terms: I_0/I which is the ratio between the fluorescence intensity of the solution exposed to light on unmodified PU (I_0) on the fluorescence intensity of the solution exposed on the film tested (I), and the second term $1+\tau_0 k_q[Q]$.

In the second term τ_0 was the fluorescence decay rate at 25 °C in absence of a quencher (3.6 ns) and k_q was the constant of quenching at 25 °C for a process involving only two molecules (fluorescein and ROS) while [Q] was the concentration of the quencher causing the reduction in fluorescence.[205]

According to this equation, a film containing only CV was able to generate 3.03 ± 0.60 mM of ROS for hour of exposure to light. While, in the presence of AuNRs, this value increased to 5.24 ± 0.02 mM (PU/citNa-AuNRs/CV), and it reached 5.92 ± 0.26 mM for a film containing AuNSs (PU/citNa-AuNSs/CV).

The Stern-Volmer equation could be applied to any fluorescent system in presence of a quenching agent. To confirm that the changes in fluorescence intensity were caused by the reaction with ROS and not to some other process, the results of the Stern-Volmer equation were compared with the results obtained by a calibration curve. This curve was obtained by adding to the solution exposed to light (for 1 h of exposure), different concentrations of H_2O_2 (12.5 mM, 10 mM, 7.5 mM, 5 mM, 1 mM) and measuring their fluorescence quenching efficiency (Figure 3.4.30).

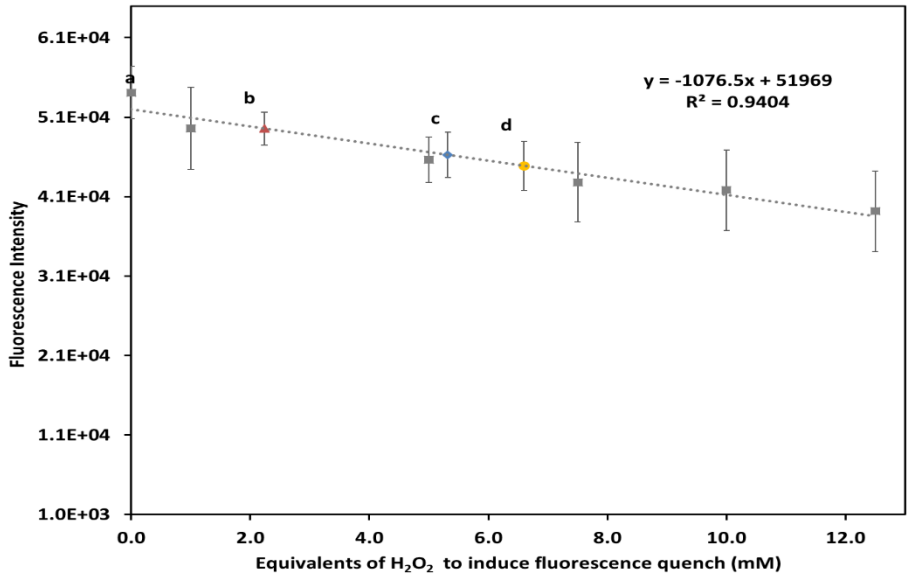

Figure 3.4.30. Fluorescence intensity against the estimated concentration of ROS by measuring the intensity of sodium fluorescein solution in the presence of different concentration of a) H_2O_2, b) PU/CV, c) PU/citNa-AuNRs/CV, d) PU/citNa-AuNSs/CV.

In the conditions used for the experiments H_2O_2 was able to interact with organic molecules and metal ions, to generate ROS (e.g. ·OH or ·OOH).[206] But in the alkaline condition used in the experiment, H_2O_2 was relatively stable and interacted only with the activated state of the fluorescein converting it to the oxidized form (which possessed reduced fluorescence intensity), similarly as the ROS generated by the film would do.[207]

But inside the fluorescence analysis plate, there were no transition metal ions or UV light sources to catalyses the formation of ROS from H_2O_2, which reduced the reaction speed between the two molecules. For this reason, the fluorescence analyses of these samples were acquired twice: one just after adding H_2O_2 and the other after overnight incubation. Thus, measuring the fluorescence of the solution after the reaction reached completion.[196]

The concentration of ROS produced by the films either according to the Stern-Volmer equation or the calibration curve (Figure 3.4.30) were comparable: PU/CV 2.24 ± 1.93 mM (Figure 3.4.30.b), PU/citNa-AuNRs/CV 5.32 ± 2.65 mM (Figure 3.4.30.c) and PU/citNa-AuNSs/CV 6.60 ± 2.87 mM (Figure 3.4.30.d).

The values obtained through the calibration curve (Figure 3.4.30.a), were comparable with the results of the Stern-Volmer equation, but they had a greater variability compared to the results calculated using the equation. This was due to the accumulation of the errors on the points of the calibration curve with the error on the fluorescent intensity of the samples.

Independently from the method used to calculate the amount of ROS generated by the film, the film samples containing anisotropic gold nanoparticles and dye showed a greater ROS production than the samples modified only with CV. While on the other hand, both methods used to estimate the concentration of ROS produced by the film, indicated that the films modified with AuNSs were able to produce the largest amount of ROS.

Increasing the ROS production of 0.72 mM or 1.28 mM depending on the method of estimation used, if compared to the film modified with AUNRs. The reason why, the plasmonic coupling between the spectra of CV and AuNSs was able to produce a larger amount of ROS compared to the couple AuNRs/CV was a consequence of the components of the SPR spectra involved in the overlapping (Figure 3.4.31).

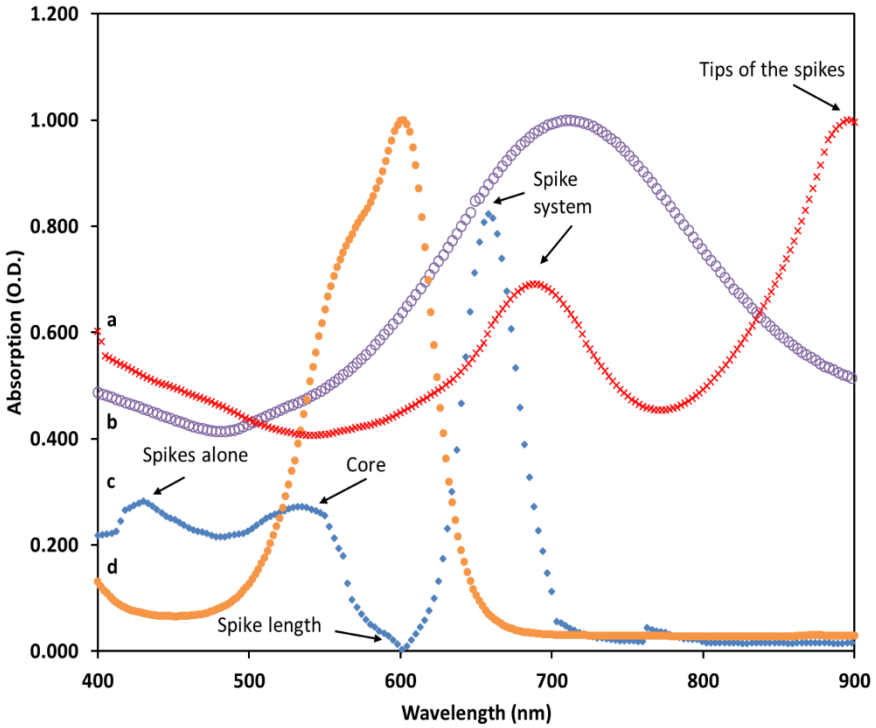

Figure 3.4.31. Comparison between the absorption peaks of a) simulation of AuNSs with the average dimensions calculated by TEM images, b) UV-visible absorption of AuNSs, c) simulation of AuNSs with ratio between the size of core and spikes (5:1) and d) absorption spectra of crystal violet diffused in the polymer.

According to the simulations (previously discussed in section 2.4.6) three of the SPR components of AuNSs overlapped with the dye: i) the resonance of the core (Figure 3.4.31.c), ii) the resonance of the spikes along their length, both overlapping completely with the dye absorption (Figure 3.4.31.c) and iii) the resonance of the spike system which overlap partially (Figure 3.4.31.a & c).

On the other hand, the spectra of AuNRs had a strong absorption peak very near to the main peak of CV (Figure 3.4.32.a & b) but at the same time they only possessed two partial overlapping, which caused a reduction of efficiency of their plasmonic coupling with the dye (Figure 3.4.32).

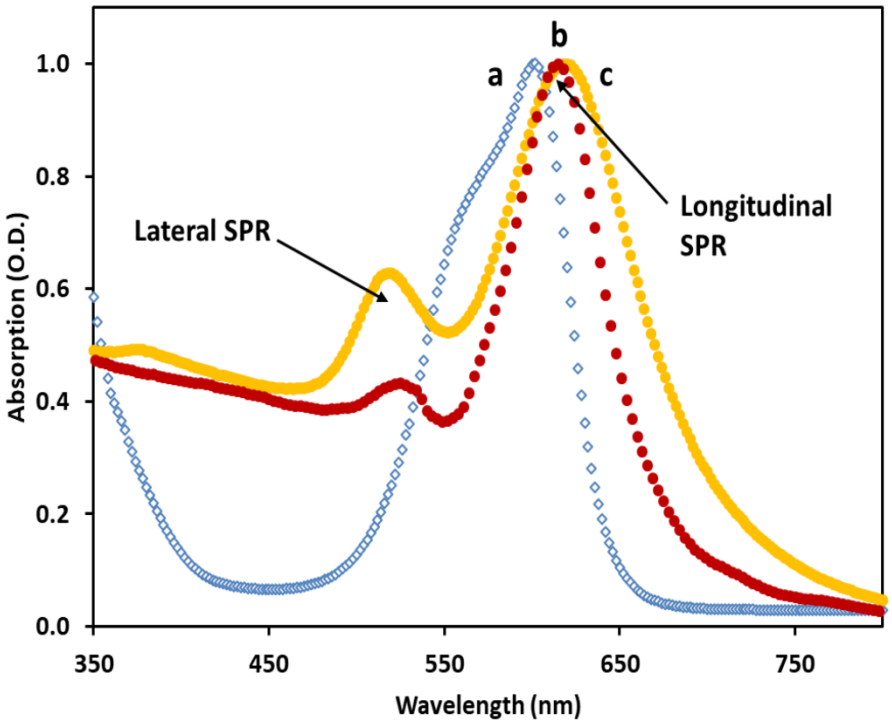

Figure 3.4.32. Comparison between the absorption peaks of a) crystal violet embedded in the polymer, b) absorption of AuNRs solution and c) simulated absorption of AuNRs (with the dimensions obtained from TEM images).

3.5. Conclusion

In this chapter different aspects of the film preparation were studied. The presence of the particles in the polymer was confirmed with UV-visible (section 3.4.2), which was used to calculate the amount of the AuNRs embedded in the polymer and the efficiency of the encapsulation process (section 3.4.2.2).

In the following section, a series of different dyes were studied as possible substitute for CV in the antimicrobial film (section 3.4.3). Spectral analysis

of the films with or without AuNRs have been performed to study their behaviour in the films and their interaction with the AuNRs (sections 3.4.3.3 and 3.4.3.4).

The molecules tested showed a general tendency to interact with the particles and transfer energy with them, but could not produce comparable antimicrobial effects to the combination CV/citNa-AuNRs/PU (section 3.4.3.5). These experiments, confirmed the theory that to trigger the antimicrobial effect was necessary an actual plasmonic coupling between two components not a simple energy transfer, which would more likely results in the release of energy in different ways than the production of ROS (section 3.4.3.6).[208]

Two methods to introduce the dye inside the film have been tested: one based on the diffusion from water and the other from acetone (section 3.4.4). The diffusion from acetone was more efficient but generated films less active against *E. coli*. Thus, the method was abandoned.

The next step in the film characterization was the study of the interactions between gold nanoparticles and CV either in solution or in the polymeric film (sections 3.4.5) and the study of the effect of the plasmonic coupling on the light absorption of the couple CV-AuNPs.

Finally, the ROS production of the film produced was studied, testing different methods to detect ROS (section 3.4.6). These methods were able to demonstrate the relation between the film activity and the presence of oxidizers and the difference of activity of the film modified with different particles.

Chapter 4: Antimicrobial characterization and film efficiency

4.1. Introduction

The preparation of an antimicrobial film described in this thesis was a complex endeavour in which many different components had to be carefully tuned and it required an extensive study and characterization.

The path leading to the film preparation was initiated in the second chapter with the synthesis of gold nanoparticles (sections 2.3.1 - 2.3.3 and 2.4.1 - 2.4.3) and their characterization (sections 2.3.4 - 2.3.7 and 2.4.4 - 2.4.6) to continue with their embedding in the film (sections 3.3.2, 3.3.3, 3.4.2 and 3.4.3) and to the selection of the PS dye (sections 3.3.5 and 3.4.3) and of its diffusion in the film (sections 3.3.4 and 3.4.4). Thus studying the interactions between particles and dye in solution and in the film (section 3.4.5) and finally, to characterize the ROS production of the films (sections 3.3.6 and 3.4.6).

But for all the preliminary characterization of the film and its components, the film behaviour against *E. coli* and *S. aureus* involved too many variables (as seen previously in this work for the experiments with different dyes (section 3.4.3.5) and the experiments to measure the activity of the film after diffusing the dye from water or acetone solution (section 3.4.4.1.3) to be correctly predicted without correlating the theoretical considerations with an extensive study of the experimental results of the antimicrobial action of the different films.

As for all the microbiological experiments, the reproducibility of the results was directly connected to the operator's ability to comply to established

procedure. Thus, reducing the opportunity of contaminations and errors. The amount of errors was still substantial, because the film activity depended on many components for its action and the tests against fresh and mutating bacteria introduced a certain degree of unpredictability to the results.

The variations to the experimental set up and the analysis of the parameters influencing the action of the films and the strategies used to minimize their influence on the results are reported in section 4.4.1, while the microbiological differences between Gram(+) and Gram(-) bacteria and their defences against ROS were discussed in section 4.4.3 and finally the results of the antimicrobial films against Gram(-) and Gram(+) bacteria were discussed and analysed in section 4.4.3.

4.2. Materials

The experiments in this chapter used all the reagents listed in sections 2.2 and 3.2. While for the biological experiments were also used: tryptone soya agar (TSA, Casein soya bean digest agar) EP/USP/JP/BP CM0131 from Oxoid ltd and sodium chloride (NaCl, ≥ 99%) from Sigma Aldrich.

4.3. Methods

4.3.1. *Bacteria culture*

The antimicrobial experiments in this thesis were performed against ATCC6538 *S. aureus* as model of Gram(+) bacteria and ATCC25922 *E. coli* as model of Gram(-) previously introduced in sections 1.1.7.1 and 1.1.8.1.

A small quantity of it was collected with a sterile laboratory swab and used to inoculate a TSA plate, the plate media was also used as a base for the freezing media and very rich in nutrients. Thus, it helped the bacteria to

recover from the shock caused by the thawing. The plate was incubated for 24 h in a Red Line Binder incubator at 35 – 37 °C, with controlled humidity. After the incubation, few colonies from it were collected and redispersed in NaCl 0.85 %. The resulting dispersion was used to inoculate a nutrient agar (NA) plate. 24 h after the colonies on the NA plate were collected and used to prepare the stock dispersions used for the antimicrobial experiments. The NA used in this work had the following composition: Lab-Lemco powder (meat extract) 1 g/L, yeast extract 2 g/L, peptone 5 g/L, NaCl 5 g/L, agar 15 g/L; pH 7.4 ± 0.2 @ 25 °C, this type of agar gel was rich of nutrient, cheap and suitable to grow both *E. coli* and *S. aureus*. Thus, it was used for most of the microbiological procedures.

4.3.2. *Quantification of bacteria in solution*

The concentration of bacteria dispersed in NaCl 0.85% was quantified measuring the O.D. value at 600 nm with a UV-visible spectrophotometer (introduced in section 2.3.5). This method only measures the scattering of the solution which reduced the absorption at 600 nm, this method could give reliable results only for 0.25 O.D. reduction of light intensity, which corresponded to a dispersion containing 10^8 cells/mL. Other concentrations were obtained by dilution of this stock.

4.3.3. *Bacteria propagation*

Bacteria growing on a NA plate, inside an incubator (section 4.3.1), grew fast and quickly exhausted the nutrient on the plate. Bacteria grown with limited supplies of nutrients tended to produce mutations in order to keep reproducing.

To have reproducible antimicrobial data, the bacteria used for the experiment (section 4.3.5) have to be from a fresh stock propagated less 24 h before. To propagate bacteria, two colonies from a previous plate were collected with an inoculating hoop and dispersed in 2 mL of autoclaved saline solution (NaCl 0.85%).

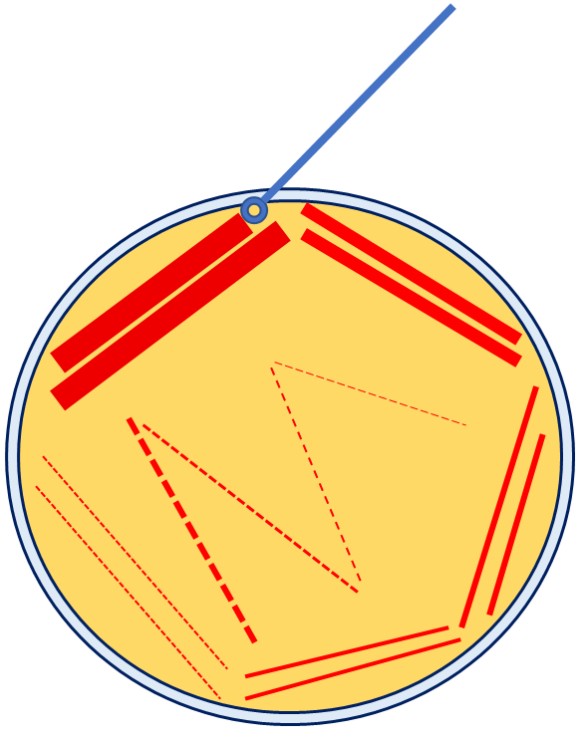

Figure 4.3.1. Schematic picture of the inoculation method for plates, from higher concentration thick red lines to lower concentrations thin dotted lines.

A drop of the resulting dispersion was collected with a loop and spread on the NA plate flat for the first two lines (thick red lines), than sideways all around the sides of the plate and finally the leftovers of the dispersion were spread flat in the centre of the plate (Figure 4.3.1). Plates between the 1st and the 4th propagation were consider optimal for the antimicrobial experiments.

4.3.4. *Plate counting method*

As stated in the section 4.3.2 the concentration of bacteria (both live and dead) in solution could be measured directly only for a solution containing 10^8 bacteria per mL, but the spectrophotometric analysis could not distinguish between dead and alive bacteria.

To determine the quantity of vital bacteria in a solution, an aliquot of bacteria dispersion was diluted to a serial dilution (1/10, 1/100, 1/1000) then used for inoculating NA plates. When inoculated on a plate the isolated bacteria generated new colonies that could be counted after overnight growth.

For example, the majority of the antimicrobial tests in this thesis were performed starting from 25 µL of a solution containing 10^6 bacteria/mL (5 x 10^4 max cfu). After the experiment the bacteria solution was redispersed in 2 mL (1.25 x 10^4 max cfu/mL) and 1 mL of this solution was used to inoculate a plate, max cfu on the plate 1.25 x 10^4, other plates could be inoculated with 100 µL of the solution 1.25 x 10^3 max cfu (1/10x) and finally some plates were inoculated with 100 µL of a solution 10 times diluted (1/100x) for a max of cfu of 1.25 x 10^2.

Depending on the type of experiment some of the plates will be too crowded to measure (>300 bacteria per plate) or the population in the plate will be too small (<30). For this reason, a certain number of repetitions were required to obtain statistically relevant results out of this method (6-12 different experiments per sample). As consequence of the scale of the bacteria population was that in order to obtain relevant data was necessary to have a good estimation of the order of magnitude expected so to plan the range of dilution to be plated.

The distribution of the bacteria on the plate played a great role on the reproducibility of the technique. To improve reproducibility an aliquot of bacteria solution between 0.1 to 1 mL was poured on a plate using a 1 mL pipette and spread using a lazy-L cell spreader and a rotating support.

A uniform spreading of the bacteria avoided the formation of clusters with overlapped bacterial colonies while leaving some space between the colonies. If well spread, the colonies would be able to feed uniformly. Thus, being able to grow all of the same size and shape.

After the inoculation, plates required some time to lose the excess of moisture, this was obtained by leaving the plates in the flow of air in the bio safety cabinet until dried. For plates inoculated with 1 mL this process could require more than half of an hour. This passage was important, because the moisture from a wet plate could form drops, which would interfere with the bacteria distribution on the plate and if left on the plate could carry the bacteria outside it and cause cross contamination in the incubator.

4.3.5. *Antimicrobial experiments set up*

The antimicrobial activity of the films was tested when exposed to light in a sterile biosafety hood, while maintaining a constant humidity with the procedure summarized in Figure 4.3.2.

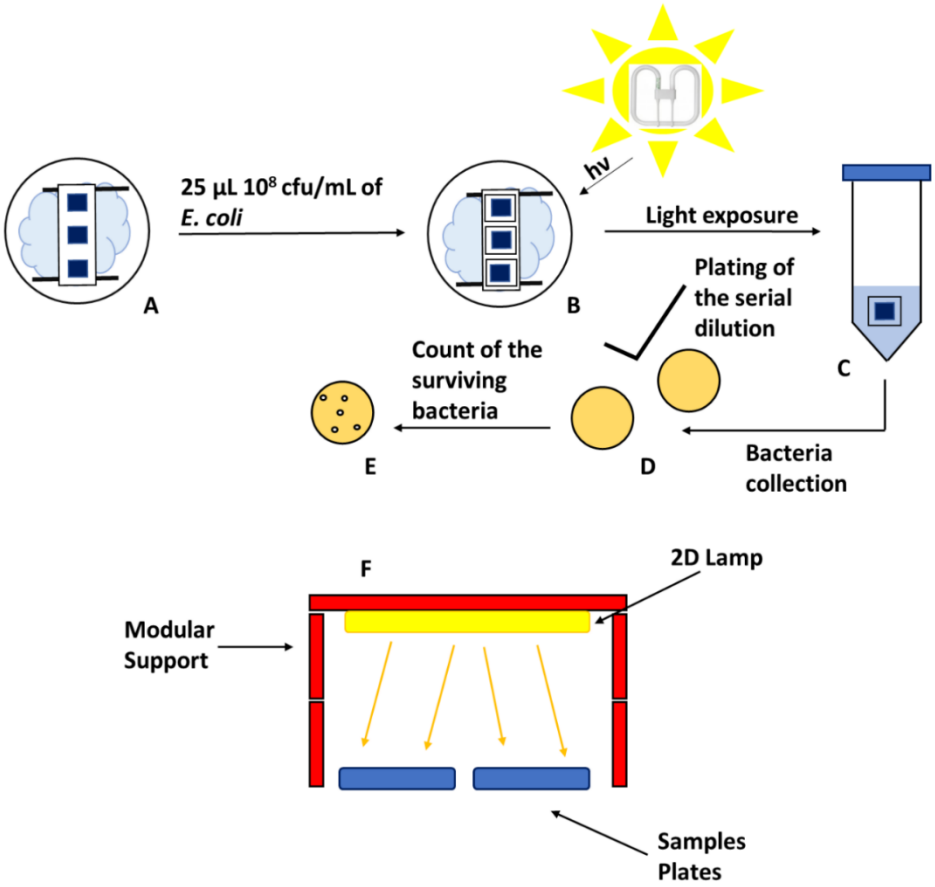

Figure 4.3.2. Scheme of the antibacterial film testing procedure: (A) PU/AuNRs/CV film samples are supported on a slide over some bi-distilled water to prevent dehydration, (B) after the inoculation with bacteria cells, the samples are protected with glass coverslips, (C) film samples and coverslips are washed with NaCl 0.9% to recover the remaining bacteria if any, (D) the bacteria solution is serially diluted and plated on nutrient agar and (E) the colony formed are counted; (F) schematic representation of the lamp set up.

The light source used for the tests was a 28 W Wattmiser GE 2D lamp, a high efficiency neon lamp commonly diffused in Europeans hospital and commercial buildings.

The angle between the ballast and the lighted surface was important to have a uniform light intensity distribution on all the test area. The lamp ballast was attached to a hard plastic support, covered in tin foil to reflect uniformly the light from the lamp and be easier to sterilize using a tissue soaked in EtOH 70%. The light support was placed on two stands, which were used to regulate the distance between the test area and the lamp and consequently the intensity of the light reaching the film samples.

The amount of light reaching a surface depend from the distance from the light source, and it follow the relation (Equation 4.3.1):

$$B = \frac{L}{4\pi D^2} \qquad (4.3.1)$$

With B being the intensity of light reaching a unit of surface placed to a distance D from the light source in a unit of time. L is the light intensity emitted in the solid angle.

Because the light bulb used in the experiments was bidimensional and supported by a reflective ballast the mathematical calculation of the light flux was not accurate enough to be used in the experiments.

The lux values used in this thesis have been determined using a Mini Digital Light Lux Meter - Sinometer LondaJ LX-1010B using a sensor with 1 cm^2 of surface. The sensor was moved in different points of the experimental area during the measurement to check the uniformity of the light exposure. The experiments in this thesis had been performed on three light intensity settings: 11’700, 9’400, 8’700 lux; for a time of exposure from 1, 1.5, 2, 3 and 4 h.

The films were tested as 1 cm^2 tiles, three film samples were placed on a microscope slide, inoculated with 25 µL of bacterial dispersion (either *E. coli* or *S. aureus*) and each covered with a microscope coverslip to prevent excessive dehydration of the samples due to the ventilation of the biosafety hood.

To further reduce the risk of dehydration of the bacteria solution, every microscope slide was placed on two sterilized toothpicks and suspended in a petri dish on 1 to 3 mL of ultrapure water. A maximum of 12 samples divided in 4 groups of three film tiles could be processed at the same time.

In a typical experiment 6 film tiles (PU/NPs/CV), 3 polymer control (PU) and 3 films modified with the dye (PU/CV) were tested at the same time. For experiments lasting more than 2 h aliquots of 10 µL of sterile ultrapure water were added to the bacteria solution to compensate the moisture loss. At the same time 1 mL of water was added to the reservoir below the microscope slide.

Maintaining the moisture of the samples tested, reduced the variability of the results and limited the stress suffered by the bacteria minimize the losses caused by light exposure. Without any intervention, the bacteria solution would dry after 2.5 h when exposed to the experimental conditions.

In a typical experiment, the samples would be hydrated after 1.5 h from the beginning of the light exposure and any following hours after that. To obtain a reproducible starting point for the experiment, 1 cm^2 of the film was inoculated with 25 µL of bacterial dispersion with concentration varying between 10^8 to 10^6 cfu/mL for a starting point of 2.5 x 10^6 to 2.5 x 10^4 cfu.

More concentrated samples were less reliable in their response to the film action, for this reason they were used only for evaluate the efficiency of the film for the longer time point of the most active films (PU/citNa-AuNSs/CV and PU/citNa-AuNRs/CV) usually in a large number and with more diluted samples as comparison.

After the end of the exposure, the samples were collected in 50 mL vials together with their coverslip, washed with 2 mL of NaCl 0.85% g/mL and vortexed, in order to collect all the surviving bacteria. The solution obtained was aliquoted on NA plates and incubated for an overnight at 35° or 37° C with controlled humidity in a Binder incubator (Red Line). During the incubation, every surviving bacteria in contact with the nutrients on the agar plate, grew forming visible colonies that were counted the day after, to calculate the efficiency of system.[209]

4.3.5.1. Antimicrobial experiments set up in a closed container

The first series of experiments performed on the film samples had a different set up compared to the one used for the rest of the study (Figure 4.3.2). In these initial experiments the film samples were placed in a closed petri dish on a microscope slide, on the top of two toothpicks with a small amount of water below. The petri dishes were sealed with parafilm while for the samples to be tested in the dark tin foil was wrapped around the sealed petri dish.

Up to 4 different dishes were then placed in a closed box with the internal surfaces cover with tinfoil, the lid of the box was used as ballast for the lamp. This set up, was able to uniformly light as much as 12 film samples divided in 4 plates. The sample to be tested in the dark were also introduced in the box to avoid differences of temperature between the samples.

4.3.5.2. Test of the hyperthermia effect connected to the film action

The acquisition of the polymer film temperature was obtained cutting the film in 1 cm^2 tiles and dispose them on microscope slides with coverslips while registering the temperature using a K-type thermocouple while registering the temperature every 30 seconds for 2 h of light exposure. The results were collected in triplicates.

4.3.6. *Data collection and mathematical analysis*

The main problem connected to the analysis of the antimicrobial activity data was to determine when they were relevant or not. A way to determine that, was to collect a certain number of repetitions for every measurements (and comparing the distribution of results of the samples to the controls). To obtain a statistical relevant number of repetitions for each datapoint, at least 6 groups of 3 samples of the film in every experimental conditions were produced (18 repetition per datapoint).

The method used to compare distributions of results was a variation of the Student's-t test, named Welch test.[210] Which was specifically designed to study the correlation between two data distributions with different degrees of variation (while being still applicable to samples with equal variance).[211] The Welch test used two terms of comparison: the parameter t, defined in Equation 4.3.2 and the "degrees of freedom" (d.f.) defined in Equation 4.3.3, in order to evaluate the overlapping between distributions representing two different observables.

$$t = \overline{X_1} - \overline{X_2} \Big/ \sqrt{\left(\frac{s_1^2}{N_1} + \frac{s_2^2}{N_2}\right)} \qquad (4.3.2)$$

Were $\overline{X_n}$ (1 or 2) was the average value of the distribution analysed, s_n was the variance of the distribution, N_n was the number of data composing the distribution.

$$d.f. = \frac{\left(\frac{s_1^2}{n_1}+\frac{s_2^2}{n_2}\right)^2}{\frac{\left(s_1^2/n_1\right)^2}{n_1-1}+\frac{\left(s_2^2/n_2\right)^2}{n_2-1}} \quad (4.3.3)$$

The d.f. value represent an estimation of the independence of the results of the different distributions, expressed as the total deviation from the average, χ^2 ($\chi_n = s_n^2/n_n$) compared to the respective degrees of freedom of the two distributions.

The values obtained by these equations were fed to the analysis of variance (ANOVA) program, which calculated the area below the first distribution curve of results and compared it to the area below the second and with the overlapping between the two distributions. The result of the ANOVA program was reported as a “p” which indicated a value or percent of overlapping. Two distributions were considered independent when the overlapping was lower than 5 % ($p < 0.05$).

The increase of the number of repetitions in a distribution could help to clarify the presence of an overlapping and the importance of it compared with the bulk of the distribution. For example, a distribution of 6 experiments which values had only a small difference with a control, would have a relatively large p value. If the number of measurements were increased, relative weight of the results far from the average would be reduced and the percent of overlapping with the control caused by them would decrease at the same rate.

The experimental conditions inflicted some stress to the bacteria reducing their vitality for the longer times of exposure (sections 4.4.3.1 and 4.4.3.2). For this reason, the statistical relevance of the results could not be calculated against the same control for different time points. In order to obtain relevance comparable results, the activity of every film at every time point was compared with the amount of vital bacteria remaining on the surface of the unmodified polymer (PU, reported as “a” in Figure 4.4.9 and Figure 4.4.10). The log units of bacterial reduction were calculated comparing the surviving bacteria after the exposure to the films with the amount of bacteria inoculated at the beginning of the experiment.

4.4. Results and discussion

4.4.1. *Factors influencing the antimicrobial activity of the film*

4.4.1.1. Experimental conditions set for variability control

One of the main issues when working with living bacteria was to obtain a reproducible baseline value for the results of the experiments. Because during the microbiological experiments numerous factors were able to influence the reproducibility of the results by either killing the bacteria or protecting them.

To contain the fluctuations of the experimental results a series of procedures were established. The first and more reliable of them was the repetition of every measurement (as reported in section 4.3.6).

Another important precaution (previously introduced in section 4.3.3) was to use bacteria between the second and the fifth generation on NA gel, because the bacteria of the first generation were stressed by the change in environment and they could only form small colonies. Thus, complicating the counting process. On the other hand, after the fifth generation the risk

of random mutations increased drastically making difficult to obtain a reliable count of the bacteria colonies.

The control of the saline concentrations in the bacteria dispersion was also necessary to obtain reliable antimicrobial results. Because during the experimental procedure, the samples containing bacteria were exposed to light in a ventilated environment (biological safety hood). This environment slowly dried the bacteria dispersions (which were only 25 µL at the beginning of the experiment) concentrating the salts soluted in it. The periodical injection of small aliquots of ultrapure water (≈10 µL per h) prevented the build-up of the concentration, reducing the risk of killing the bacteria with osmotic stress (further details in section 4.3.5).[212]

Lastly, all biological experiments required an unbroken sterile environment to obtain meaningful and consistent results.

4.4.1.2. Antibacterial experiments in a closed container

The test in a closed container (method in section 4.3.5.1) were introduced as a practical workaround to avoid using a biosafety hood for hours while performing the antimicrobial experiments.

This method had some advantages: it was much neater, operating in closed boxes and relying on the bio-safety hood only for the preparation of the samples and their analysis, while requiring only cloth sterilization of the external surface of the petri dishes and it offered a constant humidity and temperature inside the closed petri dish.

On the other hand, this set up offered a worst simulation of the real life use of the film, because this antimicrobial film was supposed to be used on surfaces in medical facility or food preparation factory with a strong

illumination to reduce the contamination of the contact surfaces, thus open to the environment. Furthermore, when tested in a closed container the film samples could reach a temperature of 34 - 37 °C, because the lamp could warm limited space of the box. Thus, introducing another element of distance between the experiment and the theoretical using conditions of the film.

Analysing the preliminary experiments with this set up, exposing the polymer film to light when contained in a petri dish reduced the film efficiency of approximatively 1-log (Figure 4.4.1).

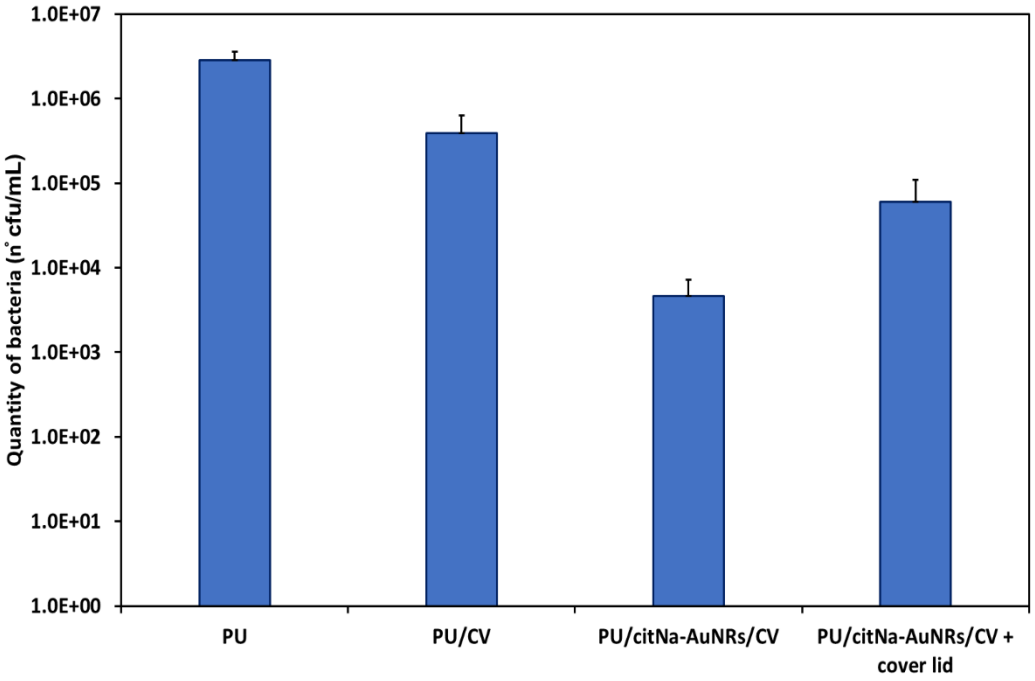

Figure 4.4.1. Comparison between the activity of the film with the standard set up and the experiment in a closed petri dish. From left to right: PU alone, PU/CV polymer modified with the dye, PU/citNa-AuNRs/CV complete antimicrobial film in standard conditions, film in a closed petri dish.

This efficiency reduction was not due to the light intensity reaching the sample inside the box, because according to luxmeter measurements (section 4.3.5), the plastic lid of the petri dish did not reduce the intensity of the light reaching the film. However, this was true only for the beginning of the procedure, after some time exposed to light, the rising temperature

and the humidity inside the container caused the fogging of the dish lid causing scattering the incident light and reducing the light intensity reaching the film.

Another problem with this kind of experiment was the risk of cross contamination between the samples on the same microscope slide and the environment inside the petri dish, the closed space and the warm humid condition helped the spread of the bacteria in the water and surfaces in the dish, which complicated the actual measurement of the bacteria surviving on the surface of the film.

This final point made this method not suitable for the antimicrobial testing, the standard set up used for the actual experiments required a longer sterilization procedure but was less prone to casual contaminations thus, was easier to keep sterile. Additionally, it could be easily modified to increase or to decrease the intensity of the light reaching the samples and was able to better simulate the application conditions of the film.

4.4.1.3. Test on the hyperthermia effect in the film

As previously seen in section 1.1.3.2, one of the possible consequences of exciting gold nanoparticles with the same wavelength of their L-SPR peak was the generation of the hyperthermal effect.

In literature there were many examples of this property used to eliminate cancer cells or against bacteria biofilms.[20,213] To understand if the hyperthermic effect played a role in the activity of the antimicrobial surface, the temperature of the film was tracked during the light exposure (set up in section 4.3.5.2).

During the 2 h of exposure at 11.7 klux, the temperature measurements for the polymer PU (Figure 4.4.2.a) alone and of the film containing CV/citNa-AuNRs/PU (Figure 4.4.2.b) did not reveal any visible variation in the heating rate of the two films. Thus, it excluded the presence of a macroscopic hyperthermia effect.

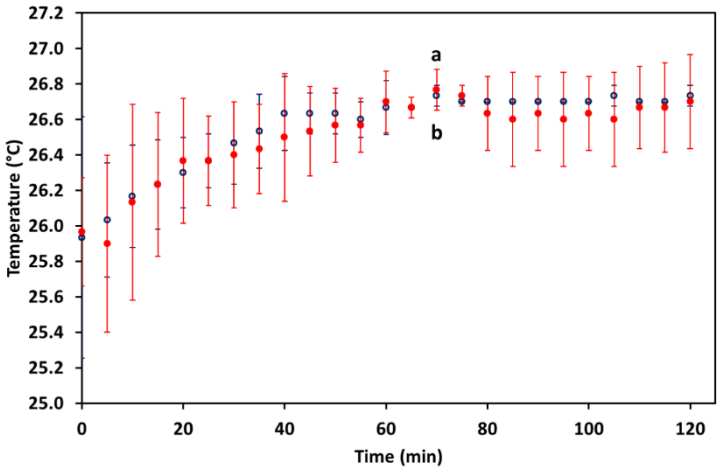

Figure 4.4.2. Temperature profile of a) the unmodified film and b) CV/citNa-AuNRs/PU while exposed to light (2 h, 11.7 klux).

This was another direct confirmation that the interaction between the nanoparticles and the dye (leading to the formation ROS), was able to offer to the nanorods a more efficient way to release energy compared to the formation of thermal phonons (section 1.1.3.2).

4.4.1.4. Importance of spectra overlapping for the development of antimicrobial effect

To confirm the importance of using nanoparticles which had a strong anisotropy and SPR absorption overlapping to the absorption peaks of the CV (544 and 594 nm, when in the polymer, section 3.4.5.2), control experiments using spherical gold nanoparticles (AuNPs) and nanorods with longer AR were performed. These experiments were conducted on *E. coli* for 2 h of exposure at 11.7 klux, using the same conditions that were used for the antimicrobial test (section 4.3.5).

The first control was performed using AuNPs with average diameter of 13 nm and stabilized with sodium citrate, max absorption 520 nm (Figure 4.4.3.a). While the second control contained AuNRs stabilized with citNa having an AR of 3 - 4 and their maximal LSPR absorption centred in 784 nm. The average dimensions of these nanorods were between 35 – 40 nm of length and 9 – 12 nm of diameter (Figure 4.4.3.b).

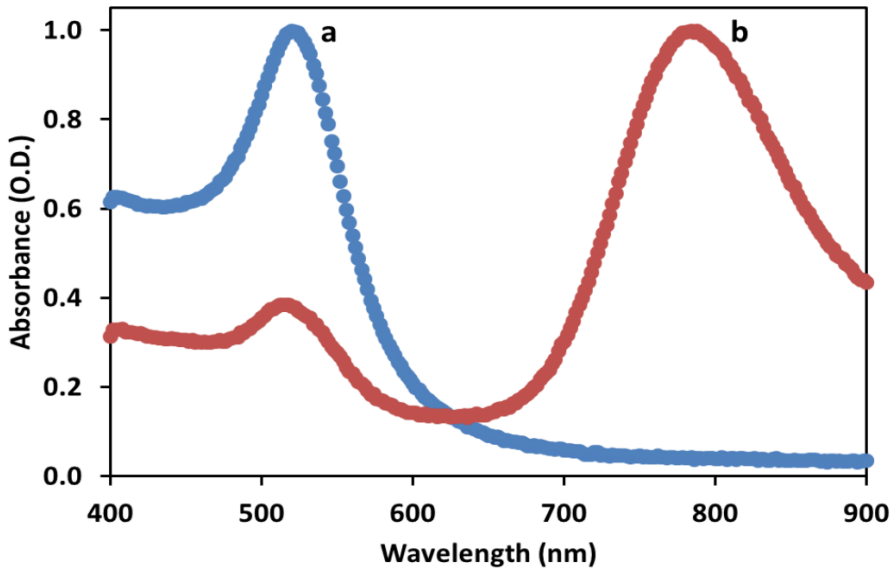

Figure 4.4.3. UV-visible spectra of a) citNa-AuNPs 13 nm of diameter and b) citNa-AuNRs (800 nm) with aspect ratio 3 – 4.

None of the controls tested generated an improvement of activity when compared with samples containing the dye alone, as expected from the limited overlapping between the dye absorption and the particles SPR (Figure 4.4.4).

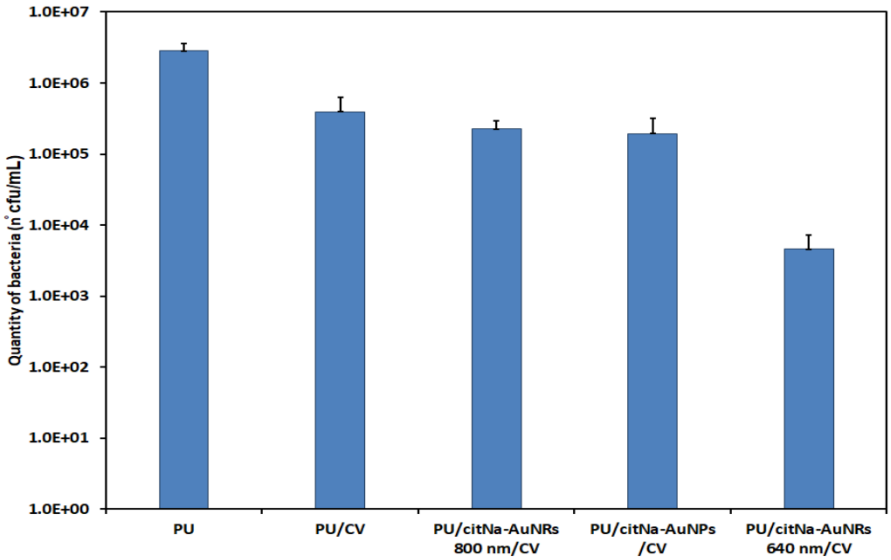

Figure 4.4.4. Antimicrobial effect against E. coli for 2 h of light exposure (11.7 klux) on films with different pairs CV – AuNPs. From left to right: PU alone, PU and CV dye, CV and AuNRs with longer AR, CV and spherical AuNPs and CV and AuNRs with shorter AR..

Samples containing AuNPs, were expected from the examples in literature, to have no antimicrobial activity for spherical AuNPs larger than 5 nm.[159,214] But confirming experimentally these results allowed to exclude the possibility that the boost in the antimicrobial activity generated by the particles in the film could be caused by a heavy-atom interaction or a catalytic effect happening in the point of contact between the dye and metallic gold. Which were both phenomena causing antimicrobial activity for other systems reported in literature.[138,161]

The experiment with AuNRs with longer AR, was aimed to confirm that the overlapping of the spectra, was more important than the type of plasmonic

resonance (transversal and longitudinal SPR for rods) when attempting to induce plasmonic coupling between a dye and a type of particles.

Considering, that the introduction of the longer AuNRs did not change the activity of the film, this experiment clearly demonstrated that the position of the plasmonic peak of the AuNRs in relation with the dye was fundamental to establish the plasmonic coupling. Indirectly this experiment also confirmed that the presence of coupling was necessary to the activation of the film, demonstrating that not all the anisotropic nanoparticles could boost the ROS production of the film.

4.4.1.5. Antibacterial effects of different intensity of illumination

A common characteristic of all the antimicrobial surfaces activated by light was the correlation between the amount of light used to power the activity of the film and its antimicrobial effect. For example in literature have been reported systems able to kill 4-log of S. aureus in 6 h when exposed to white light while using only half hour to reach the same amount when powered with laser light (section 1.2.3). But, the same examples possessed a relevant activity in absence of light which complicated the study of their mechanism of action.[138,159,160] Thus, an in-depth study of the influence of the light intensity on the rate of the antimicrobial activity of the films and of their behaviour in the dark was necessary to better understand the action of the

films and the parameters influencing the real life use of the film in commercial applications.

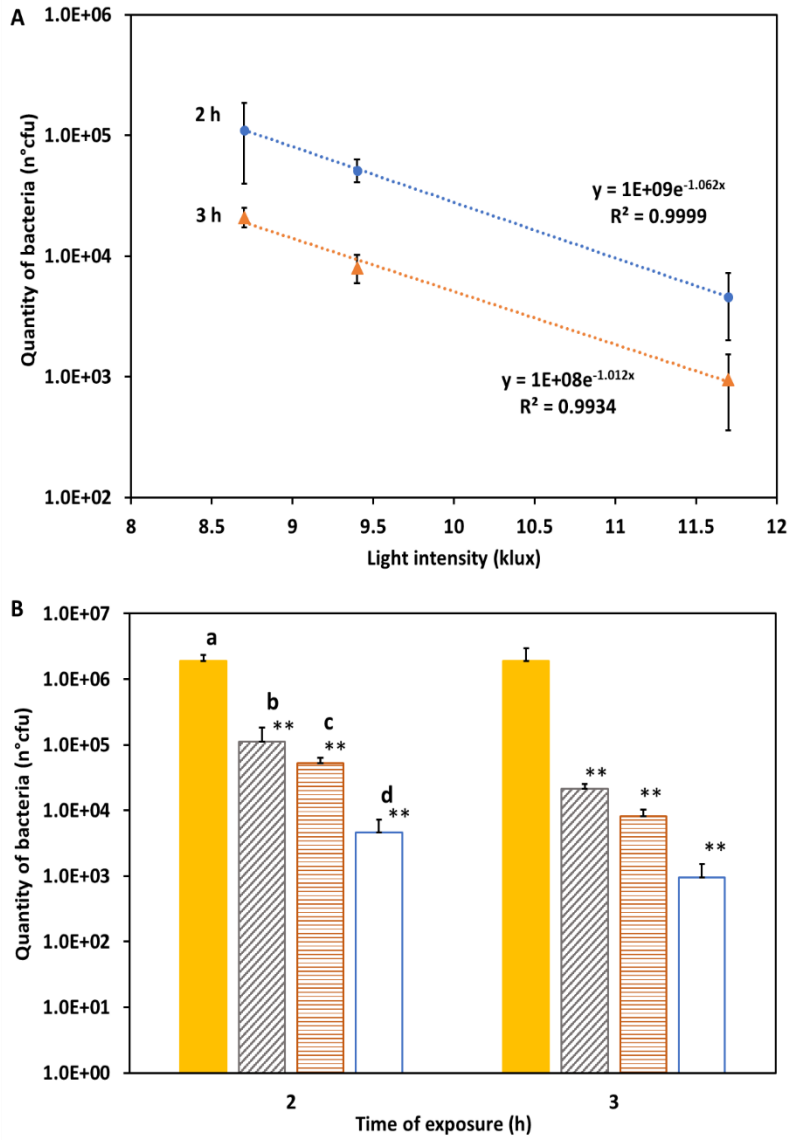

*Figure 4.4.5. Effect of light power on the antimicrobial activity of the film against E.coli. A) Bacteria count after 2 h and 3 h of light exposition in relation of the light intensity used; dotted lines represent the exponential relation between light intensity and the reduction of the bacteria population. B) Bacteria count for different light intensity after 2 and 3 h: a) for samples kept in the dark; b) for a light exposure of 8.7 klux; c) for a light exposure of 9.4 klux and d) for a light exposure of 11.7 klux; ** $p < 0.01$.*

The activity of the film was initially tested in the absence of light (Figure 4.4.5.B.a) to have a reference for the activity of other polymeric films and to demonstrate the light dependent nature of the antimicrobial properties

of the film. Then, the film (PU/citNa-AuNRs/CV) was exposed to different levels of light intensity from 11.7 klux to 9.4 klux and 8.7 klux and for 2 and 3 h hours of exposure. In order to determine the reaction of the antimicrobial film to the change in illumination and if the time of exposure influenced this reaction.

The analysis of the results showed that the film samples kept in the dark did not possessed any intrinsic toxicity (Figure 4.4.5.B.a), confirming that light-film interactions were pivotal to the generation of the antibacterial effect.

Furthermore, as expected from literature, the magnitude of bacteria reduction was directly correlated to the level of illumination, because the experiments showed that reducing the light given to the film to produce ROS slowed down the rate of bacteria killings.

As the light intensity was increased the efficiency of the system incremented exponentially (Figure 4.4.5.B.b – d). The dependence from the intensity of the light was consistent either for the samples exposed for 2 and 3 h (Figure 4.4.5, A), demonstrating that the time of exposure did not influence the dependence to light exposure of the film.

The dependence of the antimicrobial activity to the light intensity was one of the most sensitive point for the application of the film for commercial applications. The films required an intense light source to develop fully their potential antimicrobial activity, as demonstrated from Figure 4.4.5 where the efficiency of the film decayed quickly with the reduction of the light intensity.

In the conditions of full illumination the film proposed in this thesis, had an activity of order of magnitudes greater than most of the similar systems

proposed in literature.[138,215] But regardless of which film is the most active, some of the systems proposed in literature seems able to produce some antimicrobial activity while using very low light intensity.[161]

Excluding the difficulty of converting the measurements performed from different groups in a coherent and comparable frame, the difference in light sensitivity of these different types of antimicrobial surfaces could be connected on the type of gold nanoparticles used to boost the ROS production.

As discussed in section 1.2.3, the most efficient gold nanostructures working at lower light intensity, reported in literature, were cluster of 25 to 50 gold atoms stabilized by thiol-dodecane which in presence of CV were able to catalyse the production of ROS.[138,161]

The system proposed in this thesis instead, used larger gold nanoparticles (AuNRs, AuNSs) to generate a plasmonic coupling with the dye, the pair was able to generate a greater amount of ROS compared to the dye alone, because the large cross section and extinction coefficient of the particles allowed to supply the dye with more energy to use to produce ROS.[10,11]

In the frame of a possible application of the film, the need of a strong illumination to activate the film it could have some advantages:

i) having the film deactivated in normal working conditions (≤ 1 klux) would reduce the time given to bacteria to develop bacteria resistance to the film;

ii) the film would be activated only during the cleaning procedures or when a constant sterility would be required (as in surgical theatres), thus reducing the photobleaching and extending the film life to months of use;[160]

iii) the absence of an activity in the dark, suggested that the film did not possess macroscopic toxicity which would limit its application in areas exposed to the public.

4.4.2. *Characteristics of bacteria influencing the activity of the film*

As introduced previously (sections 1.1.7.1 and 1.1.8.1), *S. aureus* and *E. coli* were used as model of the Gram(+) and Gram(-) bacteria which could be found on common contact surfaces. As described in the introduction, these bacteria are different in size and dimensions, but they also differ in the structure of their cell wall and mechanism used to protect themselves from the contact with ROS. In the following sections the structure of the cell walls and the mechanisms of defence against ROS of *S. aureus* and *E. coli* will be studied to understand their behaviour when exposed to the ROS produced by the films.

4.4.2.1. S. aureus

4.4.2.1.1. Cell wall

As all the Gram(+) bacteria *S. aureus* has a relatively simple cellular wall, composed by thin phospholipidic double layer (10 – 20 nm) protected by thick barrier of peptidoglycan (30 - 100 nm). The peptidoglycan barrier protects Gram(+) bacteria from physical dangers (e.g. harsh conditions and osmotic stress). This barrier, in bacteria grown in harsher environments is thicker and it can comprise up to the 60% of the total weight of the bacteria.[216]

Peptidoglycans meshes constitute the 60% of the Gram(+) cell wall and they are mostly composed of three components. The first two, N-acetylmuramic acid (NAM) and N-acetylglucosamine (NAG), form rigid chains that cover the surface of the bacteria and are connected by oligopeptides which create a tri-dimensional reticulation (Figure 4.4.6).

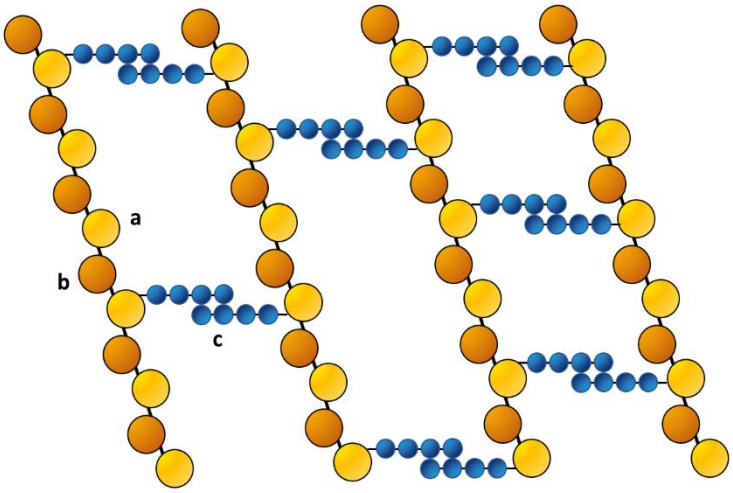

Figure 4.4.6. Peptidoglycan barrier structure and components, a) N-acetylmuramic acid, b) N-acetylglucosamine and c) oligopeptide.

The third and most common component of the *S. aureus* barrier are the teichoic acids: lipoteichoic acids (LTA) and wall teichoic acids (WTA). LTA form chains perpendicular to the peptidoglycan mesh crossing it throughout all its thickness and anchoring the structure to the phospholipidic layer below it (Figure 4.4.7).

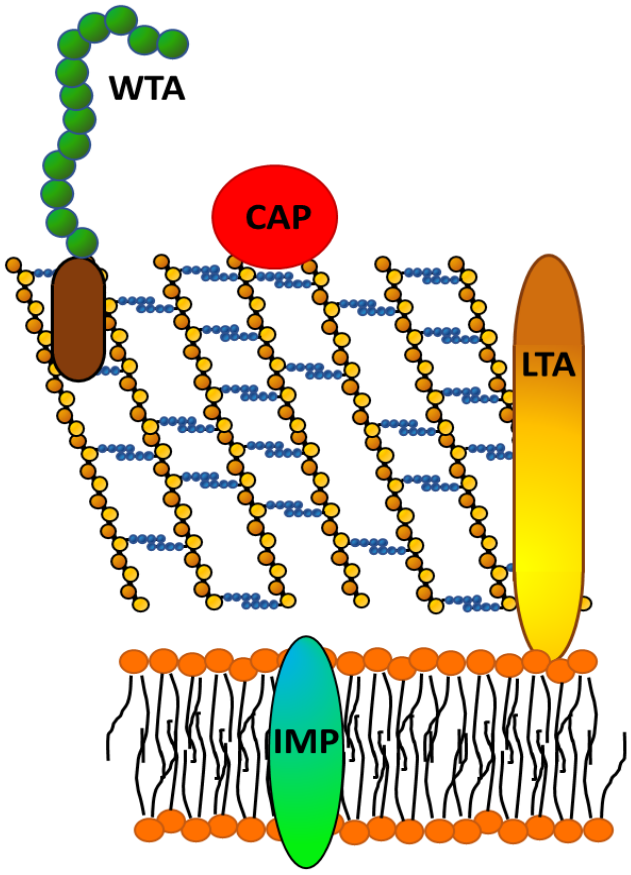

Figure 4.4.7. Structure of an S. aureus cell wall with schematic representation of the wall teichoic acids (WTA), covalently attached proteins (CAP), peptidoglycan barrier, lipoteichoic acids (LTA), internal membrane and internal membrane proteins (IMP).

The WTA are anchored to the surface of *S. aureus* and they extend for approximatively 60 repetitive units out of it. Their function could vary but in average WTA are strongly negatively charged, property which allow them to interact with positive ions and to change the permeability, fluidity and packing of the cell wall.

Covalently attached proteins (CAP) and internal membrane proteins (IMP) both contribute to functionalize the cell wall, playing multiple roles necessary to the survival of the bacteria (e.g. ions exchange, feeding etc.).

4.4.2.1.2. Defences against ROS

The cell wall of *S. aureus* is very resistant to physical stresses, but it does not offer great protection from chemical species, especially if these chemicals are not electrostatically charged.

To compensate for the permeability of their barrier, *S. aureus* is able to deploy a combination of defence mechanisms designed to reduce and contain the damages caused by the contact with ROS.

The most evident of these defences is their pigmentation. The *S. aureus* colour is caused by the presence of carotenoids. These molecules possess a large delocalized aromatic system capable of trapping the radicals while they are penetrating into the bacterial barrier.[217] In combination with the teichoic acids of the cell wall the carotenoids are also used by the bacteria as protection from the neutrophils (e.g. during the infection of the human body). Because neutrophils (part of the immune system) are able to phagocyte bacteria and release ROS to destroy them.[218]

The pigmentation contributed to the defence of *S. aureus* against ROS in collaboration with a high concentrations of metal ions as iron, zinc, copper and manganese present in their intracellular media that has the function of interacting with radicals and convert them in harmless compounds.[219]

Metal ions were used as cofactor for the activity of many enzymes in the intracellular media. For this reason, *S. aureus* was able to extract them by the host (the infected patient) and concentrate them with specialized enzymes.

S. aureus was able to extract iron from human *heme* and *ferritin* using the *staphyloferritin* and a series of membrane iron-dependent proteins

sequenced by the *Isd* gene. Inside the bacteria the ions of iron are processed by the ferric uptake regulator (Fur) and stashed in specialized proteins (ferritin, bacterioferritin co-migratory proteins, etc.), to prevent them from forming free radicals.

Manganese (Mn^{2+}) is more reactive than iron, in physiological condition. Thus, it is a prime candidate for the interaction with ROS (either forming them or deactivating them). This property of Mn^{+2} generates a competition in the intracellular space, between bacteria and host for its control during an infection.

Zinc is fundamental to the functionality of many enzymes but for its charge/size ratio could be very toxic to both cells and bacteria, for this reason many transport proteins were developed to encapsulate free Zn^{2+} and to stop it from interacting with other vulnerable enzymes. These transport proteins are also used as response against radicals using Zn ions as a radical trap.

Copper ($Cu^{+2/+1}$) is a less common in the human body but it is fundamental to some functional enzymes of the cellular respiration and for this reason it is also used by *S. aureus* to deactivate ROS.

If the bacteria is exposed to a concentration of ROS high enough that the passive protections are no more sufficient, it could deploy a group of enzymes designed to deactivate specific type of ROS or to convert them in less dangerous species.

This phase of the ROS defence was called detoxification and it is not a safe process for the bacteria, ROS are extremely fast in damaging biological materials, as well as the enzymes used to neutralize them. These enzymes

are not perfectly efficient and inevitably get damaged by the large amount of active molecules generated by the process. When the ROS concentration overcome the capability of the bacteria to generate more enzymes or it saturates the activity rate of the surviving enzymes, the bacteria quickly die.

The most important family of enzymes used against ROS is the superoxide dismutase (SOD). These enzymes are present in *S. aureus* in the form A and M which are both based on manganese and work in tandem.

The action of SOD-A focuses on the elimination of the superoxide generated inside the bacteria, while SOD-M acts as a response to the superoxide from outside sources. These enzymes convert O_2^- to H_2O_2 which is still very active but less dangerous than superoxide. The increasing concentration levels of H_2O_2 lead to the activation of the catalase A (*katA*). When activated, this enzyme converts large amounts of H_2O_2 to water and NADH. Small amounts of H_2O_2 as the one generated during the cellular respiration are processed by other enzymes of the family of the peroxiredoxins which are slower to act. Finally, the last enzyme family involved in the detoxification of ROS are the flavohemoglobins which are used by the bacteria to eliminate the nitrate based radicals ($^{\cdot}NO$, $^{-}ONOO$, etc.).

The last phase of the *S. aureus* reaction against ROS is the production of numerous proteins able to fix damages to other proteins and DNA. The repairing process works only for bacteria exposed to small amounts of ROS, because the cumulating damages on DNA and proteins quickly overcome the bacteria capability to produce functional proteins to fix the damages.

4.4.2.2. E. coli

4.4.2.2.1. Cell wall

The Gram(-) cell wall is more complex and thinner (10 – 15 nm in total) than in Gram(+) bacteria.[216]

Instead of being constituted of a single layer as for Gram(+) bacteria, the cell wall of Gram(-) is composed of three layers: i) outer membrane, ii) periplasm and iii) cell membrane (Figure 4.4.8).

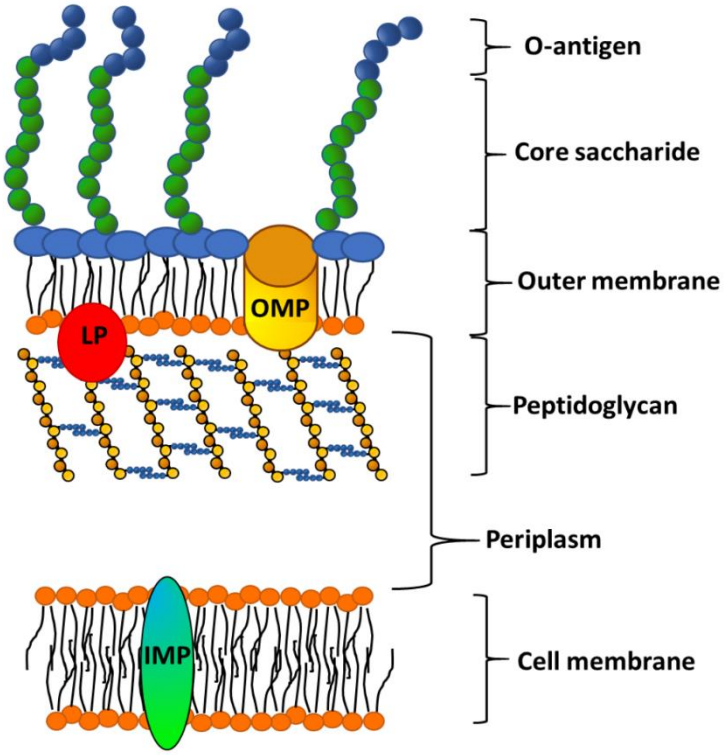

Figure 4.4.8. Structure of an E. coli cell wall, with schematic representation of the O-antigen constituted by liposaccharides (LPS), outer membrane proteins (OMP), lipoproteins (LP) and integral membrane proteins (IMP).

The outer membrane is the most external component of the cell wall, this membrane is different from the typical phospholipidic bilayer because its most external half of the bilayer, the external leaflet, is composed of glycolipids which are used as anchors by filaments of lipopolysaccharides (LPS).

The internal leaflet (of the outer membrane) is composed of phospholipids and functionalized with outer membrane proteins and lipoproteins. The external leaflet is particularly significative for human pathogenicity because LPS are able to trigger the immune response of humans and for some variety of *E. coli* this could led to endotoxicity and septicaemia (section 1.1.8.1).[220]

Another function of the external leaflet of the outer membrane was to act as a first filter against dangerous substances. This is possible because the terminal part of the LPS are negatively charged and able to attract positive ions reducing the outer membrane surface and neutralising the total electrostatic charge of the bacteria. This concentration of charges acts as a repellent for hydrophobic molecules, while at the same time the polysaccharide chains on the surface of the bacteria are largely saturated thus, tightly packed and forming an efficient hydrophobic barrier, blocking charged molecules.[216] Additionally, the outer membrane contributed to the mobility of the bacteria because this layer supported the flagella which allowed the bacteria to move.

The second section of the cell wall of *E. coli* is included in the space between the outer and cell membrane, which contains a peptidoglycan scaffold and the periplasmic fluid, from which gave the name to this section (periplasm). The peptidoglycan scaffold is strongly attached to the outer membrane through lipoproteins (LP) and it acts as a rigid skeleton for the bacteria. The peptidoglycan scaffold also prevents the disaggregation of the outer membrane and protects *E. coli* from osmotic shocks. The other component of the periplasm is constituted of a thick fluid rich of proteins which transports nutrient and ions between the two membranes.

A secondary function of the periplasm is to act as an isolated reservoir for the dangerous enzymes produced by the bacteria (e.g. RNAase, alkaline phosphatase, etc.) with a mechanism of action similar to a lysosome of a eukaryotic cell.[221]

The third and inner most component of the *E. coli* is the cell membrane constituted by a phospholipidic bilayer ornated by numerous IMP.

The main phospholipidic components of the cell membrane of *E. coli* are phosphatidyl ethanolamine and phosphatidyl glycerol which are mixed with small amounts of other phospholipids to regulate the rigidity, permeability and functionalization of the membrane.

E. coli is a prokaryotic cell, which means that the cell membrane contains all the functional proteins necessary to the bacteria metabolism while in eukaryotic cells, they would be distributed on the surface of the different organelles. The concentration of functionality on the cell membrane make it a pivotal target for the bacteria destruction caused by the antimicrobial film. Because once pierced the bacteria cannot function while at the same time, the enzymes in the periplasm would trigger its self-digestion.

4.4.2.2.2. Defences against ROS

As seen for *S. aureus* the defence of the bacteria against ROS involves numerous layers of response, all contributing to reduce the effect of ROS on the bacteria.

The first and most direct defence system employed by *E. coli* is its complex cell wall. The double layered structure offers a barrier against chemical agents limiting the amount of harmful substances reaching the internal and vulnerable parts of the bacteria.

If some superoxide pass the cell wall, it activates two proteins SoxR and SoxS. SoxR detects redox stresses, while SoxS is a transcriptional activator, which could switch on a large number of genes and chromosomes.

After the biosynthesis SoxR lays quiescent in its reduced form, but in presence of superoxide it is quickly oxidised, causing the activation of the *soxS* gene. When activated, *soxS* induces the production of the SoxS protein which triggers the bacteria to change the aconitase B and fumarases A and B, to aconitase A and fumarase C which are more resistant to ROS.[222]

Another protein correlated to the *E. coli* response to ROS is the OxyR regulon, which is activated in the presence of H_2O_2. When OxyR is active, it pushes the production of catalase (KatG) and of other proteins designed to repair the damages to proteins and to genetic material (DNA and RNA).

E. coli constantly possess a low levels of SOD enzymes both located in the cytoplasm than in the periplasm to balance the production of superoxide caused by the bacteria respiration. When the SoxR protein activates the concentration of SOD enzyme increase.

E. coli has two cytoplasmic SOD enzymes, one containing Mn^{2+} (MnSOD) while the other contains Fe^{2+} (FeSOD), while it has only a periplasmic SOD containing both Cu and Zn (CuZnSOD also called SodC).

The variety of different types of SODs available to *E. coli* bacteria reduced their dependence to the presence of specific elements in the growth environment allowing *E. coli* to grow in an environment poor of ions.

The action of the SOD produced H_2O_2 which is detoxified by a two different processes: one always active and one triggered by the OxyR regulon.[223]

The primary scavenger of H_2O_2 in *E. coli* is the peroxiredoxin AhpCF, a NADH peroxidase made by two components, used to control the average amount of H_2O_2 present in the cytoplasm.

When the concentration of H_2O_2 raises above 0.1 μM it triggers the OxyR regulon causing the production of catalase G (KatG), this enzyme when activated can neutralise a concentration of H_2O_2 up to the millimolar range before reaching saturation.

As seen for the Gram(+) bacteria the detoxification stage of ROS response is only a temporary defence, because the high reactivity of ROS quickly damages the enzymes used to contrast them.

If the exposure to ROS is terminated before the bacteria death, it can recover using the repairing proteins activated by OxyR.[223]

In average Gram(-) bacteria are better equipped to isolate themselves from exogenous ROS and they have a wider variety of response pattern to ROS when compared to Gram(+) bacteria. On the other hand, the permeability of the cell wall of Gram(+) bacteria forces them to always deploy a high background concentration of SOD and catalase enzymes to survive in aerobic conditions, thus speeding up the response to increases of ROS concentrations.

These two approaches to ROS defence influenced how these bacteria reacted to external sources of ROS and the efficacy of the antimicrobial film against them.

4.4.3. *Antimicrobial activity test against different bacterium types*

In this section is discussed the result of the activity of the film either modified with AuNRs or AuNSs against Gram(+) and Gram(-) bacteria.

As indicated previously (section 4.3.1), *S. aureus* (ATCC6538) and *E. coli* (ATCC25922) were the two species of bacteria used as models to test the activity of the film against Gram(+)and Gram(-) species. These bacteria differed in size (sections 1.1.7.1 and 1.1.8.1), type of cellular membrane (sections 4.4.2.1.1 and 4.4.2.2.1) and mechanisms used to defend from the contact with ROS (sections 4.4.2.1.2 and 4.4.2.2.2).

To summarize, *E. coli* is a Gram(-) rod like bacterium with average size of 0.25 µm to 1.5 µm. Its external barrier is composed of two phospholipidic membranes, which are separated by a peptidoglycan barrier and by few nanometres of interstitial space reaching a total thickness between 10 to 15 nm.[216] The complexity of cell wall structure of Gram(-) bacteria made them resistant against oxidative and chemical stresses, limiting the amount of harmful substances reaching the internal and vulnerable parts of the bacteria (further detailed in section 4.4.2.2.1). At the same time, *E. coli* employed different mechanisms to reduce the damages caused by the ROS (section 4.4.2.2.2).[223]

S. aureus on the other hand, was a spherical Gram(+) bacteria with average diameter of 0.5 to 1 µm. Gram(+) bacteria possessed only one thick external membrane composed by multiple layers of peptidoglycans with structures composed of sugars and amino acids. This barrier could vary in thickness between 30 to 100 nm (section 4.4.2.1.1).[216] In summary, when compared with the cell wall of Gram(-) bacteria, the barrier of Gram(+) bacteria is more permeable to chemical species and more resistant to physical stresses. To compensate for the permeability of their barrier *S. aureus* are able to deploy a combination of defence mechanisms to reduce and contain the damages caused by the contact with ROS (section 4.4.2.1.2).[217,219]

4.4.3.1. *Effect on E. coli*

The antimicrobial activity of the films against *E. coli* was tested in the conditions reported in section 4.3.5. In this test small tiles of the antimicrobial films and controls were inoculated with the same amount of bacteria (≈5 x 10^6 cfu of *E. coli*). These samples were exposed to light and the solution on them was collected at different time points (1, 1.5, 2, 3, 4) to estimate the rate on which the film was able to kill the bacteria.

As seen in the previous section many variables could influence the final result of the experiments (section 4.4.1), for this reason the results of the activity of the films containing CV and AuNRs or AuNSs (Figure 4.4.9.e & f) were reported with the controls containing: PU alone, PU/AuNRs, PU/AuNSs, PU/CV (Figure 4.4.9.a, b, c & d, respectively).

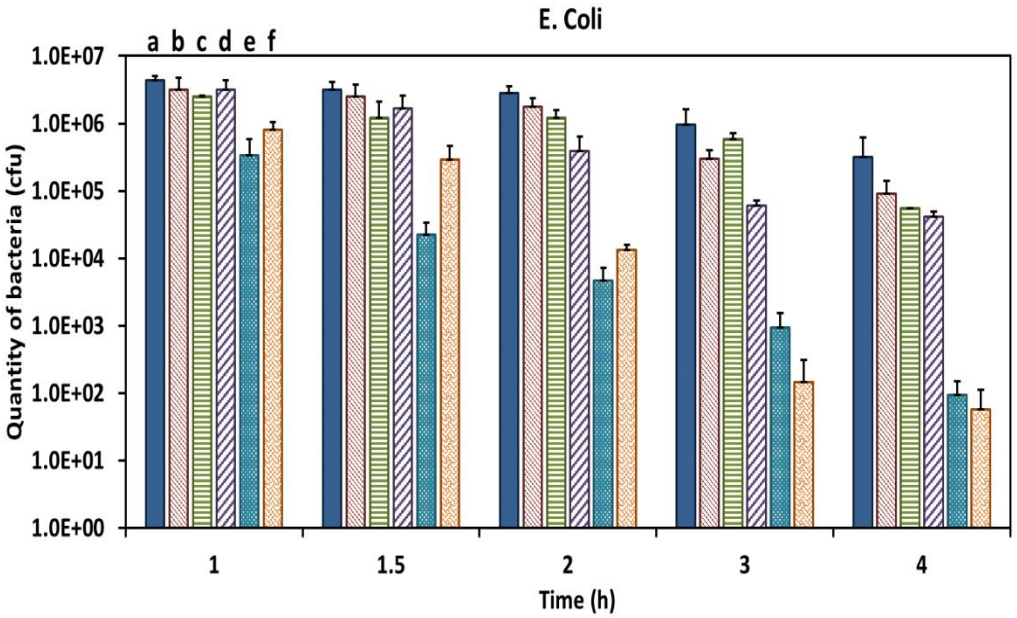

Figure 4.4.9. Antimicrobial experiments result of the antimicrobial film against E. Coli for 1 to 4 h of light exposure at 11.7 klux. Labelled from a to f the film tested: a) PU, b) PU/citNa-AuNRs, c) PU/citNa-AuNSs, d) PU/CV, e) PU/citNa-AuNRs/CV and f) PU/citNa-AuNSs/CV. All the results of PU/citNa-AuNRs/CV and PU/citNa-AuNSs/CV were statistically different compared to PU for the same time of exposure ($p \leq 0.001$).

Analysing the antimicrobial action of the films containing CV and AuNRs (PU/citNa-AuNRs/CV) for the different timepoints, a reduction of the

bacteria population of several orders of magnitude (log units) can be observed. Leading after the first hour of light exposure to 1-log reduction. Which increased to 1.5-log after 1.5 h to suddenly increase to 2.5 – 3-log units by the 2 h timepoint, 3.5-log unit after the 3 h and 4-log unit after 4 h of exposure to light (Figure 4.4.9.e).

For film samples containing AuNSs and CV (PU/citNa-AuNSs/CV) the bacteria reduction followed a different progression: reducing the bacteria population of 1-log unit after 1 h of light exposure, 1.25-log for 1.5 h, 2-log unit after 2 h, that stepped up to more than 4-log unit after 3 h and 5-log unit for the last time point (4 h) (Figure 4.4.9.f).

Comparing the activity of the films containing the different particles it is evident that different kinds of nanoparticles changed the efficiency and the kinetics of the antibacterial effect when introduced in the film. Samples containing AuNRs caused a quick reduction of the bacteria for the initial time points (1-log unit after 1 h, 1.5-log after 1.5 h and 2.5 – 3-log unit after 2 h) to slow down for the two last time points. While samples containing AuNSs generated a limited antimicrobial effect for the first two timepoints which ramped up to reach 5-log unit for 4 h of exposure.

The results of PU/citNa-AuNRs/CV and PU/citNa-AuNSs/CV for the last time point were close in absolute value, because 5-log unit of reduction was near to the limit of detection of the technique used to determine the amount of bacteria surviving.

Exposing the bacteria to the light, on the polymer (PU) without modifications had only a small effect on the bacteria population. Causing a

measurable reduction of approximatively 1-log unit only after 3 and 4 h of exposure (Figure 4.4.9.a).

Films containing only nanoparticles had limited activity, reducing the bacteria population of a quantifiable amount only for longer time points (1-log unit after 3 h and 1.5-log unit for 4 h for both AuNRs and AuNSs) (Figure 4.4.9.b & c).

While the films modified with CV (PU/CV, Figure 4.4.9.d) maintained some activity compared to the particles alone (Figure 4.4.9.b & c), 1-log unit for 2 h of exposure, 1.5-log unit for 3 h and 2-log unit for 4 h (Figure 4.4.9.d), but still hundreds of times lower than the activity of CV and AuNRs and one thousand times lower than CV and AuNSs.

Studying the comparison between the antimicrobial experiments with films and with controls gives a clear indication of the mechanism of action of the components of the film. With the gold nanoparticles able to collect large amounts of energy but offering low activities without a PS while the dye possessed a natural antibacterial action, which was greatly boosted by the introduction of gold nanoparticles.

As seen in section 1.1.5 the plasmonic coupling between particles and dye was influenced by their spectral overlapping which led to a larger production of ROS (section 3.4.6). Against *E. coli*, the larger production of ROS generated by the films containing AuNSs resulted in the increase of efficiency for the longer time points, probably caused by the progressive overwhelming of the bacteria defences. While the films containing AuNRs, which produced less ROS resulting in the death of less bacteria when progressing the experiment to longer timepoints.

A peculiarity of the kinetics of the films modified with AuNRs was that this type of films balanced the lower antibacterial efficiency for longer time of exposure (3 – 4 h), with a larger antimicrobial effect for the shorter time points. The reason of this phenomenon it is not clear, but it could be caused by the some of the mechanisms of defence that *E. coli* has against ROS, as for example the change from aconitase B to the fumarases A and B or the production of SODs (section 4.4.2.2.2) that requires some time to be activated or a previous and limited exposure to ROS.

This discrepancy between the antimicrobial activity progression of different particles indicates that the ROS production was not the only factor influencing the activity of the film. Regardless of kinetic considerations film samples modified only with the dye had much reduced activity than any of the films containing particles due to the limited ROS production of the dye without the interaction with the particles.

4.4.3.2. *Effect on S. aureus*

As for the experiments against *E. coli*, the activity of the antibacterial film on *S. aureus* was tested using the procedure reported previously (section 4.3.5). The action of the films against this type of bacteria was more difficult to interpret, because the film was less effective against it and less dependent on the amount of ROS generated by the films (Figure 4.4.10).

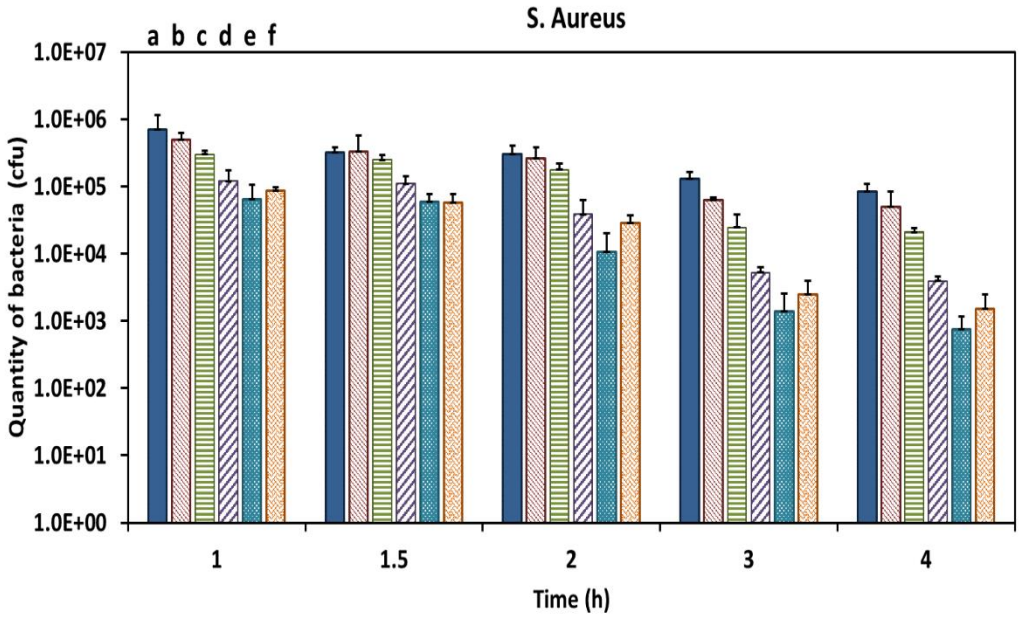

Figure 4.4.10. Antimicrobial experiments result of the antimicrobial film against E. Coli. a) PU, b) PU/citNa-AuNRs, c) PU/citNa-AuNSs, d) PU/CV, e) PU/citNa-AuNRs/CV and f) PU/citNa-AuNSs/CV. All the results of PU/CV, PU/citNa-AuNRs/CV and PU/citNa-AuNSs/CV were statistically different compared to PU for the same time of exposure ($p \leq 0.05$).

Studying the activity of the film in detail, it can be seen that the films containing AuNRs and CV (PU/citNa-AuNRs/CV, Figure 4.4.10.e) reduced the population of bacteria by 1-log unit after 1 h and 1.5 h of exposure, 1.5-log unit for 2 h, 2.5-log unit for 3 h, and 3-log unit for 4 h. While films containing CV and AuNSs (PU/citNa-AuNSs/CV, Figure 4.4.10.f) reduced the bacteria population by 1-log unit for 1 h exposure, 1.2-log unit for 1.5 h, 1.5-log unit for 2 h, 2-log unit for 3 h and 2.5-log unit for 4 h.

Finally the films containing CV alone (PU/CV, Figure 4.4.10.d) killed 0.5-log unit of bacteria for 1 h and 1.5 h of exposure, 1-log unit for 2 h and 2-log unit for 3 and 4 h.

For this type of bacteria, the experimental conditions caused only a small loss of population, reducing the population of *S. aureus* of less than 1-log unit for 4 h of exposure.

The films containing nanoparticles alone had only a minor effect on the population of bacteria, showing only 1-log of reduction of the *S. aureus* population for the last two time points (regardless of the kind of nanoparticles used), this result was too close to the effect of the experimental conditions alone to be considered statistically relevant $p > 0.05$.

As discussed earlier (section 4.4.2.1), *S. aureus* bacteria were not very susceptible to the ROS because they could produce radical quenching molecules and pigmentation, while deploying enzymes able to decompose ROS. All contained in a hard and thick cell barrier making them resistant to physical stresses. The experiments in this thesis confirmed the notion by showing how *S. aureus* bacteria were less sensitive to the increase of ROS caused by the introduction of AuNRs and AuNSs in the film.

It is also important to observe that the reduction of Gram(+) bacteria did not seems correlated to the amount of ROS produced by the films, as much as seen for Gram(-) bacteria. Against *S. aureus* CV alone seems more efficient than against *E. coli* (Figure 4.4.9.d and Figure 4.4.10.d), while the films containing gold nanoparticles had a reduced effect on the bacteria population. With the film containing CV and AuNSs (CV/citNa-AuNSs/PU,

Figure 4.4.10.f) which produced the largest amount of ROS per hour (section 3.4.6.3), able to kill less Gram(+) bacteria than the one containing AuNRs and CV (CV/citNa-AuNRs/PU, Figure 4.4.10.e).

The reason of this discrepancy between ROS production and antimicrobial action has not been completely explained, but it clearly indicates that the antimicrobial action involves more than the simple ROS production, in the next section (4.4.3.3) the differences between the two model bacteria are explored and some possible explanation for their behaviour with ROS will be proposed.

4.4.3.3. Comparison of different activity against the bacterium types

The response of Gram(+) bacteria to the ROS produced by the film was in contrast with the findings for antimicrobial surfaces found in literature and to the general behaviour of these type of bacteria against ROS.[138,161,224,225]

The discrepancy between the ROS production and the activity of the film against Gram(+) and Gram(-) bacteria indicated that the film action did not depend exclusively form the quantity of ROS produced by the film, but it implies that other factors contributed to the action of the film.

One possible explanation of the discrepancy between ROS production and activity, could be connected to the different mechanism of action of ROS on Gram(+) and Gram(-) bacteria. Radical species kills Gram(+) bacteria by damaging the DNA after passing through the pores in the bacterial barrier (section 4.4.2.1.1). While their action on Gram(-) depends on their ability to damage both the layers of their cell walls and thus causing the bacteria to burst (section 4.4.2.2.1).[226]

These considerations suggested that ROS generated by the film were not able to pass the membranes while instead attacked the bacteria from outside.

Another reason that could explain the difference in antimicrobial activity could be the difference in the energy absorbed by the coupled plasmonic systems containing AuNRs and AuNSs (Figure 3.4.26 and studied in section 3.4.6.3). The amount of energy absorbed by the coupled system could influence energy available for the formation of ROS, resulting in larger amount of ROS but also to the formation of more energetic and reactive ROS molecules (section 1.1.4.3).

As introduced previously (section 1.1.4.3) the radical species called ROS are composed of a mixture of several types of reactive molecules ($^1O_2$, O_3^-, $\cdot OH$, $\cdot OOH$, H_2O_2, $\cdot CO_3$, $\cdot NO$), these molecules had different potential energy of formation and mean free paths which changed the time they could spend in solution before reacting with something and be converted in less reactive molecules (O_2, H_2O, NO_2, etc.).[227] Because the interactions between gold nanoparticles and dye increased the energy available to produce ROS, a greater amount of ROS was produced (section 3.4.6 and Figure 3.4.30), but at the same time it could catalyse the formation of specific species, encouraging the generation of ROS with a higher formation energy.

The production of specific ROS is extremely complicated to demonstrate because all ROS are very reactive and unstable, and they generally interact with the same type of indicators. Specific indicators exist but they are not completely specific, and moreover they were damaged by the test conditions (mostly the exposure to light). But the results of the

antimicrobial experiments could give an indication of the type of ROS formed by the films.

As reported in literature, different types of bacteria are more vulnerable to specific types of ROS, for example Gram(-) bacteria are more vulnerable to ·OH, ·OOH radicals while Gram(+) were more vulnerable to $^1O_2$, O_3^- species.[81]

Thus, suggesting that the film with AuNSs was mostly producing ·OH, ·OOH radicals while AuNRs was producing a larger amount of $^1O_2$, O_3^- species. Another possible explanation could be that the species formed were so reactive, as they could destroy the thin cell walls of Gram(-). However, the cell wall of Gram(+) bacteria was 10 times thicker, therefore the ROS produced by the film were less effective against it.

4.5. Conclusions

In this chapter the activity of the film against bacteria was studied. The first part analysed the experimental conditions necessary to control the reproducibility of the antimicrobial experiments, in the second, the characteristics of the bacteria tested were explored, while in the third the films efficiency against different types of bacteria was analysed.

In order to better understand the parameters influencing the action of the film different experiments were performed: as studying the effect of a closed container surrounding the film or investigating if the hyperthermia properties of the particles in the film participated to the action of the film.

While at the same time, studying the relation between activity of the film and intensity of light exposure to gain insight on the mechanism of action of the film and on the limits of possible applications.

Then in the second part of this chapter the characteristics of the bacteria used as model of Gram(+) and Gram(-) bacteria were analysed as the mechanisms used by these bacteria to defend themselves from ROS.

Finally, the activity of the film against bacteria have been studied. Analysing time of exposure between 1 and 4 h and difference in their activity against Gram(+) and Gram(-) bacteria. The analysis of the results in relation to the ROS production and to the interactions between dye and gold nanoparticles have been used to gain insight on the mechanism of action of the film.

Chapter 5: Summary, conclusions and further directions

5.1. Summary

The main contribution of this thesis to the "state of the art" of the antimicrobial surfaces was the successful preparation of antibacterial PU films with embedded metal nanoparticles and a sensitizer dye. The hypothesis that with careful tuning of the aspect ratio of anisotropic metal nanoparticles could be possible to improve the plasmonic coupling with a photosensitizer dye and boost the ROS production of a polymeric film, was confirmed. While the efficiency of the ROS production of the film as a way to kill Gram(+) and Gram(-) bacteria was evaluated.

To confirm the hypothesis, synthetic procedures to obtain gold nanorods and gold nanostars with SPR peaks compatible with the absorption of crystal violet were selected and refined (sections 2.4.1 - 2.4.3) and followed by an extensive characterization of their physical-chemical and optical properties (sections 2.4.4 - 2.4.6).

A series of standardized procedures to introduce particles and the dye in the film have been developed and the resulting films analysed (sections 3.4.2 - 3.4.4). The interaction between particles and dye both in solution or in the film was studied and characterized (section 3.4.5).

The results of the interactions analysis were compared with the overlapping of the SPR absorption peaks mathematically simulated with the PS dye, to obtain information on the resonance components contributing to the overlapping (section 3.4.6).

The amount of ROS produced by the film was quantified with fluorescent probes (section 3.4.6) and its antimicrobial efficiency, tested in relation to

the light intensity, time of exposure or type of bacteria (section 4.4.1). The effect against Gram(+) and Gram(-) was studied and compared with the ROS production activity of the films and their structure (section 4.4.3).

In summary, the work contained in this thesis demonstrated that the SPR of anisotropic nanoparticles could interact with crystal violet PS dye within a polyurethane film to generate a larger amount of ROS than the dye alone. The interaction studied showed a relation between the electrical field polarization caused by the SPR and the increased ROS production.

The components of the SPR absorption overlapping with the dye have been demonstrated to contribute to the efficiency of the ROS. Bacteria of all the Gram types have demonstrated to be vulnerable to the action of the film. With Gram(-) bacteria being the most effected with 5-log of reduction after 4 h of light exposure while Gram(+) bacteria were reduced of 3-log in the same amount of time (section 4.4.3).

5.2. Conclusions

The increasing capability of Gram(+) and Gram(-) bacteria to develop resistance against drugs is a threat against the global public health.[4,228] Developing new antibiotics is a slow and complex endeavour which requires multiples steps of development and clinical testing.[229]

Thus, the only realistic strategy to reduce the health risk of these types of bacteria is to improve the disinfection methods, in order to reduce the risk of contact with resistant bacteria.[230,231]

In this thesis, an antimicrobial film was developed able to kill the bacteria on its surface when exposed to a certain level of light intensity. This film is capable of contactless disinfection which could greatly contribute on the

disinfection performance of the routine cleaning procedure of medical surfaces.

At the same time the film avoids most of the drawbacks of terminal disinfection (e.g. surfaces degradation, toxicity, time consumed in the procedure, etc.),[130,232] being able to kill bacteria, only when activated with light and to avoid toxicity when not activated. The activation required only an intense commercially available white light, thus, it maintained the environment accessible during the disinfection procedure.[10,11]

When exposed to 11.7 klux of white light from a commercially available neon lamp the film embedded with AuNSs was able to eliminate 5-log unit of Gram(-) and 2.5-log unit of Gram(+) in 4 h of light exposure. While, on the other hand, the film modified with AuNRs eliminated 4-log unit of Gram(-) and 3-log unit of Gram(+) in the same amount of time.[11]

Compared to similar film reported in literature, while requiring a relatively high light intensity, the film developed was able to generate a larger antimicrobial effect in a shorter amount of time, especially against Gram(-) bacteria which were generally more resistant against ROS based methods.[138,161,233]

There are previous examples of antimicrobial films reported in literature constituted by polyurethane, CV dye and gold nanostructures able to catalyse the production of ROS when exposed to light (e.g. MacDonald 2016, Walker 2017), but they used small nanocluster of gold (≈2 nm, diameter) to trigger a photocatalytic effect.[77,138]

The specific mechanisms of ROS generation of these systems, were not confirmed, but they required relatively low light intensity and maintained a

certain activity in the dark, which could not be explained with photocatalysis.[138,161]

The size and the shape of the gold nanostructures used in the creation of the film had a fundamental role in its mechanism of action. From literature and direct observation (section 4.4.1.4),[138] it was clear that spherical gold nanoparticles above 10 nm in diameters showed no activity. On the other hand, AuNRs of 32 nm in length and 16 nm in diameter had demonstrated to greatly increase the activity of the film and furthermore AuNSs of 35 nm core diameter and 16 nm of spike length were able to generate a greater amount of ROS, compared to all the other nanostructures.

This discrepancy in the antimicrobial behaviour was caused by the fundamental difference between metal clusters and plasmonic anisotropic nanoparticles. The first behaving as a semiconductor and too small to interact with visible light, while the others were large enough to have a defined SPR in the visible range and they could be tuned to overlap with the absorption peak of the dye.

The comprehension of the complex interaction between the absorption bands generated by the SPR effect of anisotropic nanoparticles and the excited state of the PS dye was the main aim of the theoretical section of this work of thesis. Which led to the study of the SPR absorption of the particles both in solution and in the film and to the comparison of the analysis results to the simulation of the fluctuation of their electrical field caused by the SPR effect and its geometrical components (SPR along the length and the diameter for AuNRs or core, spike and spike system for AuNSs). Followed by an intensive study of the interaction dye-particles and

of the ROS production to understand which of the parameters influenced the antibacterial activity of the films.

The study of the films and solutions containing CV and gold nanoparticles identified the plasmonic coupling as the main mean of interaction between them and the couple AuNSs-CV as the one forming the strongest coupling. This couple being able to increase the ROS production of 0.72 mM per hour of light exposure when compared to the AuNRs-CV couple and to improve the production of the film containing dye alone of ≈ 3 mM/h.

The study of the antimicrobial action of these films showed a different rate of activity against Gram(-) and Gram(+) bacteria, with the first largely more vulnerable to the action of the film compared to the second. These behaviours were in direct contrast with the observations on cluster systems reported in literature which were more efficient against Gram(+) bacteria,[138] which was another indication of the radical difference in mechanisms of action of the two systems.[10,11]

5.3. Further directions

The research in this thesis demonstrated that gold nanostructures could be used to boost the ROS production, if their shape and aspect ratio was tuned to obtain an overlap between their SPR absorption and the absorption peak of the dye. The intensity of the electrical field polarization caused by the SPR had also been proved to be important to increase the ROS production of the plasmonic couple dye-particle.

Of all the PS tested in this thesis only CV had been demonstrated to be able to generate the stronger plasmonic coupling with the nanoparticles prepared and to generate an increase of ROS production.

Further developments of the simulation effort would be necessary to identify new PS molecules able to couple strongly with the nanoparticles with the aim to develop films able to have a faster antimicrobial activity and lower activation energy.

A peculiarity of the films developed was that they were able to kill bacteria at a different rate according to their Gram type; future experiments could be performed to determine the exact composition of the ROS produced and their effect against different Gram types.

The different response of the bacteria to the film suggested the possibility of the development of films calibrated to attack specific types of bacteria or films containing different types of particles able to trigger the elimination of different types of bacteria with increasing illumination levels.

Finally, the nanoparticles developed in this work have great potential for many different research applications. Some applications have been demonstrated, either by me or by from different collaborators of the research group all around the world (more details in the appendix). The short nanorods in particular have shown a relative resistance to aggregation and could be functionalized with different substrate making it an attractive device for further nanotechnological applications.

Appendix

A.1. Short spin off projects and collaborations

A.1.1. Nanoparticles for microwave frequencies hyperthermia.

The development of gold nanoparticles to use as focus for microwave hyperthermia was an ongoing project developed in collaboration with the Physics department of the University of Malta.

The work for this project has been conducted in collaboration with Julian Bonello of the Electromagnetics research laboratory under the supervision of professor Charles v Sammut. The project was funded with the support of the European collaboration in science and technology (COST) program by two short term scientific mission (STSM) grants focused on:

- Preparation of peptide stabilized gold nanoparticles for microwave frequencies hyperthermia
- Preparation of peptide stabilized gold nanostars for microwave frequencies hyperthermia

A.1.2. Effect of curcumin silver nanoparticles on human-pterygium derived keratinocytes.

The synthetic and characterization part of this project has been conducted at the HBL laboratories of the Royal Institution of Great Britain in London in collaboration with Gianmarco Stati of the Histology department of the university “G. d’Annunzio” of Chieti. The aim of the project was the synthesis and characterization of curcumin/silver nanoparticles for the treatment of human-pterygium which was a semi-tumoral disease of the cornea.

A.2. Minor contributions

- Exploration of gold nanorods as theragnostic AuNRs/polymer devices

Main investigator: Dr Hiroshi Yabu, Tohoku University Advanced Institute for Materials Research (AIMR), Japan

Contribution to the project: Synthesis and characterization of AuNRs of different lengths and aspect ratio to use as support for polymeric substrate.

- Gold nanoparticle for the field detection of the bacteria contamination of cooling tower water.

Main investigator: Dr Sian Yang Ow, IMRE A*STAR, Singapore

Contribution to the project: Synthesis protocol and surface modification procedure for short AuNRs.

A.2.1. Projects with master students

- Packman H., "Investigating the role of silver nitrate in the synthesis of gold nanorods"
- Gray J., "Finetuning the Aspect Ratio of Gold Nanorods"
- Hymas G., MacBride S., Popov I., "Development of nanoparticles modified sensor membrane for thermal detection of bacteria"

Publications, Presentations and Grants

1. Publications

1. **Rossi F.**, Thanh N.T.K., Su X. “Gold Nanorods Embedded in Polymeric Film for Killing Bacteria by Generating Reactive Oxygen Species with Light”. ACS Applied Biomaterials. 2019; 2 (7), 3059–67.

Available from: http://pubs.acs.org/doi/10.1021/acsabm.9b00343

2. **Rossi F.**, Khoo E.H., Su X., Thanh N.T.K. “Study of the Effect of Anisotropic Gold Nanoparticles on Plasmonic Coupling with a Photosensitizer for Antimicrobial Film.” ACS Applied Biomaterials. 2020; 3 (1), 315–26.

Available from: https://pubs.acs.org/doi/10.1021/acsabm.9b00838

3. Sharma S.K., Shrivastava N., **Rossi F.**, Tung L.D., Thanh N.T.K. “Nanoparticles-based magnetic and photo induced hyperthermia for cancer treatment.” Nano Today. 2019; 29, 100795.

Available from: https://linkinghub.elsevier.com/retrieve/pii/S174801321930115X

4. Bonello J., **Rossi F.**, Thanh N.T.K., Farhat I., Farrugia L., Sammut, C.V. “An investigation into the use of CALNN capped gold nanoparticles for improving microwave heating” 2019 International Conference on Electromagnetics in Advanced Applications (ICEAA). 2019; 1058 – 1061.

Available from: https://ieeexplore.ieee.org/document/8878917/

2. Presentations

2.1. Oral presentations

- *An investigation into the use of CALNN capper Gold Nanoparticles for improving microwave heating.* Presented at COST MyWAVE MC meeting & Working Group Meeting, 13 – 14 January 2020, University of Lisbon, Lisbon.
- *Development of gold nanoparticle embedded polymeric film for light induced sterilization of surfaces.* Presented at MSc Open Day, 25 March 2019, UCL, London.
- *Development of gold nanoparticle embedded polymeric film for light induced sterilization of surfaces.* Presented at PhD progress review talk, 10 October 2018, UCL, London.

2.2. Poster presentations

- **Rossi F.**, Thanh N.T.K., "*Nanorods for Hyperthermia Study*". Presented at Functional Nanomaterials in Industrial Applications: Academic Industry Meet, 29 – 31 March 2016, UCLAN, Preston, UK.
- **Rossi F.**, Sandeep S., Wang L., MacRobert S., Thanh N.T.K., "*Preparation of Biocompatible Gold Nanorods for Biomedical Applications*". Presented at Nanoparticles with Morphological and Functional Anisotropy: Faraday Discussion, 04 – 06 July 2016, University of Strathclyde, Glasgow, UK.

3. Grants

- MyWave Cost Action 17115 – 45286: Preparation of peptide stabilized gold nanostars for microwave frequencies hyperthermia.

- MyWave Cost Action 17115 – 45165: Preparation of peptide stabilized gold nanoparticles for microwave frequencies hyperthermia.

References

1 N. D. Friedman, E. Temkin and Y. Carmeli, The negative impact of antibiotic resistance, *Clin. Microbiol. Infect.*, 2016, **22**, 416–422.

2 Centers for Disease Control and Prevention, Data Portal | HAI | CDC, https://www.cdc.gov/hai/data/portal/index.html, (accessed 9 September 2020).

3 R. D. Scott, S. D. Culler and K. J. Rask, Understanding the economic impact of health care-associated infections: A cost perspective analysis, *J. Infus. Nurs.*, 2019, **42**, 61–69.

4 M. Cecchini and D. L. Monnet, *Antimicrobial Resistance Tackling the Burden in the European Union*, 2019.

5 P. C. Carling and J. M. Bartley, Evaluating hygienic cleaning in health care settings: What you do not know can harm your patients, *Am. J. Infect. Control*, 2010, **38**, S41–S50.

6 S. J. Dancer, Controlling Hospital-Acquired Infection: Focus on the Role of the Environment and New Technologies for Decontamination, *Clin. Microbiol. Rev.*, 2014, **27**, 665–690.

7 D. Irving, D. A. Lamprou, M. Maclean, S. J. MacGregor, J. G. Anderson and M. H. Grant, A comparison study of the degradative effects and safety implications of UVC and 405 nm germicidal light sources for endoscope storage, *Polym. Degrad. Stab.*, 2016, **133**, 249–254.

8 C. Gugliotta, G. Deiana, M. Dettori, G. Sotgiu, A. Azara and P. Castiglia, Prevalence study on health-care associated infections and on the use of antimicrobials carried out with the light protocol of the European centre for disease prevention and control, *Ann. di Ig.*, 2020, **32**, 357–367.

9 S. S. Magill, E. O'Leary, S. J. Janelle, D. L. Thompson, G. Dumyati, J. Nadle, L. E. Wilson, M. A. Kainer, R. Lynfield, S. Greissman, S. M. Ray, Z. Beldavs, C. Gross, W. Bamberg, M. Sievers, C. Concannon, N. Buhr, L. Warnke, M. Maloney, V. Ocampo, J. Brooks, T. Oyewumi, S. Sharmin, K. Richards, J. Rainbow, M. Samper, E. B. Hancock, D. Leaptrot, E. Scalise, F. Badrun, R. Phelps and J. R. Edwards, Changes in prevalence of health care-associated infections in U.S. Hospitals, *N. Engl. J. Med.*, 2018, **379**, 1732–1744.

10 F. Rossi, N. T. K. N. T. K. Thanh and X. D. X. Di Su, Gold Nanorods Embedded in Polymeric Film for Killing Bacteria by Generating Reactive Oxygen Species with Light, *ACS Appl. Bio Mater.*, 2019, **2**, 3059–3067.

11 F. Rossi, E. H. Khoo, X. Su and N. T. K. Thanh, Study of the Effect of Anisotropic Gold Nanoparticles on Plasmonic Coupling with a Photosensitizer for Antimicrobial Film, *ACS Appl. Bio Mater.*, 2020, **3**, 315–326.

12 Engineering ToolBox, Met. Alloy. - Melting Temp., https://www.engineeringtoolbox.com/melting-temperature-metals-d_860.html,

(accessed 16 March 2020).

13 M. Cartwright, Gold in Antiquity - Ancient History Encyclopedia, https://www.ancient.eu/gold/, (accessed 16 March 2020).

14 M. Loos, in *Carbon Nanotube Reinforced Composites: CNR Polymer Science and Technology*, 2014, pp. 1–36.

15 F. E. Wagner, S. Haslbeck, L. Stievano, S. Calogero, Q. A. Pankhurst and K. P. Martinek, Before striking gold in gold-ruby glass, *Nature*, 2000, **407**, 691–692.

16 L. B. Hunt, The true story of Purple of Cassius - The birth of gold-based glass and enamel colours, *Gold Bull.*, 1976, **9**, 134–139.

17 X. The Bakerian Lecture. —Experimental relations of gold (and other metals) to light, *Philos. Trans. R. Soc. London*, 1857, **147**, 145–181.

18 The Royal Institution, Michael Faraday's gold colloids | The Royal Institution: Science Lives Here, https://www.rigb.org/our-history/iconic-objects/iconic-objects-list/faraday-gold-colloids, (accessed 17 March 2020).

19 E. C. Dreaden, A. M. Alkilany, X. Huang, C. J. Murphy and M. A. El-Sayed, The golden age: Gold nanoparticles for biomedicine, *Chem. Soc. Rev.*, 2012, **41**, 2740–2779.

20 S. K. Sharma, N. Shrivastava, F. Rossi, L. D. Tung and N. T. K. Thanh, Nanoparticles-based magnetic and photo induced hyperthermia for cancer treatment, *Nano Today*, 2019, **29**, 100795.

21 L. A. Kolahalam, I. V. Kasi Viswanath, B. S. Diwakar, B. Govindh, V. Reddy and Y. L. N. Murthy, Review on nanomaterials: Synthesis and applications, *Mater. Today Proc.*, 2019, **18**, 2182–2190.

22 M. L. Personick and C. A. Mirkin, Making sense of the mayhem behind shape control in the synthesis of gold nanoparticles, *J. Am. Chem. Soc.*, 2013, **135**, 18238–18247.

23 J. Turkevich, P. C. Stevenson and J. Hillier, *Discuss. Faraday Soc.*, 1951, 11, 55–75.

24 J. Turkevich, Colloidal gold. Part II - Colour, coagulation, adhesion, alloying and catalytic properties, *Gold Bull.*, 1985, **18**, 125–131.

25 G. Frens, Controlled Nucleation for the Regulation of the Particle Size in Monodisperse Gold Suspensions, *Nat. Phys. Sci.*, 1973, **241**, 20–22.

26 J. Kimling, M. Maier, B. Okenve, V. Kotaidis, H. Ballot and A. Plech, Turkevich method for gold nanoparticle synthesis revisited, *J. Phys. Chem. B*, 2006, **110**, 15700–15707.

27 T. E. Everhart, Persistence pays off: Sir Charles Oatley and the scanning electron microscope, *J. Vac. Sci. Technol. B Microelectron. Nanom. Struct.*, 1996, **14**, 3620–3624.

28 A. Bogner, P. H. Jouneau, G. Thollet, D. Basset and C. Gauthier, A history of scanning electron microscopy developments: Towards 'wet-STEM' imaging, *Micron*, 2007, **38**, 390–401.

29 R. Allen and H. Petrow, *US Pat. 4,044,193*, 1977.

30 N. R. Jana, L. Gearheart, and C. J. Murphy, Seed-mediated growth approach for shape-controlled synthesis of spheroidal and rod-like gold nanoparticles using a surfactant template, *Adv. Mater.*, 2001, **13**, 1389–1393.

31 B. Nikoobakht, Z. L. Wang and M. A. El-Sayed, Self-assembly of gold nanorods, *J. Phys. Chem. B*, 2000, **104**, 8635–8640.

32 B. Nikoobakht and M. A. El-Sayed, Preparation and Growth Mechanism of Gold Nanorods (NRs) Using Seed - Mediated Growth Method, *Chem. Mater.*, 2003, **15**, 1957–1962.

33 C. L. Nehl, H. Liao and J. H. Hafner, Optical properties of star-shaped gold nanoparticles, *Nano Lett.*, 2006, **6**, 683–688.

34 D. Kozanoglu, D. H. Apaydin, A. Cirpan and E. N. Esenturk, Power conversion efficiency enhancement of organic solar cells by addition of gold nanostars, nanorods, and nanospheres, *Org. Electron.*, 2013, **14**, 1720–1727.

35 Y. Fang, W. S. Chang, B. Willingham, P. Swanglap, S. Dominguez-Medina and S. Link, Plasmon emission quantum yield of single gold nanorods as a function of aspect ratio, *ACS Nano*, 2012, **6**, 7177–7184.

36 E. S. Kooij, W. Ahmed, C. Hellenthal, H. J. W. Zandvliet and B. Poelsema, From nanorods to nanostars: Tuning the optical properties of gold nanoparticles, *Colloids Surfaces A Physicochem. Eng. Asp.*, 2012, **413**, 231–238.

37 N. Li, P. Zhao and D. Astruc, Anisotropic Gold Nanoparticles: Synthesis, Properties, Applications, and Toxicity, *Angew. Chemie Int. Ed.*, 2014, **53**, 1756–1789.

38 R. M. Pallares, X. Su, S. H. Lim and N. T. K. Thanh, Fine-tuning of gold nanorod dimensions and plasmonic properties using the Hofmeister effects, *J. Mater. Chem. C*, 2015, **4**, 53–61.

39 J. Becker, A. Trügler, A. Jakab, U. Hohenester and C. Sönnichsen, The Optimal Aspect Ratio of Gold Nanorods for Plasmonic Bio-sensing, *Plasmonics*, 2010, **5**, 161–167.

40 Y. Wang, A. B. Serrano, K. Sentosun, S. Bals and L. M. Liz-Marzán, Stabilization and Encapsulation of Gold Nanostars Mediated by Dithiols, *Small*, 2015, **11**, 4314–4320.

41 B. Nikoobakht, M. A. El-Sayed, E.-S. Mostafa A. and M. A. El-Sayed, Preparation and growth mechanism of gold nanorods (NRs) using seed-mediated growth method, *Chem. Mater.*, 2003, **15**, 1957–1962.

42 W. Leng, P. Pati and P. J. Vikesland, Room temperature seed mediated growth of

gold nanoparticles: mechanistic investigations and life cycle assesment, *Environ. Sci. Nano*, 2015, **2**, 440–453.

43 J. G. Mehtala, D. Y. Zemlyanov, J. P. Max, N. Kadasala, S. Zhao and A. Wei, Citrate-Stabilized Gold Nanorods, *Langmuir*, 2014, **30**, 13727–13730.

44 G. F. Catá, H. C. Rojas, A. P. Gramatges, C. M. Zicovich-Wilson, L. J. Álvarez and C. Searle, Initial structure of cetyltrimethylammonium bromide micelles in aqueous solution from molecular dynamics simulations, *Soft Matter*, 2011, **7**, 8508–8515.

45 L. Scarabelli, A. Sánchez-Iglesias, J. Pérez-Juste and L. M. Liz-Marzán, A 'Tips and Tricks' Practical Guide to the Synthesis of Gold Nanorods, *J. Phys. Chem. Lett.*, 2015, **6**, 4270–4279.

46 M. Wuithschick, A. Birnbaum, S. Witte, M. Sztucki, U. Vainio, N. Pinna, K. Rademann, F. Emmerling, R. Kraehnert and J. Polte, Turkevich in New Robes: Key Questions Answered for the Most Common Gold Nanoparticle Synthesis, *ACS Nano*, 2015, **9**, 7052–7071.

47 Q. Zhang, H. Jing, G. G. Li, Y. Lin, D. A. Blom and H. Wang, Intertwining Roles of Silver Ions, Surfactants, and Reducing Agents in Gold Nanorod Overgrowth: Pathway Switch between Silver Underpotential Deposition and Gold-Silver Codeposition, *Chem. Mater.*, 2016, **28**, 2728–2741.

48 S. R. Jackson, J. R. McBride, S. J. Rosenthal and D. W. Wright, Where's the silver? imaging trace silver coverage on the surface of gold nanorods, *J. Am. Chem. Soc.*, 2014, **136**, 5261–5263.

49 F. Schulz, T. Homolka, N. G. Bastús, V. Puntes, H. Weller and T. Vossmeyer, Little adjustments significantly improve the Turkevich synthesis of gold nanoparticles, *Langmuir*, 2014, **30**, 10779–10784.

50 S. Atta, M. Beetz and L. Fabris, Understanding the role of AgNO 3 concentration and seed morphology in the achievement of tunable shape control in gold nanostars, *Nanoscale*, 2019, **11**, 2946–2958.

51 M. M. Vega, A. Bonifacio, V. Lughi, S. Marsi, S. Carrato and V. Sergo, Long-term stability of surfactant-free gold nanostars, *J. Nanoparticle Res.*, , DOI:10.1007/s11051-014-2729-z.

52 C. N. R. Rao, G. U. Kulkarni, A. Govindaraj, B. C. Satishkumar and P. J. Thomas, Metal nanoparticles, nanowires, and carbon nanotubes, *Pure Appl. Chem.*, 2000, **72**, 21–33.

53 X. Huang and M. A. El-Sayed, Gold nanoparticles: Optical properties and implementations in cancer diagnosis and photothermal therapy, *J. Adv. Res.*, 2010, **1**, 13–28.

54 V. Amendola, R. Pilot, M. Frasconi, O. M. Maragò and M. A. Iatì, Surface plasmon resonance in gold nanoparticles: a review, *J. Phys. Condens. Matter*, 2017, **29**, 203002.

55 V. H. Nguyen and B. H. Nguyen, Quantum theory of plasmon, *Adv. Nat. Sci. Nanosci. Nanotechnol.*, 2014, **5**, 025001.

56 M. A. Noginov, V. A. Podolskiy, G. Zhu, M. Mayy, M. Bahoura, J. A. Adegoke, B. A. Ritzo and K. Reynolds, Compensation of loss in propagating surface plasmon polariton by gain in adjacent dielectric medium, *Opt. Express*, 2008, **16**, 1385.

57 M. Hu, J. Chen, Z.-Y. Li, L. Au, G. V. Hartland, X. Li, M. Marquez and Y. Xia, Gold nanostructures: engineering their plasmonic properties for biomedical applications, *Chem. Soc. Rev.*, 2006, **35**, 1084.

58 S. D. Gedney, Introduction to the Finite-Difference Time-Domain (FDTD) Method for Electromagnetics, *Synth. Lect. Comput. Electromagn.*, 2011, **6**, 1–250.

59 T. Corridoni, M. D'Anna and H. Fuchs, Damped Mechanical Oscillator: Experiment and Detailed Energy Analysis, *Phys. Teach.*, 2014, **52**, 88–90.

60 S. Sambandan, in *Circuit Design Techniques for Non-Crystalline Semiconductors*, CRC Press, 2012, pp. 17–50.

61 P. Signell, S. Andrew, K. Eugene, J. R. M. Saavedra, A. Asenjo-Garcia, F. J. García De Abajo, T. Corridoni, M. D'Anna, H. Fuchs, R. H. M. Groeneveld, R. Sprik, A. Lagendijk, J. R. M. Saavedra, A. Asenjo-Garcia, F. J. García De Abajo, S. Link and M. A. El-Sayed, Hot-Electron Dynamics and Thermalization in Small Metallic Nanoparticles, *ACS Photonics*, 2016, **3**, 1637–1646.

62 C. Clavero, Plasmon-induced hot-electron generation at nanoparticle/metal-oxide interfaces for photovoltaic and photocatalytic devices, *Nat. Photonics*, 2014, **8**, 95–103.

63 C. S. Kumarasinghe, M. Premaratne, Q. Bao and G. P. Agrawal, Theoretical analysis of hot electron dynamics in nanorods, *Sci. Rep.*, 2015, **5**, 1–15.

64 M. D. Daniell and J. S. Hill, A HISTORY OF PHOTODYNAMIC THERAPY, *ANZ J. Surg.*, 1991, **61**, 340–348.

65 R. Kropp, Niels Ryberg Finsen, *Pneumologie*, 2016, **70**, S180–S184.

66 K. I. Møller, B. Kongshoj, P. A. Philipsen, V. O. Thomsen and H. C. Wulf, How Finsen's light cured lupus vulgaris, *Photodermatol. Photoimmunol. Photomed.*, 2005, **21**, 118–124.

67 T. B. Fitzpatrick and M. A. Pathak, Part IV: Basic Considerations of the Psoralens: Historical Aspects of Methoxsalen and Other Furocoumarins, *J. Invest. Dermatol.*, 1959, **32**, 229–231.

68 J. Zhang, C. Jiang, J. P. Figueiró Longo, R. B. Azevedo, H. Zhang and L. A. Muehlmann, An updated overview on the development of new photosensitizers for anticancer photodynamic therapy, *Acta Pharm. Sin. B*, 2018, **8**, 137–146.

69 R. R. Allison and C. H. Sibata, Oncologic photodynamic therapy photosensitizers: A clinical review, *Photodiagnosis Photodyn. Ther.*, 2010, **7**, 61–75.

70 A. P. Castano, T. N. Demidova and M. R. Hamblin, Mechanisms in photodynamic therapy: part one—photosensitizers, photochemistry and cellular localization, *Photodiagnosis Photodyn. Ther.*, 2004, **1**, 279–293.

71 A. M. Maley and J. L. Arbiser, *Exp. Dermatol.*, 2013, 22, 775–780.

72 A. C. Smith and M. A. Hussey, Gram stain protocols, *Am. Soc. Microbiol.*, 2005, **1**, 14.

73 N. A. Littlefield, B. N. Blackwell, C. C. Hewitt and D. W. Gaylor, Chronic toxicity and carcinogenicity studies of gentian violet in mice, *Toxicol. Sci.*, 1985, **5**, 902–912.

74 M. Balabanova, L. Popova and R. Tchipeva, Dyes in dermatology, *Clin. Dermatol.*, 2003, **21**, 2–6.

75 Open Chemistry Database, Gentian violet | C25H30ClN3 - PubChem, https://pubchem.ncbi.nlm.nih.gov/compound/Gentian-violet#section=Solubility, (accessed 5 February 2020).

76 G. B. Hwang, E. Allan and I. P. Parkin, White Light-Activated Antimicrobial Paint using Crystal Violet, *ACS Appl. Mater. Interfaces*, 2016, **8**, 15033–15039.

77 T. Walker, M. Canales, S. Noimark, K. Page, I. Parkin, J. Faull, M. Bhatti and L. Ciric, A Light-Activated Antimicrobial Surface Is Active Against Bacterial, Viral and Fungal Organisms, *Sci. Rep.*, 2017, **7**, 1–10.

78 C. A. Robertson, D. H. Evans and H. Abrahamse, Photodynamic therapy (PDT): A short review on cellular mechanisms and cancer research applications for PDT, *J. Photochem. Photobiol. B Biol.*, 2009, **96**, 1–8.

79 D. Magde and M. W. Windsor, Picosecond internal conversion in crystal violet, *Chem. Phys. Lett.*, 1974, **24**, 144–148.

80 A. C. Bhasikuttan, A. V. Sapre and L. V. Shastri, Photoinduced electron transfer in crystal violet (CV+)-bovine serum albumin (BSA) system: Evaluation of reaction paths and radical intermediates, *J. Photochem. Photobiol. A Chem.*, 2002, **150**, 59–66.

81 L. Huang, Y. Xuan, Y. Koide, T. Zhiyentayev, M. Tanaka and M. R. Hamblin, Type I and Type II mechanisms of antimicrobial photodynamic therapy: An in vitro study on Gram-negative and Gram-positive bacteria, *Lasers Surg Med*, 2012, **44**, 490–499.

82 S. Noimark, E. Salvadori, R. Gómez-Bombarelli, A. J. MacRobert, I. P. Parkin and C. W. M. Kay, Comparative study of singlet oxygen production by photosensitiser dyes encapsulated in silicone: Towards rational design of anti-microbial surfaces, *Phys. Chem. Chem. Phys.*, 2016, **18**, 28101–28109.

83 M. Lahav, V. Heleg-Shabtai, J. Wasserman, E. Katz, I. Willner, H. Durr, Y. Z. Hu and S. H. Bossmann, Photoelectrochemistry with integrated photosensitizer-electron acceptor and Au-nanoparticle arrays, *J. Am. Chem. Soc.*, 2000, **122**, 11480–11487.

84 R. S. Swathi and K. L. Sebastian, Resonance energy transfer from a fluorescent dye molecule to plasmon and electron-hole excitations of a metal nanoparticle, *J. Chem. Phys.*, 2007, **126**, 234701.

85 B. Zhou, Y. T. Chen, X. L. Zhen, L. Lou, Yong-Sheng Wang and Q. L. Suo, Fluorescent resonance energy transfer of organic fluorescent dyes with gold nanoparticles and their analytical application, *Gold Bull.*, 2018, **51**, 145–151.

86 A. Bisht, J. Cuadra, M. Wersäll, A. Canales, T. J. Antosiewicz and T. Shegai, Collective Strong Light-Matter Coupling in Hierarchical Microcavity-Plasmon-Exciton Systems, *Nano Lett.*, 2019, **19**, 189–196.

87 H. Chen, T. Ming, L. Zhao, F. Wang, L.-D. Sun, J. Wang and C.-H. Yan, Plasmon–molecule interactions, *Nano Today*, 2010, **5**, 494–505.

88 G. Zengin, G. Johansson, P. Johansson, T. J. Antosiewicz, M. Käll and T. Shegai, Approaching the strong coupling limit in single plasmonic nanorods interacting with J-aggregates, *Sci. Rep.*, 2013, **3**, 1–8.

89 P. Zijlstra, P. M. R. Paulo and M. Orrit, Optical detection of single non-absorbing molecules using the surface plasmon of a gold nanorod, *Nat. Nanotechnol.*, 2012, **7**, 379–382.

90 M. K. Khaing Oo, Y. Yang, Y. Hu, M. Gomez, H. Du and H. Wang, Gold Nanoparticle-Enhanced and Size-Dependent Generation of Reactive Oxygen Species from Protoporphyrin IX, *ACS Nano*, 2012, **6**, 1939–1947.

91 X. Huang, I. H. El-Sayed, W. Qian and M. A. El-Sayed, Cancer cell imaging and photothermal therapy in the near-infrared region by using gold nanorods, *J. Am. Chem. Soc.*, 2006, **128**, 2115–2120.

92 M. J. R. Previte, K. Aslan, Y. Zhang and C. D. Geddes, Metal-enhanced surface plasmon-coupled phosphorescence, *J. Phys. Chem. C*, 2007, **111**, 6051–6059.

93 W. Ni, Z. Yang, H. Chen, L. Li and J. Wang, Coupling between Molecular and Plasmonic Resonances in Freestanding Dye−Gold Nanorod Hybrid Nanostructures, *J. Am. Chem. Soc.*, 2008, **130**, 6692–6693.

94 T. Kawawaki, Y. Takahashi and T. Tatsuma, Enhancement of dye-sensitized photocurrents by gold nanoparticles: Effects of plasmon coupling, *J. Phys. Chem. C*, 2013, **117**, 5901–5907.

95 B. Hu, X. Cao, K. Nahan, J. Caruso, H. Tang and P. Zhang, Surface plasmon-photosensitizer resonance coupling: An enhanced singlet oxygen production platform for broad-spectrum photodynamic inactivation of bacteria, *J. Mater. Chem. B*, 2014, **2**, 7073–7081.

96 G. Cui and W. H. Fang, State-specific heavy-atom effect on intersystem crossing processes in 2-thiothymine: A potential photodynamic therapy photosensitizer, *J. Chem. Phys.*, 2013, **138**, 044315.

97 WHO, *Global guidelines for the prevention of surgical site infection.*, Geneva, 2nd edn., 2016.

98 W. A. Rutala and D. J. Weber, in *Bennett & Brachman's Hospital Infections: Sixth Edition*, 2017.

99 E. Amodio and C. Dino, Use of ATP bioluminescence for assessing the cleanliness of hospital surfaces: A review of the published literature (1990–2012), *J. Infect. Public Health*, 2014, **7**, 92–98.

100 C. A. U. Jennifer H. Han, Nancy Sullivan, Brian F. Leas, David A. Pegues, Janice L. Kaczmarek, Cleaning Hospital Room Surfaces to Prevent Health Care– Associated Infections, *Ann. Intern. Med.*, 2015, **163**, 598–607.

101 B. Allegranzi, S. B. Nejad, C. Combescure, W. Graafmans, H. Attar, L. Donaldson and D. Pittet, Burden of endemic health-care-associated infection in developing countries: systematic review and meta-analysis, *Lancet*, 2011, **377**, 228–241.

102 E. Scallan, R. M. Hoekstra, F. J. Angulo, R. V Tauxe, M.-A. Widdowson, S. L. Roy, J. L. Jones and P. M. Griffin, Foodborne illness acquired in the United States--major pathogens., *Emerg. Infect. Dis.*, 2011, **17**, 7–15.

103 H. A. Khan, A. Ahmad and R. Mehboob, Nosocomial infections and their control strategies, *Asian Pac. J. Trop. Biomed.*, 2015, **5**, 509–514.

104 C. Dieter, in *WFCC Technical Information Sheets*, WFCC-Education Committee 1991, Braunschweig (Germany), 1991, pp. 1–5.

105 B. B. Biswas, P. S. Basu and M. K. Pal, Gram Staining and Its Molecular Mechanism, *Int. Rev. Cytol.*, 1970, **29**, 1–27.

106 H. Wisplinghoff, H. Seifert, R. P. Wenzel and M. B. Edmond, Current Trends in the Epidemiology of Nosocomial Bloodstream Infections in Patients with Hematological Malignancies and Solid Neoplasms in Hospitals in the United States, *Clin. Infect. Dis.*, 2003, **36**, 1103–1110.

107 A. F. Monegro and H. Regunath, *Hospital Acquired Infections*, StatPearls Publishing, 2020.

108 Scarlet fever - NHS, https://www.nhs.uk/conditions/scarlet-fever/, (accessed 23 April 2020).

109 Group B strep - NHS, https://www.nhs.uk/conditions/group-b-strep/, (accessed 23 April 2020).

110 M. N. Byappanahalli, M. B. Nevers, A. Korajkic, Z. R. Staley and V. J. Harwood, Enterococci in the Environment, *Microbiol. Mol. Biol. Rev.*, 2012, **76**, 685–706.

111 L. Lo Grasso, D. Chillura-Martino and R. Alduina, in *Actinobacteria - Basics and Biotechnological Applications*, InTech, 2016.

112 A. Gnanamani, P. Hariharan and M. Paul-Satyaseela, in *Frontiers in*

Staphylococcus aureus, InTech, 2017.

113 A. F. Gillaspy, J. J. Iandolo, Y. W. Tang and C. W. Stratton, in *Encyclopedia of Microbiology*, Elsevier, 2019, pp. 309–320.

114 H. Boucher, L. G. Miller and R. R. Razonable, Serious infections caused by methicillin-resistant Staphylococcus aureus, *Clin. Infect. Dis.*, , DOI:10.1086/653519.

115 D. J. Diekema, P. R. Hsueh, R. E. Mendes, M. A. Pfaller, K. V. Rolston, H. S. Sader and R. N. Jones, The microbiology of bloodstream infection: 20-year trends from the SENTRY antimicrobial surveillance program, *Antimicrob. Agents Chemother.*, 2019, **63**, 1–10.

116 Neisseria - an overview | ScienceDirect Topics, https://www.sciencedirect.com/topics/medicine-and-dentistry/neisseria, (accessed 30 April 2020).

117 Moraxella - an overview | ScienceDirect Topics, https://www.sciencedirect.com/topics/medicine-and-dentistry/moraxella, (accessed 30 April 2020).

118 M. Velázquez and J. M. Feirtag, Helicobacter pylori: characteristics, pathogenicity, detection methods and mode of transmission implicating foods and water, *Int. J. Food Microbiol.*, 1999, **53**, 95–104.

119 Vibrio | bacteria | Britannica, https://www.britannica.com/science/vibrio, (accessed 30 April 2020).

120 M. F. Brady and N. Pervin, *Acinetobacter*, StatPearls Publishing, 2020.

121 H. M. Wexler, Bacteroides: the Good, the Bad, and the Nitty-Gritty, *Clin. Microbiol. Rev.*, 2007, **20**, 593–621.

122 J. L. Ramos and R. C. Levesque, *Pseudomonas*, Springer US, Boston, MA, 2006, vol. 4.

123 A. Wasey and P. Salen, *Escherichia Coli (E Coli 0157 H7)*, StatPearls Publishing, 2018.

124 Z. D. Blount, The unexhausted potential of E. coli, *Elife*, , DOI:10.7554/eLife.05826.

125 E. Kintz, J. Brainard, L. Hooper and P. Hunter, Transmission pathways for sporadic Shiga-toxin producing E. coli infections: A systematic review and meta-analysis, *Int. J. Hyg. Environ. Health*, 2017, **220**, 57–67.

126 European Centre for Disease Prevention and Control, *Incidence and attributable mortality of healthcare-associated infections in intensive care units in Europe 2008-2012.*, 2018.

127 N. R. Naylor, K. B. Pouwels, R. Hope, N. Green, K. L. Henderson, G. M. Knight, R.

Atun, J. V. Robotham and S. R. Deeny, The health and cost burden of antibiotic resistant and susceptible Escherichia coli bacteraemia in the English hospital setting: A national retrospective cohort study, *PLoS One*, 2019, **14**, e0221944.

128 CDC. Center for Disease Control and Prevention, Best Practices for Environmental Cleaning in Healthcare Facilities : in Resource-Limited Settings, 2019, 1–91.

129 B. Singh and N. Sharma, Mechanistic implications of plastic degradation, *Polym. Degrad. Stab.*, 2008, **93**, 561–584.

130 L. Doan, H. Forrest, A. Fakis, J. Craig, L. Claxton and M. Khare, Clinical and cost effectiveness of eight disinfection methods for terminal disinfection of hospital isolation rooms contaminated with Clostridium difficile 027, *J. Hosp. Infect.*, 2012, **82**, 114–121.

131 S. Noimark, K. Page, J. C. Bear, C. Sotelo-Vazquez, R. Quesada-Cabrera, Y. Lu, E. Allan, J. A. Darr and I. P. Parkin, Functionalised gold and titania nanoparticles and surfaces for use as antimicrobial coatings, *Faraday Discuss.*, 2014, **175**, 273–287.

132 J. H. Han, N. Sullivan, B. F. Leas, D. A. Pegues, J. L. Kaczmarek and C. A. Umscheid, *Ann. Intern. Med.*, 2015, 163, 598–607.

133 J. M. Boyce, Modern technologies for improving cleaning and disinfection of environmental surfaces in hospitals, *Antimicrob. Resist. Infect. Control*, 2016, **5**, 1–10.

134 C. Adlhart, J. Verran, N. F. Azevedo, H. Olmez, M. M. Keinänen-Toivola, I. Gouveia, L. F. Melo and F. Crijns, Surface modifications for antimicrobial effects in the healthcare setting: a critical overview, *J. Hosp. Infect.*, 2018, **99**, 239–249.

135 D. R. Monteiro, L. F. Gorup, A. S. Takamiya, A. C. Ruvollo-Filho, E. R. de Camargo and D. B. Barbosa, The growing importance of materials that prevent microbial adhesion: antimicrobial effect of medical devices containing silver, *Int. J. Antimicrob. Agents*, 2009, **34**, 103–110.

136 D. J. Weber and W. A. Rutala, Self-disinfecting surfaces: Review of current methodologies and future prospects, *Am. J. Infect. Control*, 2013, **41**, S31–S35.

137 W. Kangwansupamonkon, V. Lauruengtana, S. Surassmo and U. Ruktanonchai, Antibacterial effect of apatite-coated titanium dioxide for textiles applications, *Nanomedicine Nanotechnology, Biol. Med.*, 2009, **5**, 240–249.

138 T. J. MacDonald, K. Wu, S. K. Sehmi, S. Noimark, W. J. Peveler, H. Du Toit, N. H. Voelcker, E. Allan, A. J. MacRobert, A. Gavriilidis and I. P. Parkin, Thiol-Capped Gold Nanoparticles Swell-Encapsulated into Polyurethane as Powerful Antibacterial Surfaces under Dark and Light Conditions, *Sci. Rep.*, 2016, **6**, 1–11.

139 S. Hayat, S. Muzammil, M. H. Rasool, Z. Nisar, S. Z. Hussain, A. N. Sabri and S. Jamil, In vitro antibiofilm and anti-adhesion effects of magnesium oxide nanoparticles against antibiotic resistant bacteria, *Microbiol. Immunol.*, 2018, **62**, 211–220.

140 L. V. de Araujo, C. R. Guimarães, R. L. da S. Marquita, V. M. J. Santiago, M. P. de Souza, M. Nitschke and D. M. G. Freire, Rhamnolipid and surfactin: Anti-adhesion/antibiofilm and antimicrobial effects, *Food Control*, 2016, **63**, 171–178.

141 A. F. De Faria, D. S. T. Martinez, S. M. M. Meira, A. C. M. de Moraes, A. Brandelli, A. G. S. Filho and O. L. Alves, Anti-adhesion and antibacterial activity of silver nanoparticles supported on graphene oxide sheets, *Colloids Surfaces B Biointerfaces*, 2014, **113**, 115–124.

142 Q. Liu and L. Liu, Novel Light-Responsive Hydrogels with Antimicrobial and Antifouling Capabilities, *Langmuir*, 2019, **35**, 1450–1457.

143 K. Gao, Y. Su, L. Zhou, M. He, R. Zhang, Y. Liu and Z. Jiang, Creation of active-passive integrated mechanisms on membrane surfaces for superior antifouling and antibacterial properties, *J. Memb. Sci.*, 2018, **548**, 621–631.

144 B. Song, E. Zhang, X. Han, H. Zhu, Y. Shi and Z. Cao, *ACS Appl. Mater. Interfaces*, 2020, 12, 21330–21341.

145 I. Niyonshuti, V. Krishnamurthi, D. Okyere, L. Song, M. Benamara, X. Tong, Y. Wang and J. Chen, Polydopamine Surface Coating Synergizes Antimicrobial Activity of Silver Nanoparticles, *ACS Appl. Mater. Interfaces*, 2020, **12**, 40067–40077.

146 O. Gherasim, A. M. Grumezescu, V. Grumezescu, F. Iordache, B. S. Vasile and A. M. Holban, Bioactive Surfaces of Polylactide and Silver Nanoparticles for the Prevention of Microbial Contamination, *Materials (Basel).*, 2020, **13**, 768.

147 K. P. Pontin, K. A. Borges, T. Q. Furian, D. Carvalho, D. E. Wilsmann, H. R. P. Cardoso, A. K. Alves, G. Z. Chitolina, C. T. P. Salle, H. L. de Souza Moraes and V. P. do Nascimento, Antimicrobial activity of copper surfaces against biofilm formation by Salmonella Enteritidis and its potential application in the poultry industry, *Food Microbiol.*, 2020, 103645.

148 U. Bogdanović, V. Vodnik, M. Mitrić, S. Dimitrijević, S. D. Škapin, V. Žunič, M. Budimir and M. Stoiljković, Nanomaterial with high antimicrobial efficacycopper/polyaniline nanocomposite, *ACS Appl. Mater. Interfaces*, 2015, **7**, 1955–1966.

149 R. Qi, R. Guo, F. Zheng, H. Liu, J. Yu and X. Shi, Controlled release and antibacterial activity of antibiotic-loaded electrospun halloysite/poly(lactic-co-glycolic acid) composite nanofibers, *Colloids Surfaces B Biointerfaces*, 2013, **110**, 148–155.

150 R. C. Petersen, Triclosan antimicrobial polymers, *AIMS Mol. Sci.*, 2016, **3**, 88–103.

151 F. Hui and C. Debiemme-Chouvy, *Biomacromolecules*, 2013, 14, 585–601.

152 M. D'Almeida, N. Attik, J. Amalric, C. Brunon, F. Renaud, H. Abouelleil, B. Toury and B. Grosgogeat, Chitosan coating as an antibacterial surface for biomedical applications, *PLoS One*, , DOI:10.1371/journal.pone.0189537.

153 N. Hilal, V. Kochkodan, L. Al-Khatib and T. Levadna, Surface modified polymeric membranes to reduce (bio)fouling: A microbiological study using E. coli, *Desalination*, 2004, **167**, 293–300.

154 A. Beaussart, C. Retourney, F. Quilès, R. Dos Santos Morais, C. Gaiani, H. P. Fiérobe and S. El-Kirat-Chatel, Supported lysozyme for improved antimicrobial surface protection, *J. Colloid Interface Sci.*, 2021, **582**, 764–772.

155 V. Leung, A. Szewczyk, J. Chau, Z. Hosseinidoust, L. Groves, H. Hawsawi, H. Anany, M. W. Griffiths, M. Monsur Ali and C. D. M. Filipe, Long-Term Preservation of Bacteriophage Antimicrobials Using Sugar Glasses, *ACS Biomater. Sci. Eng.*, 2018, **4**, 3802–3808.

156 M. Yasir, D. Dutta, K. R. Hossain, R. Chen, K. K. K. Ho, R. Kuppusamy, R. J. Clarke, N. Kumar and M. D. P. Willcox, Mechanism of Action of Surface Immobilized Antimicrobial Peptides Against Pseudomonas aeruginosa, *Front. Microbiol.*, 2020, **10**, 3053.

157 S. Zerbib, L. Vallet, A. Muggeo, C. de Champs, A. Lefebvre, D. Jolly and L. Kanagaratnam, Copper for the Prevention of Outbreaks of Health Care–Associated Infections in a Long-term Care Facility for Older Adults, *J. Am. Med. Dir. Assoc.*, 2020, **21**, 68-71.e1.

158 C.-J. Chung, H.-I. Lin, H.-K. Tsou, Z.-Y. Shi and J.-L. He, An antimicrobial TiO2 coating for reducing hospital-acquired infection, *J. Biomed. Mater. Res. Part B Appl. Biomater.*, 2008, **85B**, 220–224.

159 S. Perni, C. Piccirillo, J. Pratten, P. Prokopovich, W. Chrzanowski, I. P. Parkin and M. Wilson, The antimicrobial properties of light-activated polymers containing methylene blue and gold nanoparticles, *Biomaterials*, 2009, **30**, 89–93.

160 S. K. Sehmi, S. Noimark, J. C. Bear, W. J. Peveler, M. Bovis, E. Allan, A. J. MacRobert and I. P. Parkin, Lethal photosensitisation of Staphylococcus aureus and Escherichia coli using crystal violet and zinc oxide-encapsulated polyurethane, *J. Mater. Chem. B*, 2015, **3**, 6490–6500.

161 G. B. Hwang, H. Huang, G. Wu, J. Shin, A. Kafizas, K. Karu, H. Du Toit, A. M. Alotaibi, L. Mohammad-Hadi, E. Allan, A. J. MacRobert, A. Gavriilidis and I. P. Parkin, Photobactericidal activity activated by thiolated gold nanoclusters at low flux levels of white light, *Nat. Commun. 2020 111*, 2020, **11**, 1–10.

162 D. E. Mustafa, T. Yang, Z. Xuan, S. Chen, H. Tu and A. Zhang, Surface Plasmon Coupling Effect of Gold Nanoparticles with Different Shape and Size on Conventional Surface Plasmon Resonance Signal, *Plasmonics*, 2010, **5**, 221–231.

163 T. V. Tsoulos, L. Han, J. Weir, H. L. Xin and L. Fabris, A closer look at the physical and optical properties of gold nanostars: an experimental and computational study, *Nanoscale*, 2017, **9**, 3766–3773.

164 D. A. Giljohann, D. S. Seferos, W. L. Daniel, M. D. Massich, P. C. Patel and C. A. Mirkin, Gold nanoparticles for biology and medicine, *Angew. Chemie - Int. Ed.*,

2010, **49**, 3280–3294.

165 A. P. Leonov, J. Zheng, J. D. Clogston, S. T. Stern, A. K. Patri and A. Wei, Detoxification of Gold Nanorods by Treatment with Polystyrenesulfonate, *ACS Nano*, 2008, **2**, 2481–2488.

166 Molecular Devices, SpectraMax M2/M2e Microplate Readers, https://www.moleculardevices.com/sites/default/files/en/assets/data-sheets/br/spectramax-m2-m2e-microplate-readers.pdf, (accessed 31 July 2019).

167 ImageJ, https://imagej.net/Welcome, (accessed 17 October 2018).

168 C. Deraedt, L. Salmon, S. Gatard, R. Ciganda, R. Hernandez, M. Mayor and D. Astruc, Sodium borohydride stabilizes very active gold nanoparticle catalysts, *Chem. Commun.*, 2014, **50**, 14194–14196.

169 P. Sahu and B. L. V. Prasad, Time and Temperature Effects on the Digestive Ripening of Gold Nanoparticles: Is There a Crossover from Digestive Ripening to Ostwald Ripening?, *Langmuir*, 2014, **30**, 10143–10150.

170 K. Park, M. S. Hsiao, H. Koerner, A. Jawaid, J. Che and R. A. Vaia, Optimizing seed aging for single crystal gold nanorod growth: The critical role of gold nanocluster crystal structure, *J. Phys. Chem. C*, 2016, **120**, 28235–28245.

171 W. Zhao, F. Gonzaga, Y. Li and M. A. Brook, Highly Stabilized Nucleotide-Capped Small Gold Nanoparticles with Tunable Size, *Adv. Mater.*, 2007, **19**, 1766–1771.

172 S. Malola, L. Lehtovaara, J. Enkovaara and H. Häkkinen, Birth of the localized surface plasmon resonance in monolayer-protected gold nanoclusters, *ACS Nano*, 2013, **7**, 10263–10270.

173 N. C. Das, H. Cao, H. Kaiser, G. T. Warren, J. R. Gladden and P. E. Sokol, Shape and Size of Highly Concentrated Micelles in CTAB/NaSal Solutions by Small Angle Neutron Scattering (SANS), *Langmuir*, 2012, **28**, 11962–11968.

174 L. Coppola, R. Gianferri, I. Nicotera, C. Oliviero and G. A. Ranieri, Structural changes in CTAB/H2O mixtures using a rheological approach, *Phys. Chem. Chem. Phys.*, 2004, **6**, 2364–2372.

175 D. K. Smith, N. R. Miller and B. A. Korgel, Iodide in CTAB prevents gold nanorod formation, *Langmuir*, 2009, **25**, 9518–9524.

176 H.-M. Gao, H. Liu, H.-J. Qian, G.-S. Jiao and Z.-Y. Lu, Multiscale simulations of ligand adsorption and exchange on gold nanoparticles, *Phys. Chem. Chem. Phys.*, 2018, **20**, 1381–1394.

177 W. Ye, K. Krüger, A. Sánchez-Iglesias, I. García, X. Jia, J. Sutter, S. Celiksoy, B. Foerster, L. M. Liz-Marzán, R. Ahijado-Guzmán and C. Sönnichsen, CTAB Stabilizes Silver on Gold Nanorods, *Chem. Mater.*, 2020, **32**, 1650–1656.

178 F. Hubert, F. Testard and O. Spalla, Cetyltrimethylammonium bromide silver bromide complex as the capping agent of gold nanorods, *Langmuir*, 2008, **24**,

9219–9222.

179 A. M. Alkilany and C. J. Murphy, Toxicity and cellular uptake of gold nanoparticles: what we have learned so far?, 2010, **12**, 2313–2333.

180 B. Petkova, S. Tcholakova, M. Chenkova, K. Golemanov, N. Denkov, D. Thorley and S. Stoyanov, Foamability of aqueous solutions: Role of surfactant type and concentration, *Adv. Colloid Interface Sci.*, 2020, **276**, 102084.

181 Z. Zhang and M. Lin, Fast loading of PEG–SH on CTAB-protected gold nanorods, *RSC Adv.*, 2014, **4**, 17760.

182 N. G. Khlebtsov, Determination of size and concentration of gold nanoparticles from extinction spectra, *Anal. Chem.*, 2008, **80**, 6620–6625.

183 W. Haiss, N. T. K. Thanh, J. Aveyard and D. G. Fernig, Determination of Size and Concentration of Gold Nanoparticles from UV−Vis Spectra, *Anal. Chem.*, 2007, **79**, 4215–4221.

184 K. M. Usher, S. W. Hansen, J. S. Amoo, A. P. Bernstein and M. E. P. McNally, Precision of Internal Standard and External Standard Methods in High Performance Liquid Chromatography.

185 J. L. West and N. J. Halas, Engineered Nanomaterials for Biophotonics Applications: Improving Sensing, Imaging, and Therapeutics, *Annu. Rev. Biomed. Eng.*, 2003, **5**, 285–292.

186 E. W. Weisstein, Capsule, https://mathworld.wolfram.com/Capsule.html, (accessed 2 October 2020).

187 M. Nuriya, S. Fukushima, A. Momotake, T. Shinotsuka, M. Yasui and T. Arai, Multimodal two-photon imaging using a second harmonic generation-specific dye, *Nat. Commun.*, 2016, **7**, 1–10.

188 B. L. Darby, B. Auguié, M. Meyer, A. E. Pantoja and E. C. Le Ru, Modified optical absorption of molecules on metallic nanoparticles at sub-monolayer coverage, *Nat. Photonics*, 2016, **10**, 40–45.

189 M. M. Sajid, S. B. Khan, N. A. Shad, N. Amin and Z. Zhang, Visible light assisted photocatalytic degradation of crystal violet dye and electrochemical detection of ascorbic acid using a BiVO4/FeVO4 heterojunction composite, *RSC Adv.*, 2018, **8**, 23489–23498.

190 A. Kotta, S. A. Ansari, N. Parveen, H. Fouad, O. Y. Alothman, U. Khaled, H. K. Seo, S. G. Ansari and Z. A. Ansari, Mechanochemical synthesis of melamine doped TiO2 nanoparticles for dye sensitized solar cells application, *J. Mater. Sci. Mater. Electron.*, 2018, **29**, 9108–9116.

191 K. Drozdowicz-Tomsia, F. Xie, N. Calander, I. Gryczynski, K. Gryczynski and E. M. Goldys, Depolarized light scattering from colloidal gold nanoparticles, *Chem. Phys. Lett.*, 2009, **468**, 69–74.

192 Crystal Violet certified by the Biological Stain Commission | Sigma-Aldrich, http://www.sigmaaldrich.com/catalog/product/sigma/c0775?lang=en&region=US, (accessed 5 February 2020).

193 T. Bora, H. H. Kyaw, S. Sarkar, S. K. Pal and J. Dutta, Highly efficient ZnO/Au Schottky barrier dye-sensitized solar cells: Role of gold nanoparticles on the charge-transfer process, *Beilstein J. Nanotechnol.*, 2011, **2**, 681–690.

194 H. B. Lueck, B. L. Rice and J. L. McHale, Aggregation of triphenylmethane dyes in aqueous solution: Dimerization and trimerization of crystal violet and ethyl violet, *Spectrochim. Acta Part A Mol. Spectrosc.*, 1992, **48**, 819–828.

195 I. D. Johnson, in *Handbook Of Biological Confocal Microscopy*, Springer US, Boston, MA, 2006, pp. 353–367.

196 F. Rezende, R. P. Brandes and K. Schröder, Detection of Hydrogen Peroxide with Fluorescent Dyes, *Antioxid. Redox Signal.*, 2018, **29**, 585–602.

197 B. Ou, M. Hampsch-Woodill, J. Flanagan, E. K. Deemer, R. L. Prior and D. Huang, Novel fluorometric assay for hydroxyl radical prevention capacity using fluorescein as the probe., *J. Agric. Food Chem.*, 2002, **50**, 2772–7.

198 D. Alberto, G.-C. Carmen and B. Bartolomé, Extending Applicability of the Oxygen Radical Absorbance Capacity (ORAC−Fluorescein) Assay, *J. Agric. Food Chem.*, 2004, **52**, 48–54.

199 L. Song, C. A. G. O. Varma, J. W. Verhoeven and H. J. Tanke, Influence of the triplet excited state on the photobleaching kinetics of fluorescein in microscopy., *Biophys. J.*, 1996, **70**, 2959–68.

200 Y. Abe, S. Okada, R. Nakao, T. Horii, H. Inoue, S. Taniguchi and S. Yamabe, A molecular orbital study on the reactivity of L-ascorbic acid towards OH radical, *J. Chem. Soc. Perkin Trans. 2*, 1992, 2221.

201 P. Branduardi, T. Fossati, M. Sauer, R. Pagani, D. Mattanovich and D. Porro, Biosynthesis of vitamin C by yeast leads to increased stress resistance., *PLoS One*, 2007, **2**, e1092.

202 B. P. Eddy and M. Ingram, INTERACTIONS BETWEEN ASCORBIC ACID AND BACTERIA, *Bacteriol. Rev.*, 1953, **17**, 93–107.

203 S. Mowry and P. J. Ogren, Kinetics of Methylene Blue Reduction by Ascorbic Acid, *J. Chem. Educ.*, 1999, **76**, 970–974.

204 L. Song, E. J. Hennink, I. T. Young and H. J. Tanke, Photobleaching kinetics of fluorescein in quantitative fluorescence microscopy, *Biophys. J.*, 1995, **68**, 2588–2600.

205 M. Arik, N. Çelebi and Y. Onganer, Fluorescence quenching of fluorescein with molecular oxygen in solution, *J. Photochem. Photobiol. A Chem.*, 2005, **170**, 105–111.

206 J. Abbot and D. G. Brown, Stabilization of iron-catalysed hydrogen peroxide decomposition by magnesium, *Can. J. Chem.*, 1990, **68**, 1537–1543.

207 K. J. Youtsey and L. I. Grossweiner, Photochemical reactions of fluorescein dyes with hydrogen peroxide, *J. Phys. Chem.*, 1969, **73**, 447–448.

208 M. P. Singh and G. F. Strouse, Involvement of the LSPR Spectral Overlap for Energy Transfer between a Dye and Au Nanoparticle, *J. Am. Chem. Soc.*, 2010, **132**, 9383–9391.

209 A. Turano and F. Pirali, in *Laboratory Diagnosis of Infectious Diseases*, Springer New York, New York, NY, 1988, pp. 8–13.

210 T. D. Gauthier and M. E. Hawley, in *Introduction to Environmental Forensics*, Elsevier, 2007, pp. 129–183.

211 B. L. Welch, The Generalization of `Student's' Problem when Several Different Population Variances are Involved, *Biometrika*, 1947, **34**, 28.

212 L. N. Csonka, Physiological and genetic responses of bacteria to osmotic stress, *Microbiol. Rev.*, 1989, **53**, 121–147.

213 T. K. Nguyen, H. T. T. Duong, R. Selvanayagam, C. Boyer and N. Barraud, Iron oxide nanoparticle-mediated hyperthermia stimulates dispersal in bacterial biofilms and enhances antibiotic efficacy, *Sci. Rep.*, 2015, **5**, 1–15.

214 S. Perni, C. Piccirillo, A. Kafizas, M. Uppal, J. Pratten, M. Wilson and I. P. Parkin, Antibacterial Activity of Light-Activated Silicone Containing Methylene Blue and Gold Nanoparticles of Different Sizes, *J. Clust. Sci.*, 2010, **21**, 427–438.

215 J. Bozja, J. Sherrill, S. Michielsen and I. Stojiljkovic, Porphyrin-based, light-activated antimicrobial materials, *J. Polym. Sci. Part A Polym. Chem.*, 2003, **41**, 2297–2303.

216 T. J. Silhavy, D. Kahne and S. Walker, The bacterial cell envelope., *Cold Spring Harb. Perspect. Biol.*, 2010, **2**, 1–16.

217 G. Y. Liu, A. Essex, J. T. Buchanan, V. Datta, H. M. Hoffman, J. F. Bastian, J. Fierer and V. Nizet, Staphylococcus aureus golden pigment impairs neutrophil killing and promotes virulence through its antioxidant activity, *J. Exp. Med.*, 2005, **202**, 209–215.

218 A. W. Segal, How neutrophils kill bacteria, *Annu. Rev. Immunol.*, 2005, **23**, 197–223.

219 R. Gaupp, N. Ledala and G. A. Somerville, Staphylococcal response to oxidative stress, *Front. Cell. Infect. Microbiol.*, 2012, **2**, 1–19.

220 Y. Yamamoto, A. Harashima, H. Saito, K. Tsuneyama, S. Munesue, S. Motoyoshi, D. Han, T. Watanabe, M. Asano, S. Takasawa, H. Okamoto, S. Shimura, T. Karasawa, H. Yonekura and H. Yamamoto, Septic Shock Is Associated with Receptor for Advanced Glycation End Products Ligation of LPS, *J. Immunol.*, 2011,

186, 3248–3257.

221 S. I. Miller and N. R. Salama, The gram-negative bacterial periplasm: Size matters, *PLOS Biol.*, 2018, **16**, e2004935.

222 S. I. Liochev and I. Fridovich, Fumarase C, the stable fumarase of Escherichia coli, is controlled by the soxRS regulon, *Proc. Natl. Acad. Sci. U. S. A.*, 1992, **89**, 5892–5896.

223 J. A. Imlay, Cellular defenses against superoxide and hydrogen peroxide James, *Annu. Rev. Biochem.*, 2008, **77**, 755–776.

224 A. Jain, R. Bhargava and P. Poddar, Probing interaction of Gram-positive and Gram-negative bacterial cells with ZnO nanorods, *Mater. Sci. Eng. C*, 2013, **33**, 1247–1253.

225 E. Alpaslan, B. M. Geilich, H. Yazici and T. J. Webster, PH-Controlled Cerium Oxide Nanoparticle Inhibition of Both Gram-Positive and Gram-Negative Bacteria Growth, *Sci. Rep.*, 2017, **7**, 1–12.

226 L. Han, S. Patil, D. Boehm, V. Milosavljević, P. J. Cullen and P. Bourke, Mechanisms of Inactivation by High-Voltage Atmospheric Cold Plasma Differ for Escherichia coli and Staphylococcus aureus., *Appl. Environ. Microbiol.*, 2016, **82**, 450–8.

227 F. Al Housari, D. Vione, S. Chiron and S. Barbati, Reactive photoinduced species in estuarine waters. Characterization of hydroxyl radical, singlet oxygen and dissolved organic matter triplet state in natural oxidation processes, *Photochem. Photobiol. Sci.*, 2010, **9**, 78–86.

228 *Biggest Threats and Data | Antibiotic/Antimicrobial Resistance | CDC*, Atlanta, U.S., 2013.

229 J. O'Neill, in *The Review on Antimicrobial Resistance*, ed. J. O'Neill, UK Government, London, UK, 2015, p. 42.

230 V. Russotto, A. Cortegiani, S. M. Raineri and A. Giarratano, Bacterial contamination of inanimate surfaces and equipment in the intensive care unit, *J. Intensive Care*, 2015, **3**, 54.

231 M. Dettenkofer and C. Block, Hospital disinfection: Efficacy and safety issues, *Curr. Opin. Infect. Dis.*, 2005, **18**, 320–325.

232 D. J. Anderson, R. W. Moehring, D. J. Weber, S. S. Lewis, L. F. Chen, J. C. Schwab, P. Becherer, M. Blocker, P. F. Triplett, L. P. Knelson, Y. Lokhnygina, W. A. Rutala and D. J. Sexton, Effectiveness of targeted enhanced terminal room disinfection on hospital-wide acquisition and infection with multidrug-resistant organisms and Clostridium difficile: a secondary analysis of a multicentre cluster randomised controlled trial with crossover, *Lancet Infect. Dis.*, 2018, **18**, 845–853.

233 E. Ozkan, E. Allan and I. P. Parkin, White-Light-Activated Antibacterial Surfaces Generated by Synergy between Zinc Oxide Nanoparticles and Crystal Violet, *ACS*

Omega, 2018, **3**, 3190–3199.